Reading the Rain in Rocks: A late deglacial speleothem record from Sumatra, Indonesia

Jennifer Beth Wurtzel

Research School of Earth Sciences

November 2017

A thesis submitted for the degree of Doctor of Philosophy of
The Australian National University

Declaration

The work presented in this thesis is an accurate account of original research performed during the academic program towards the degree of Doctor of Philosophy at The Australian National University. I certify that this thesis does not incorporate any material either previously submitted for a degree or diploma at any university, or previously published or written by another person, except where due reference is made in the text.

Jennifer Beth Wurtzel

November 17, 2017

"It is only by combing the information furnished by all the earth sciences that we can hope to determine 'truth' here, that is to say, to find the picture that sets out all the known facts in the best arrangement and that therefore has the highest degree of probability. Further, we have to be prepared always for the possibility that each new discovery, no matter what science furnishes it, may modify the conclusions we draw."

Alfred Wegener, 1929, *The Origins of Continents and Oceans (4th ed.)*

Acknowledgments

First and foremost, this thesis would not have been possible without the support and guidance of my PhD supervisor, Nerilie Abram. Nerilie, thank you for giving me the opportunity to learn and explore on my own, and for reining me back in when I occasionally strayed and lost myself down rabbit holes. The scope of my project was both exciting and terrifying at times and I feel fortunate to have had you as a role model and mentor throughout the roller coaster ride that has been my PhD.

I would also like to thank my co-supervisor, Mike Gagan, who started the process of bringing me to ANU nearly 8 years ago! It was a long road but I'm so glad I made it. Mike, I'm so grateful for the opportunity to work on the Sumatran speleothems and for your assistance in acquiring those last bedrock samples that helped cement the unusual geological narrative of Tangga Cave. More thanks to the rest of my panel members, Dave Heslop, Steve Eggins, and Matt England, who provided valuable feedback at various stages of my PhD, helping me to refine methodology and statistics.

There would be no data without the brilliant technical staff in the paleoclimate lab and around RSES. Thank you to Heather Scott-Gagan, Joan Cowley, and Joe Cali for showing me the ways of the lab, and for keeping the MAT 253 up and running for pretty much my entire PhD. Thanks to Les Kinsley and Graham Mortimer for assistance with generating trace element and U/Th data on the LA-ICP-MS and Neptune. I am extremely grateful to Ulli Troitzsch for the many hours retrieving vital mineralogical data in the XRD and Raman spectroscopy labs and to Jodie Bradby and the Research School of Physics for use of the Raman. You were all with me on the unexpected journey from stalagmite to aragonite stalagmite to aragonite-calcite stalagmite.

Of course, there also would have been no research without samples, so I highly appreciate the hard work of all those who assisted with 2012 fieldwork in Sumatra, particularly our Indonesian colleagues, Professor Wahyoe Hantoro from the Indonesian Institute of Sciences (LIPI), and Dr. Hamdi Rifai from the State

University of Padang. Additional thanks for braving the Sumatran jungle to acquire speleothems goes out to Djupriano Djupri, Engkos Kosasih, Isnally Rifki, Claire Krause, and David Wools-Cobb.

There were many collaborators and co-authors who contributed to this thesis. For the beautiful geochronology on my speleothems, I am ever grateful to John Hellstrom and Petra Bajo at the University of Melbourne. For assistance with interpreting speleothem petrography, I am incredibly appreciative for the time and insight of Silvia Frisia at the University of Newcastle. I thank Jesse Nusbaumer and Allegra LeGrande from NASA GISS, whom have provided valuable model output as well as patient explanation of the data. Sophie Lewis, thank you for getting me started with GISS, but more importantly, thank you for the coffees and chats, and for being one of my most precious mentors.

This research was made possible by financial support from the Research School of Earth Sciences (International Student Fee Waiver), the Australian National University (ANU International PhD Scholarship and the ANU Research Supplementary Scholarship), the Australian Research Council (DP110101161, DP140102059), and the ARC Centre of Excellence for Climate System Science (CE110001028). I am also grateful to RSES, the DA Brown Travel Scholarship and the Australia Quaternary Association for financial support to attend domestic and international conferences, including the Karst Record 7 in Melbourne, Australia (2014), INQUA XIX Congress in Nagoya, Japan (2015), AGU Fall Meeting in San Francisco, USA (2015) and the Karst Record 8 in Austin, USA (2017).

To Claire, Ali and Nick, thank you for paving the way, showing me the ropes, celebrating the occasions, commiserating when needed, and being all-around awesome. There are not enough thanks in the world to cover how grateful I am to Claire and Ali for their continued support, both emotional and academic. You guys are my Canberran family.

Many others at RSES have provided comraderie over the years. Thanks especially to the many who joined me for writing sessions; Bethany, Hannah, Eleanor, Louise, Morgan, Rick, Kate, Katie and Kelsie. This thesis is most certainly a product of your

company. Also on the subject of writing support, I am grateful to ANU Higher Degree Research Skills and Training (especially Victoria and Inger) and PARSA for the frequent Shut Up and Write sessions, and for the Thesis Boot Camp, which really got the ball rolling.

My family has been incredibly supportive ever since I decided to be a scientist when I was 5, to get a PhD when I was 12, and to stay in school until I was 32 (it's been a long, long journey). To my Mom, Dad, little brother Ben, and my Grandmas Judy and Irene, thank you for cheering me on the whole way, even when it took me around the world.

To my husband, Jim – as promised, you've levelled up. I can't imagine what life would be if you hadn't gotten on that plane with me four years ago. There's too much to say, so let's keep it simple: thank you for *all the things.*

Abstract

The Intertropical Convergence Zone (ITCZ) is a key component of Hadley cell circulation. In the Indo-Pacific Warm Pool (IPWP) region, the seasonal migration of the ITCZ defines much of the precipitation variability over the Maritime Continent. The seasonal migration of the ITCZ in this region is also closely related to the Australasian monsoon, which brings critical rainfall to Asia and Indo-Australia, cumulatively home to approximately 40% of the global population. On interannual timescales, rainfall in the IPWP region is also connected with zonal climate variability of the El Niño-Southern Oscillation and Indian Ocean Dipole systems. Understanding the IPWP's climate sensitivities is therefore crucial to the improvement of long-term prediction of rainfall and drought.

Abrupt changes in Atlantic Meridional Overturning Circulation (AMOC) are known to have affected the strength of the Asian monsoon during glacial and deglacial climate states. However, there is still much uncertainty around the hydroclimate response of the IPWP region to abrupt climate changes in the North Atlantic. Speleothems are powerful archives for paleoclimatic reconstruction, providing absolute-dated and often highly-resolved records of past climate. Several speleothem oxygen-isotope ($\delta^{18}O$) records from the central IPWP and Asian summer monsoon regions provide decadally-resolved time-series of past rainfall variability since the last glacial period. Many studies have suggested a southward shift in the ITCZ in the IPWP region during phases of reduced AMOC. However, existing IPWP proxies have seasonal biases and conflicting responses, making it difficult to determine the true extent of North Atlantic forcing in this climatically important region. In Chapter 2 of this thesis, I present a precisely-dated, high-resolution record of eastern Indian Ocean hydroclimate variability spanning the last 16 ky (thousand years) from $\delta^{18}O$ measurements in an aragonite-calcite speleothem from central Sumatra. This represents the western-most speleothem record from the IPWP region and fills an important spatial gap in terrestrial hydroclimate, facilitating assessment of Warm Pool sensitivity at its lateral extent.

Petrographic and geochemical analysis reveals that the sample is principally composed of aragonite but is punctuated by intervals of primary calcite growth. In addition to mineralogical determination by Raman spectroscopy, trace element

analysis by laser ablation ICP-MS reveals strongly antiphased behaviour between magnesium and strontium attributed to the strong preference of those elements for the calcite and aragonite lattices, respectively. In Chapter 4, this relationship is utilized to develop a quantitative correction for the stable isotope fractionation offset between the two calcium carbonate polymorphs identified in the speleothem and to quantify partitioning coefficients for those elements into aragonite.

The corrected $\delta^{18}O$ record demonstrates a clear deglacial structure that includes ^{18}O enrichment during the Younger Dryas (~12.9-11.7 ka; thousand years ago) and ^{18}O depletion during the Bølling-Allerød (~14.7-12.9 ka), similar to the pattern seen in speleothems of the Asian and Indian monsoon realms. In contrast, other speleothem records from the IPWP show slight increases or no change in $\delta^{18}O$ during the Younger Dryas. To better interpret the spatial pattern of speleothem $\delta^{18}O$ change during the Younger Dryas, Chapter 3 uses back-trajectory air parcel analysis to identify primary moisture source regions and seasonal distributions of moisture to IPWP speleothem sites. This information is evaluated alongside modelled GISS ModelE-R vapour source distributions to evaluate how moisture sources may have changed during simulated hosing events analogous to the Younger Dryas.

Chapter 4 considers the environmental controls that could account for the mineralogy of the Sumatran speleothem sample. Shifts between aragonite and calcite phases in the speleothem are partly driven by environmental variability, with aragonite associated with drier phases like the Younger Dryas and calcite generally associated with increased detrital material. However, these changes are more likely to be related to cave hydrology and filtration rates than directly reflective of rainfall amounts.

Together, this research establishes a robust basis for interpreting the climatic history retained in the 16 ky speleothem $\delta^{18}O$ record for Tangga Cave and provides context relative to other speleothem records from the Indo-Pacific Warm Pool region. This work demonstrates the extended reach of North Atlantic abrupt forcing into the eastern tropical Indian Ocean, supporting this conclusion with systematic analysis of the modern hydroclimate system through use of isotope enabled climate models and back-trajectory air parcel analysis.

Table of Contents

List of Tables

List of Figures

1 Introduction

1.1 Overview

In May 2012, a reconnaissance expedition collected a small number of stalagmites from caves in the central region of Sumatra, Indonesia. Stalagmites are powerful archives for paleoclimatic reconstruction, providing absolute-dated and often highly-resolved records of past rainfall. Rainfall in Sumatra is highly sensitive to changes in the sea surface temperature (SST) gradient of the Indian Ocean, a phenomenon known as the Indian Ocean Dipole (IOD), which has been linked to drought and flooding across the Indian Ocean rim. The initial goal of this work was to use the stalagmites to reconstruct local rainfall and identify IOD states during the Holocene. In conjunction with the other regional Holocene records from the Indian Ocean rim and Indo-Pacific Warm Pool (IPWP), a Sumatran rainfall record would provide novel insight into the roles of internal Indian Ocean dynamics and large-scale global events on Holocene climate in the Warm Pool region.

Nine stalagmites were initially sampled at low-resolution for stable isotopes to determine viability for this reconstruction. Though most of the low-resolution records demonstrated muted variability, relatively large events were observed in the bottom section of one stalagmite, and later attributed to the Younger Dryas and deglaciation. Upon this discovery, the focus of this research shifted from the Holocene to the last glacial termination.

The last glacial termination (~19-10 ka) started after the Last Glacial Maximum (LGM; ~21 ka) and was characterized by multiple millennial-scale shifts in global climate (Clark et al., 2012; Denton et al., 2010). Records of the last deglaciation from Greenland ice cores exhibit a sequence of abrupt climatic shifts, starting with the cold interval, Heinrich Stadial 1 (HS1, ~17.5-14.7 ka; thousand years ago) (Figure 1.1) (Barker et al., 2009; Heinrich, 1988). This was followed by an abrupt warm Greenland interstadial (GI-1) also known as the Bølling-Allerød chronozone (BA, ~14.7-12.9 ka)) and a transition back to Greenland stadial conditions during the Younger Dryas chronozone (YD; also GS-1, ~12.9-11.7 ka) that culminated in

Holocene warmth starting ~11.7 ka (Björck et al., 1998; NGRIP members, 2004; Rasmussen et al., 2014; Stuiver and Grootes, 2000; Walker et al., 1999).

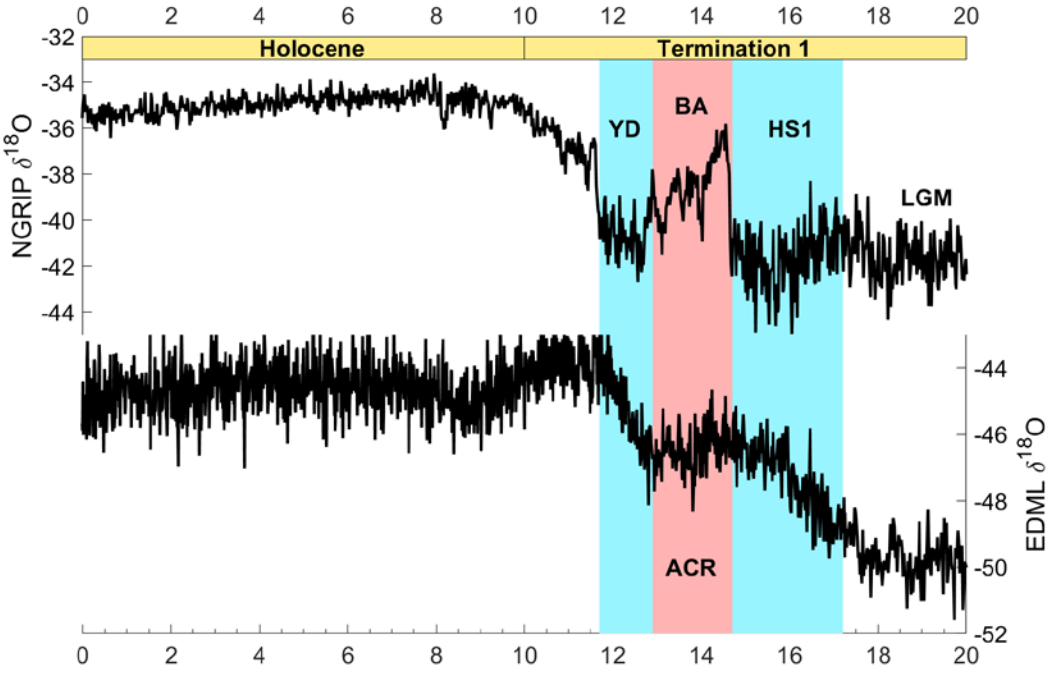

Figure 1.1 – (top) The deglacial progression of Greenland air temperature reconstructed from $\delta^{18}O$ measurements in the NGRIP ice core (NGRIP members, 2004). The deglacial progression of Antarctic air temperature reconstructed from $\delta^{18}O$ measurements in the EPICA Dronning Maud Land ice core (Oerter et al., 2004). Shaded blue bars indicate timing of Heinrich Stadial 1 (HS1) and Younger Dryas (YD). Shaded red bar indicates timing of Bølling-Allerød (BA; northern hemisphere) and Antarctic Cold Reversal (ACR; southern hemisphere).

Proxy records from the high latitudes suggest a 'bipolar seesaw' response, in which cooling (warming) in the northern hemisphere occurs in concert with warming (cooling) trends in the southern hemisphere (Barker et al., 2009; Blunier and Brook, 2001). For example, during the Greenland stadials, YD and HS1, Antarctica experienced warming temperatures, while during GI-1 (the Bølling-Allerød), Antarctic warming stalled or cooled during the Antarctic Cold Reversal (ACR) (Figure 1.1).

Northern hemisphere millennial-scale cold events like the YD and HS1 are thought to stem from weakening in the strength of Atlantic Meridional Overturning Circulation (AMOC), which reduced northward heat transport, cooled the northern high latitudes, and had widespread impacts on precipitation (Broecker et al., 2010;

Clark et al., 2002). Model and proxy data show that a robust response to a slowdown of AMOC is a warming in the southern hemisphere (the bipolar seesaw) (Knutti et al., 2004; Stocker et al., 2007; Vellinga and Wu, 2004), mean southward shift of the Intertropical Convergence Zone (ITCZ) in the tropics (Chiang and Bitz, 2005; Hughen et al., 1996; Zhang and Delworth, 2005) and a weakening of the Indian and Asian monsoon systems (Pausata et al., 2011; Shakun et al., 2007; Tierney et al., 2015; Wang et al., 2001).

The YD signal has been well-established in the North Atlantic (Hughen et al., 1996; McManus et al., 2004) and Eurasia (Bar-Matthews et al., 1999; Dykoski et al., 2005; Genty et al., 2006). However, the response of the Indo-Pacific tropics to the Younger Dryas is still not well resolved in either marine (Gibbons et al., 2014) or terrestrial records (Ayliffe et al., 2013; Denniston et al., 2013; Griffiths et al., 2009). Coupled ocean-atmosphere simulations have demonstrated that increasing greenhouse gases can lead to collapses of AMOC (Cai, 1996; Manabe and Stouffer, 1994; Swingedouw et al., 2007). In light of future changes, it is crucial to develop our understanding of past global responses to North Atlantic-forced abrupt events.

To that end, I present a precisely-dated, high-resolution record of eastern Indian Ocean hydroclimate variability spanning the last 16 ky (thousand years) from oxygen isotope ($\delta^{18}O$) measurements in an aragonite-calcite speleothem from Tangga Cave in central Sumatra. Aragonite has high levels of uranium, lending itself to precise uranium-thorium dating with small sample sizes (Zhang et al., 2013). The controls on isotope fractionation and trace element incorporation into aragonite are still being defined, but many studies have already successfully used aragonite speleothems for paleoclimatic reconstructions (Cosford et al., 2008; Green et al., 2015; Holmgren et al., 2003; Kotlia et al., 2016; Li et al., 2011).

Few studies to-date have used speleothems composed of both aragonite and calcite for paleo-reconstruction, or for the assessment of isotopic fractionation and trace element incorporation into aragonite (Jamieson et al., 2016; McMillan et al., 2005; Wassenburg et al., 2012; Wassenburg et al., 2013; Wassenburg et al., 2016) and many of these have focused on the effects of recrystallization from aragonite to

calcite (Domínguez-Villar et al., 2016; Lachniet et al., 2012; Ortega et al., 2005). The presence of primary calcite intervals within the aragonite specimen presented in this study posed both a challenge when generating a climate record and a unique opportunity to explore aragonite-calcite systematics.

1.2 Background

1.2.1 Study site and geologic setting

Sumatra is a large island in the western part of the Indonesian archipelago, located on a diagonal northwest-southeast axis between 6°N, 95°E and 6°S, 106°E. It lies within the Indo-Pacific Warm Pool (IPWP), ands forms part of the eastern border of the Indian Ocean. This area is subject to multiple sources of climatic variability, including the seasonal migration of the ITCZ, the Australasian Monsoon, the Indian Ocean Dipole (IOD), and the El Niño-Southern Oscillation (ENSO) (Figure 1.2).

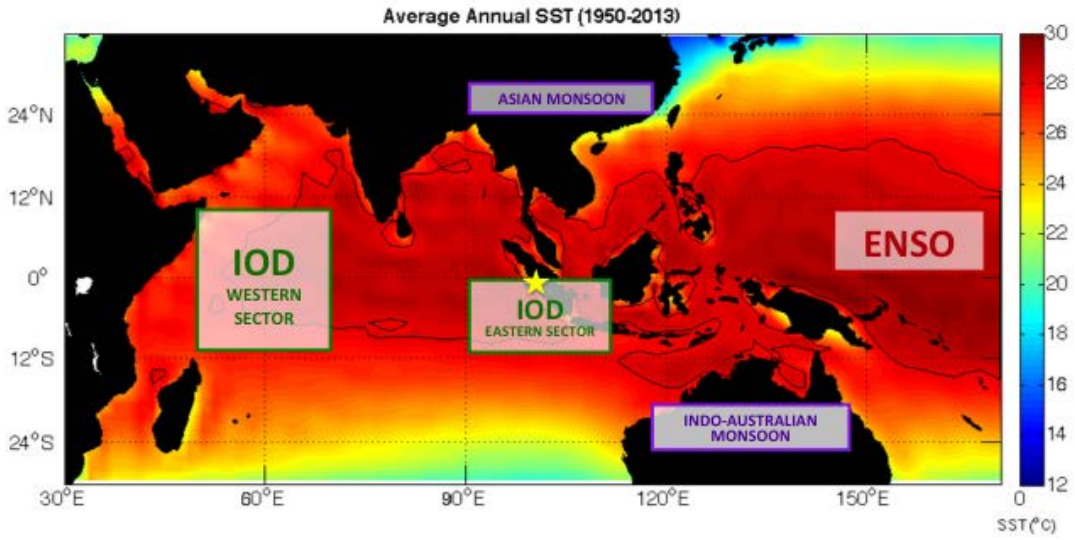

Figure 1.2 - Indo-Pacific region and influential climate modes. Color scale represents average annual SST. Black line denotes 28°C contour, the IPWP boundary. Yellow star indicates approximate location of Tangga Cave.

Tangga Cave (0.36 °S, 100.76 °E) is located in the forests of the Barisan Mountains of central West Sumatra, about 100 km inland from the Indian Ocean (Figure 1.3). The caves in this region lie within a Lower Carboniferous to Mid-Permian limestone member of the Kuantan Formation (Barber et al., 2005). Tangga Cave sits at ~600 m elevation in a valley surrounded by higher altitude formations. It

lies in the eastern proximity of several active volcanic mountains of up to 2600 m high.

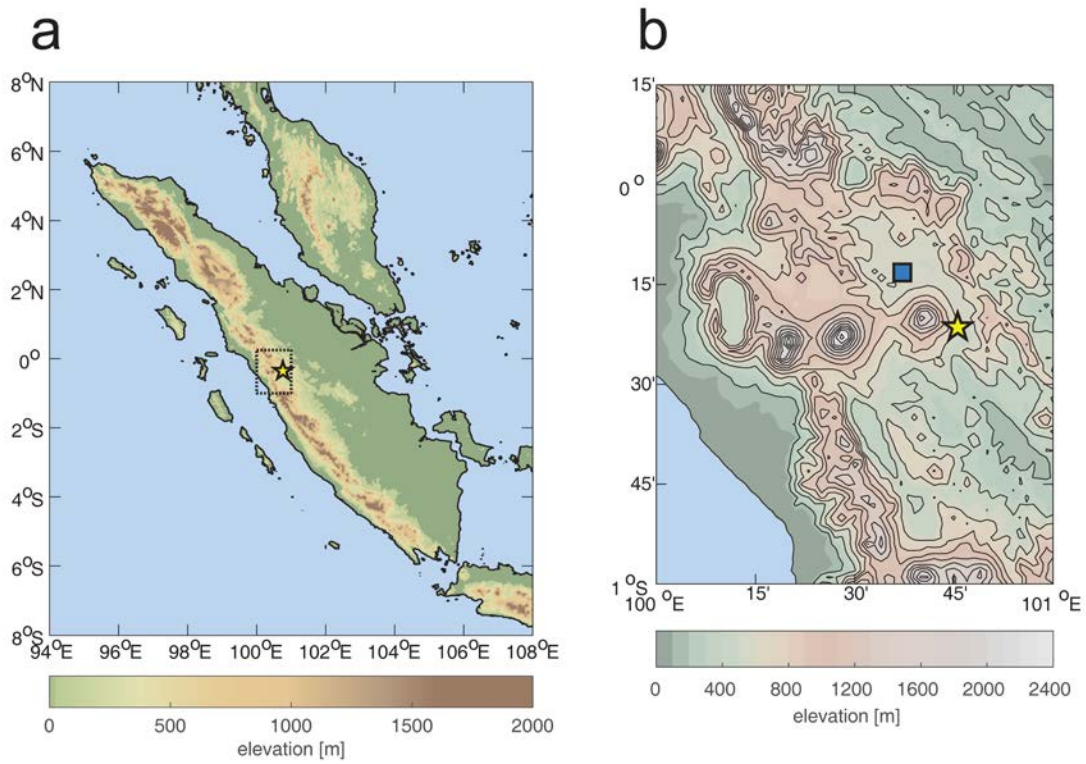

Figure 1.3 – (a) Topographic of Sumatra with study site marked by star. Dashed box denotes area of Figure 1.3b. (b) Close-up of topography around study site (star). Blue box indicates near-by city Payakumbuh.

1.2.2 Modern climatic controls

1.2.2.1 Indo-Pacific Warm Pool

The IPWP is the largest body of warm water (>28°C) on Earth (Yan et al., 1992) and plays a major role in the distribution of heat and moisture through ocean-atmosphere coupling (Thunell et al., 1994). The IPWP extends from the western tropical Pacific Ocean through the group of island nations known as the Maritime Continent, into the eastern tropical Indian Ocean (Figure 1.2). It lies at the intersection of climate variability influenced by ENSO, the Asian monsoon, and the Indian Ocean Dipole. The role of ENSO in the Pacific has garnered significant attention over the years, and is the focus of a large body of literature (e.g., Cane, 2005; Chang et al., 2006; Charles et al., 1997; Dai and Wigley, 2000; Merkel et al., 2010; Stuecker et al., 2017). With two-thirds of the world's population living in the

Asian monsoon realm, monsoon dynamics are also the subject of decades worth of study (e.g., An, 2000; Ramage, 1971).

The low-salinity IPWP connects the Pacific Ocean to the Indian Ocean via the Indonesian Throughflow (ITF), and as such, plays a key role in regulating the relative heat and salinity budgets of these two oceans. This, in turn, has important implications regarding the responses and feedbacks of ENSO, the IOD and the Australasian monsoon (Lukas et al., 1996).

1.2.2.2 Intertropical convergence zone

The ITCZ refers to the convective cloud band of heavy rainfall that occurs near the equator. It is associated with the ascending branch of the Hadley circulation, where the trade winds converge near the equator (Waliser and Gautier, 1993). The mean latitudinal location of this convergence varies throughout the year, following the seasonal angle of the sun. During boreal summer (JJA), when solar insolation at ~23.5°N is at a maximum, the ITCZ is at its northernmost latitude (Figure 1.4a). Conversely, during austral summer (DJF), when maximum solar insolation is at ~23.5°S, the ITCZ is at its southern extent (Figure 1.4b).

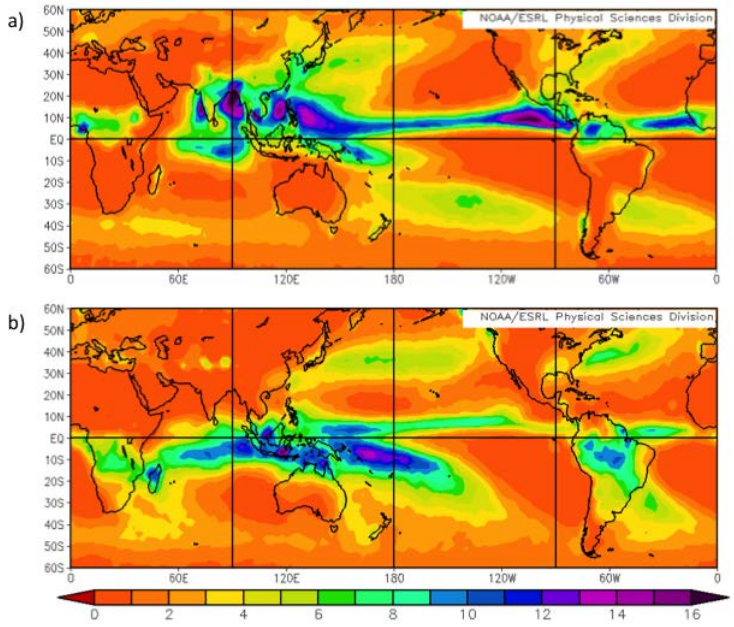

Figure 1.4 - Xie-Arkin precipitation data (mm/day) representing the mean (1979-present) a) northerly (austral winter, JJA) and b) southerly (austral summer, DJF) extents of the ITCZ [Xie and Arkin, 1997].

It is important to note that the latitudinal extremes can vary zonally, such that the presence of continents tends to lead to more extreme shifts in the latitudinal range of the ITCZ (Xie, 1996). For instance, in the eastern Pacific, seasonal shifts are minimal, with the ITCZ remaining in the northern hemisphere year-round. In the western Pacific and Indian Ocean, the ITCZ can range from nearly 20°N over southeast Asia and the Indian subcontinent to as far south as northern Australia.

1.2.2.3 Australasian monsoon

Traditionally, the word 'monsoon' refers to a regional-scale seasonal reversal of prevailing winds and associated rainfall driven by a land-sea thermal gradient. In regions dominated by the monsoon, this leads to distinct wet and dry seasons, which dictate the lives of the inhabitants (Webster et al., 1998).

More recently, the concept of a 'global monsoon' has been introduced as the global-scale seasonal overturning of the atmosphere its associated precipitation, which links the various monsoons around the globe (Trenberth et al., 2000; Wang et al., 2017) (Figure 1.5).

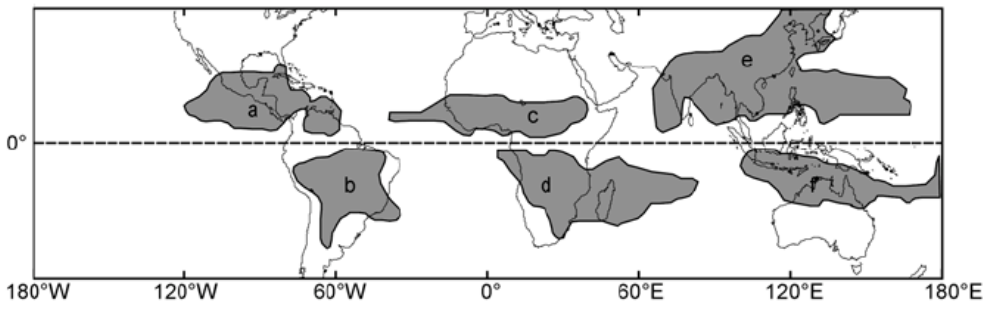

Figure 1.5 - Six monsoon regions according to annual precipitation range: a) North American, b) South American, c) North African, d) South African, e) Asian, f) Indo-Australian (Source: Wang, 2009)

The IPWP is primarily affected by the Australasian monsoon and the relationship between its northern (Asian) and southern (Indo-Australian) hemisphere components (Figure 1.5e-f). The Asian summer monsoon (ASM) is driven by the summer heating of the Tibetan Plateau that strengthens the thermal contrast with the Indian and Pacific Oceans (An, 2000). The rainfall variability associated the ASM affects two thirds of the global population, who rely on the consistency of the

monsoon for agriculture and water resources. The ASM is comprised of the Indian summer monsoon (ISM) and the East Asian summer monsoon (EASM), each of which can be distinguished geographically by their source (Figure 1.6) (Cheng et al., 2012).

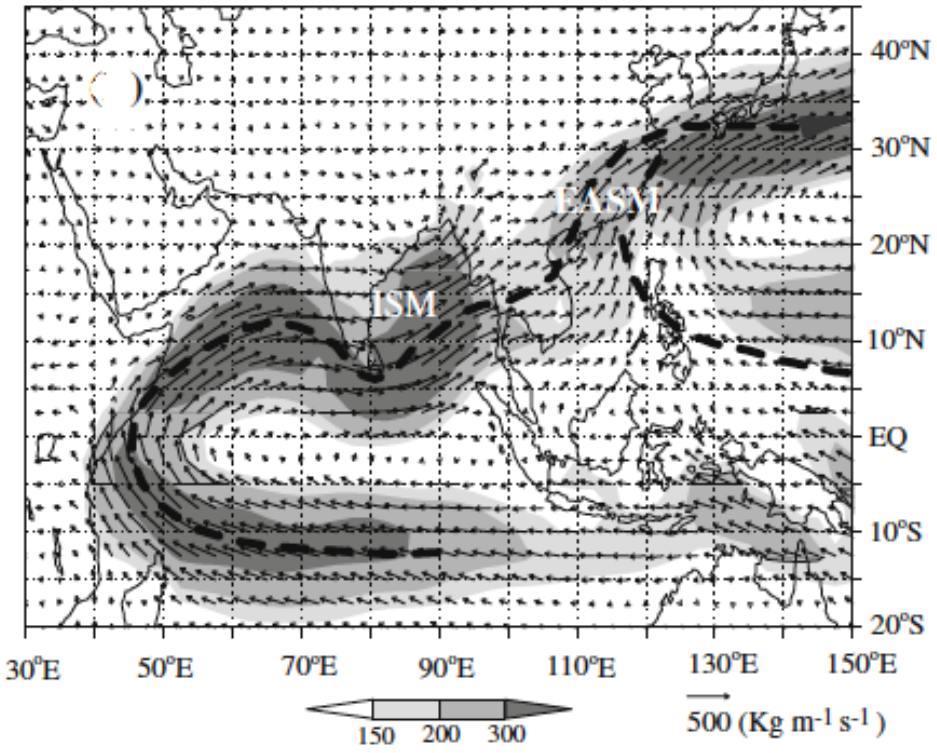

Figure 1.6 - Asian summer monsoon moisture transport patterns averaged for 1990-1999 (MJJ). ISM=Indian Summer Monsoon, EASM=East Asian Summer Monsoon (Source: Cheng et al., 2012)

The Indo-Australian Monsoon (IASM) is the austral summer, southern hemisphere component of the Australasian monsoon. The IASM is relatively weak compared to the ASM and far less well-studied, such that debate exists over whether the IASM is driven by mechanisms of thermal contrast similarly to the Asian monsoon or by extension of ITCZ migration (Chao and Chen, 2001; Gadgil, 2018; Suppiah, 1992). Early studies of the Australian monsoon suggest that it can be classified into three monsoonal flow types (Figure 1.7). Westerly winds deflected by the Pilbara heat low in the northwest of Australia make up the 'pseudo-monsoon', while in the east, easterly Pacific trade winds make up the 'quasi-monsoon.' The 'true monsoon' refers to the area between the other two flows, where air masses with tropical

westerly and northwesterly origins dominate (Allan, 1985; Gentilli, 1971; Suppiah, 1992).

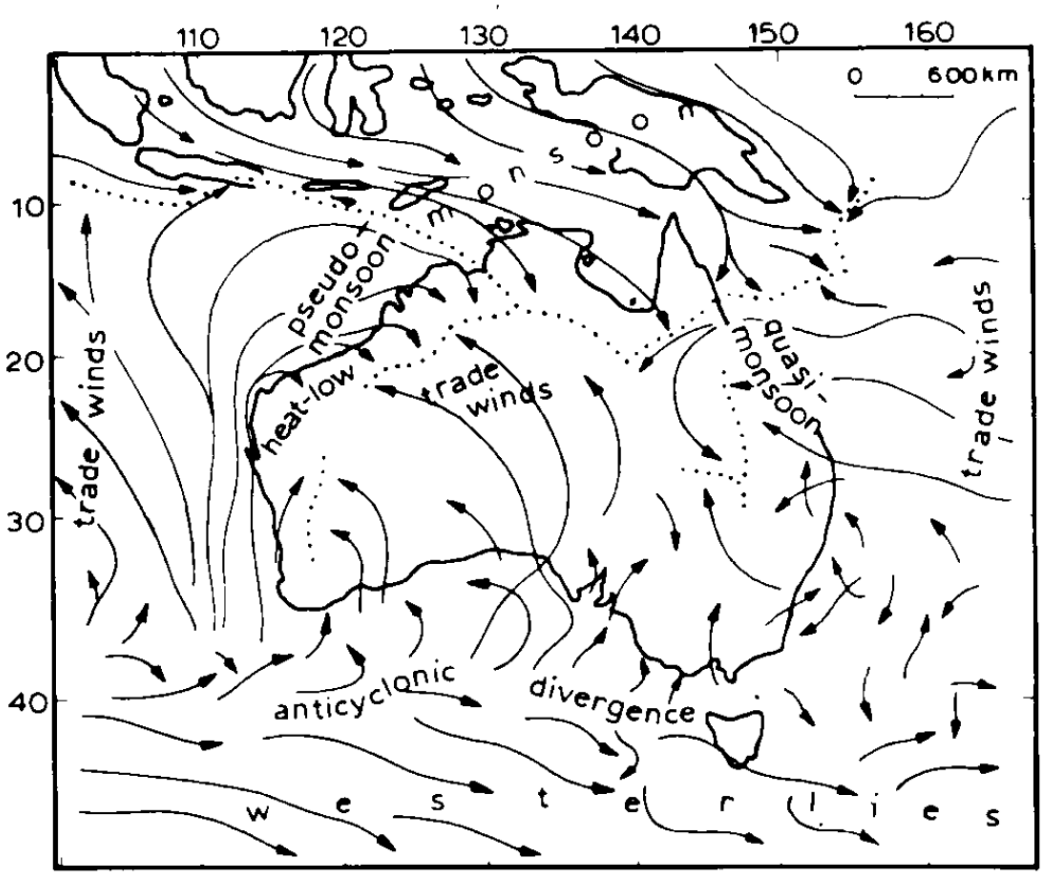

Figure 1.7 - Classification of the Australian monsoon wind system (Source: Gentilli, 1971)

1.2.2.4 El Niño-Southern Oscillation

The El Niño-Southern Oscillation (ENSO) refers to the interannual (2-7y band) variability associated with anomalies in Walker circulation and zonal SST gradients across the tropical Pacific Ocean (Cane, 2005). The 'normal' state of atmospheric circulation in the Pacific Ocean is when the surface trade winds flow west across the equatorial Pacific and air rises over Indonesia, subsequently returning east via upper level winds and sinking in the eastern Pacific (Figure 1.8a) (Bjerknes, 1969). The strength of the easterly trade winds at the surface is regulated by the Southern Oscillation, an interannual fluctuation in sea level pressure (SLP) between the western and central-eastern Pacific, which is, in part, driven by the difference in

SSTs between the perpetually warm western Pacific and the generally cooler eastern Pacific (Kraus and Businger, 1994).

It was Jacob Bjerknes who recognized that the coupled nature of the Pacific SST and Southern Oscillation SLP variations could be considered a single ocean-atmosphere phenomenon, the El Niño-Southern Oscillation. (Bjerknes, 1969; Cane, 2005). El Niño occurs when the eastern Pacific Ocean warms, causing a weakening or reversal of Walker Circulation due to a reduced zonal pressure gradient (Figure 1.8b). The weaker trade winds enhance the initial warm anomaly, which continues to reduce the SST and pressure gradient across the Pacific. This positive ocean-atmosphere feedback is referred to as the 'Bjerknes feedback.' The cold state, La Niña, reflects a strengthening of the Walker circulation resulting from cool anomalies in the eastern Pacific, which enhance the zonal SST gradient (Wang et al., 2012).

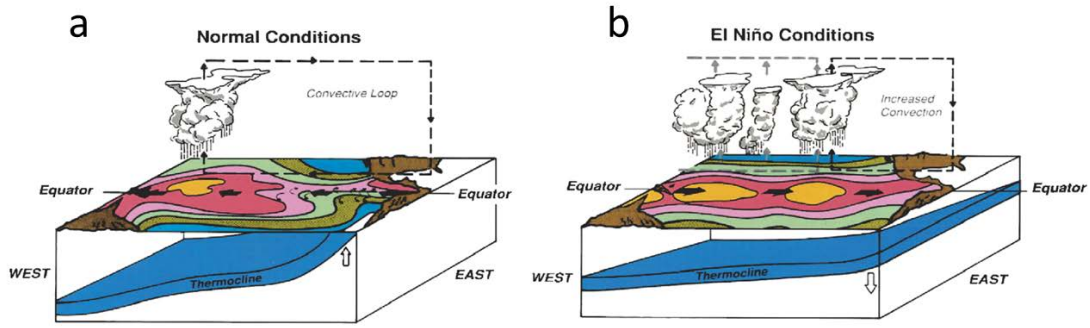

Figure 1.8 – (a) "Normal" Walker circulation in the equatorial Pacific Ocean, in which strong atmospheric convection occurs over Indonesia where the thermocline is deep, and air descends in the eastern Pacific over a shallow thermocline. An enhancement of this circulation constitutes a La Niña. (b) In El Niño conditions, the thermocline deepens in the east, warming SSTs there, and causing a weakening or reversal of Walker circulation in the eastern Pacific. (Source: Cane, 2005)

Though ENSO originates in the Pacific, its effects are far-reaching, and it interacts with other climate modes, such as the Australasian monsoon and the IOD. Through its effects on the reducing the strength of convection over the IPWP, El Niño events tend to coincide with reduced summer monsoon rainfall over India (Webster et al., 1998). El Niño events may also precondition the tropical Indian Ocean for a positive IOD event.

1.2.2.5 Indian Ocean Dipole

Until about fifteen years ago, the role of the tropical Indian Ocean in modulating global climate was thought not to extend beyond the realm of the Indian monsoon (Schott et al., 2009). In 1997, record-breaking weather anomalies in countries on the Indian Ocean rim drew widespread attention. Drought and wildfire spread through Indonesia, causing health problems and extensive coral reef death (Abram et al., 2003) (Emmanuel, 2000). Extreme rainfall displaced hundreds of thousands of people in eastern Africa (Black, 2003; Clark et al., 2003). The severity of the climate led to renewed interest and research in Indian Ocean air-sea dynamics, culminating in the identification of an internal mode of variability known as the Indian Ocean Zonal Mode, or the Indian Ocean Dipole (IOD). The IOD is now recognized as a coupled ocean-atmosphere mode of climate variability that occurs across the tropical Indian Ocean (Saji et al., 1999), stemming from an oscillatory pattern of zonal sea surface temperatures (SSTs) in the Indian Ocean. The dipole mode index (DMI) quantifies this pattern as the difference between SST anomalies in the western (50°E-70°E, 10°S-10°N) and eastern (90°E-110°E, 10°S-Equator) sectors of the Indian Ocean (Saji et al., 1999).

In the negative phase of the IOD, the Indian Ocean's normally weak westerlies are enhanced, and a warm SST anomaly appears in the eastern tropical Indian Ocean, accompanied by increased rainfall over Indonesia (Figure 1.9). Conversely, a positive IOD event is characterized by the development of a cool SST anomaly off the Sumatra-Java coast in May-June, accompanied by southeasterly wind anomalies. At the same time, warm SST anomalies occur in the western Indian Ocean, reversing the basin's climatological SST gradient, and replacing the usually weak westerlies at this time of year with anomalous easterly zonal winds. The wind anomalies enhance coastal upwelling off Sumatra, which in turn acts to reinforce the cooling in the eastern Indian Ocean, with anomalous conditions peaking in October (Saji et al., 1999; Webster et al., 1999). The boreal summer development of the IOD leading to maximum anomalies in boreal autumn is a consistent feature of IOD evolution. Composite analysis of multiple IOD events confirms this seasonally phase-locked nature (Saji et al., 1999).

Since its recognition, the IOD has been linked to patterns of drought and rainfall across the Indian Ocean region, including east Africa (Black, 2003; Clark et al., 2003), Indonesia (D'Arrigo and Smerdon, 2008), India, (Ashok et al., 2001), and Australia (Ashok et al., 2003; England et al., 2006).

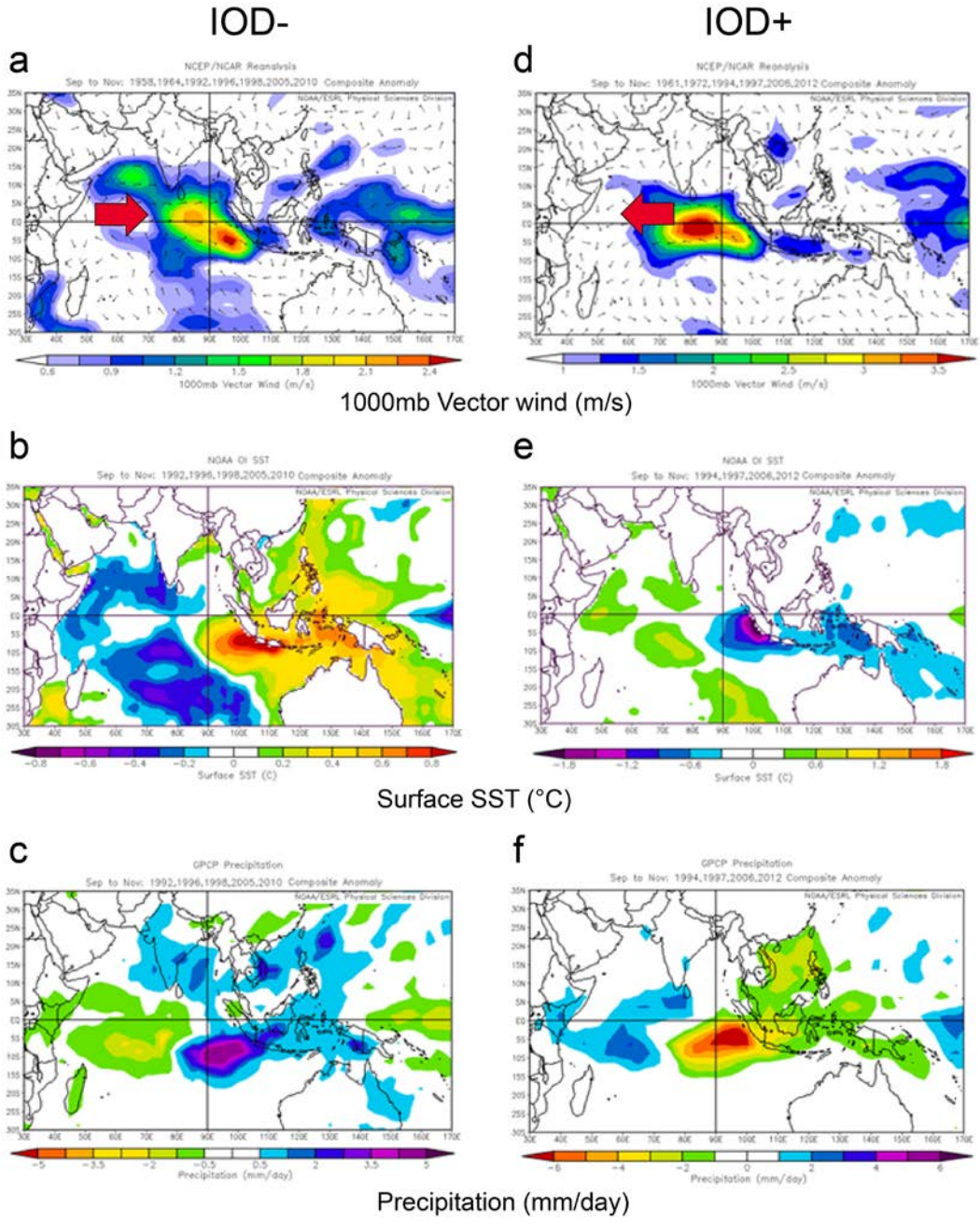

Figure 1.9 – Composite a,d) NCEP/NCAR Reanalysis Wind, b,e) NOAA OI SST, and c,f) GPCP precipitation anomalies in SON for a-c) negative IOD years and d-f) positive IOD years. Negative IOD years used for the composite are 1958, 1964, 1992, 1996, 2005, and 2010. Positive IOD years are 1961, 1972, 1994, 1997, 2006, and 2012. [provided by the NOAA/OAR/ESRL PSD, Boulder, Colorado, USA, from their website at http://www.esrl.noaa.gov/psd/]

In Australia, the effect of a positive IOD event is to reduce austral winter rainfall in parts of Western Australia, South Australia and southern Victoria (Ashok et al., 2003). As such, positive IOD events have been associated with particularly damaging bushfire seasons, like that of the Victorian Black Saturday wildfires in 2009, by creating drier-than-average, and therefore more fire-prone, conditions in the summers following a positive IOD winter (Cai et al., 2009). Conversely, a negative IOD event is associated with above-average winter-spring rainfall over parts of southern Australia (Bureau of Meteorology, 2016). On longer time-scales, persistent positive IOD conditions in the Indian Ocean have been cited as the dominant driver behind several of Australia's most iconic droughts including the recent Millennium Drought (1996-2010) and the 1895-1902 Federation Drought (Bureau of Meteorology, 2015; Ummenhofer et al., 2009).

1.2.2.6 Observed climate at Tangga Cave, Sumatra

Determining the degree to which ENSO and IOD modulate rainfall at Tangga Cave was an important step early on in this research. In order to determine the influence of these systems on precipitation at Tangga Cave, I isolated years in which the Niño3.4 SST anomaly index (one of several indices used to quantify ENSO strength) and the Saji Indian Ocean DMI (Saji et al., 1999) exceeded a threshold of two standard deviations from their mean. Precipitation data from only these extreme event years were then extracted from the Climatic Research Unit Timeseries 3.23 (CRU TS3.23) gridded data and averaged by month to represent seasonal rainfall variations during the positive and negative modes of ENSO and the IOD, respectively (Figure 1.10). The pattern of rainfall in ENSO years, and to a lesser degree IOD years, was found to not vary significantly from the climatological mean. Therefore, ENSO appears to play a limited role in modulating rainfall at Tangga.

Seasonal rainfall variations during El Niño years look very similar to that of the long-term mean. Likewise, La Niña events do not seem to significantly affect rainfall, though there is slightly increased rainfall from June through October, which may be reflective of increased convection in the IPWP region (Figure 1.10a).

A 2003 study of Indonesian rainfall domains supports our results of a suppressed ENSO influence in this region. Spectral analysis of precipitation in northwest Indonesia reveals no power in the 4-7 year ENSO band, and no correlation exists between rainfall and local or remote SST in this region (Aldrian and Susanto, 2003).

Despite falling directly within the eastern IOD domain, the negative IOD phase also appears to have no impact on rainfall at Tangga Cave (Figure 1.10b). The positive IOD, on the other hand, exhibits a clear influence on precipitation during peak IOD months (Sept-Oct), contributing to a ~33% decline in rainfall (Figure 1.10b). This may occur because the positive expression of the IOD is stronger than the negative phase.

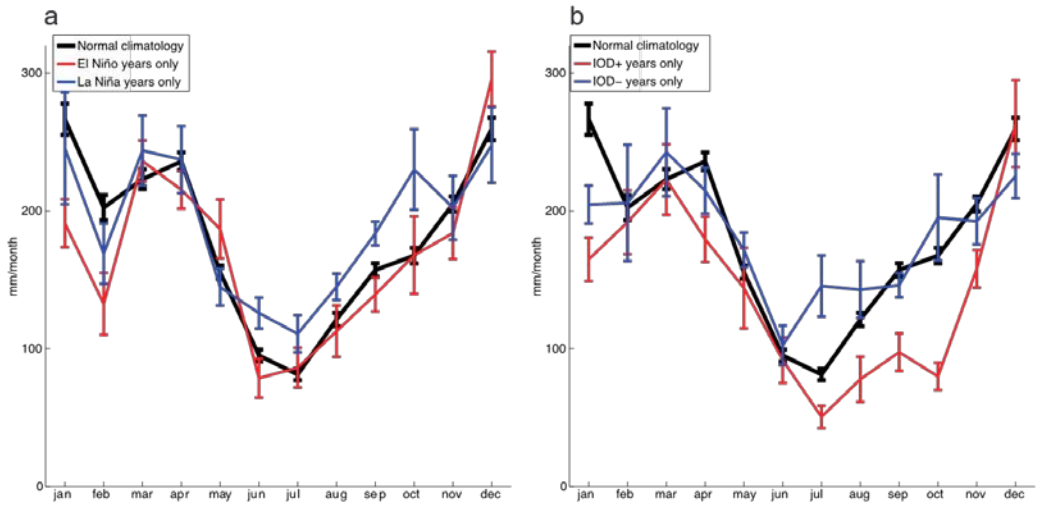

Figure 1.10 - Mean Tangga Cave climatology (1901-2012, black line) vs. a) average precipitation during El Niño years (red line) and La Niña years (blue line), and b) average precipitation for IOD+ years (red line) and IOD- years (blue line)

A more detailed account of modern climatology at Tangga Cave will be provided in Chapters 2 and 3.

1.2.3 Speleothems as paleoclimate proxies

1.2.3.1 Formation

The word *speleothem* comes from the Greek for cave deposit and refers to any of the secondary calcium carbonate formations ($CaCO_3$) that occur in the cave system. As rainwater percolates through the soil above a cave, it combines with carbon

dioxide (CO_2) via organic processes in the soil, forming weak carbonic acid (H_2CO_3) (Figure 1.11). This high P_{CO2} (partial pressure of CO_2) solution percolates downward, dissolving carbonate bedrock (usually limestone or dolomite), until it reaches the undersaturated air of the cave, where it then degasses CO_2 from the solution and precipitates $CaCO_3$ (Fairchild and Baker, 2012; Lascu and Feinberg, 2011). As the speleothem grows, it incorporates environmental signals into its geochemical structure in the form of stable isotope and trace element variations. Because they are usually chemically stable and form within a relatively closed system, speleothems are a valuable resource for paleoclimatic reconstruction.

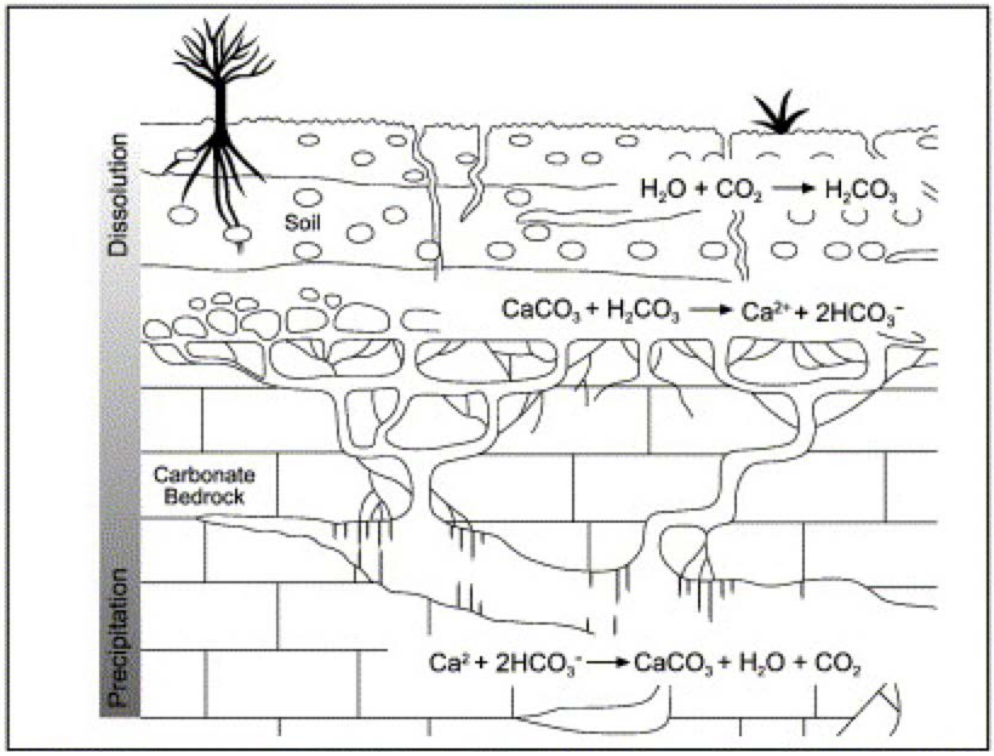

Figure 1.11 - Diagram showing dissolution and precipitation zones in and above cave system, and the associated chemical reactions (Source: Fairchild et al., 2006).

1.2.3.2 Uranium/Thorium dating

Measurement of uranium/thorium (U/Th) is the foremost method used for speleothem geochronology, and can be used to date materials from modern to up to 600 ka (Cheng et al., 2016; Cheng et al., 2013; Richards and Dorale, 2003). Like

other types of radiometric dating, the method relies on the disequilibria between the parent and daughter isotopes that arise when the former is deposited into a closed system (Ku, 2000). The time of deposition can be determined by measuring the extent to which the radionuclide system has returned to secular equilibrium, defined as the state at which the activity ratios between parent and daughter isotope equals one (Bourdon et al., 2003). U/Th dating relies on the decay chain between ^{238}U (4.5 Gy half-life) into ^{234}U (245 ky), which in turn decays into ^{230}Th (75 ky) (Bourdon et al., 2003; Cheng et al., 2000). Recently, the half-life times and uncertainties for ^{234}U and ^{230}Th have been refined such that modern dating precisions (2σ) can be as accurate as ±10 y at 10 ka, ±1 ky at 300 ka, and ±12 ky at 600 ka (Cheng et al., 2013).

Uranium is incorporated into the stalagmite carbonate as it precipitates. Importantly, insoluble thorium is excluded, such that the only sources of Th-230 are the radioactive decay of U-234 and detrital Th that enters the speleothem at the time of deposition. Uranium and thorium are immobile in the stalagmite, and it is assumed that the speleothem is a closed system (Hellstrom, 2006).

Early analytical dating methods (i.e., alpha spectrometry) were limited by the large sample sizes (~10g) required, but in the last couple decades, the development of thermal ionization mass spectrometry (TIMS) and multi-collector inductively coupled plasma mass spectrometry (MC-ICP-MS), which require as little as milligrams of sample, has made feasible the generation of precise and relatively inexpensive dates (Fairchild and Baker, 2012).

1.2.3.3 Stable isotopes

Stable oxygen isotopes are the most commonly measured variable in speleothems. The oxygen isotope ratio ($\delta^{18}O$) of speleothem carbonate was first recognized as a viable climate proxy in the 1960s (Broecker et al., 1960; Hendy and Wilson, 1968). Since then, advances in dating (Edwards et al., 1987) and sampling techniques (Wurster et al., 1999) have propelled speleothems to the forefront of paleoclimate research. They are generally measured by mass spectrometry after digesting the

sample carbonate in concentrated acid to generate CO_2. Isotope ratios are expressed in 'delta' (δ) notation:

$$\delta^{18}O = \left(\frac{\frac{^{18}O}{^{16}O_{sample}} - \frac{^{18}O}{^{16}O_{standard}}}{\frac{^{18}O}{^{16}O_{standard}}} \right) \times 1000$$

where the standard, VPDB (Vienna Pee Dee Belemnite) for carbonates, is defined as 0.0‰. Therefore, negative values are described as being depleted in ^{18}O or 'light' and positive values are considered enriched or 'heavy' (Lachniet, 2009).

Under isotopic equilibrium conditions, the $\delta^{18}O$ of the speleothem carbonate is influenced only by cave temperature and the $\delta^{18}O$ of the dripwater (Gascoyne, 1992). In practice, we assume that the isotopic value of the dripwater primarily controls the carbonate $\delta^{18}O$, because cave air temperatures remain relatively constant throughout the year and are similar to the air above the cave, which in the tropics, also remains relatively constant. The influence of temperature in isotopic composition of precipitation is also approximately negated by the opposite-signed temperature fractionation during carbonate formation (McDermott, 2004).

Despite removing cave temperature from the equation, the remaining $\delta^{18}O$ dripwater signal may also be subject to a number of influences relating to the air parcel's source and path to the cave (Lachniet, 2009). The initial control on the $\delta^{18}O$ signal is the isotopic value of the ocean, which varies regionally as a function of salinity. Because the light (^{16}O) isotope is preferentially evaporated, areas of high evaporation will be left enriched in the heavy (^{18}O) isotope (Lachniet, 2009). The evaporated moisture, now isotopically light relative to the ocean, may then be transported as atmospheric vapour, where it will fractionate according to Rayleigh distillation, a model by which the heavier isotopes are preferentially fractionated into condensate, leaving the remaining vapour in the air parcel isotopically depleted (Fairchild and Baker, 2012). Condensation, and therefore more negative air parcel isotopic ratios, may be instigated by decreasing temperature (which may

accompany an increase in latitude), increasing altitude or orography, and/or increasing distance from the coast (Gat et al., 2001).

On glacial/interglacial timescales, the bulk ocean isotopic composition also changes via the 'ice volume effect.' During glacial periods, increased amounts of isotopically-light water become stored in the ice sheets on land, resulting in an isotopically heavy ocean. Thus, evaporation and condensation during times of more extensive ice sheets carry an enriched signal (Lachniet, 2009).

The observation that an inverse relationship exists between rainwater $\delta^{18}O$ and annual or monthly precipitation amount is called the 'amount effect' (Dansgaard, 1964; Rozanski et al., 1993). Though the amount effect has often been interpreted as the depletion of an air mass due to progressive condensation from high convective rainout (Vuille et al., 2003), it has more recently been shown that there are additional complex microphysical cloud processes at work (Risi et al., 2008). Despite the microscale processes involved, the ultimate effect is still that increased precipitation amount results in more negative isotopic ratios. Best observed on timescales of intraseasonal and longer, the amount effect dominates the $\delta^{18}O$ signal in the tropics, where strong vertical convection is common (Lachniet, 2009; Risi et al., 2008).

Lastly, even after the rainwater reaches the ground, there are still processes that can alter the $\delta^{18}O$ signal that gets recorded in the speleothem, including, but not limited to, kinetic effects, mineralogy, vegetation density, and soil porosity (Lachniet, 2009). Kinetic fractionation can be tested with replication preferably encompassing different cave systems, since it is unlikely that two speleothems with similar isotope profiles could have been subject to the same disequilibrium kinetic processes (such as rapid CO_2 degassing) (Dorale and Liu, 2009). Mineralogy can also be tested for and the $\delta^{18}O$ signal corrected based on aragonite-calcite transitions. Under equilibrium conditions, aragonite will fractionate with $\delta^{18}O$ values ~0.6-1‰ heavier than calcite (Kim et al., 2007).

Though carbon isotopes are generally measured simultaneously with oxygen isotopes, the results are not often reported due to the difficulty in interpreting $\delta^{13}C$ (Fairchild and Baker, 2012). However, $\delta^{13}C$ may provide valuable information about surface processes such as vegetation change or overall productivity above the cave (Baldini et al., 2005; Cosford et al., 2009). Carbon isotopes are not discussed in this thesis, as it is beyond the scope of the work presented.

1.2.3.4 Trace elements

In recent years, trace elements have increasingly emerged as useful additional indicators of paleoclimatic change (Fairchild and Treble, 2009). For example, divalent trace element variations have been show to reflect rainfall amount through karst processes such as prior calcite precipitation (PCP) and incongruent dolomite dissolution (Johnson et al., 2006; Sinclair, 2011), and varying aquifer residence time (Roberts et al., 1998). Furthermore, trace elements can be reflective of soil and bedrock characteristics (Rutlidge et al., 2014) (Hartland et al., 2012).

Studies of trace elements in speleothems often focus on trace elements that are incorporated into calcite through substitution for the Ca^{2+} cation in the $CaCO_3$ structure, such as Mg^{2+}, Sr^{2+}, and Ba^{2+} (Fairchild and Treble, 2009). Though trace elements can also be incorporated through the occlusion of particulates into the crystal lattice, and by adsorption onto the crystal surface, the method of cation exchange is the most easily quantified (Gascoyne, 1983). The ratio in the carbonate (Tr/Ca_{CaCO3}) can be described by the concentration of the trace element in the fluid solution ($Tr/Ca_{solution}$) and the distribution (or partition) coefficient (D_{Tr})(Gascoyne, 1983; Morse and Bender, 1990), such that:

$$Tr/Ca_{CaCO_3} = D_{Tr} \times (Tr/Ca)_{solution}$$

Despite this simple model, $Tr/Ca_{solution}$ can vary due to environmental parameters (i.e., precipitation, vegetation, prior calcite precipitation) in and above the cave, and D_{Tr} can vary with physical parameters (i.e., temperature, growth rate, mineralogy) (Fairchild and Treble, 2009; Finch et al., 2001).

1.2.3.5 Aragonite speleothems

Speleothems most commonly precipitate as either calcite or the metastable $CaCO_3$ polymorph, aragonite. Most paleoclimatic reconstructions use calcite stalagmites because aragonite is thermodynamically unstable and therefore subject to post-depositional alteration to calcite, known as secondary calcite (Finch et al., 2001; Frisia et al., 2002). U/Th dating and interpretation of isotopes and trace elements becomes ambiguous in secondary calcite because the transformation takes place in an open system (Frisia et al., 2002; Lachniet et al., 2012). However, if no diagenetic alteration has taken place, aragonite speleothems can be robust archives for paleoclimatic studies, in part due to their high uranium concentrations, making them very easy to date (Zhang et al., 2013). Because stable aragonite can persist indefinitely, aragonitic speleothems have already been successfully employed in paleo-reconstructions (Cosford et al., 2008; Li et al., 2011). Petrography and geochemistry of aragonite speleothems is discussed in more detail in Chapter 4.

1.3 Research Objectives

In this thesis, I will address three fundamental questions:

1) What was the state of hydroclimate in the Indo-Pacific Warm Pool during the last deglaciation, particularly during the Younger Dryas? How do North Atlantic abrupt events manifest in the IPWP?
2) What are the major sources of moisture to Indo-Pacific speleothem sites and how have these sources changed over time? How might these sources contribute to the variability in rainfall $\delta^{18}O$?
3) What can we learn about aragonite-calcite systematics in the karst system? What are the aragonite distribution coefficients for trace elements of interest? What are the hydrologic controls on aragonite-calcite precipitation?

1.4 Structure of the Thesis

This thesis contains five chapters. Chapters 2 through 4 are organized as a series of manuscripts that are either submitted to, or in preparation for, international peer-reviewed journals. As a result, some sections may be repetitive.

Chapter 1 of this thesis provides an overview of the motivation behind this project and the fundamental questions that were addressed. This chapter introduces key background information relating to regional climatology and speleothems as paleoclimate proxies.

Chapter 2 of this thesis presents a high resolution, late deglacial speleothem $\delta^{18}O$ record from Tangga Cave in West Sumatra, Indonesia and discusses its climatic implications. This record represents the first deglacial speleothem record from the eastern Indian Ocean part of the Indo-Pacific Warm Pool. The Sumatran speleothem demonstrates a clear deglacial structure that includes ^{18}O enrichment during the Younger Dryas and ^{18}O depletion during the Bølling-Allerød, similar to the pattern seen in speleothems of the Asian and Indian monsoon realms. The speleothem $\delta^{18}O$ changes at this site are best explained by changes in rainfall amount and changes in the contributions from different moisture pathways. Reduced rainfall in Sumatra during the Younger Dryas is most likely driven by reductions in convection along the northern or southern monsoon transport pathways to Sumatra. Considered with other regional proxies, the record from Sumatra suggests the response of the IPWP to North Atlantic freshwater forcing is not solely driven by southward shifts of the ITCZ, but also weakened Hadley cell convection.

Chapter 2 of this thesis has been accepted for publication in *Earth and Planetary Science Letters* (Wurtzel et al., 2018). I am the primary investigator and author of this paper. Co-authors Nerilie Abram and Sophie Lewis provided crucial feedback, intellectual discussion, and proofreading. Petra Bajo and John Hellstrom provided U/Th dating for speleothem TA12-2. Ulrike Troitzsch helped with XRD and Raman

analysis. Dave Heslop assisted with statistical methods for the mineralogical isotopic fractionation correction.

Chapter 3 of this thesis provides a systematic modern climate analysis of the eight speleothem sites discussed in Chapter 2 in order to better understand what controls oxygen isotopic variability in speleothem records**.** This chapter uses a twentieth century isotope-enabled model to examine the role of the amount effect at each site, then uses back-trajectory air parcel modelling nudged with reanalysis data to assess modern moisture sources. The back-trajectory model is then compared to vapour source distributions from a twentieth century water tracer-enabled simulation of NASA GISS's ModelE2-R. Finally, preliminary vapour source distribution results are presented from an existing freshwater hosing simulation of GISS ModelE-R in order to assess paleo-moisture source changes during North Atlantic abrupt events like the Younger Dryas. I find that changes in topography and contributions from alternative sources are likely to have an impact on the rainfall $\delta^{18}O$ signal and that these changes should be taken into account when interpreting speleothem $\delta^{18}O$.

I am the primary investigator and author of this paper. Modelled vapour source distribution data from NASA GISS ModelE-R was provided by Sophie Lewis, Allegra LeGrande and Jesse Nusbaumer. IsoGSM data was provided by Kei Yoshimura. This work is being prepared for submission to *Climate of the Past*.

Chapter 4 of this thesis describes the unique petrography of aragonite-calcite speleothem TA12-2. Laser-ablation trace element analysis helped identify calcite intervals in the primarily aragonite speleothem. The many abrupt transitions between primary aragonite and primary calcite provide an opportunity to investigate differences in isotope fractionation and trace element incorporation between the two carbonate phases. We use new isotope data from calcite stalagmite TA12-8, collected from a different chamber in the same cave as TA12-2, to quantify oxygen isotope offsets. Distribution coefficients for Mg, Sr, U, and Ba into aragonite are estimated using twenty transitions from within TA12-2. This

chapter further discusses what environmental factors are likely controlling the phase changes between aragonite and calcite, and the trace element variability.

I am the primary investigator and author of this paper. Ulli Troitzsch provided laboratory assistance for XRD analysis. Silvia Frisia assisted with micro-fluorescent microscopy and the interpretation of thin section petrography. This work is being prepared for submission to *Geochimica et Cosmochimica Acta*.

Chapter 5 is the final chapter of this thesis. It summarizes the major findings and discusses potential avenues of future work.

References

Abram, N.J., Gagan, M.K., McCulloch, M.T., Chappell, J., Hantoro, W.S. (2003). Coral reef death during the 1997 Indian Ocean Dipole linked to Indonesian wildfires. Science 301, 952-955. http://dx.doi.org/10.1126/science.1083841

Aldrian, E., Susanto, R.D. (2003). Identification of three dominant rainfall regions within Indonesia and their relationship to sea surface temperature. International Journal of Climatology 23, 1435-1452. http://dx.doi.org/10.1002/joc.950

Allan, R.J. (1985). The Australasian Summer Monsoon, Teleconnections, and Flooding in the Lake Eyre Basin.

An, Z. (2000). The history and variability of the East Asian paleomonsoon climate. Quaternary Science Reviews 19, 171-187. http://dx.doi.org/10.1016/S0277-3791(99)00060-8

Ashok, K., Guan, Z., Yamagata, T. (2001). Impact of the Indian Ocean dipole on the relationship between the Indian monsoon rainfall and ENSO. Geophysical Research Letters 28, 4499-4502. http://dx.doi.org/10.1029/2001gl013294

Ashok, K., Guan, Z., Yamagata, T. (2003). Influence of the Indian Ocean Dipole on the Australian winter rainfall. Geophysical Research Letters 30, 1821. http://dx.doi.org/10.1029/2003gl017926

Ayliffe, L.K., Gagan, M.K., Zhao, J.-x., Drysdale, R.N., Hellstrom, J.C., Hantoro, W.S., Griffiths, M.L., Scott-Gagan, H., Pierre, E.S., Cowley, J.A., Suwargadi, B.W. (2013). Rapid interhemispheric climate links via the Australasian monsoon during the last deglaciation. Nature Communications 4, 2908. http://dx.doi.org/10.1038/ncomms3908

Baldini, J.U.L., McDermott, F., Baker, A., Baldini, L.M., Mattey, D.P., Railsback, L.B. (2005). Biomass effects on stalagmite growth and isotope ratios: A 20th century analogue from Wiltshire, England. Earth and Planetary Science Letters 240, 486-494. http://dx.doi.org/10.1016/j.epsl.2005.09.022

Bar-Matthews, M., Ayalon, A., Kaufman, A., Wasserburg, G.J. (1999). The Eastern Mediterranean paleoclimate as a reflection of regional events: Soreq cave,

Israel. Earth and Planetary Science Letters 166, 85-95. http://dx.doi.org/10.1016/S0012-821X(98)00275-1

Barber, A.J., Crow, M.J., Milsom, J. (2005), Sumatra: geology, resources and tectonic evolution. Geological Society of London.

Barker, S., Diz, P., Vautravers, M.J., Pike, J., Knorr, G., Hall, I.R., Broecker, W.S. (2009). Interhemispheric Atlantic seesaw response during the last deglaciation. Nature 457, 1097-1102. http://dx.doi.org/10.1038/nature07770

Bjerknes, J. (1969). Atmospheric teleconnections from the equatorial Pacific. Monthly Weather Review 97, 163-172. http://dx.doi.org/10.1175/1520-0493(1969)097<0163:ATFTEP>2.3.CO;2

Björck, S., Walker Michael, J.C., Cwynar Les, C., Johnsen, S., Knudsen, K.L., Lowe, J.J., Wohlfarth, B. (1998). An event stratigraphy for the Last Termination in the North Atlantic region based on the Greenland ice‐core record: a proposal by the INTIMATE group. Journal of Quaternary Science 13, 283-292. http://dx.doi.org/10.1002/(SICI)1099-1417(199807/08)13:4<283::AID-JQS386>3.0.CO;2-A

Black, E. (2003). The impact of Indian and Pacific Ocean processes on the East African short rains. CLIVAR Exchanges 8, 40-42.

Blunier, T., Brook, E.J. (2001). Timing of Millennial-Scale Climate Change in Antarctica and Greenland During the Last Glacial Period. Science 291, 109. http://dx.doi.org/10.1126/science.291.5501.109

Bourdon, B., Henderson, G.M., Lundstrom, C.C., Turner, S.P. (2003), Uranium-series Geochemistry. Mineralogical Society of America.

Broecker, W.S., Denton, G.H., Edwards, R.L., Cheng, H., Alley, R.B., Putnam, A.E. (2010). Putting the Younger Dryas cold event into context. Quaternary Science Reviews 29, 1078-1081. http://dx.doi.org/10.1016/j.quascirev.2010.02.019

Broecker, W.S., Olson, E.A., Orr, P.C. (1960). Radiocarbon measurements and annual rings in cave formations. Nature 185, 93-94. http://dx.doi.org/10.1038/185093a0

Bureau of Meteorology (2015). 'Recent rainfall, drought and southern Australia's long-term rainfall decline.' Available at: http://www.bom.gov.au/climate/updates/articles/a010-southern-rainfall-decline.shtml

Bureau of Meteorology (2016). 'Indian Ocean influences on Australian climate.' Available at: http://www.bom.gov.au/climate/iod/#tabs=Negative-IOD-impacts

Cai, W. (1996). Surface thermohaline forcing conditions and the response of the present-day global ocean climate to global warming. Journal of Geophysical Research: Oceans 101, 1079-1093. http://dx.doi.org/10.1029/95jc03137

Cai, W., Cowan, T., Raupach, M. (2009). Positive Indian Ocean Dipole events precondition southeast Australia bushfires. Geophysical Research Letters 36, L19710. http://dx.doi.org/10.1029/2009gl039902

Cane, M.A. (2005). The evolution of El Niño, past and future. Earth and Planetary Science Letters 230, 227-240. http://dx.doi.org/10.1016/j.epsl.2004.12.003

Chang, P., Yamagata, T., Schopf, P., Behera, S.K., Carton, J., Kessler, W.S., Meyers, G., Qu, T., Schott, F., Shetye, S., Xie, S.P. (2006). Climate fluctuations of tropical coupled systems—The role of ocean dynamics. Journal of Climate 19, 5122-5174. http://dx.doi.org/10.1175/Jcli3903.1

Chao, W.C., Chen, B. (2001). The Origin of Monsoons. Journal of the Atmospheric Sciences 58, 3497-3507. http://dx.doi.org/10.1175/1520-0469(2001)058<3497:TOOM>2.0.CO;2

Charles, C.D., Hunter, D.E., Fairbanks, R.G. (1997). Interaction between the ENSO and the Asian Monsoon in a coral record of tropical climate. Science 277, 925-928. http://dx.doi.org/10.1126/science.277.5328.925

Cheng, H., Edwards, R.L., Hoff, J., Gallup, C.D., Richards, D.A., Asmerom, Y. (2000). The half-lives of uranium-234 and thorium-230. Chemical Geology 169, 17-33. http://dx.doi.org/10.1016/S0009-2541(99)00157-6

Cheng, H., Edwards, R.L., Sinha, A., Spötl, C., Yi, L., Chen, S., Kelly, M., Kathayat, G., Wang, X., Li, X., Kong, X., Wang, Y., Ning, Y., Zhang, H. (2016). The Asian monsoon over the past 640,000 years and ice age terminations. Nature 534, 640-646. http://dx.doi.org/10.1038/nature18591

Cheng, H., Lawrence Edwards, R., Shen, C.-C., Polyak, V.J., Asmerom, Y., Woodhead, J., Hellstrom, J.C., Wang, Y., Kong, X., Spötl, C., Wang, X., Calvin Alexander Jr, E. (2013). Improvements in ^{230}Th dating, ^{230}Th and ^{234}U half-life values, and U–Th isotopic measurements by multi-collector inductively coupled plasma mass spectrometry. Earth and Planetary Science Letters 371–372, 82-91. http://dx.doi.org/10.1016/j.epsl.2013.04.006

Cheng, H., Sinha, A., Wang, X., Cruz, F.W., Edwards, R.L. (2012). The Global Paleomonsoon as seen through speleothem records from Asia and the Americas. Climate Dynamics 39, 1045-1062. http://dx.doi.org/10.1007/s00382-012-1363-7

Chiang, J.C.H., Bitz, C.M. (2005). Influence of high latitude ice cover on the marine Intertropical Convergence Zone. Climate Dynamics 25, 477-496. http://dx.doi.org/10.1007/s00382-005-0040-5

Clark, C.O., Webster, P.J., Cole, J.E. (2003). Interdecadal variability of the relationship between the Indian Ocean zonal mode and East African coastal rainfall anomalies. Journal of Climate 16, 548-554. http://dx.doi.org/10.1175/1520-0442(2003)016<0548:Ivotrb>2.0.Co;2

Clark, P.U., Pisias, N.G., Stocker, T.F., Weaver, A.J. (2002). The role of the thermohaline circulation in abrupt climate change. Nature 415, 863-869. http://dx.doi.org/10.1038/415863a

Clark, P.U., Shakun, J.D., Baker, P.A., Bartlein, P.J., Brewer, S., Brook, E., Carlson, A.E., Cheng, H., Kaufman, D.S., Liu, Z., Marchitto, T.M., Mix, A.C., Morrill, C., Otto-Bliesner, B.L., Pahnke, K., Russell, J.M., Whitlock, C., Adkins, J.F., Blois, J.L., Clark, J., Colman, S.M., Curry, W.B., Flower, B.P., He, F., Johnson, T.C., Lynch-Stieglitz, J., Markgraf, V., McManus, J., Mitrovica, J.X., Moreno, P.I., Williams, J.W. (2012). Global climate evolution during the last deglaciation. Proceedings of the National Academy of Sciences 109, E1134. http://dx.doi.org/10.1073/pnas.1116619109

Cosford, J., Qing, H., Eglington, B., Mattey, D., Yuan, D., Zhang, M., Cheng, H. (2008). East Asian monsoon variability since the Mid-Holocene recorded in a high-resolution, absolute-dated aragonite speleothem from eastern China. Earth and Planetary Science Letters 275, 296-307. http://dx.doi.org/10.1016/j.epsl.2008.08.018

Cosford, J., Qing, H., Mattey, D., Eglington, B., Zhang, M. (2009). Climatic and local effects on stalagmite $\delta^{13}C$ values at Lianhua Cave, China. Palaeogeography, Palaeoclimatology, Palaeoecology 280, 235-244. http://dx.doi.org/10.1016/j.palaeo.2009.05.020

D'Arrigo, R., Smerdon, J.E. (2008). Tropical climate influences on drought variability over Java, Indonesia. Geophysical Research Letters 35. http://dx.doi.org/10.1029/2007gl032589

Dai, A., Wigley, T.M.L. (2000). Global patterns of ENSO-induced precipitation. Geophysical Research Letters 27, 1283-1286. http://dx.doi.org/10.1029/1999GL011140

Dansgaard, W. (1964). Stable isotopes in precipitation. Tellus 16, 436-468.

Denniston, R.F., Wyrwoll, K.-H., Asmerom, Y., Polyak, V.J., Humphreys, W.F., Cugley, J., Woods, D., LaPointe, Z., Peota, J., Greaves, E. (2013). North Atlantic forcing of millennial-scale Indo-Australian monsoon dynamics during the Last Glacial period. Quaternary Science Reviews 72, 159-168. http://dx.doi.org/10.1016/j.quascirev.2013.04.012

Denton, G.H., Anderson, R.F., Toggweiler, J.R., Edwards, R.L., Schaefer, J.M., Putnam, A.E. (2010). The Last Glacial Termination. Science 328, 1652-1656. http://dx.doi.org/10.1126/science.1184119

Domínguez-Villar, D., Krklec, K., Pelicon, P., Fairchild, I.J., Cheng, H., Edwards, L.R. (2016). Geochemistry of speleothems affected by aragonite to calcite recrystallization - potential inheritance from the precursor mineral. Geochimica et Cosmochimica Acta. http://dx.doi.org/10.1016/j.gca.2016.11.040

Dorale, J.A., Liu, Z.H. (2009). Limitations of Hendy Test Criteria in Judging the Paleoclimatic Suitability of Speleothems and the Need for Replication. Journal of Cave and Karst Studies 71, 73-80.

Dykoski, C.A., Edwards, R.L., Cheng, H., Yuan, D., Cai, Y., Zhang, M., Lin, Y., Qing, J., An, Z., Revenaugh, J. (2005). A high-resolution, absolute-dated Holocene and deglacial Asian monsoon record from Dongge Cave, China. Earth and Planetary Science Letters 233, 71-86. http://dx.doi.org/10.1016/j.epsl.2005.01.036

Edwards, R.L., Chen, J.H., Wasserburg, G.J. (1987). ^{238}U-^{234}U-^{230}Th-^{232}Th systematics and the precise measurement of time over the past 500,000 years. Earth and Planetary Science Letters 81, 175-192. http://dx.doi.org/10.1016/0012-821X(87)90154-3

Emmanuel, S.C. (2000). Impact to lung health of haze from forest fires: The Singapore experience. Respirology 5, 175-182. http://dx.doi.org/10.1046/j.1440-1843.2000.00247.x

England, M.H., Ummenhofer, C.C., Santoso, A. (2006). Interannual rainfall extremes over southwest Western Australia linked to Indian Ocean climate variability. Journal of Climate 19, 1948-1969. http://dx.doi.org/10.1175/Jcli3700.1

Fairchild, I.J., Baker, A. (2012), Speleothem science: from process to past environments. Wiley-Blackwell.

Fairchild, I.J., Smith, C.L., Baker, A., Fuller, L., Spötl, C., Mattey, D., McDermott, F., E.I.M.F. (2006). Modification and preservation of environmental signals in speleothems. Earth-Science Reviews 75, 105-153. http://dx.doi.org/10.1016/j.earscirev.2005.08.003

Fairchild, I.J., Treble, P.C. (2009). Trace elements in speleothems as recorders of environmental change. Quaternary Science Reviews 28, 449-468. http://dx.doi.org/10.1016/j.quascirev.2008.11.007

Finch, A.A., Shaw, P.A., Weedon, G.P., Holmgren, K. (2001). Trace element variation in speleothem aragonite: potential for palaeoenvironmental reconstruction. Earth and Planetary Science Letters 186, 255-267. http://dx.doi.org/10.1016/S0012-821x(01)00253-9

Frisia, S., Borsato, A., Fairchild, I.J., McDermott, F., Selmo, E.M. (2002). Aragonite-calcite relationships in speleothems (Grotte De Clamouse, France): Environment, fabrics, and carbonate geochemistry. Journal of Sedimentary Research 72, 687-699. http://dx.doi.org/10.1306/020702720687

Gadgil, S. (2018). The monsoon system: Land–sea breeze or the ITCZ? Journal of Earth System Science 127, 1. http://dx.doi.org/10.1007/s12040-017-0916-x

Gascoyne, M. (1983). Trace-element partition coefficients in the calcite-water system and their paleoclimatic significance in cave studies. Journal of Hydrology 61, 213-222. http://dx.doi.org/10.1016/0022-1694(83)90249-4

Gascoyne, M. (1992). Palaeoclimate determination from cave calcite deposits. Quaternary Science Reviews 11, 609-632. http://dx.doi.org/10.1016/0277-3791(92)90074-I

Gat, J.R., Mook, W.G., Meijer, H.A.J. (2001). Environmental isotopes in the hydrological cycle (Atmospheric Water). Principles and Applications UNESCO/IAEA Series 2, 63-67.

Gentilli, J. (1971), Climates of Australia and New Zealand. Elsevier Pub. Co.

Genty, D., Blamart, D., Ghaleb, B., Plagnes, V., Causse, C., Bakalowicz, M., Zouari, K., Chkir, N., Hellstrom, J., Wainer, K., Bourges, F. (2006). Timing and dynamics of the last deglaciation from European and North African δ13C stalagmite profiles—comparison with Chinese and South Hemisphere stalagmites. Quaternary Science Reviews 25, 2118-2142. http://dx.doi.org/10.1016/j.quascirev.2006.01.030

Gibbons, F.T., Oppo, D.W., Mohtadi, M., Rosenthal, Y., Cheng, J., Liu, Z., Linsley, B.K. (2014). Deglacial $\delta^{18}O$ and hydrologic variability in the tropical Pacific and Indian Oceans. Earth and Planetary Science Letters 387, 240-251. http://dx.doi.org/10.1016/j.epsl.2013.11.032

Green, H., Pickering, R., Drysdale, R., Johnson, B.C., Hellstrom, J., Wallace, M. (2015). Evidence for global teleconnections in a late Pleistocene speleothem record of water balance and vegetation change at Sudwala Cave, South Africa.

Quaternary Science Reviews 110, 114-130. http://dx.doi.org/10.1016/j.quascirev.2014.11.016

Griffiths, M.L., Drysdale, R.N., Gagan, M.K., Zhao, J.-x., Ayliffe, L.K., Hellstrom, J.C., Hantoro, W.S., Frisia, S., Feng, Y.-X., Cartwright, I., St. Pierre, E.J., Fischer, M.J., Suwargadi, B.W. (2009). Increasing Australian-Indonesian monsoon rainfall linked to early Holocene sea-level rise. Nature Geoscience 2, 636-639. http://dx.doi.org/10.1038/Ngeo605

Hartland, A., Fairchild, I.J., Lead, J.R., Borsato, A., Baker, A., Frisia, S., Baalousha, M. (2012). From soil to cave: Transport of trace metals by natural organic matter in karst dripwaters. Chemical Geology 304–305, 68-82. http://dx.doi.org/10.1016/j.chemgeo.2012.01.032

Heinrich, H. (1988). Origin and consequences of cyclic ice rafting in the Northeast Atlantic Ocean during the past 130,000 years. Quaternary Research 29, 142-152. http://dx.doi.org/10.1016/0033-5894(88)90057-9

Hellstrom, J.C. (2006). U–Th dating of speleothems with high initial ^{230}Th using stratigraphical constraint. Quaternary Geochronology 1, 289-295. http://dx.doi.org/10.1016/j.quageo.2007.01.004

Hendy, C.H., Wilson, A.T. (1968). Palaeoclimatic data from speleothems. Nature 219, 48-51. http://dx.doi.org/10.1038/219048a0

Holmgren, K., Lee-Thorp, J.A., Cooper, G.R.J., Lundblad, K., Partridge, T.C., Scott, L., Sithaldeen, R., Siep Talma, A., Tyson, P.D. (2003). Persistent millennial-scale climatic variability over the past 25,000 years in Southern Africa. Quaternary Science Reviews 22, 2311-2326. http://dx.doi.org/10.1016/S0277-3791(03)00204-X

Hughen, K.A., Overpeck, J.T., Peterson, L.C., Trumbore, S. (1996). Rapid climate changes in the tropical Atlantic region during the last deglaciation. Nature 380, 51-54. http://dx.doi.org/10.1038/380051a0

Jamieson, R.A., Baldini, J.U.L., Brett, M.J., Taylor, J., Ridley, H.E., Ottley, C.J., Prufer, K.M., Wassenburg, J.A., Scholz, D., Breitenbach, S.F.M. (2016). Intra- and inter-annual uranium concentration variability in a Belizean stalagmite controlled by prior aragonite precipitation: a new tool for reconstructing hydro-climate using aragonitic speleothems. Geochimica et Cosmochimica Acta 190, 332-346. http://dx.doi.org/10.1016/j.gca.2016.06.037

Johnson, K.R., Hu, C., Belshaw, N.S., Henderson, G.M. (2006). Seasonal trace-element and stable-isotope variations in a Chinese speleothem: The potential for high-resolution paleomonsoon reconstruction. Earth and Planetary Science Letters 244, 394-407. http://dx.doi.org/10.1016/j.epsl.2006.01.064

Kim, S.-T., O'Neil, J.R., Hillaire-Marcel, C., Mucci, A. (2007). Oxygen isotope fractionation between synthetic aragonite and water: Influence of temperature and Mg^{2+} concentration. Geochimica et Cosmochimica Acta 71, 4704-4715. http://dx.doi.org/10.1016/j.gca.2007.04.019

Knutti, R., Fluckiger, J., Stocker, T.F., Timmermann, A. (2004). Strong hemispheric coupling of glacial climate through freshwater discharge and ocean circulation. Nature 430, 851-856. http://dx.doi.org/10.1038/nature02786

Kotlia, B.S., Singh, A.K., Zhao, J.-X., Duan, W., Tan, M., Sharma, A.K., Raza, W. (2016). Stalagmite based high resolution precipitation variability for past four

centuries in the Indian Central Himalaya: Chulerasim cave re-visited and data re-interpretation. Quaternary International. http://dx.doi.org/10.1016/j.quaint.2016.04.007

Kraus, E.B., Businger, J.A. (1994), Atmosphere-Ocean Interaction. Oxford University Press, USA.

Ku, T.-L. (2000). Uranium-Series Methods, in: Noller, J.S., Sowers, J.M., Lettis, W.R. (Eds.), Quaternary Geochronology. American Geophysical Union, Washington, D. C., pp. 101-114.

Lachniet, M.S. (2009). Climatic and environmental controls on speleothem oxygen-isiotope values. Quaternary Science Reviews 28, 412-432. http://dx.doi.org/10.1016/j.quascirev.2008.10.021

Lachniet, M.S., Bernal, J.P., Asmerom, Y., Polyak, V. (2012). Uranium loss and aragonite–calcite age discordance in a calcitized aragonite stalagmite. Quaternary Geochronology 14, 26-37. http://dx.doi.org/10.1016/j.quageo.2012.08.003

Lascu, I., Feinberg, J.M. (2011). Speleothem magnetism. Quaternary Science Reviews 30, 3306-3320. http://dx.doi.org/10.1016/j.quascirev.2011.08.004

Li, H.-C., Lee, Z.-H., Wan, N.-J., Shen, C.-C., Li, T.-Y., Yuan, D.-X., Chen, Y.-H. (2011). The $\delta^{18}O$ and $\delta^{13}C$ records in an aragonite stalagmite from Furong Cave, Chongqing, China: A-2000-year record of monsoonal climate. Journal of Asian Earth Sciences 40, 1121-1130. http://dx.doi.org/10.1016/j.jseaes.2010.06.011

Lukas, R., Yamagata, T., McCreary, J.P. (1996). Pacific low-latitude western boundary currents and the Indonesian throughflow. Journal of Geophysical Research: Oceans 101, 12209-12216. http://dx.doi.org/10.1029/96jc01204

Manabe, S., Stouffer, R.J. (1994). Multiple-century response of a coupled ocean-atmosphere model to an increase of atmospheric carbon dioxide. Journal of Climate 7, 5-23. http://dx.doi.org/10.1175/1520-0442(1994)007<0005:Mcroac>2.0.Co;2

McDermott, F. (2004). Palaeo-climate reconstruction from stable isotope variations in speleothems: a review. Quaternary Science Reviews 23, 901-918. http://dx.doi.org/10.1016/j.quascirev.2003.06.021

McManus, J.F., Francois, R., Gherardi, J.-M., Keigwin, L.D., Brown-Leger, S. (2004). Collapse and rapid resumption of Atlantic meridional circulation linked to deglacial climate changes. Nature 428, 834-837. http://dx.doi.org/10.1038/nature02494

McMillan, E.A., Fairchild, I.J., Frisia, S., Borsato, A., McDermott, F. (2005). Annual trace element cycles in calcite–aragonite speleothems: evidence of drought in the western Mediterranean 1200–1100 yr BP. Journal of Quaternary Science 20, 423-433. http://dx.doi.org/10.1002/jqs.943

Merkel, U., Prange, M., Schulz, M. (2010). ENSO variability and teleconnections during glacial climates. Quaternary Science Reviews 29, 86-100. http://dx.doi.org/10.1016/j.quascirev.2009.11.006

Morse, J.W., Bender, M.L. (1990). Partition coefficients in calcite: Examination of factors influencing the validity of experimental results and their application to natural systems. Chemical Geology 82, 265-277. http://dx.doi.org/10.1016/0009-2541(90)90085-L

NGRIP members (2004). High-resolution record of Northern Hemisphere climate extending into the last interglacial period. Nature 431, 147-151. http://dx.doi.org/10.1038/nature02805

Oerter, H., Graf, W., Meyer, H., Wilhelms, F. (2004). The EPICA ice core from Dronning Maud Land: first results from stable-isotope measurements. Annals of Glaciology 39, 307-312. http://dx.doi.org/10.3189/172756404781814032

Ortega, R., Maire, R., Devès, G., Quinif, Y. (2005). High-resolution mapping of uranium and other trace elements in recrystallized aragonite–calcite speleothems from caves in the Pyrenees (France): Implication for U-series dating. Earth and Planetary Science Letters 237, 911-923. http://dx.doi.org/10.1016/j.epsl.2005.06.045

Pausata, F.S.R., Battisti, D.S., Nisancioglu, K.H., Bitz, C.M. (2011). Chinese stalagmite $\delta^{18}O$ controlled by changes in the Indian monsoon during a simulated Heinrich event. Nature Geoscience 4, 474-480. http://dx.doi.org/10.1038/ngeo1169

Ramage, C.S. (1971), Monsoon Meteorology. Academic Press, New York.

Rasmussen, S.O., Bigler, M., Blockley, S.P., Blunier, T., Buchardt, S.L., Clausen, H.B., Cvijanovic, I., Dahl-Jensen, D., Johnsen, S.J., Fischer, H., Gkinis, V., Guillevic, M., Hoek, W.Z., Lowe, J.J., Pedro, J.B., Popp, T., Seierstad, I.K., Steffensen, J.P., Svensson, A.M., Vallelonga, P., Vinther, B.M., Walker, M.J.C., Wheatley, J.J., Winstrup, M. (2014). A stratigraphic framework for abrupt climatic changes during the Last Glacial period based on three synchronized Greenland ice-core records: refining and extending the INTIMATE event stratigraphy. Quaternary Science Reviews 106, 14-28. http://dx.doi.org/10.1016/j.quascirev.2014.09.007

Richards, D.A., Dorale, J.A. (2003). Uranium-series chronology and environmental applications of speleothems. Reviews in Mineralogy and Geochemistry 52, 407-460. http://dx.doi.org/10.2113/0520407

Risi, C., Bony, S., Vimeux, F. (2008). Influence of convective processes on the isotopic composition ($\delta^{18}O$ and δD) of precipitation and water vapor in the tropics: 2. Physical interpretation of the amount effect. Journal of Geophysical Research: Atmospheres 113, D19306. http://dx.doi.org/10.1029/2008JD009943

Roberts, M.S., Smart, P.L., Baker, A. (1998). Annual trace element variations in a Holocene speleothem. Earth and Planetary Science Letters 154, 237-246. http://dx.doi.org/10.1016/S0012-821x(97)00116-7

Rozanski, K., Araguás-Araguás, L., Gonfiantini, R. (1993). Isotopic patterns in modern global precipitation, Climate Change in Continental Isotopic Records. American Geophysical Union, pp. 1-36.

Rutlidge, H., Baker, A., Marjo, C.E., Andersen, M.S., Graham, P.W., Cuthbert, M.O., Rau, G.C., Roshan, H., Markowska, M., Mariethoz, G., Jex, C.N. (2014).

Dripwater organic matter and trace element geochemistry in a semi-arid karst environment: Implications for speleothem paleoclimatology. Geochimica et Cosmochimica Acta 135, 217-230. http://dx.doi.org/10.1016/j.gca.2014.03.036

Saji, N.H., Goswami, B.N., Vinayachandran, P.N., Yamagata, T. (1999). A dipole mode in the tropical Indian Ocean. Nature 401, 360-363. http://dx.doi.org/10.1038/43854

Schott, F.A., Xie, S.-P., McCreary, J.P. (2009). Indian Ocean circulation and climate variability. Reviews of Geophysics 47, RG1002. http://dx.doi.org/10.1029/2007rg000245

Shakun, J.D., Burns, S.J., Fleitmann, D., Kramers, J., Matter, A., Al-Subary, A. (2007). A high-resolution, absolute-dated deglacial speleothem record of Indian Ocean climate from Socotra Island, Yemen. Earth and Planetary Science Letters 259, 442-456. http://dx.doi.org/10.1016/j.epsl.2007.05.004

Sinclair, D.J. (2011). Two mathematical models of Mg and Sr partitioning into solution during incongruent calcite dissolution: Implications for dripwater and speleothem studies. Chemical Geology 283, 119-133. http://dx.doi.org/10.1016/j.chemgeo.2010.05.022

Stocker, T.F., Timmermann, A., Renold, M., Timm, O. (2007). Effects of Salt Compensation on the Climate Model Response in Simulations of Large Changes of the Atlantic Meridional Overturning Circulation. Journal of Climate 20, 5912-5928. http://dx.doi.org/10.1175/2007JCLI1662.1

Stuecker, M.F., Timmermann, A., Jin, F.F., Chikamoto, Y., Zhang, W., Wittenberg, A.T., Widiasih, E., Zhao, S. (2017). Revisiting ENSO/Indian Ocean Dipole phase relationships. Geophysical Research Letters 44, 2481-2492. http://dx.doi.org/10.1002/2016GL072308

Stuiver, M., Grootes, P.M. (2000). GISP2 Oxygen Isotope Ratios. Quaternary Research 53, 277-284. http://dx.doi.org/10.1006/qres.2000.2127

Suppiah, R. (1992). The Australian summer monsoon: a review. Progress in Physical Geography 16, 283-318. http://dx.doi.org/10.1177/030913339201600302

Swingedouw, D., Braconnot, P., Delecluse, P., Guilyardi, E., Marti, O. (2007). Quantifying the AMOC feedbacks during a 2×CO_2 stabilization experiment with land-ice melting. Climate Dynamics 29, 521-534. http://dx.doi.org/10.1007/s00382-007-0250-0

Thunell, R., Anderson, D., Gellar, D., Miao, Q. (1994). Sea-Surface temperature estimates for the tropical western Pacific during the Last Glaciation and their implications for the Pacific Warm Pool. Quaternary Research 41, 255-264. http://dx.doi.org/10.1006/qres.1994.1029

Tierney, J.E., Pausata, F.S.R., deMenocal, P. (2015). Deglacial Indian monsoon failure and North Atlantic stadials linked by Indian Ocean surface cooling. Nature Geoscience advance online publication. http://dx.doi.org/10.1038/ngeo2603

Trenberth, K.E., Stepaniak, D.P., Caron, J.M. (2000). The global monsoon as seen through the divergent atmospheric circulation. Journal of Climate 13, 3969-

3993. http://dx.doi.org/10.1175/1520-0442(2000)013<3969:Tgmast>2.0.Co;2

Ummenhofer, C.C., England, M.H., McIntosh, P.C., Meyers, G.A., Pook, M.J., Risbey, J.S., Gupta, A.S., Taschetto, A.S. (2009). What causes southeast Australia's worst droughts? Geophysical Research Letters 36, L04706. http://dx.doi.org/10.1029/2008GL036801

Vellinga, M., Wu, P. (2004). Low-Latitude Freshwater Influence on Centennial Variability of the Atlantic Thermohaline Circulation. Journal of Climate 17, 4498-4511. http://dx.doi.org/10.1175/3219.1

Vuille, M., Bradley, R.S., Werner, M., Healy, R., Keimig, F. (2003). Modeling $\delta^{18}O$ in precipitation over the tropical Americas: 1. Interannual variability and climatic controls. Journal of Geophysical Research: Atmospheres 108, 4174. http://dx.doi.org/10.1029/2001JD002038

Waliser, D.E., Gautier, C. (1993). A satellite-derived climatology of the ITCZ. Journal of Climate 6, 2162-2174. http://dx.doi.org/10.1175/1520-0442(1993)006<2162:Asdcot>2.0.Co;2

Walker, M.J.C., Björck, S., Lowe, J.J., Cwynar, L.C., Johnsen, S., Knudsen, K.L., Wohlfarth, B., group, I. (1999). Isotopic 'events' in the GRIP ice core: a stratotype for the Late Pleistocene. Quaternary Science Reviews 18, 1143-1150. http://dx.doi.org/10.1016/S0277-3791(99)00023-2

Wang, C., Deser, C., Yu, J.-Y., DiNezio, P., Clement, A. (2012). El Niño and Southern Oscillation (ENSO): A review, Coral Reefs of the Eastern Pacific. Springer, pp. 3-19.

Wang, P. (2009). Global monsoon in a geological perspective. Chinese Science Bulletin 54, 1113-1136. http://dx.doi.org/10.1007/s11434-009-0169-4

Wang, P.X., Wang, B., Cheng, H., Fasullo, J., Guo, Z., Kiefer, T., Liu, Z. (2017). The global monsoon across time scales: Mechanisms and outstanding issues. Earth-Science Reviews 174, 84-121. http://dx.doi.org/10.1016/j.earscirev.2017.07.006

Wang, Y., Cheng, H., Edwards, R.L., An, Z., Wu, J., Shen, C.-C., Dorale, J.A. (2001). A high-resolution absolute-dated Late Pleistocene monsoon record from Hulu Cave, China. Science 294, 2345-2348. http://dx.doi.org/10.1126/science.1064618

Wassenburg, J.A., Immenhauser, A., Richter, D.K., Jochum, K.P., Fietzke, J., Deininger, M., Goos, M., Scholz, D., Sabaoui, A. (2012). Climate and cave control on Pleistocene/Holocene calcite-to-aragonite transitions in speleothems from Morocco: Elemental and isotopic evidence. Geochimica et Cosmochimica Acta 92, 23-47. http://dx.doi.org/10.1016/j.gca.2012.06.002

Wassenburg, J.A., Immenhauser, A., Richter, D.K., Niedermayr, A., Riechelmann, S., Fietzke, J., Scholz, D., Jochum, K.P., Fohlmeister, J., Schröder-Ritzrau, A., Sabaoui, A., Riechelmann, D.F.C., Schneider, L., Esper, J. (2013). Moroccan speleothem and tree ring records suggest a variable positive state of the North Atlantic Oscillation during the Medieval Warm Period. Earth and Planetary Science Letters 375, 291-302. http://dx.doi.org/10.1016/j.epsl.2013.05.048

Wassenburg, J.A., Scholz, D., Jochum, K.P., Cheng, H., Oster, J., Immenhauser, A., Richter, D.K., Häger, T., Jamieson, R.A., Baldini, J.U.L., Hoffmann, D., Breitenbach, S.F.M. (2016). Determination of aragonite trace element distribution coefficients from speleothem calcite-aragonite transitions. Geochimica et Cosmochimica Acta 190, 347-367. http://dx.doi.org/10.1016/j.gca.2016.06.036

Webster, P.J., Magaña, V.O., Palmer, T.N., Shukla, J., Tomas, R.A., Yanai, M., Yasunari, T. (1998). Monsoons: Processes, predictability, and the prospects for prediction. Journal of Geophysical Research: Oceans 103, 14451-14510. http://dx.doi.org/10.1029/97jc02719

Webster, P.J., Moore, A.M., Loschnigg, J.P., Leben, R.R. (1999). Coupled ocean-atmosphere dynamics in the Indian Ocean during 1997-98. Nature 401, 356-360. http://dx.doi.org/10.1038/43848

Wurster, C.M., Patterson, W.P., Cheatham, M.M. (1999). Advances in micromilling techniques: a new apparatus for acquiring high-resolution oxygen and carbon stable isotope values and major/minor elemental ratios from accretionary carbonate. Computers & Geosciences 25, 1159-1166. http://dx.doi.org/10.1016/S0098-3004(99)00052-7

Wurtzel, J.B., Abram, N.J., Lewis, S.C., Bajo, P., Hellstrom, J.C., Troitzsch, U., Heslop, D. (2018). Tropical Indo-Pacific hydroclimate response to North Atlantic forcing during the last deglaciation as recorded by a speleothem from Sumatra, Indonesia. Earth and Planetary Science Letters 492, 264-278. http://dx.doi.org/10.1016/j.epsl.2018.04.001

Xie, S.-P. (1996). Westward propagation of latitudinal asymmetry in a coupled ocean–atmosphere model. Journal of the Atmospheric Sciences 53, 3236-3250. http://dx.doi.org/10.1175/1520-0469(1996)053<3236:Wpolai>2.0.Co;2

Yan, X.-H., Ho, C.-R., Zheng, Q., Klemas, V. (1992). Temperature and size variabilities of the Western Pacific Warm Pool. Science 258, 1643-1645. http://dx.doi.org/10.1126/science.258.5088.1643

Zhang, H.-L., Yu, K.-F., Zhao, J.-X., Feng, Y.-X., Lin, Y.-S., Zhou, W., Liu, G.-H. (2013). East Asian Summer Monsoon variations in the past 12.5ka: High-resolution $\delta^{18}O$ record from a precisely dated aragonite stalagmite in central China. Journal of Asian Earth Sciences 73, 162-175. http://dx.doi.org/10.1016/j.jseaes.2013.04.015

Zhang, R., Delworth, T.L. (2005). Simulated tropical response to a substantial weakening of the Atlantic thermohaline circulation. Journal of Climate 18, 1853-1860. http://dx.doi.org/10.1175/Jcli3460.1

2 Tropical Indo-Pacific hydroclimate response to North Atlantic forcing during the last deglaciation as recorded by a speleothem from Sumatra, Indonesia

2.1 Introduction

The last glacial termination was characterized by multiple millennial-scale shifts in global climate. Records of the last deglaciation from Greenland exhibit a sequence of abrupt climatic shifts, starting with the cold interval, Heinrich Stadial 1 (HS1, ~17.5-14.7 ka; thousand years ago) (Heinrich, 1988). This was followed by an abrupt warm event (the Bølling-Allerød (BA, ~14.7-12.9 ka)), a transition back to near glacial conditions during the Younger Dryas (YD; ~12.9-11.7 ka) that culminated in Holocene warmth starting ~11.7 ka (NGRIP members, 2004; Stuiver and Grootes, 2000).

Though the precise cause of abrupt cold events is still debated, there is strong evidence to suggest that they are related to the instability of large ice sheets during glacial terminations (Broecker et al., 2010; Denton et al., 2010). The YD and HS1 events have been identified in North Atlantic marine sediments as increases in ice-rafted debris associated with increased iceberg and meltwater discharge (Bond et al., 1993). The freshwater input into the North Atlantic severely weakened Atlantic Meridional Overturning Circulation (AMOC), reducing northward ocean heat transport, and cooling the Northern Hemisphere (McManus et al., 2004). In response, the Southern Hemisphere warmed during the cold stadials, HS1 and the YD, and warming stalled during the Antarctic Cold Reversal (ACR), the southern counterpart to the BA (Barker et al., 2009; Knutti et al., 2004; Pedro et al., 2011). In response to this "bipolar seesaw", in which reorganization of ocean circulation during stadials redistributes heat from the Northern Hemisphere to the Southern

Hemisphere, there is an accompanying reorganization of atmospheric circulation as the mean position of the Intertropical Convergence Zone (ITCZ) shifts southward (Chiang and Bitz, 2005; Zhang, 2005). This, in turn, drives the Southern Hemisphere westerlies southward, reduces Antarctic sea ice extent, increases upwelling and CO_2 ventilation in the Southern Ocean, and feeds back into deglacial warming (Bostock et al., 2013; Denton et al., 2010).

Proxy data from the Cariaco Basin show evidence for this mean southward movement of the ITCZ through a reduction in rainfall in the tropical Atlantic during the YD (Hughen et al., 1996). The Greenland deglacial sequence had far-reaching impacts on precipitation well beyond the North Atlantic. In the Asian and Indian Summer Monsoon realm, speleothem records from Dongge (Dykoski et al., 2005), Hulu (Wang et al., 2001), and Mawmluh Caves (Dutt et al., 2015) exhibit ^{18}O enrichment, interpreted as severely weakened monsoon intensity, during HS1 and the YD, and ^{18}O depletion (monsoon strengthening) during the BA (Figure 2.1). Several mechanisms have been proposed to connect the North Atlantic to the Indian and Asian Monsoons. These include a stationary Rossby wave atmospheric teleconnection between the North Atlantic and India (Mohtadi et al., 2014), perturbations in the position of the Northern Hemisphere subtropical westerly jet (Marzin et al., 2013), and changes to the mean state of Pacific Walker circulation (Zhang and Delworth, 2005). Despite uncertainty about the teleconnection mechanism, abundant empirical evidence exists connecting climate changes in the tropical Indian Ocean region with the North Atlantic, and significant progress has been made towards understanding the regional manifestation of the YD in the Asian monsoon realm.

Both model (Pausata et al., 2011) and proxy (Tierney et al., 2015) data indicate that the regional response in the Indian Ocean to North Atlantic cold snaps is a cooling of western tropical Indian Ocean SSTs. The results of Pausata et al. (2011) suggest that changes in Indian Ocean SSTs during North Atlantic stadials is the primary contributor to changes in the Indian Monsoon with cooler Indian Ocean SSTs causing a reduction in precipitation transported over the Indian Ocean and

Indian subcontinent. As a result, speleothem records of precipitation along this path (e.g., Mawmluh, Dongge, and Hulu Caves) exhibit either reduced rainfall during the YD and HS1, or isotopically enriched signals due to reduced rain-out along the transport path (or a combination of both).

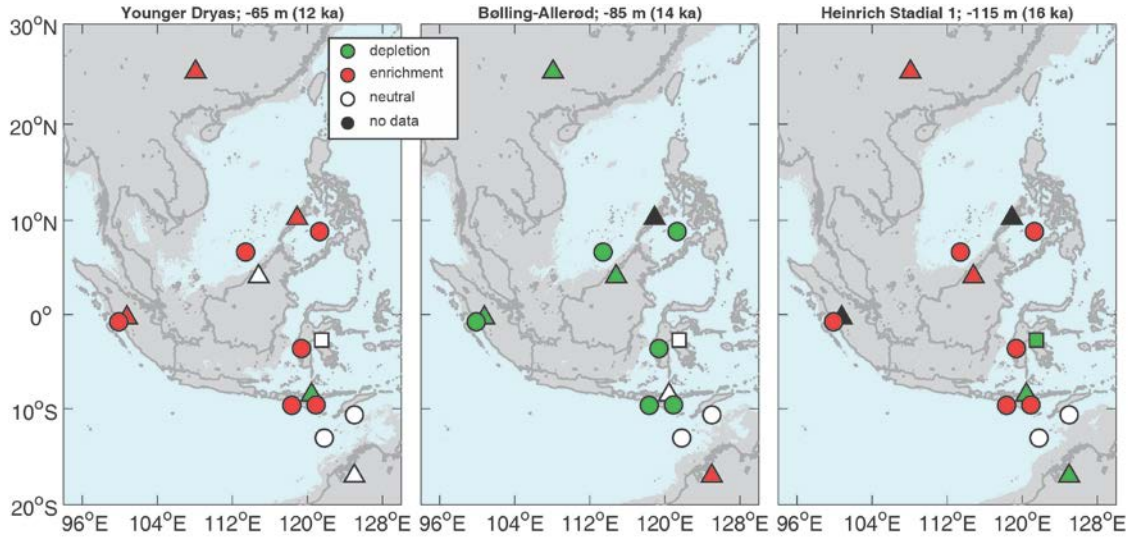

Figure 2.1 – Maps of IPWP proxies discussed in text for three intervals of interest: Heinrich Stadial 1 (16 ka), Bølling-Allerød (14 ka), and the Younger Dryas (12 ka). Marker shapes denote seawater $\delta^{18}O$ (circles), speleothem $\delta^{18}O$ (triangles), and leaf wax δD (square) and marker colours denote direction of the anomaly in terms of depletion of ^{18}O or D (green), enrichment of ^{18}O or D (red), neutral (white), and no data available for the interval (black). Anomalies are classified relative to the preceding interval (YD:BA, BA:HS1, HS1:LGM). The dark grey outline indicates modern coastline, while medium grey shading represents exposed shelf during periods of lower sea level. Sea level was inferred from the curve of Lambeck et al. (2014).

Despite clear North Atlantic signals in Asian speleothems, the manifestation of high-latitude millennial-scale climate events in the Indo-Pacific Warm Pool remains a subject of ambiguity, due to the conflicting information on hydrological variability during the last termination interpreted from the limited number of high-resolution proxy records from this region. For example, speleothem $\delta^{18}O$ from Borneo (Partin et al., 2007) and leaf wax δD from Sulawesi (Konecky et al., 2016) show no response to the Younger Dryas or Bølling-Allerød (Figure 2.1) . However, seawater-$\delta^{18}O$ ($\delta^{18}O_{sw}$) estimates from the South China Sea (Steinke et al., 2006), Sulu Sea (Rosenthal et al., 2003), and Makassar Strait (Schröder et al., 2016) exhibit a deglacial pattern including the YD, BA, and HS1. In the southern IPWP, speleothems from Flores record ^{18}O depletion, suggesting an increase in rainfall during the YD and HS1 that has been interpreted as a mean southward shift of the

ITCZ (Ayliffe et al., 2013; Griffiths et al., 2009). In contrast, two seawater-$\delta^{18}O$ reconstructions from just south of Flores suggest a reduction in rainfall during the YD and HS1 (Gibbons et al., 2014; Levi et al., 2007), while two more in the Timor Sea show no change (Stott et al., 2004; Xu et al., 2008). Furthermore, there is evidence to suggest that northern Australia received enhanced austral summer monsoon rainfall during HS1, and reduced rainfall during the BA, however the YD signal is unclear in these records (Denniston et al., 2013a; Muller et al., 2008).

Cool SSTs in the tropical western Indian Ocean during cold stadials are not mirrored in the tropical eastern Indian Ocean (Mohtadi et al., 2014). Planktonic foraminiferal Mg/Ca-SST reconstructions from offshore West Sumatra show little temperature response to either the YD or HS1 (Mohtadi et al., 2014), similar to other SST reconstructions from the IPWP (Gibbons et al., 2014). There is, however, a clear hydrologic change seen in the seawater oxygen isotope reconstruction from the same site. The $\delta^{18}O_{sw}$ records a strong increase (decrease) during the YD and HS1 (BA), interpreted by the authors as a change in local salinity due to reduced (increased) rainfall, which they attribute to reorganization of Hadley circulation in the Indian Ocean (Mohtadi et al., 2014).

Because the IPWP lies at the intersection between numerous hydrological climate phenomena that have widespread zonal (Walker circulation) and meridional (Hadley circulation, ITCZ, Australasian monsoon) ramifications, it is important to gain a clearer understanding of how this region responded to abrupt climate changes in the past. In light of disparities between IPWP reconstructions of the last deglacial, it is prudent to consider both marine and terrestrial proxies, as well as consider seasonality and meridional-zonal controls on hydrologic variability. Here we present a deglacial-Holocene rainfall record spanning 16,500 years from a precisely-dated, decadally-resolved primary aragonite-calcite stalagmite from central West Sumatra. This is the first speleothem record from the Indian Ocean sector of the IPWP, and the westernmost for all IPWP speleothem sites. The cave site is located ~100 km from sediment core SO189-39KL, and provides a complementary terrestrial perspective to the marine reconstruction. We compare

our record to other hydroclimate records in the Asian and Indian Summer Monsoon (ASM/ISM) realms and in the Indo-Pacific Warm Pool region. We use these results to examine spatial and seasonal differences in Asia and Indo-Pacific Warm Pool hydroclimate during the Bølling-Allerød and Younger Dryas periods. We additionally compare a detailed modern climatology with results from a general circulation model equipped with vapour source distribution (VSD) tracers to infer which moisture sources may be driving precipitation changes under hosing conditions.

2.2 Study site and climatology

Tangga Cave (0°21'S, 100°45'E, 600 m) is located in the Barisan Mountains of central West Sumatra, Indonesia (Figure 2.2). The caves here are in carbonate host rocks formed in the mid-Miocene (Wilson, 2002).

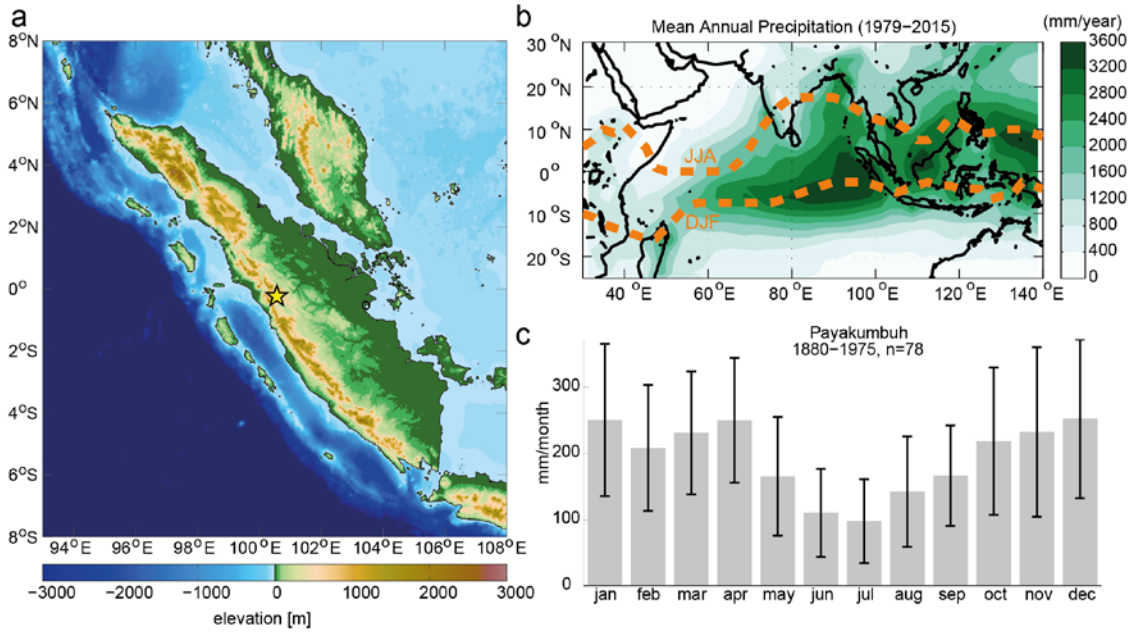

Figure 2.2 - (a) Topographic map of Sumatra with study site marked by star. (b) Mean annual precipitation (1979 – 2015) in the Indo-Pacific region from CPC Merged Analysis of Precipitation (Xie and Arkin, 1997). The position of maximum meridional rainfall (inferred from minimum outgoing long-wave radiation of Liebmann and Smith (1996)) during JJA and DJF is indicated. (c) Mean monthly rainfall from Payakumbuh (~20 km from cave site).

2.2.1 Modern climatology

Modern climatology at Tangga Cave was calculated using meteorological data from a nearby (~20 km) weather station in Payakumbuh village (-0.22°N, 100.62°E) that was active between 1880–1941 and 1951–1975 (Peterson and Vose, 1997). No stations within 100 km were in operation after 1975. Average annual rainfall exceeds 2000 mm yr^{-1} (Figure 2.2) . Rain is received throughout the year, but with a relative minimum in June-July-August. Using NOAA's Hybrid Single Particle Lagrangian Integrated Trajectory (HYSPLIT4) model with the NCEP/NCAR Reanalysis V2 gridded dataset, we analyzed daily back trajectories of rain-bearing air masses to our study site from January 2000 to December 2010 (Draxler and Hess, 1997). Cluster analysis of the 6-day back trajectories of rainfall events (> 8.5 mm/day) identifies three primary sources of rainfall delivered to Tangga Cave (Figure 2.3a). Approximately 69% of average annual rainfall is sourced from the equatorial eastern Indian Ocean (59% local, 10% distal), and arrives throughout the year. From late-April through mid-November, rainfall can also be sourced from the Timor Sea, and this accounts for 17% of the annual average. These trajectories are associated with the southeasterly trades that form during the boreal summer monsoon. From late November through mid-March, this SE trade wind source is cut off and replaced by a long-range South China Sea source. These northeasterly trajectories are associated with circulation patterns of the austral summer monsoon, and contribute 9% of the average annual rainfall to Tangga Cave. Approximately 5% of annual rainfall does not fall into the 3 major trajectory clusters. The cluster contributions show excellent agreement with an earlier study using seven tagged Indo-Pacific water source regions in a single-layer, Rayleigh-type, isotope-enabled GCM (Suwarman et al., 2013). These results corroborate previous studies that suggest rainfall variability in western and northern Sumatra is not dominated by monsoon seasonality (Aldrian and Susanto, 2003; Mohtadi et al., 2014).

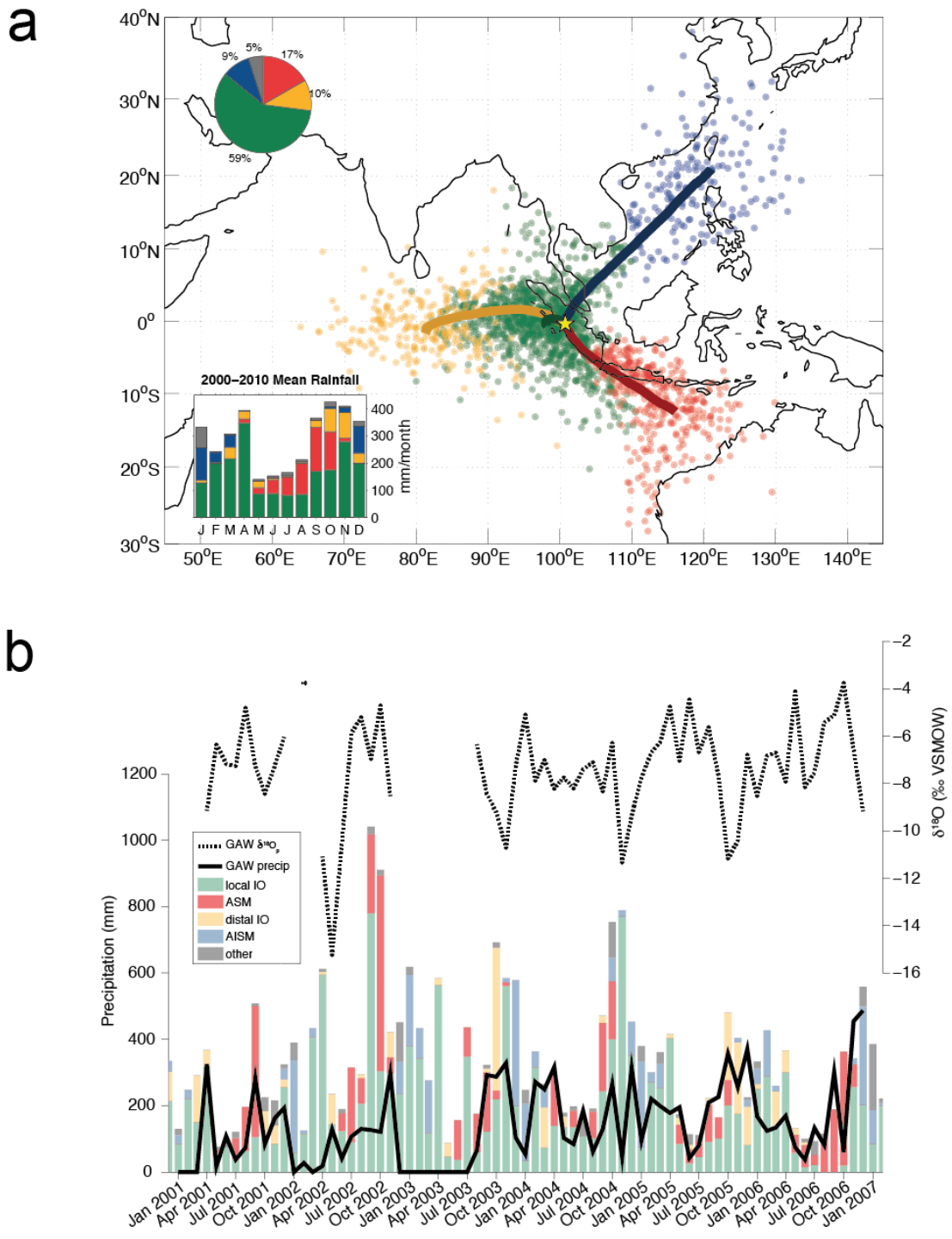

Figure 2.3 - (a) Four primary paths of source moisture to Tangga Cave. Paths were generated using cluster analysis of rain-bearing 6-day back-trajectories over 2000 – 2010 period. Red, blue, yellow and green lines indicate results of HYSPLIT trajectory cluster analysis, with pie chart representing % annual rainfall from each of those sources. Grey represents unassigned trajectories. Inset shows mean monthly rainfall over the analysis period at Tangga Cave from ERA-interim 0.7° gridded data (Dee et al., 2011) with colors corresponding to source cluster. Colored dots represent starting points of all rain-bearing 6-day back trajectories corresponding to cluster. (b) HYSPLIT monthly source contributions for 2001 – 2006 using ERA-interim precipitation data. Color coding is the same as in Figure 2.3a. Black lines are precipitation amount (solid) and precipitation $\delta^{18}O$ (dashed) from Kototabang (GAW) station (0.12°S, 100.19°E, 865 m).

2.2.2 Controls on rainfall $\delta^{18}O$ at Tangga Cave

Regional rainfall stations with isotope data demonstrate that Indonesian rainfall can be described by four groups based on seasonal isotopic variability (Belgaman et al., 2017). These four rainfall types correspond to the rainfall regions as defined by Aldrian and Dwi Susanto (2003). Rainfall in central Sumatra has similar isotopic characteristics to northern Sumatra and western Borneo, consisting of two peaks each year of high $\delta^{18}O$ related to seasonal migration of the ITCZ. Rainfall $\delta^{18}O$ in this domain tends to show only a weak amount effect (Belgaman et al., 2017).

Drip and rainwater monitoring were not feasible at the cave site in this study. However, limited monthly rainfall isotope data is available from nearby station, Kototabang (100.19°E, 0.12°S, 865 masl, GAW), spanning the interval from February 2001 to January 2007 and consisting of 59 rainfall $\delta^{18}O$ observations (Kurita et al., 2009). Analysis of Kototabang station data over this period shows that ~24% of isotopic variance is explained by the local amount effect at 95% significance (Suwarman et al., 2013). However, multiple studies have demonstrated that the contribution of the amount effect is stronger on longer time-scales (Kurita et al., 2009; Moerman et al., 2013) and when considering larger regions (the "regional amount effect") (Moerman et al., 2013). Correlation of Kototabang $\delta^{18}O$ with GPCP v2.3 precipitation shows that a similar relationship (r=-0.4 to -0.5) exists over a broader region of the eastern Indian Ocean (Figure 2.4a).

For the purpose of examining the modern relationship of precipitation $\delta^{18}O$ to rainfall at the study site over a longer time interval, we use existing output from the spectrally nudged, isotope-enabled general circulation model, IsoGSM (Yoshimura et al., 2008). Previous studies have shown that IsoGSM data correlates well with GNIP station data in the ASM/ISM monsoon region (Sinha et al., 2015; Yang et al., 2016). IsoGSM data from the 1.8 x 1.9° grid point nearest Tangga Cave demonstrates that up to 32% of the variance in isotopic values of annual average rainfall on interannual timescales is controlled by the local amount effect,

compared to the 24% predicted by Kototabang station (Figure 2.4b). There is a strong correlation between station and modeled oxygen isotope data (r=0.55; Figure 2.4c) over the period of overlap; however, the correlation between station and modeled precipitation data is very weak (r=0.21; Figure 2.4d). The low correlation between observed and simulated precipitation likely stems from highly spatially variable rainfall over the mountain ranges of Sumatra; there may be significant differences in local amount between Kototabang and the study site, which is averaged in the IsoGSM grid box. The strong correlation that exists in the isotope data is further evidence that the isotopes are regionally coherent, even if rainfall amount is not.

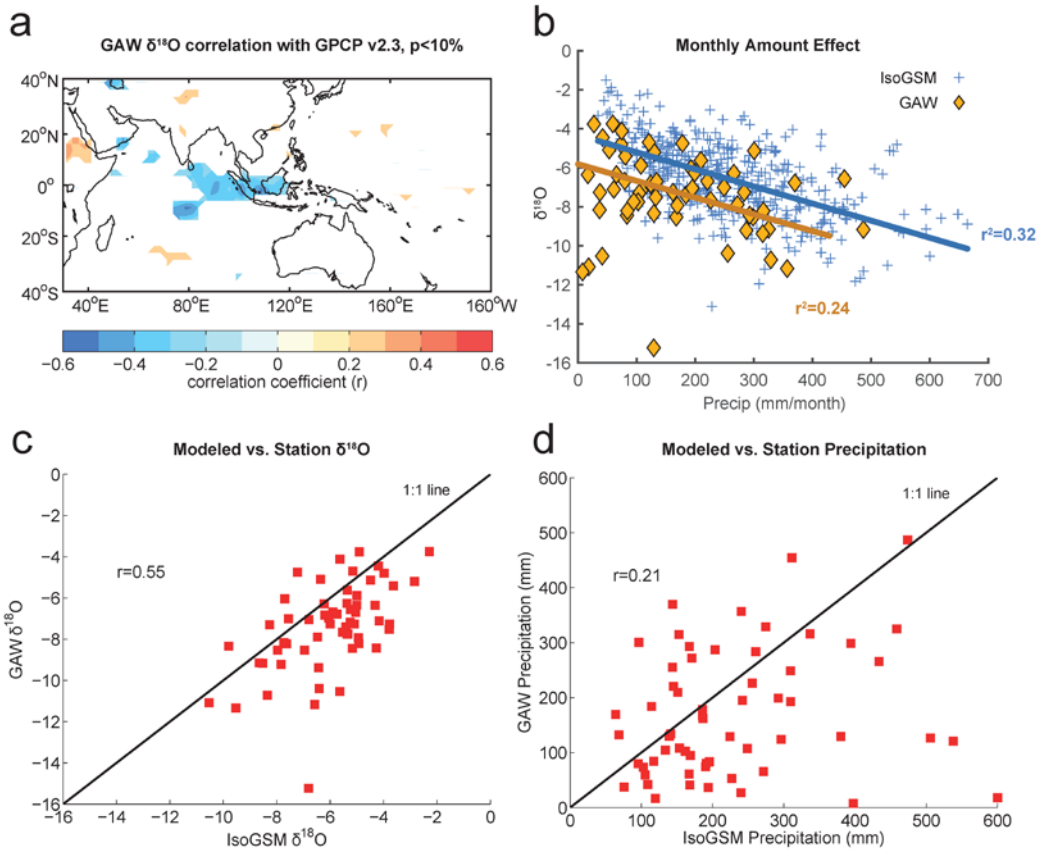

Figure 2.4 – (a) Map showing the correlation coefficient of Kototabang (GAW) station precipitation δ18O with mean annual precipitation from GPCP v2.3 over the period 2001 – 2006. Colors represent r-values significant at 90% level. (b) Linear regression between IsoGSM simulated monthly precipitation amount and simulated monthly precipitation δ18O (blue crosses) at grid point closest to Tangga Cave (1979 – 2013), and linear regression between GAW precipitation amount and monthly δ18O (orange diamonds), demonstrating amount effect. (c) Correlation between observed monthly precipitation δ18O (GAW) and simulated monthly precipitation δ18O (IsoGSM) for the period 2001 – 2006. (d) Correlation between observed monthly precipitation amount (GAW) and simulated precipitation amount (IsoGSM) for months with rainfall>0 mm for the period 2001 – 2006.

Previous modelling studies using tagged moisture source suggest that Asian summer monsoon rainfall is subject to less rainout during transport than Indian Ocean rainfall, despite a longer transport pathway, causing ASM rainfall arriving at the site to be relatively enriched in ^{18}O (Belgaman et al., 2016; Suwarman et al., 2013). Conversely, Indian Ocean moisture transport is subject to greater condensation along its path, producing more negative $\delta^{18}O$ at the site. On a seasonal scale, these moisture source characteristics should enhance the amount effect. In austral winter (June-August; JJA), there is a higher proportion of enriched ASM rainfall arriving at Tangga Cave. Additionally, less average rainfall during JJA should contribute to the more positive $\delta^{18}O$ signal. Conversely, during transition seasons when the ITCZ is overhead (March-May and September-November; MAM and SON), there is increased rainfall and a higher proportion of Indian Ocean sources, both of which should contribute to lighter $\delta^{18}O$.

To assess the combined influence of moisture source with amount effect, we compared the Kototabang precipitation and isotope time series with changes in contributions from HYSPLIT-derived sources over the same time period (Figure 2.3b). This analysis highlights the dominance of the local Indian Ocean moisture source throughout the year. Three large ^{18}O depletion events (April-May 2002, October-November 2003, October-November 2005) occur during spring/autumn when rainfall is generally high and when Indian Ocean contributions (local and distal) are highest, supporting the idea that moisture source and amount effect act in the same direction. Surprisingly, the largest rainfall event (September-October 2002) is associated with relatively enriched values; however, this may be as a result of the above-average proportion of enriched ASM rainfall offsetting the amount effect. It appears then that while negative $\delta^{18}O$ excursions tend to be associated with increased rainfall, increased rainfall does not necessarily produce a negative $\delta^{18}O$ excursion. Heavier $\delta^{18}O$ values are generally associated with an increase in ASM rainfall sources. In particular, the heaviest values occur during September-October 2006 when local Indian Ocean sources were replaced solely by ASM sources as a result of a strong Indian Ocean Dipole event (Abram et al., 2008).

This analysis, along with the broader correlation of Kototabang isotopes with eastern Indian Ocean rainfall amount, suggests that the local eastern Indian Ocean source is the dominant driver of isotopic depletion in rainfall $\delta^{18}O$ at the cave site, both through changes in amount of rainfall being derived from this source and through changes in proportion of this source through time.

Modern seawater oxygen isotope data demonstrates less than a 0.1‰ variation between the three trajectory source regions (LeGrande and Schmidt, 2006). Estimates of LGM seawater isotopic anomalies suggest that the South China Sea may have been relatively depleted by up to 0.3‰ or enriched up to 0.4‰ and the Indian Ocean and Timor Seas may have been enriched by up to 0.5‰ relative to present (Waelbroeck et al., 2014). Assuming a constant fractionation factor over a constant distance over time, there is a maximum 0.5‰ change related to moisture source composition from a single source. With respect to the isotope variability recorded by the Tangga Cave record since the LGM (see Section 4), these values are relatively small. Likewise, the effect of mixing these two moisture sources at a given time in the past, though dependent on the mixing proportion, is limited to the maximum anomaly of +0.5‰, and could be less if the enriched and depleted source averaged out. Therefore, we do not expect source moisture composition changes to be a primary contributor to changes in the speleothem isotope record. Furthermore, Tangga Cave moisture sources appear unlikely to have been influenced by sea level changes, as the trajectories do not generally traverse over exposed shelf. Based on the analyses presented here and regional coherence with other speleothem records, we interpret speleothem $\delta^{18}O$ at the cave site as an annually integrated signal of rainfall amount (dominated by eastern Indian Ocean contributions) as well as the combined influence of multiple moisture transport paths with varying isotopic compositions.

2.3 Materials and methods

2.3.1 Speleothem sampling

The entrance to Tangga Cave is at the base of a sinkhole covered with jungle vegetation. The cave narrows considerably ~50m from the entrance, and descends steeply to a lower level with an underground river passage. The main sample used in this study, TA12-2, was collected from a small chamber located ~105 m from the cave entrance. The specimen was found in a toppled position on a muddy substrate in the lower level of the cave (but above the river).

TA12-2 was slabbed and hand polished before sampling (Figure 2.5). The total length is ~50 cm with a relatively constant diameter of ~4 cm. TA12-2 is visibly laminated with alternating light and dark layers for the top 38 cm. Between 38-44 cm, it is comprised of white needle-like crystalline material, and the final section from 44-50 cm has similar laminations to the upper section.

The central slab was sampled continuously for stable isotope analysis at 0.5mm resolution along its central growth axis using a micromill with a 1mm diameter mill bit. Powders for U-series sampling were collected adjacent to the isotope transect. The offcut slab that faced the milled slab surface was hand-broken (to avoid losing material by sawing) into seven pieces less than 9.5cm length. These pieces were used for used for laser ablation inductively coupled plasma mass spectrometer (ICP-MS) trace element analysis and Raman spectroscopy. After laser analysis, these pieces were used to create petrographic thin sections along the entire length of the specimen. The entrance to Tangga Cave is at the base of a sinkhole covered with jungle vegetation. The cave narrows considerably ~50m from the entrance, and descends steeply to a lower level with an underground river passage. The main sample used in this study, TA12-2, was collected from a small chamber located ~105 m from the cave entrance. The specimen was found in a toppled position on a muddy substrate in the lower level of the cave (but above the river).

2.3.2 Mineralogical determination

TA12-2 was initially screened for mineralogy using X-ray diffraction at two points along the specimen, which indicated an aragonitic composition. However, subsequent detailed trace element analysis indicated that some layers are instead composed of calcite. The techniques described below were used to determine mineralogy along the length of the specimen.

2.3.2.1 Laser ablation ICP-MS trace element analysis

Trace element measurements were made at the Australian National University using an ArF Excimer laser ablation system (193 nm; Lambda Physik LPX120i) coupled with a single collector Varian 820 quadrupole inductively coupled plasma mass spectrometer (ICP-MS). All sample tracks were pre-ablated using a 265 μm spot size at 10 Hz moving at 200 μm/s in order to pre-clean the trace element analysis track. Analyses were conducted by pulsing the laser at 5Hz with a 40 μm round ablation spot moving at 40 μm/s. Twenty elemental masses (^{11}B, ^{23}Na, ^{24}Mg, ^{25}Mg, ^{27}Al, ^{31}P, ^{43}Ca, ^{44}Ca, ^{47}Ti, ^{55}Mn, ^{66}Zn, ^{86}Sr, ^{88}Sr, ^{89}Y, ^{137}Ba, ^{138}Ba, ^{139}La, ^{208}Pb, ^{232}Th, ^{238}U) were measured for transects running along the growth axis of TA12-2. Analysis was also performed on three standards (NIST612, NIST610, in-house coral NEP 3B) and for background counts. The standards and background were measured before and after each analysis transect to correct for drift. All data was corrected relative to the NIST612 glass standard, and normalized to ^{43}Ca, using a MATLAB script written by the author. Calcite and aragonite phases are evident in the Sr and Mg content of the speleothem.

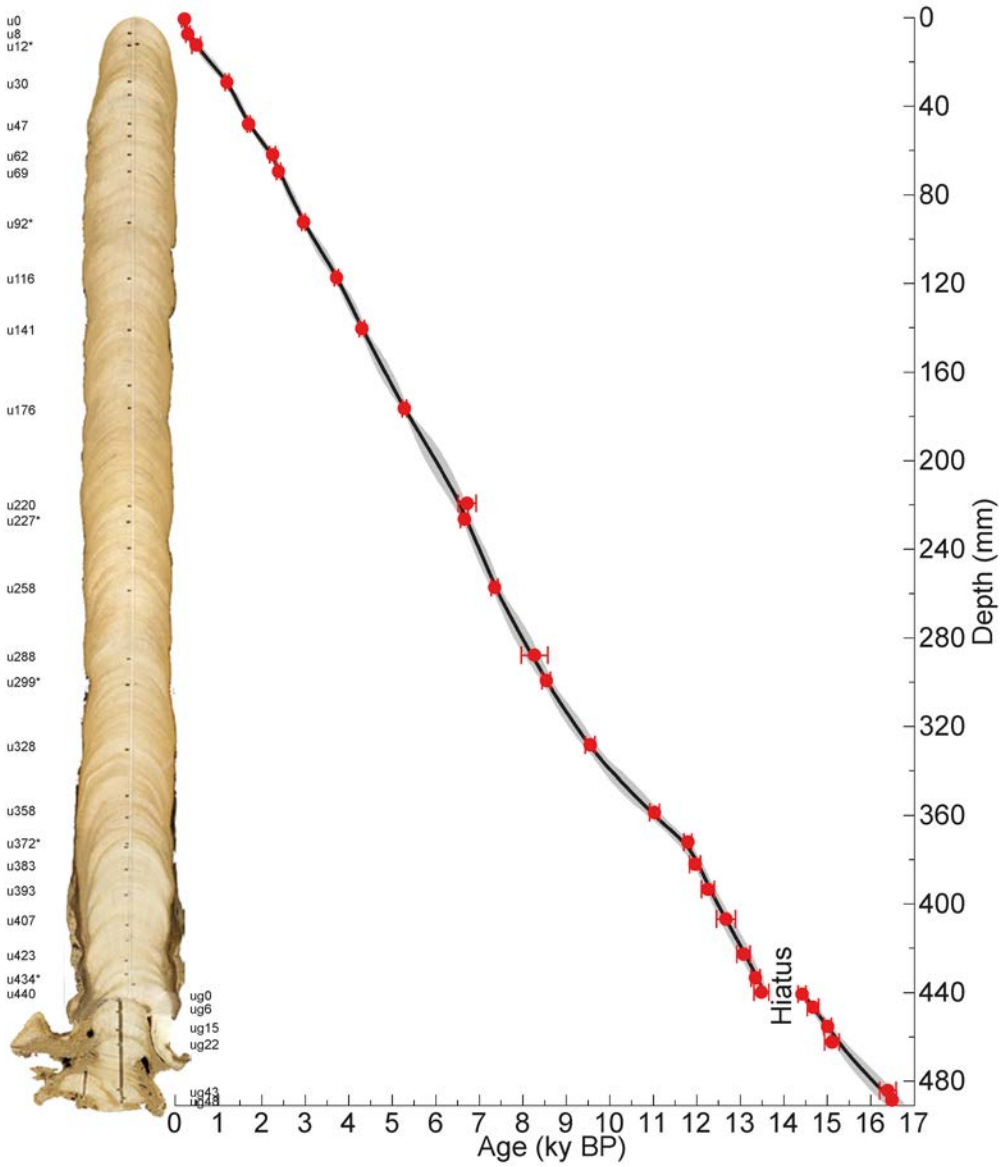

Figure 2.5 - Image of TA12-2 next to U/Th age-depth model for TA12-2. Red circles with 2σ error indicate where dates were taken. Black line is age-depth model. 2σ confidence interval is marked in grey. Age model and uncertainties were generated in Bacon software for R (Blaauw and Christen, 2011). Groove on image shows milling transect for $\delta^{18}O$ samples. Holes beside milling transect show locations where powders were collected for U/Th analysis (Note: not all powders analyzed). *Dates generated at RSES, ANU.

2.3.2.2 Raman spectroscopy

Raman spectroscopy is a non-destructive method that can be used to identify the relative amounts of mineral phases using the vibrational modes of different crystal lattices. In the case of carbonate, the different crystal structures of aragonite and calcite produce distinct Raman spectra, despite sharing the same $CaCO_3$ composition (White, 2006). Raman analysis was performed along the same

analysis track as the trace element laser ablation analysis. Raman analysis was carried out at the ANU's Research School of Physics on a Renishaw InVin Raman spectrometer, using a 632 nm red laser at 50% power with 1200 mm^{-1} grating. A 20x objective lens with a 1.93 µm diameter spot size was used in conjunction with a 1 second acquisition time. Spectra were collected in a broad spectral frequency range from 120-1974 cm^{-1}, but the low frequency range between 150-300 cm^{-1} was used for identifying the diagnostic peaks for calcite (280 cm^{-1}) and aragonite (206 cm^{-1}).

2.3.2.3 Thin section petrography

Thin sections were created from the same offcut slab pieces used for trace element analysis. These pieces were further reduced in size to create a full 13-piece transect of 2x1" thin sections. The unpolished thin sections were prepared at the ANU and photographed at high magnification using a Leica Power Mosaic at the RSES. Thin sections were used to verify the mineralogical classifications derived from trace element and analysis and Raman spectroscopy. Further analysis and identification of mineralogy and diagenetic features was performed at the School of Environmental and Life Sciences at the University of Newcastle. Mineralogical analysis of the thin section samples will be discussed in a subsequent publication, and for the purposes of this manuscript are only used as additional verification of aragonite-calcite phases identified by trace element and Raman spectroscopy methods.

2.3.2.4 Mineralogy

High-resolution laser ablation ICP-MS trace element analysis revealed abrupt anti-phased shifts in magnesium and strontium of several orders of magnitude (Figure 2.6). Magnesium and strontium are known to be preferentially incorporated into calcite and aragonite lattices, respectively (Finch et al., 2001). As such, the distinct shifts in TA12-2 speleothem trace element composition are indicative of alternating layers of aragonite and calcite. The sample is predominantly aragonite, but abrupt excursions to high Mg (low Sr) composition are indicative of calcite layers in the speleothem.

This interpretation is supported by Raman analysis, which definitively identifies the two $CaCO_3$ polymorphs. Raman spectroscopy reveals TA12-2 to be primarily composed of aragonite with irregular intervals of calcite deposition mainly occurring between 180 – 250 mm depth, 280 – 370 mm depth, and 460 – 470 mm depth. Thin section petrography further confirms that these calcite layers precipitated as primary material and that the sample as a whole has undergone only minor secondary micro-replacement to calcite (Silvia Frisia, pers. comm.). This retention of the primary mineralogical phases is critical to the interpretation of the Tangga climate record, as recrystallization of aragonite to calcite can result in the loss of the original $\delta^{18}O$ signal and loss of uranium (Bajo et al., 2016). U/Th dating results obtained from two different laboratories are in good agreement (Table 2.1). This consistency as well as the stratigraphic sequence of all 31 dates support the notion that even if TA12-2 experienced minor U-loss, it is highly likely that chronology presented in this study is accurate and representative of primary depositional conditions.

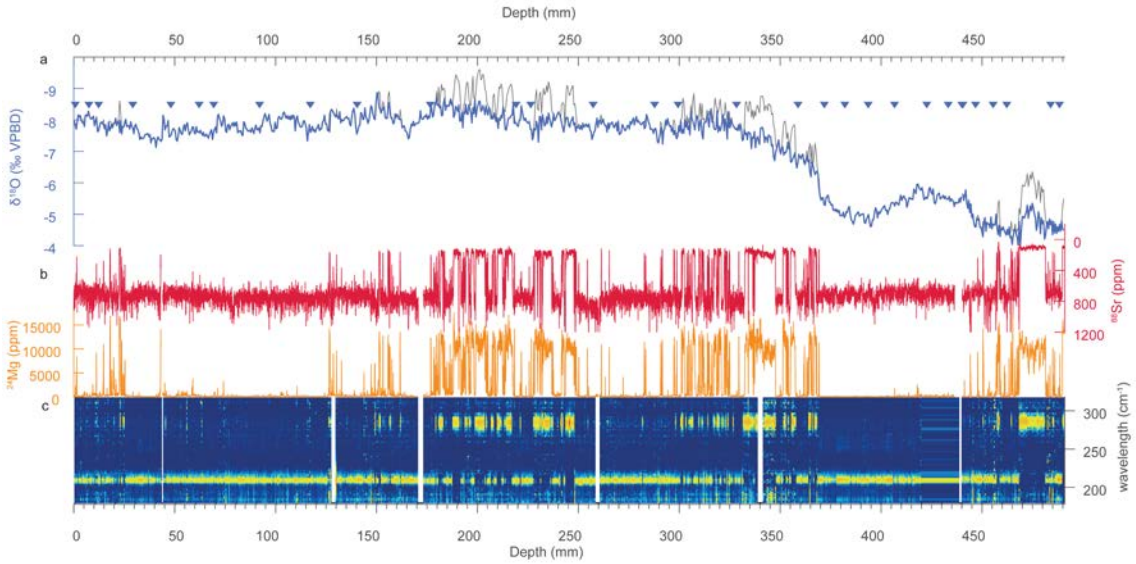

Figure 2.6 – Mineral identification and oxygen isotope correction. Depth vs. a) raw speleothem $\delta^{18}O$ (grey) corrected to aragonite values using 1‰ offset (blue), b) strontium (red) in ppm plotted on reverse y-axis and magnesium (orange) in ppm plotted on log-scale, d) Raman power spectra showing diagnostic wavelength bands for calcite (280 cm^{-1}) and aragonite (206 cm^{-1}). Antiphased behaviour in the trace elements and power in the Raman calcite band corresponds to anomalous depletions in the oxygen isotope record relative aragonite values. Aragonite layers were targeted for U/Th date samples (blue triangles).

2.3.3 Geochronology

Age control for the TA12-2 sample is based on thirty-one uranium-thorium (U/Th) dates. Aragonite layers were targeted for dating due to their high uranium concentrations (>10ppm), and powders of 2-6mg were used. Six dates were generated at the ANU on a Thermo Finnigan Neptune Plus multi-collector ICP-MS using the methods described in McCulloch and Mortimer (2008). Twenty-five dates were generated at the University of Melbourne on a Nu Instruments Plasma multi-collector ICP-MS using the methods of Hellstrom (2003).

The U-Th dating results are summarized in Table 1. Ages are given in thousands of years before present (ky BP; where "present" is defined as 1950 A.D.). All 31 U-series dates for TA12-2 fall in stratigraphic order within error. For all but the top sample, uranium concentrations exceeded 8 ppm, due to the high incorporation of uranium into the aragonite lattice. There was significant variation in the $^{230}Th/^{232}Th$ measurements ranging from 1.7 to 1339.

Ages were corrected for the initial ^{230}Th concentration using the stratigraphical constraint model of Hellstrom (2006), an initial [$^{230}Th/^{232}Th$] of 0.5 ± 0.2 and the U and Th decay constants of Cheng et al. (2013). Ages were calculated and corrected for initial [$^{230}Th/^{232}Th$] in MATLAB using Monte Carlo simulations ($n=10^4$) to account for 2σ uncertainties in each of the input variables and to determine errors on the resulting ages (Hellstrom, 2003; Scroxton, 2014). A hiatus occurs at a depth of 440mm and spans ~0.88 ky between 13.5 ± 0.11 ky BP and 14.4 ± 0.10 ky BP (Figure 2.5). The depth-age model for the speleothem was constructed separately for above and below the unconformity using a Bayesian Monte Carlo approach with the statistical software package, Bacon, for R (Blaauw and Christen, 2011) Results from Bacon compared well with the model using methods from (Hellstrom, 2006) but allowed more flexibility in dealing with the hiatus.

2.3.4 Stable isotope analysis

2.3.4.1 Analytical methods

Measurements of $\delta^{18}O$ were made on aliquots of milled powder weighing between 110 and 140 µg at the Australian National University using a Finnigan MAT-253 Isotope Ratio Mass Spectrometer coupled with an automated Kiel IV Carbonate device using 105% H_3PO_4 at 75°C for carbonate reactions. Results are corrected using international standards NBS-19 ($\delta^{18}O$=-2.20‰ VPDB) and NBS-18 ($\delta^{18}O$=-23.00‰ VPDB; note: To maintain long-term consistency of $\delta^{18}O$ results from the RSES stable isotope facility, the old value of NBS-18 $\delta^{18}O$ composition is used). The internal standard of ANU-M2 ($\delta^{18}O$=-7.32‰) was also routinely analysed as an additional data quality monitor. The analytical error for measurements of NBS-19 and ANU-M2 were calculated by finding the standard deviation across all runs. Using this method, the analytical error was 0.041‰ (n = 144, 1σ) for NBS-19 $\delta^{18}O$, and 0.070‰ (n = 44, 1σ) for ANU-M2 $\delta^{18}O$. Stable isotope values are expressed in delta notation (δ) as per mille (‰) deviations, relative to Vienna Peedee Belemnite (VPDB). The oxygen isotope profile for TA12-2 is based on 901 isotopic measurements.

2.3.4.2 Isotopic Corrections

The carbonate deposition in aragonite and calcite phases of the speleothem appears to be primary and so it is assumed that both polymorphs retain their original isotopic signals. This results in a relative depletion of ^{18}O in the calcite layers compared to aragonite, due to the different isotopic fractionation coefficients of oxygen between the two phases. This offset has been previously quantified in synthetic aragonite and *in situ* mineralogical studies to be between 0.6-1.0‰ at 25°C (Frisia et al., 2002; Kim et al., 2007).

Calcite layers in TA12-2 were defined using a 3-component Gaussian Mixture Model (GMM) (McLachlan and Peel, 2004) on the Mg-Sr laser ablation ICP-MS data set, consisting of ~18,000 data points. The optimal GMM identified a calcite component based on a high Mg-low Sr composition. All points within this cluster

were assigned as calcite and all remaining points received an aragonite assignment. The laser ablation data was then binned according to stable isotope sample depth. On average, there are about 20 laser ablation measurements per stable isotope sample. Each isotope measurement was corrected to aragonite-equivalent isotopic values based on the fraction of calcite in the corresponding trace element bin, with a maximum offset of +1‰ for a bin containing 100% calcite composition. The use of this 1‰ mineralogical correction consistently brings the $\delta^{18}O$ values of calcite layers into agreement with the $\delta^{18}O$ of adjacent aragonite values.

In addition to mineralogical effects on the TA12-2 speleothem $\delta^{18}O$, the isotopic signal originally derives from marine-sourced rainfall and is therefore subject to effects from ice volume changes in ocean $\delta^{18}O$ over glacial-interglacial time-scales. Following the approach used in other studies (Carolin et al., 2013) all of the oxygen isotope records discussed in this paper (Figure 2.7-Figure 2.8) are corrected for estimated changes in ice volume using the global sea water $\delta^{18}O$ curve developed by Bintanja et al. (2005). The only exception is the marine record, which was corrected using the Waelbroeck sea level curve by the original authors (Mohtadi et al., 2014). These corrections allow for interpretation of local salinity and rainfall changes without the additional isotopic component related to sea level (ice volume) changes over glacial-interglacial time scales.

Table 2.1 – U/Th data for stalagmite TA12-2

Sample ID	Depth (mm)	^{238}U (ppm) ±2σ	$[^{230}Th/^{232}Th]$	$[^{230}Th/^{238}U]$	$[^{234}U/^{238}U]$	Uncorrected Age[#] (ky BP)	Corrected Age[#] (ky BP)	Corr. Initial $[^{234}U/^{238}U]$
u0	0.7	0.985 ± 0.075	1.7	0.0057 ± 0.0006	1.5176 ± 0.0099	0.345 ± 0.043	0.2223 ± 0.0658	1.5180 ± 0.0099
u8	7.4	15.999 ± 1.250	2.4	0.0064 ± 0.0004	1.5197 ± 0.0182	0.395 ± 0.029	0.3000 ± 0.0481	1.5202 ± 0.0183
u12*	12.4	10.087 ± 0.009	7.6	0.0083 ± 0.0004	1.5234 ± 0.0018	0.531 ± 0.029	0.4936 ± 0.1015	1.5242 ± 0.0018
u30	29.1	9.641 ± 0.770	13.5	0.0183 ± 0.0005	1.5289 ± 0.0096	1.247 ± 0.037	1.1988 ± 0.0417	1.5308 ± 0.0096
u47	48.0	8.906 ± 0.704	27.1	0.0246 ± 0.0004	1.5056 ± 0.0117	1.730 ± 0.033	1.6971 ± 0.0349	1.5081 ± 0.0117
u62	61.9	8.823 ± 0.751	12.7	0.0333 ± 0.0007	1.5254 ± 0.0095	2.339 ± 0.053	2.2452 ± 0.0651	1.5288 ± 0.0095
u69	69.4	7.968 ± 0.636	30.1	0.0342 ± 0.0006	1.5146 ± 0.0105	2.422 ± 0.048	2.3820 ± 0.0501	1.5182 ± 0.0105
u92*	92.3	8.818 ± 0.008	54.4	0.0420 ± 0.0005	1.5208 ± 0.0023	2.984 ± 0.037	2.9587 ± 0.0410	1.5253 ± 0.0023
u116	117.4	9.852 ± 0.782	9.1	0.0518 ± 0.0006	1.5095 ± 0.0101	3.736 ± 0.052	3.7153 ± 0.0524	1.5149 ± 0.0102
u141	140.4	9.983 ± 0.784	49.8	0.0597 ± 0.0006	1.5047 ± 0.0118	4.340 ± 0.057	4.2971 ± 0.0595	1.5110 ± 0.0119
u176	176.4	10.366 ± 0.909	38.6	0.0735 ± 0.0005	1.5142 ± 0.0029	5.347 ± 0.039	5.2786 ± 0.0477	1.5220 ± 0.0029
u220	219.3	9.719 ± 1.777	46.9	0.0920 ± 0.0026	1.5052 ± 0.0096	6.789 ± 0.204	6.7194 ± 0.2067	1.5150 ± 0.0097
u227*	226.4	9.313 ± 0.012	201.5	0.0906 ± 0.0011	1.5079 ± 0.0020	6.669 ± 0.084	6.6555 ± 0.0850	1.5176 ± 0.0020
u258	257.2	11.764 ± 0.936	117.6	0.0998 ± 0.0009	1.5071 ± 0.0085	7.379 ± 0.082	7.3487 ± 0.0829	1.5178 ± 0.0086
u288	287.8	10.044 ± 1.465	7.5	0.1175 ± 0.0025	1.4930 ± 0.0073	8.836 ± 0.203	8.2664 ± 0.3038	1.5047 ± 0.0075
u299*	299.3	10.860 ± 0.011	80.4	0.1153 ± 0.0012	1.5051 ± 0.0014	8.589 ± 0.094	8.5399 ± 0.0966	1.5175 ± 0.0014
u328	328.3	13.034 ± 1.022	61.8	0.1274 ± 0.0012	1.4921 ± 0.0069	9.622 ± 0.106	9.5475 ± 0.1097	1.5056 ± 0.0070
u358	358.6	16.017 ± 1.323	139.9	0.1448 ± 0.0012	1.4879 ± 0.0080	11.040 ± 0.116	11.0263 ± 0.1153	1.5034 ± 0.0082
u372*	372.1	12.924 ± 0.008	1339.0	0.1552 ± 0.0011	1.4978 ± 0.0020	11.794 ± 0.090	11.7922 ± 0.0897	1.5147 ± 0.0020
u383	382.0	10.943 ± 0.855	822.1	0.1572 ± 0.0013	1.4968 ± 0.0080	11.964 ± 0.125	11.9564 ± 0.1258	1.5139 ± 0.0082
u393	393.4	10.943 ± 0.847	194.6	0.1605 ± 0.0016	1.4908 ± 0.0083	12.282 ± 0.149	12.2523 ± 0.1491	1.5081 ± 0.0085
u407	406.8	10.683 ± 0.894	678.7	0.1649 ± 0.0025	1.4866 ± 0.0081	12.677 ± 0.215	12.6682 ± 0.2166	1.5044 ± 0.0083
u423	422.7	10.570 ± 0.846	498.9	0.1704 ± 0.0016	1.4912 ± 0.0080	13.083 ± 0.151	13.0699 ± 0.1501	1.5097 ± 0.0082
u434*	433.3	16.166 ± 0.012	1195.4	0.1732 ± 0.0012	1.4873 ± 0.0021	13.348 ± 0.101	13.3452 ± 0.1003	1.5061 ± 0.0021
u440	439.9	15.786 ± 1.331	23.9	0.1769 ± 0.0013	1.4768 ± 0.0081	13.756 ± 0.134	13.4856 ± 0.1718	1.4954 ± 0.0083

*Samples run at RSES

[#] Age in ka; thousands of years before present where present is defined as 1950 A.D. Ages are calculated using decay constants specified in Cheng *et al.* (2013). All ratios [bracketed] are reported as activities. The uncertainty is reported as 2σ error. Corrected ages use an initial $[^{230}Th/^{232}Th]$ of 0.5 ± 0.2 for the detrital component.

Table 2.1– U/Th data for stalagmite TA12-2

Sample ID	Depth (mm)	^{238}U (ppm) ±2σ	$[^{230}Th/^{232}Th]$	$[^{230}Th/^{238}U]$	$[^{234}U/^{238}U]$	Uncorrected Age# (ky BP)	Corrected Age# (ky BP)	Corr. Initial $[^{234}U/^{238}U]$
ug0	0	19.579 ± 1.571	66.1	0.1831 ± 0.0013	1.4532 ± 0.0030	14.520 ± 0.075	14.4174 ± 0.0855	1.4721 ± 0.0031
ug6	6.5	13.368 ± 1.019	177.7	0.1859 ± 0.0012	1.4577 ± 0.0078	14.709 ± 0.132	14.6710 ± 0.1330	1.4771 ± 0.0080
ug15	15.1	17.353 ± 1.424	98.4	0.1891 ± 0.0009	1.4489 ± 0.0026	15.079 ± 0.082	15.0061 ± 0.0865	1.4682 ± 0.0027
ug22	22.1	18.569 ± 1.481	213.1	0.1898 ± 0.0017	1.4487 ± 0.0076	15.141 ± 0.168	15.1078 ± 0.1697	1.4683 ± 0.0078
ug43	44.0	17.043 ± 1.351	61.0	0.2057 ± 0.0018	1.4478 ± 0.0073	16.517 ± 0.180	16.3920 ± 0.1866	1.4691 ± 0.0075
ug48	48.2	17.727 ± 1.483	57.5	0.2073 ± 0.0009	1.4505 ± 0.0029	16.622 ± 0.086	16.4869 ± 0.1013	1.4720 ± 0.0030

*Samples run at RSES

Age in ka; thousands of years before present where present is defined as 1950 A.D. Ages are calculated using decay constants specified in Cheng *et al.* (2013). All ratios [bracketed] are reported as activities. The uncertainty is reported as 2σ error. Corrected ages use an initial $[^{230}Th/^{232}Th]$ of 0.5 ± 0.2 for the detrital component.

2.4 Results and discussion

2.4.1 Speleothem $\delta^{18}O$ record

The 0.5 mm isotope sample resolution of TA12-2 is equivalent to a 15-year sample resolution on average. The oldest part of the speleothem record (~16.5 ka) is characterized by relatively heavy values (~ -5.2‰). The first prominent feature in the record is a negative excursion of ~1‰ centered around 15.8 ky BP. This is followed by an abrupt 1‰ shift at 14.7 ky BP to lighter oxygen isotope values, which corresponds to the onset of the Bølling-Allerød period. A short hiatus interrupts the record at 14.4 ky BP but growth resumes at 13.5 ky BP at near-similar isotopic values. This hiatus occurs where a natural break developed in the specimen after collection, and it is not clear if it represents a true cessation of growth or the absence of sampled material from this period due to a slight difference in the orientation of the speleothem slabs. The largest anomaly in the record begins at 13 ky BP and lasts until 11.5 ky BP with oxygen isotope values rising by 1.5‰ to a maximum of -5.1‰. Recovery occurs abruptly as isotope values decrease by 1.1‰ within 200 years. This anomaly corresponds remarkably well with the Younger Dryas event and occurs in a speleothem section that is fully aragonitic and unaffected by change in mineralogy. Subsequent to the YD, values decrease more gradually over the next 2000 years, until they reach an average Holocene value of -8.0‰ ± 0.58‰. Holocene isotopic values fluctuate between -7.5 and -8.5‰, reaching a maximum of -7.1‰ at 1.5 ky BP and decreasing to -8.1‰ at the top of the sample. The Holocene section of the speleothem is beyond the scope of this work and will not be discussed further.

2.4.2 Indian Ocean region

The Tangga Cave record shows many similarities to records of the Asian and Indian summer monsoons (ASM/ISM) during the last deglaciation. In particular, the Sumatran rainfall record demonstrates a clear response to North Atlantic millennial-scale events, including distinct ^{18}O enrichment during the YD and depletion during the BA periods (Figure 2.7). These features are consistent in sign and timing to those recorded in the NGRIP ice core temperature record and cave

records of the Asian and Indian summer monsoon regions (Dutt et al., 2015; Dykoski et al., 2005; NGRIP members, 2004; Wang et al., 2001) (Figure 2.7).

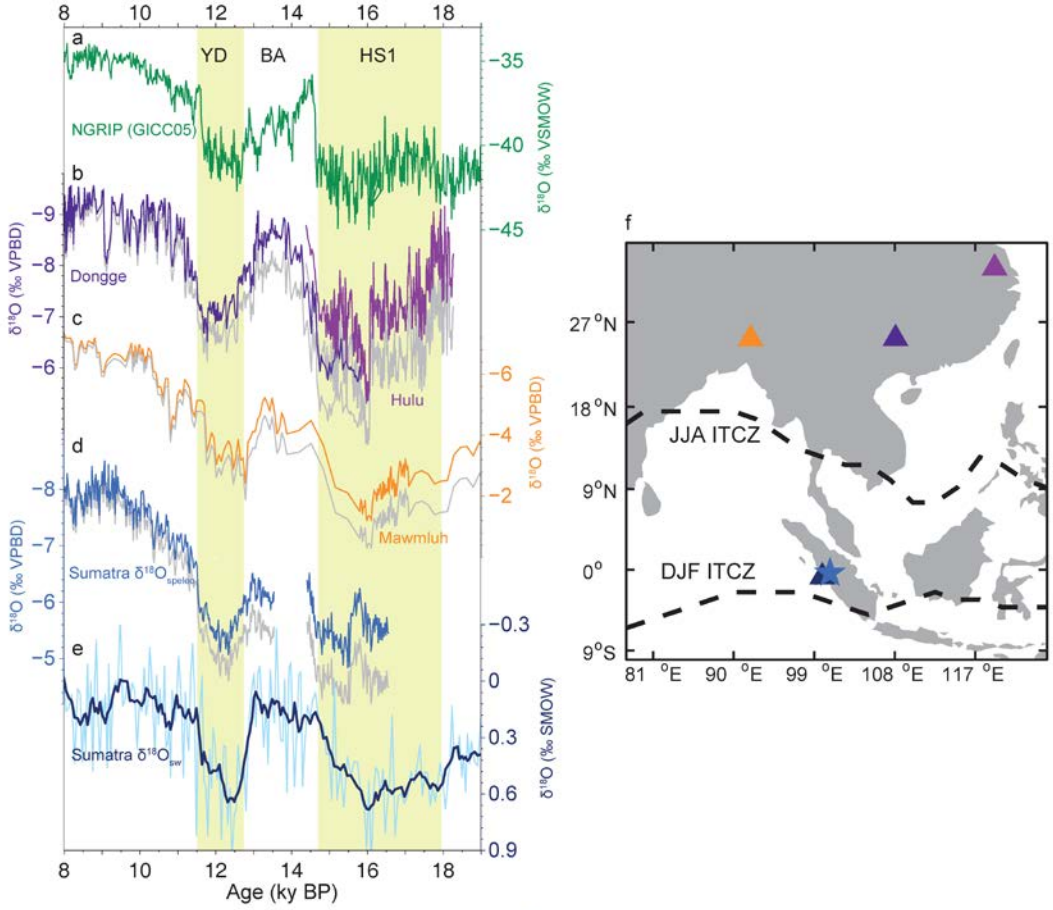

Figure 2.7 – Sumatra speleothem $\delta^{18}O$ over last deglaciation compared with other paleoclimate records. a) Greenland (NGRIP) ice core $\delta^{18}O$ with GICC05 chronology (NGRIP members, 2004; Rasmussen et al., 2006; Vinther et al., 2006) indicate of northern hemisphere high latitude temperature. b) Speleothem $\delta^{18}O$ from Dongge and Hulu Caves in China (Dykoski et al., 2005; Wang et al., 2001) and c) speleothem $\delta^{18}O$ from Mawmluh Cave in India (Dutt et al., 2015) reflecting Asian and Indian summer monsoon strength, respectively. d) Speleothem $\delta^{18}O$ from Tangga Cave in Sumatra (this study) and e) seawater $\delta^{18}O$ from SO189-39KL from offshore Sumatra in the eastern Indian Ocean (light blue) with 7-point running average (dark blue) (Mohtadi et al., 2014). The speleothem and marine records have been adjusted for ice-volume related changes in global seawater $\delta^{18}O$ (Bintanja et al., 2005) following method of Carolin et al., 2013. Vertical shading denotes timing of YD and HS1. f) Location of records shown in a-e. Colors of symbols correspond to colors of timeseries in a-e. The position of the modern maximum meridional rainfall in JJA and DJF is indicated by the dashed line.

As discussed earlier, the manifestation of North Atlantic events into India and Asia is well-established in many speleothem records (Dutt et al., 2015; Dykoski et al., 2005; Liu et al., 2013; Shakun et al., 2007; Wang et al., 2001). Their occurrence is thought to be related to a reduction of moisture transport from a cooler western

Indian Ocean following a westerly transport path across the Indian Ocean and up through the Bay of Bengal onto the Asian continent (Liu et al., 2014).

It has previously been suggested that ocean advection may play a role in the expression of the YD in the Sumatran seawater $\delta^{18}O$ history (Partin et al., 2015), however, the similarities between SO189-39KL and speleothem TA12-2 suggest an atmospheric hydroclimate signal, either via a local amount effect or a shared rainfall $\delta^{18}O$ integration history.

Isotopic values in Tangga Cave during the YD are similar to those preceding the BA, as is observed in the marine core. In contrast, the YD at Dongge and Mawmluh Caves are slightly lighter than values during HS1. Though interrupted by a growth hiatus, the onset, duration and termination of the BA are clear in the Tangga Cave speleothem, indicating a relative depletion of ^{18}O during this interval. The magnitude of the BA $\delta^{18}O$ signal at Tangga Cave is smaller relative to those in other speleothems from the ASM/ISM realm, which reach Holocene levels of isotopic depletion. The speleothem response is also smaller in magnitude than that of the adjacent marine core. As the speleothem likely records local hydrology, it is possible that the amplified BA isotopic signal in the marine core is a result of advection of continental runoff from the Bay of Bengal caused by the strengthened boreal summer monsoon in addition to increased local rainfall in the eastern equatorial Indian Ocean. Alternatively, during this period of strengthened ASM, the contributions of the relatively enriched south-easterly source to Tangga Cave may have been increased relative to the Indian Ocean contribution, resulting in a heavier than expected $\delta^{18}O$ value during the BA.

Cooler SSTs in the western Indian Ocean during the YD (Tierney et al., 2015), coupled with relatively constant SSTs in the eastern Indian Ocean (Mohtadi et al., 2014; Setiawan et al., 2015) could be used to infer a persistent negative Indian Ocean Dipole-like state (increased west-east SST gradient) in the Indian Ocean region during the YD. However, the reduced rainfall in the eastern Indian Ocean does not support a coupled increase in Indian and Pacific Walker Circulation, perhaps owing to the fact that the enhanced gradient is related to cooling

anomalies in the western Indian Ocean, rather than warming in the eastern Indian Ocean. It could also signify that rainfall changes associated with weakening of the Asian and Indian monsoons dominate over any effects caused by the change in zonal SST gradients across the tropical Indian Ocean.

Indian Ocean hydroclimate does not mirror the zonal asymmetry observed in Indian Ocean SSTs. Idealized hosing experiments have been used to infer that a reorganization of Hadley circulation in the Indian Ocean, including a mean southward shift of the ITCZ and a weakening of the boreal summer monsoon, is a key response to North Atlantic freshwater forcing such as the YD (Lewis et al., 2011; Mohtadi et al., 2014). This interpretation is supported by proxy records from the western Indian Ocean, suggesting a zonally symmetric response in hydroclimate across the Indian Ocean during the YD. Speleothem records from Yemen indicate a reduction in the Indian Monsoon (Shakun et al., 2007), which considered with the Sumatran speleothem, demonstrates a widespread weakening across the entire Indian Ocean Basin. Both Lakes Challa (3°S) and Tanganyika (6°S) record isotopic enrichment across the YD (Tierney et al., 2008; Tierney et al., 2011), while sites further south (Zambezi catchment (18°S), Lake Chilwa (15°S)) show isotopic depletion or lake level highstands (Schefuß et al., 2011; Thomas et al., 2009), likely signifying a southward shift in the ascending branch of the Hadley circulation.

The record from Sumatra supports a cross-basin YD response in Indian Ocean hydroclimate that is consistent with the signal observed in the ASM/ISM realm and in the offshore Sumatra $\delta^{18}O_{sw}$ reconstruction. Though records from Africa support a southward ITCZ shift, equatorial sites such as Tangga Cave should still be receiving rainfall from the ITCZ as it passes overhead at least once during its annual migration. Thus, a mean southwards ITCZ shift alone is unlikely to have caused the drying observed in Sumatra. Indeed, an examination of nearby proxies in the Indo-Pacific Warm Pool suggests a more complex mechanism.

2.4.3 The Younger Dryas in the Indo-Pacific Warm Pool

In the IPWP, a mean southward ITCZ shift during the YD has been inferred from amount-effect driven changes in $\delta^{18}O$ at sites on the meridional edges of the IPWP (Figure 2.8). As with rainfall $\delta^{18}O$ in Sumatra, rainfall $\delta^{18}O$ at other IPWP sites may be controlled by a combination of moisture source and regional or local amount effect, with moisture source often enhancing the amount effect signal. The other IPWP sites have been interpreted in-line with each site's listed publication. These include an increase in precipitation recorded by speleothems from Flores (Ayliffe et al., 2013; Griffiths et al., 2009), and rainfall decreases in Palawan (Philippines) in the northern IPWP (Partin et al., 2015). The ^{18}O depletion over Flores during the YD contrasts with the YD ^{18}O enrichment in the Sumatran speleothem, suggesting that different processes dominated the YD hydroclimate response at the zonal and meridional margins of the IPWP.

Like China, the Palawan site in the northern IPWP receives the majority of its rainfall during the boreal summer monsoon season and shows a distinct decrease in rainfall during the YD (Partin et al., 2015). Models suggest that much of the northern IPWP dried out during boreal summer, with some simulations suggesting concurrent increases in precipitation in the austral tropics (Lewis et al., 2010) and others indicating no anomalous austral precipitation (Partin et al., 2015; Pausata et al., 2011). The former might indicate a southward position of the ITCZ during boreal summer. However, as the ITCZ still would have migrated north during boreal summer (McGee et al., 2014; Schneider et al., 2014) reaching the boreal tropics, drying in Palawan likely indicates a reduction of convective rainfall within the ITCZ during boreal summer or a reduction in the duration of the boreal summer season, rather than a southward shift.

In the southern part of the IPWP, Liang Luar Cave in Flores currently receives 70% of its rainfall during austral summer (December-March). During the YD, the Flores speleothem suggests a slight increase in rainfall, interpreted as an intensification of austral summer monsoon rainfall associated with a austral summer southward ITCZ shift (Griffiths et al., 2009). The YD signal is ambiguous in the precipitation

record from northern Australia (Denniston et al., 2013a), however, a precipitation increase at Flores and Ball Gown Cave during HS1 suggests a similar mechanism is at play (Ayliffe et al., 2013). It is possible that the austral summer ITCZ rain belt during the YD was shifted south relative to modern, but north relative to HS1, such that Flores received increased duration of rainfall, but not NW Australia.

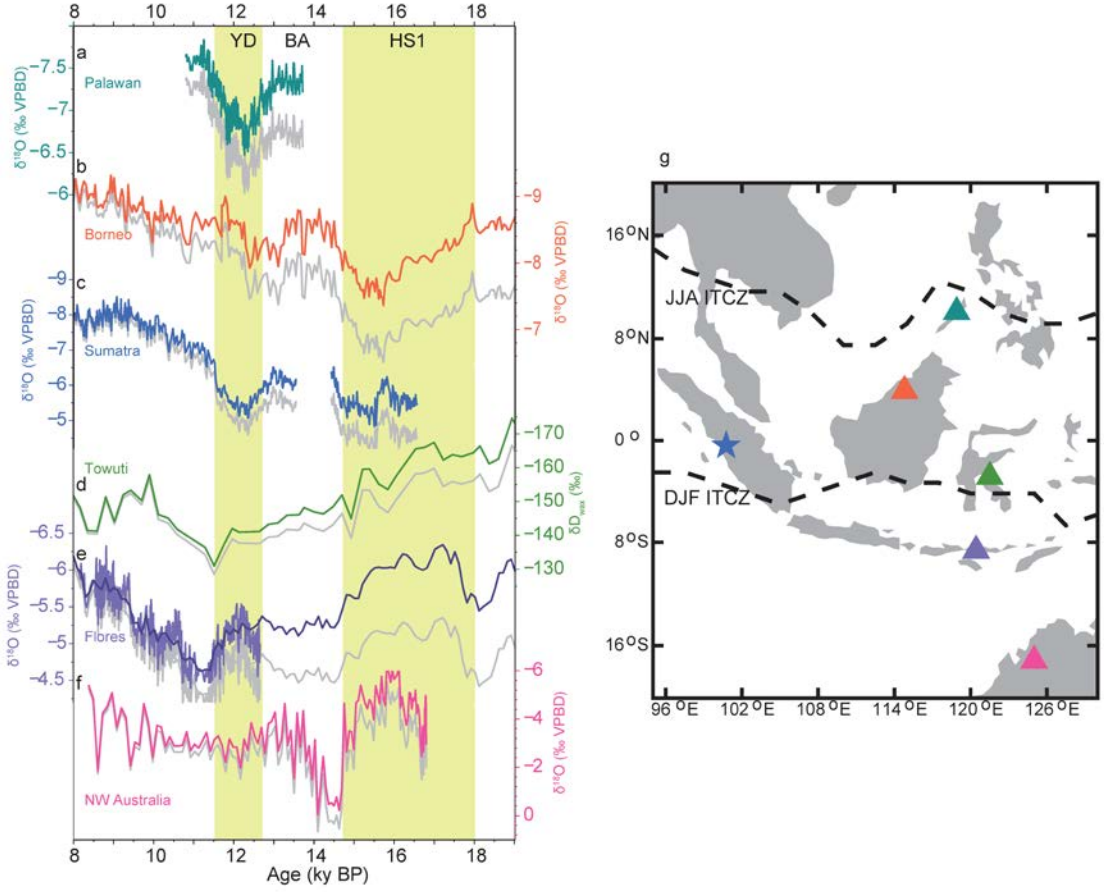

Figure 2.8 – The YD and BA climate events in proxies from the IPWP. From north to south, a) Palawan, Philippines (Partin et al., 2015); b) Gunung Buda, Borneo (Partin et al., 2007); c) Tangga Cave, Sumatra (this study); d) Lake Towuti, Sulawesi (Konecky et al., 2016); e) Liang Luar Cave, Flores (Griffiths et al., 2009); and f) Ball Gown Cave, Australia (Denniston et al., 2013b). Vertical shading denotes timing of YD and HS1. g) Location of records shown in a-f. Colors of symbols correspond to colors of timeseries in a-f. The position of the modern maximum meridional rainfall in JJA and DJF is indicated by the dashed line.

To date, no YD response has been documented from equatorial sites from the IPWP. A speleothem record from Borneo (Partin et al., 2015) and a lake sediment leaf wax record from Sulawesi (Konecky et al., 2016) both show no clear rainfall response to the YD or BA. At 3° S, leaf wax from Lake Towuti, Sulawesi, suggests

no change in rainfall during the austral summer monsoon (Konecky et al., 2016). Since both Flores and Sulawesi are biased towards the austral summer monsoon, it might be expected that intensified austral summer monsoon rainfall would manifest in the Sulawesi record during millennial-scale events. In contrast, if austral summer monsoon rainfall remained the same or decreased during the Younger Dryas, the ^{18}O depletion at Flores and neutral signal at Sulawesi must be attributed to either ITCZ duration overhead or latitudinal positioning. Flores, at the southern limit of modern ITCZ rainfall, might record increased rainfall due to its more prolonged duration under the ITCZ rain belt. Sulawesi may similarly be subject to an extended monsoon season, which may cancel out the reduction in moisture transport. Relative to Flores, which is only under the ITCZ during austral summer, Sulawesi, which is already under the ITCZ for a greater part of the year, may be less sensitive to an austral summer southward shift. Considered together, the records from Flores and Sulawesi suggest that ITCZ-related austral summer convective rainfall did not intensify, as this would result in an $\delta^{18}O$ decrease at both sites. Rather, the $\delta^{18}O$ signals at Flores and Sulawesi can be explained by changes in the duration of the ITCZ overhead associated with a southward ITCZ shift, without invoking an increase in convective rainfall.

If these assumptions are correct, then overall moisture transport along monsoon transport pathways during both boreal and austral summer was weaker or the same during the YD. Boreal summer monsoon rainfall reductions, like those observed at the Palawan site and across China and India, likely contribute to the Sumatra YD signal. However, because Sumatra also receives considerable rainfall contributions from other sources during the rest of the year, an increase in austral monsoon convective rainfall would be expected to counteract the boreal signal. However, the proxy evidence from the austral monsoon system does not necessitate an increase in moisture transport along the austral monsoon transport pathway.

Indeed, results from an idealized hosing experiment of the coupled ocean-atmosphere GISS ModelE-R (Lewis et al., 2010) support the case for reduced

monsoon-sourced rainfall to Sumatra. GISS ModelE-R is equipped with water vapour source distribution (VSD) tracers, which can be traced back through cloud processes to the site of surface evaporation. GISS ModelE-R VSD results indicate that both the austral and boreal monsoon moisture transport pathways for Tangga Cave (Figure 2.3) were decreased relative to local Indian Ocean sources during hosing (Figure 2.9).

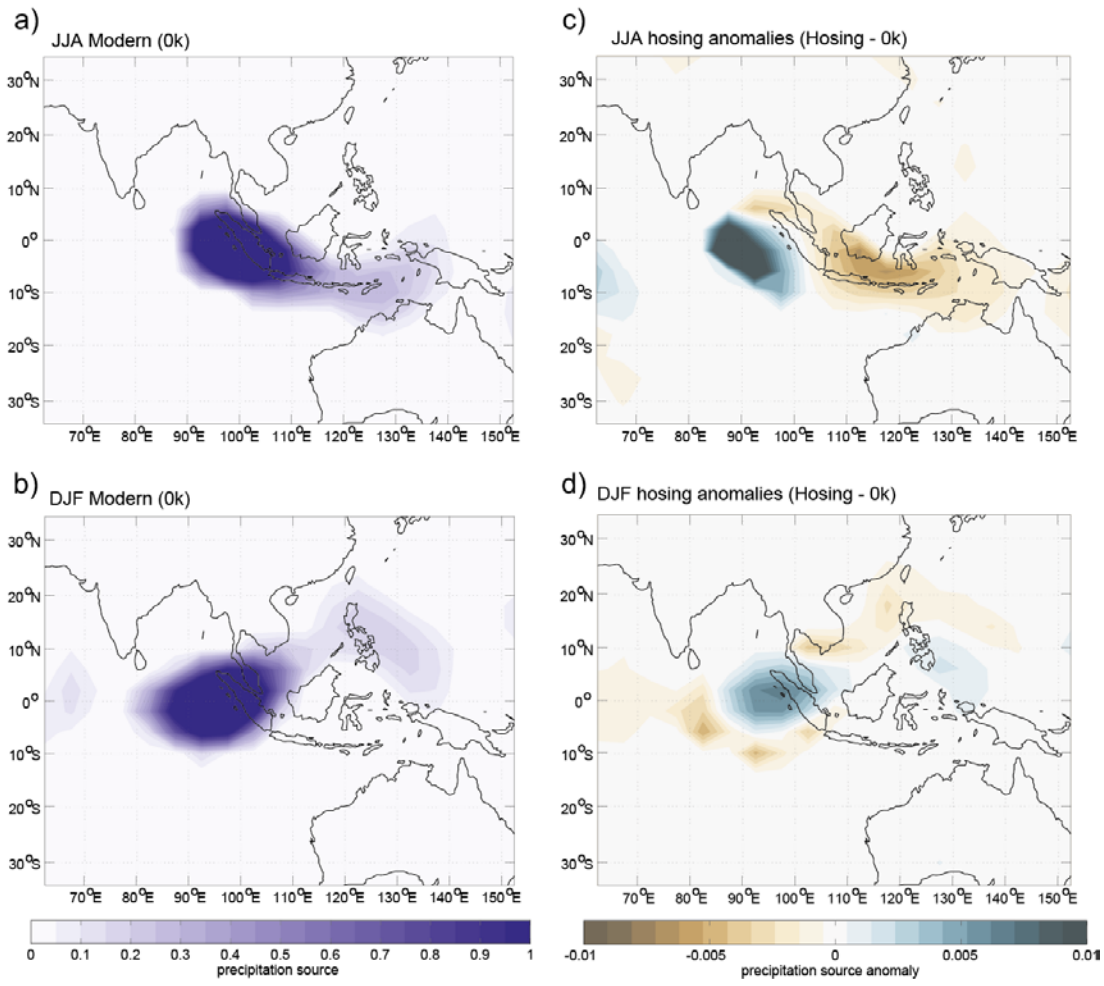

Figure 2.9 – GISS ModelE-R vapour source distribution (VSD) results for Tangga Cave, Sumatra. Modern (0k) precipitation source for a) JJA and b) DJF, and hosing precipitation source anomalies for c) JJA and d) DJF. The precipitation source distribution utilized in this study is a subset of the VSD, defined where vapour condenses to liquid. VSD resolution is ~8x10°. VSDs are unitless probability density functions.

Though this implies an increase in the proportion of relatively ^{18}O-depleted Indian Ocean sources, the fact that Tangga Cave records ^{18}O enrichment suggests there

must be a counteracting change in either the amount of rainfall from all sources or the transport distance, both of which would serve to increase $\delta^{18}O$.

Reductions in the monsoon transport pathways do not preclude involvement of the Indian Ocean moisture source to the patterns observed in Sumatra. The Indian Ocean source can contribute to ^{18}O enrichment via a similar decrease in rainfall. Alternatively, or in concert with rainfall reduction, the Indian Ocean source becomes more localized, which could have resulted in less rainout along this transport path and more enriched isotopic values. A recent modeling study accurately captures the pattern of rainfall captured by IPWP proxies during HS1 (Mohtadi et al., 2014). During a freshwater hosing experiment, the simulation suggests that a strengthening of the Indian Ocean equatorial westerly winds would accompany a southward shift of the Indian Ocean Hadley cell, creating a strong subsidence anomaly above Sumatra.

If similar mechanisms were at play during the YD, these dry winds could punctuate eastward over Sumatra, but be constrained by the ascending branch of Pacific Walker circulation somewhere in the vicinity of Borneo. The speleothem record from Borneo (Partin et al., 2007) indicates no obvious rainfall anomaly during the YD. Today, the Borneo cave site receives rainfall year-round and is strongly influenced by Pacific climate variability associated with the El Niño-Southern Oscillation (ENSO) (Moerman et al., 2013; Partin et al., 2007). It has been suggested that Borneo may receive opposing rainfall signals in summer and winter that canceled out a response to millennial scale ITCZ shifts during the YD (Partin et al., 2015). However, the Sumatra speleothem and GISS ModelE-R results indicate that net austral and boreal summer monsoon moisture transport are reduced, which should manifest as drying or enrichment at sites without a strong rainfall seasonality. An alternative is that the increasing precessional signal of boreal autumn insolation in the equatorial Pacific during the last glacial termination may dominate over North Atlantic forcing in the central Warm Pool during the YD, potentially explaining why no YD signal is observed despite the Borneo

reconstruction containing multiple Heinrich events (Carolin et al., 2013; Carolin et al., 2016; Partin et al., 2007).

Taken together, the proxy data from the Indo-Pacific Warm Pool suggest a reduction of moisture transport in both the austral and boreal monsoon transport pathways. Sites that exhibit a dry or ^{18}O-enriched YD (i.e., Palawan and Sumatra) are driven by weakening of summer monsoon transport. Sumatra may also be subject to reduced length of transport pathways during YD, leading to ^{18}O enrichment. Sites that demonstrate ^{18}O depletion interpreted as increased rainfall (i.e., Flores) observe an extended duration of the ITCZ overhead. Sites which show no response are very close to the equator and either highly seasonal (i.e. Sulawesi) such that the reduction of moisture transport may be counteracted by an increased season length, or overridden by other mechanisms that influence local precipitation, such as insolation (i.e., Borneo).

2.5 Conclusions

The new speleothem record from Sumatra demonstrates an extended spatial reach of the Younger Dryas climate anomaly into the eastern equatorial Indian Ocean region. This adds to previous evidence of a seawater $\delta^{18}O$ response offshore of Sumatra by confirming that the YD involved a rapid and marked ^{18}O enrichment of precipitation over central Sumatra and was not just an advected signal at nearby marine sites. The Sumatran speleothem record and VSD results indicate an overall weakening of moisture transport along both the boreal and austral monsoon transport pathways. This response does not preclude the involvement of a southward austral summer ITCZ shift and an Indian Ocean trade wind induced reduction of Indian Ocean-sourced rainfall. A signal of the YD climate anomaly appears at both the zonal and meridional edges of the IPWP, but is ambiguous in central IPWP records, potentially due to the overriding control of Pacific forcing during the last termination. Further isotope-enabled modelling studies will be useful to constrain the relative contributions of moisture source and amount effect, as well as further explore mechanisms that drive differences between the YD and

HS1. The new speleothem record from Sumatra has important implications for the extent of North Atlantic forcing in the tropics, particularly in light of uncertainty about the future of Atlantic Meridional Overturning Circulation (Rahmstorf et al., 2015).

References

Abram, N.J., Gagan, M.K., Cole, J.E., Hantoro, W.S., Mudelsee, M. (2008). Recent intensification of tropical climate variability in the Indian Ocean. Nature Geoscience 1, 849-853. http://dx.doi.org/10.1038/ngeo357

Aldrian, E., Susanto, R.D. (2003). Identification of three dominant rainfall regions within Indonesia and their relationship to sea surface temperature. International Journal of Climatology 23, 1435-1452. http://dx.doi.org/10.1002/joc.950

Ayliffe, L.K., Gagan, M.K., Zhao, J.-x., Drysdale, R.N., Hellstrom, J.C., Hantoro, W.S., Griffiths, M.L., Scott-Gagan, H., Pierre, E.S., Cowley, J.A., Suwargadi, B.W. (2013). Rapid interhemispheric climate links via the Australasian monsoon during the last deglaciation. Nature Communications 4, 2908. http://dx.doi.org/10.1038/ncomms3908

Bajo, P., Hellstrom, J., Frisia, S., Drysdale, R., Black, J., Woodhead, J., Borsato, A., Zanchetta, G., Wallace, M.W., Regattieri, E., Haese, R. (2016). "Cryptic" diagenesis and its implications for speleothem geochronologies. Quaternary Science Reviews 148, 17-28. http://dx.doi.org/10.1016/j.quascirev.2016.06.020

Barker, S., Diz, P., Vautravers, M.J., Pike, J., Knorr, G., Hall, I.R., Broecker, W.S. (2009). Interhemispheric Atlantic seesaw response during the last deglaciation. Nature 457, 1097-1102. http://dx.doi.org/10.1038/nature07770

Belgaman, H.A., Ichiyanagi, K., Suwarman, R., Tanoue, M., Aldrian, E., Utami, A.I.D., Kusumaningtyas, S.D.A. (2017). Characteristics of seasonal precipitation isotope variability in Indonesia. Hydrological Research Letters 11, 92-98. http://dx.doi.org/10.3178/hrl.11.92

Belgaman, H.A., Ichiyanagi, K., Tanoue, M., Suwarman, R., Yoshimura, K., Mori, S., Kurita, N., Yamanaka, M.D., Syamsudin, F. (2016). Intraseasonal Variability of $\delta^{18}O$ of Precipitation over the Indonesian Maritime Continent Related to the Madden–Julian Oscillation. SOLA 12, 192-197.

Bintanja, R., van de Wal, R.S.W., Oerlemans, J. (2005). Modelled atmospheric temperatures and global sea levels over the past million years. Nature 437, 125-128. http://dx.doi.org/10.1038/nature03975

Blaauw, M., Christen, J.A. (2011). Flexible paleoclimate age-depth models using an autoregressive gamma process. Bayesian Analysis 6, 457-474. http://dx.doi.org/10.1214/11-Ba618

Bond, G., Broecker, W., Johnsen, S., McManus, J., Labeyrie, L., Jouzel, J., Bonani, G. (1993). Correlations between climate records from North Atlantic sediments and Greenland ice. Nature 365, 143-147. http://dx.doi.org/10.1038/365143a0

Bostock, H.C., Barrows, T.T., Carter, L., Chase, Z., Cortese, G., Dunbar, G.B., Ellwood, M., Hayward, B., Howard, W., Neil, H.L., Noble, T.L., Mackintosh, A., Moss, P.T., Moy, A.D., White, D., Williams, M.J.M., Armand, L.K. (2013). A review of the Australian–New Zealand sector of the Southern Ocean over the last 30 ka (Aus-INTIMATE project). Quaternary Science Reviews 74, 35-57. http://dx.doi.org/https://doi.org/10.1016/j.quascirev.2012.07.018

Broecker, W.S., Denton, G.H., Edwards, R.L., Cheng, H., Alley, R.B., Putnam, A.E. (2010). Putting the Younger Dryas cold event into context. Quaternary Science Reviews 29, 1078-1081. http://dx.doi.org/10.1016/j.quascirev.2010.02.019

Carolin, S.A., Cobb, K.M., Adkins, J.F., Clark, B., Conroy, J.L., Lejau, S., Malang, J., Tuen, A.A. (2013). Varied response of western Pacific hydrology to climate forcings over the last glacial period. Science 340, 1564-1566. http://dx.doi.org/10.1126/science.1233797

Carolin, S.A., Cobb, K.M., Lynch-Stieglitz, J., Moerman, J.W., Partin, J.W., Lejau, S., Malang, J., Clark, B., Tuen, A.A., Adkins, J.F. (2016). Northern Borneo stalagmite records reveal West Pacific hydroclimate across MIS 5 and 6. Earth and Planetary Science Letters 439, 182-193. http://dx.doi.org/10.1016/j.epsl.2016.01.028

Cheng, H., Lawrence Edwards, R., Shen, C.-C., Polyak, V.J., Asmerom, Y., Woodhead, J., Hellstrom, J.C., Wang, Y., Kong, X., Spötl, C., Wang, X., Calvin Alexander Jr, E. (2013). Improvements in ^{230}Th dating, ^{230}Th and ^{234}U half-life values, and U–Th isotopic measurements by multi-collector inductively coupled plasma mass spectrometry. Earth and Planetary Science Letters 371–372, 82-91.

Chiang, J.C.H., Bitz, C.M. (2005). Influence of high latitude ice cover on the marine Intertropical Convergence Zone. Climate Dynamics 25, 477-496. http://dx.doi.org/10.1007/s00382-005-0040-5

Dee, D.P., Uppala, S.M., Simmons, A.J., Berrisford, P., Poli, P., Kobayashi, S., Andrae, U., Balmaseda, M.A., Balsamo, G., Bauer, P., Bechtold, P., Beljaars, A.C.M., van de Berg, L., Bidlot, J., Bormann, N., Delsol, C., Dragani, R., Fuentes, M., Geer, A.J., Haimberger, L., Healy, S.B., Hersbach, H., Hólm, E.V., Isaksen, L., Kållberg, P., Köhler, M., Matricardi, M., McNally, A.P., Monge-Sanz, B.M., Morcrette, J.J., Park, B.K., Peubey, C., de Rosnay, P., Tavolato, C., Thépaut, J.N., Vitart, F. (2011). The ERA-Interim reanalysis: configuration and performance of the data assimilation system. Quarterly Journal of the Royal Meteorological Society 137, 553-597. http://dx.doi.org/10.1002/qj.828

Denniston, R.F., Asmerom, Y., Lachniet, M., Polyak, V.J., Hope, P., An, N., Rodzinyak, K., Humphreys, W.F. (2013a). A Last Glacial Maximum through middle Holocene stalagmite record of coastal Western Australia climate. Quaternary Science Reviews 77, 101-112. http://dx.doi.org/10.1016/j.quascirev.2013.07.002

Denniston, R.F., Wyrwoll, K.-H., Asmerom, Y., Polyak, V.J., Humphreys, W.F., Cugley, J., Woods, D., LaPointe, Z., Peota, J., Greaves, E. (2013b). North Atlantic forcing of millennial-scale Indo-Australian monsoon dynamics during the Last Glacial period. Quaternary Science Reviews 72, 159-168. http://dx.doi.org/10.1016/j.quascirev.2013.04.012

Denton, G.H., Anderson, R.F., Toggweiler, J.R., Edwards, R.L., Schaefer, J.M., Putnam, A.E. (2010). The Last Glacial Termination. Science 328, 1652-1656. http://dx.doi.org/10.1126/science.1184119

Draxler, R.R., Hess, G.D. (1997), Description of the HYSPLIT_4 modeling system, NOAA Tech. Memo. ERL ARL-224. NOAA, Silver Spring, MD, p. 24.

Dutt, S., Gupta, A.K., Clemens, S.C., Cheng, H., Singh, R.K., Kathayat, G., Edwards, R.L. (2015). Abrupt changes in Indian summer monsoon strength during 33,800 to 5500 years B.P. Geophysical Research Letters 42, 5526-5532.

Dykoski, C.A., Edwards, R.L., Cheng, H., Yuan, D., Cai, Y., Zhang, M., Lin, Y., Qing, J., An, Z., Revenaugh, J. (2005). A high-resolution, absolute-dated Holocene and deglacial Asian monsoon record from Dongge Cave, China. Earth and Planetary Science Letters 233, 71-86. http://dx.doi.org/10.1016/j.epsl.2005.01.036

Finch, A.A., Shaw, P.A., Weedon, G.P., Holmgren, K. (2001). Trace element variation in speleothem aragonite: potential for palaeoenvironmental reconstruction. Earth and Planetary Science Letters 186, 255-267. http://dx.doi.org/10.1016/S0012-821x(01)00253-9

Frisia, S., Borsato, A., Fairchild, I.J., McDermott, F., Selmo, E.M. (2002). Aragonite-calcite relationships in speleothems (Grotte De Clamouse, France): Environment, fabrics, and carbonate geochemistry. Journal of Sedimentary Research 72, 687-699. http://dx.doi.org/10.1306/020702720687

Gibbons, F.T., Oppo, D.W., Mohtadi, M., Rosenthal, Y., Cheng, J., Liu, Z., Linsley, B.K. (2014). Deglacial $\delta^{18}O$ and hydrologic variability in the tropical Pacific and Indian Oceans. Earth and Planetary Science Letters 387, 240-251. http://dx.doi.org/10.1016/j.epsl.2013.11.032

Griffiths, M.L., Drysdale, R.N., Gagan, M.K., Zhao, J.-x., Ayliffe, L.K., Hellstrom, J.C., Hantoro, W.S., Frisia, S., Feng, Y.-X., Cartwright, I., St. Pierre, E.J., Fischer, M.J., Suwargadi, B.W. (2009). Increasing Australian-Indonesian monsoon rainfall linked to early Holocene sea-level rise. Nature Geoscience 2, 636-639. http://dx.doi.org/10.1038/Ngeo605

Heinrich, H. (1988). Origin and consequences of cyclic ice rafting in the Northeast Atlantic Ocean during the past 130,000 years. Quaternary Research 29, 142-152. http://dx.doi.org/10.1016/0033-5894(88)90057-9

Hellstrom, J. (2003). Rapid and accurate U/Th dating using parallel ion-counting multi-collector ICP-MS. Journal of Analytical Atomic Spectrometry 18, 1346-1351. http://dx.doi.org/10.1039/b308781f

Hellstrom, J.C. (2006). U–Th dating of speleothems with high initial ^{230}Th using stratigraphical constraint. Quaternary Geochronology 1, 289-295. http://dx.doi.org/10.1016/j.quageo.2007.01.004

Hughen, K.A., Overpeck, J.T., Peterson, L.C., Trumbore, S. (1996). Rapid climate changes in the tropical Atlantic region during the last deglaciation. Nature 380, 51-54. http://dx.doi.org/10.1038/380051a0

Kim, S.-T., O'Neil, J.R., Hillaire-Marcel, C., Mucci, A. (2007). Oxygen isotope fractionation between synthetic aragonite and water: Influence of temperature and Mg^{2+} concentration. Geochimica et Cosmochimica Acta 71, 4704-4715. http://dx.doi.org/10.1016/j.gca.2007.04.019

Knutti, R., Fluckiger, J., Stocker, T.F., Timmermann, A. (2004). Strong hemispheric coupling of glacial climate through freshwater discharge and ocean circulation. Nature 430, 851-856. http://dx.doi.org/10.1038/nature02786

Konecky, B., Russell, J., Bijaksana, S. (2016). Glacial aridity in central Indonesia coeval with intensified monsoon circulation. Earth and Planetary Science Letters 437, 15-24. http://dx.doi.org/10.1016/j.epsl.2015.12.037

Kurita, N., Ichiyanagi, K., Matsumoto, J., Yamanaka, M.D. (2009). The relationship between the isotopic content of precipitation and the precipitation amount in tropical regions. Journal of geochemical exploration 102, 113-122. http://dx.doi.org/10.1016/j.gexplo.2009.03.002

Lambeck, K., Rouby, H., Purcell, A., Sun, Y., Sambridge, M. (2014). Sea level and global ice volumes from the Last Glacial Maximum to the Holocene. Proceedings of the National Academy of Sciences 111, 15296-15303. http://dx.doi.org/10.1073/pnas.1411762111

LeGrande, A.N., Schmidt, G.A. (2006). Global gridded data set of the oxygen isotopic composition in seawater. Geophysical Research Letters 33, L12604. http://dx.doi.org/10.1029/2006gl026011

Levi, C., Labeyrie, L., Bassinot, F., Guichard, F., Cortijo, E., Waelbroeck, C., Caillon, N., Duprat, J., de Garidel-Thoron, T., Elderfield, H. (2007). Low-latitude hydrological cycle and rapid climate changes during the last deglaciation. Geochemistry, Geophysics, Geosystems 8. http://dx.doi.org/10.1029/2006gc001514

Lewis, S.C., Gagan, M.K., Ayliffe, L.K., Zhao, J.-x., Hantoro, W.S., Treble, P.C., Hellstrom, J.C., LeGrande, A.N., Kelley, M., Schmidt, G.A., Suwargadi, B.W. (2011). High-resolution stalagmite reconstructions of Australian-Indonesian monsoon rainfall variability during Heinrich stadial 3 and Greenland interstadial 4. Earth and Planetary Science Letters 303, 133-142. http://dx.doi.org/10.1016/j.epsl.2010.12.048

Lewis, S.C., LeGrande, A.N., Kelley, M., Schmidt, G.A. (2010). Water vapour source impacts on oxygen isotope variability in tropical precipitation during Heinrich events. Climate of the Past 6, 325-343. http://dx.doi.org/10.5194/cp-6-325-2010

Liebmann, B., Smith, C.A. (1996). Description of a Complete (Interpolated) Outgoing Longwave Radiation Dataset. Bulletin of the American Meteorological Society 77, 1275-1277.

Liu, Y., Henderson, G.M., Hu, C., Mason, A.J., Charnley, N.R., Johnson, K.R., Xie, S. (2013). Links between the East Asian monsoon and North Atlantic climate during the 8,200 year event. Nature Geoscience 6, 117-120. http://dx.doi.org/10.1038/Ngeo1708

Liu, Z., Wen, X., Brady, E.C., Otto-Bliesner, B., Yu, G., Lu, H., Cheng, H., Wang, Y., Zheng, W., Ding, Y., Edwards, R.L., Cheng, J., Liu, W., Yang, H. (2014). Chinese cave records and the East Asia Summer Monsoon. Quaternary Science Reviews 83, 115-128. http://dx.doi.org/10.1016/j.quascirev.2013.10.021

Marzin, C., Kallel, N., Kageyama, M., Duplessy, J.C., Braconnot, P. (2013). Glacial fluctuations of the Indian monsoon and their relationship with North

Atlantic climate: new data and modelling experiments. Climate of the Past 9, 2135-2151. http://dx.doi.org/10.5194/cp-9-2135-2013

McCulloch, M.T., Mortimer, G.E. (2008). Applications of the 238U–230Th decay series to dating of fossil and modern corals using MC-ICPMS. Australian Journal of Earth Sciences 55, 955-965. http://dx.doi.org/10.1080/08120090802097435

McGee, D., Donohoe, A., Marshall, J., Ferreira, D. (2014). Changes in ITCZ location and cross-equatorial heat transport at the Last Glacial Maximum, Heinrich Stadial 1, and the mid-Holocene. Earth and Planetary Science Letters 390, 69-79. http://dx.doi.org/10.1016/j.epsl.2013.12.043

McLachlan, G., Peel, D. (2004), Finite mixture models. John Wiley & Sons.

McManus, J.F., Francois, R., Gherardi, J.-M., Keigwin, L.D., Brown-Leger, S. (2004). Collapse and rapid resumption of Atlantic meridional circulation linked to deglacial climate changes. Nature 428, 834-837. http://dx.doi.org/10.1038/nature02494

Moerman, J.W., Cobb, K.M., Adkins, J.F., Sodemann, H., Clark, B., Tuen, A.A. (2013). Diurnal to interannual rainfall $\delta^{18}O$ variations in northern Borneo driven by regional hydrology. Earth and Planetary Science Letters 369–370, 108-119.

Mohtadi, M., Prange, M., Oppo, D.W., De Pol-Holz, R., Merkel, U., Zhang, X., Steinke, S., Luckge, A. (2014). North Atlantic forcing of tropical Indian Ocean climate. Nature 509, 76-80. http://dx.doi.org/10.1038/nature13196

Muller, J., Kylander, M., Wüst, R.A.J., Weiss, D., Martinez-Cortizas, A., LeGrande, A.N., Jennerjahn, T., Behling, H., Anderson, W.T., Jacobson, G. (2008). Possible evidence for wet Heinrich phases in tropical NE Australia: The Lynch's Crater deposit. Quaternary Science Reviews 27, 468-475. http://dx.doi.org/10.1016/j.quascirev.2007.11.006

NGRIP members (2004). High-resolution record of Northern Hemisphere climate extending into the last interglacial period. Nature 431, 147-151. http://dx.doi.org/10.1038/nature02805

Partin, J.W., Cobb, K.M., Adkins, J.F., Clark, B., Fernandez, D.P. (2007). Millennial-scale trends in west Pacific warm pool hydrology since the Last Glacial Maximum. Nature 449, 452-455. http://dx.doi.org/10.1038/nature06164

Partin, J.W., Quinn, T.M., Shen, C.C., Okumura, Y., Cardenas, M.B., Siringan, F.P., Banner, J.L., Lin, K., Hu, H.M., Taylor, F.W. (2015). Gradual onset and recovery of the Younger Dryas abrupt climate event in the tropics. Nature Communications 6, 8061. http://dx.doi.org/10.1038/ncomms9061

Pausata, F.S.R., Battisti, D.S., Nisancioglu, K.H., Bitz, C.M. (2011). Chinese stalagmite $\delta^{18}O$ controlled by changes in the Indian monsoon during a simulated Heinrich event. Nature Geoscience 4, 474-480. http://dx.doi.org/10.1038/ngeo1169

Pedro, J.B., van Ommen, T.D., Rasmussen, S.O., Morgan, V.I., Chappellaz, J., Moy, A.D., Masson-Delmotte, V., Delmotte, M. (2011). The last deglaciation: timing the bipolar seesaw. Clim. Past 7, 671-683. http://dx.doi.org/10.5194/cp-7-671-2011

Peterson, T.C., Vose, R.S. (1997). An overview of the Global Historical Climatology Network temperature database. Bulletin of the American Meteorological

Society 78, 2837-2849. http://dx.doi.org/10.1175/1520-0477(1997)078<2837:Aootgh>2.0.Co;2

Rahmstorf, S., Box, J.E., Feulner, G., Mann, M.E., Robinson, A., Rutherford, S., Schaffernicht, E.J. (2015). Exceptional twentieth-century slowdown in Atlantic Ocean overturning circulation. Nature Climate Change 5, 475-480. http://dx.doi.org/10.1038/Nclimate2554

Rasmussen, S.O., Andersen, K.K., Svensson, A.M., Steffensen, J.P., Vinther, B.M., Clausen, H.B., Siggaard-Andersen, M.L., Johnsen, S.J., Larsen, L.B., Dahl-Jensen, D., Bigler, M., Röthlisberger, R., Fischer, H., Goto-Azuma, K., Hansson, M.E., Ruth, U. (2006). A new Greenland ice core chronology for the last glacial termination. Journal of Geophysical Research: Atmospheres 111, n/a-n/a. http://dx.doi.org/10.1029/2005jd006079

Rosenthal, Y., Oppo, D.W., Linsley, B.K. (2003). The amplitude and phasing of climate change during the last deglaciation in the Sulu Sea, western equatorial Pacific. Geophysical Research Letters 30, n/a-n/a. http://dx.doi.org/10.1029/2002gl016612

Schefuß, E., Kuhlmann, H., Mollenhauer, G., Prange, M., Patzold, J. (2011). Forcing of wet phases in southeast Africa over the past 17,000 years. Nature 480, 509-512. http://dx.doi.org/10.1038/nature10685

Schneider, T., Bischoff, T., Haug, G.H. (2014). Migrations and dynamics of the intertropical convergence zone. Nature 513, 45-53. http://dx.doi.org/10.1038/nature13636

Schröder, J.F., Holbourn, A., Kuhnt, W., Küssner, K. (2016). Variations in sea surface hydrology in the southern Makassar Strait over the past 26 kyr. Quaternary Science Reviews 154, 143-156. http://dx.doi.org/10.1016/j.quascirev.2016.10.018

Scroxton, N. (2014), Late Pleistocene climate and environment from speleothems on Flores, Indonesia: vegetation, volcanoes and *Homo floresiensis*, Research School of Earth Sciences. The Australian National University, PhD Thesis, p. 488.

Setiawan, R.Y., Mohtadi, M., Southon, J., Groeneveld, J., Steinke, S., Hebbeln, D. (2015). The consequences of opening the Sunda Strait on the hydrography of the eastern tropical Indian Ocean. Paleoceanography 30, 1358-1372. http://dx.doi.org/10.1002/2015pa002802

Shakun, J.D., Burns, S.J., Fleitmann, D., Kramers, J., Matter, A., Al-Subary, A. (2007). A high-resolution, absolute-dated deglacial speleothem record of Indian Ocean climate from Socotra Island, Yemen. Earth and Planetary Science Letters 259, 442-456. http://dx.doi.org/10.1016/j.epsl.2007.05.004

Sijinkumar, A.V., Clemens, S., Nath, B.N., Prell, W., Benshila, R., Lengaigne, M. (2016). $\delta^{18}O$ and salinity variability from the Last Glacial Maximum to Recent in the Bay of Bengal and Andaman Sea. Quaternary Science Reviews 135, 79-91.

Sinha, A., Kathayat, G., Cheng, H., Breitenbach, S.F.M., Berkelhammer, M., Mudelsee, M., Biswas, J., Edwards, R.L. (2015). Trends and oscillations in the Indian summer monsoon rainfall over the last two millennia. Nature Communications 6, 6309. http://dx.doi.org/10.1038/ncomms7309

Steinke, S., Chiu, H.-Y., Yu, P.-S., Shen, C.-C., Erlenkeuser, H., Löwemark, L., Chen, M.-T. (2006). On the influence of sea level and monsoon climate on the southern South China Sea freshwater budget over the last 22,000 years. Quaternary Science Reviews 25, 1475-1488. http://dx.doi.org/10.1016/j.quascirev.2005.12.008

Stott, L., Cannariato, K., Thunell, R., Haug, G.H., Koutavas, A., Lund, S. (2004). Decline of surface temperature and salinity in the western tropical Pacific Ocean in the Holocene epoch. Nature 431, 56-59. http://dx.doi.org/10.1038/nature02903

Stuiver, M., Grootes, P.M. (2000). GISP2 Oxygen Isotope Ratios. Quaternary Research 53, 277-284. http://dx.doi.org/10.1006/qres.2000.2127

Suwarman, R., Ichiyanagi, K., Tanoue, M., Yoshimura, K., Mori, S., Yamanaka, M.D., Kurita, N., Syamsudin, F. (2013). The Variability of Stable Isotopes and Water Origin of Precipitation over the Maritime Continent. SOLA 9, 74-78. http://dx.doi.org/10.2151/sola.2013-017

Thomas, D.S.G., Bailey, R., Shaw, P.A., Durcan, J.A., Singarayer, J.S. (2009). Late Quaternary highstands at Lake Chilwa, Malawi: Frequency, timing and possible forcing mechanisms in the last 44 ka. Quaternary Science Reviews 28, 526-539. http://dx.doi.org/10.1016/j.quascirev.2008.10.023

Tierney, J.E., Pausata, F.S.R., deMenocal, P. (2015). Deglacial Indian monsoon failure and North Atlantic stadials linked by Indian Ocean surface cooling. Nature Geoscience advance online publication. http://dx.doi.org/10.1038/ngeo2603

Tierney, J.E., Russell, J.M., Huang, Y., Damsté, J.S.S., Hopmans, E.C., Cohen, A.S. (2008). Northern Hemisphere Controls on Tropical Southeast African Climate During the Past 60,000 Years. Science 322, 252-255. http://dx.doi.org/10.1126/science.1160485

Tierney, J.E., Russell, J.M., Sinninghe Damsté, J.S., Huang, Y., Verschuren, D. (2011). Late Quaternary behavior of the East African monsoon and the importance of the Congo Air Boundary. Quaternary Science Reviews 30, 798-807. http://dx.doi.org/10.1016/j.quascirev.2011.01.017

Vinther, B.M., Clausen, H.B., Johnsen, S.J., Rasmussen, S.O., Andersen, K.K., Buchardt, S.L., Dahl-Jensen, D., Seierstad, I.K., Siggaard-Andersen, M.L., Steffensen, J.P., Svensson, A., Olsen, J., Heinemeier, J. (2006). A synchronized dating of three Greenland ice cores throughout the Holocene. Journal of Geophysical Research: Atmospheres 111, n/a-n/a. http://dx.doi.org/10.1029/2005jd006921

Waelbroeck, C., Kiefer, T., Dokken, T., Chen, M.T., Spero, H.J., Jung, S., Weinelt, M., Kucera, M., Paul, A. (2014). Constraints on surface seawater oxygen isotope change between the Last Glacial Maximum and the Late Holocene. Quaternary Science Reviews 105, 102-111. http://dx.doi.org/10.1016/j.quascirev.2014.09.020

Wang, Y., Cheng, H., Edwards, R.L., An, Z., Wu, J., Shen, C.-C., Dorale, J.A. (2001). A high-resolution absolute-dated Late Pleistocene monsoon record from Hulu Cave, China. Science 294, 2345-2348. http://dx.doi.org/10.1126/science.1064618

White, W.B. (2006). Identification of cave minerals by Raman spectroscopy: new technology for non-destructive analysis. International Journal of Speleology 35, 103-107.

Wilson, M.E.J. (2002). Cenozoic carbonates in Southeast Asia: implications for equatorial carbonate development. Sedimentary Geology 147, 295-428. http://dx.doi.org/10.1016/S0037-0738(01)00228-7

Xie, P., Arkin, P.A. (1997). Global precipitation: A 17-year monthly analysis based on gauge observations, satellite estimates, and numerical model outputs. Bulletin of the American Meteorological Society 78, 2539-2558. http://dx.doi.org/10.1175/1520-0477(1997)078<2539:Gpayma>2.0.Co;2

Xu, J., Holbourn, A., Kuhnt, W., Jian, Z., Kawamura, H. (2008). Changes in the thermocline structure of the Indonesian outflow during Terminations I and II. Earth and Planetary Science Letters 273, 152-162. http://dx.doi.org/10.1016/j.epsl.2008.06.029

Yang, H., Johnson, K.R., Griffiths, M.L., Yoshimura, K. (2016). Interannual controls on oxygen isotope variability in Asian monsoon precipitation and implications for paleoclimate reconstructions. Journal of Geophysical Research: Atmospheres 121, n/a-n/a. http://dx.doi.org/10.1002/2015jd024683

Yoshimura, K., Kanamitsu, M., Noone, D., Oki, T. (2008). Historical isotope simulation using Reanalysis atmospheric data. Journal of Geophysical Research: Atmospheres 113, n/a-n/a. http://dx.doi.org/10.1029/2008jd010074

Zhang, R. (2005). Simulated tropical response to a substantial weakening of the Atlantic thermohaline circulation. Journal of Climate.

Zhang, R., Delworth, T.L. (2005). Simulated tropical response to a substantial weakening of the Atlantic thermohaline circulation. Journal of Climate 18, 1853-1860. http://dx.doi.org/10.1175/Jcli3460.1

3 Moisture source variability at eight Indo-Pacific speleothem sites

3.1 Introduction

Stable oxygen isotopes ($\delta^{18}O$) measured in speleothems have provided high-resolution, absolute-dated records of hydroclimate variability, particularly from low-latitude and monsoon regions. If deposited under isotopic equilibrium, the stalagmite $\delta^{18}O$ should reflect the $\delta^{18}O$ of the dripwater (Hendy, 1971), which in turn reflects the $\delta^{18}O$ of the precipitation ($\delta^{18}O_p$) (Cobb et al., 2007). Stalagmite records have been used to infer past rainfall changes since the Last Glacial Maximum (LGM) in South America (Cruz et al., 2005; Wang et al., 2007), India (Dutt et al., 2015), China (Dykoski et al., 2005), the Middle East (Shakun et al., 2007), and the Indo-Pacific Warm Pool (IPWP) (Ayliffe et al., 2013; Griffiths et al., 2009; Partin et al., 2007), using the observed anticorrelated relationship between $\delta^{18}O_p$ and rainfall. This relationship, known as the 'amount effect' describes the observation that more depleted $\delta^{18}O_p$ accompanies increased rainfall, driven by Rayleigh distillation in regions of intense convection (Dansgaard, 1964; Risi et al., 2008; Rozanski et al., 1993).

Recent studies have highlighted the importance of considering other factors that may influence $\delta^{18}O_p$ such as vapour origin, transport history, rainfall type and seasonality (Breitenbach et al., 2010; Dayem et al., 2010; LeGrande and Schmidt, 2006). In the tropics and midlatitudes, rainfall occurs primarily in two types – localized, high-intensity convective rainfall, and spatially-broad, low-intensity stratiform rainfall (Aggarwal et al., 2016). Stratiform rainfall tends to be isotopically lighter than convective rainfall. Therefore, $\delta^{18}O_p$ increases as the proportion of stratiform rainfall decreases. As the proportion of stratiform rainfall decreases, the proportion of convective rainfall increases, along with rainfall amount. Additionally, the $\delta^{18}O_p$ of convective rainfall decreases with increasing

convective rainfall amounts (Risi et al., 2008). These complexities associated with rainfall type can produce isotopically light rainfall at both ends of the amount spectrum, interfering with the 'amount effect' interpretation. Source region may also play an important role in modulating $\delta^{18}O_p$ through changes in transport distance and initial source composition (Lewis et al., 2010; Rozanski et al., 1993), both of which can act to affect $\delta^{18}O_p$ at the observation site without changing rainfall amounts.

Studies using isotope-enabled general circulation models (GCMs) have shown that the 'amount effect' alone is unlikely to explain $\delta^{18}O_p$ variability in the Asian summer monsoon (ASM) realm (Liu et al., 2014; Pausata et al., 2011). Instead, upstream depletion originating in the Indian summer monsoon (ISM) domain likely propagate along the monsoon transport pathways to speleothems in southeast Asia (Baker et al., 2015). Likewise, rainfall monitoring studies in the IPWP have demonstrated that the amount effect is variable across the IPWP and does not always explain the majority of $\delta^{18}O_p$ variability, though the correlation between rainfall and $\delta^{18}O_p$ does tend to increase with greater timescales (Belgaman et al., 2017; Kurita et al., 2009). Furthermore, tagged water simulations show that many sites across the IPWP receive moisture from multiple sources, raising the possibility of transport history influences on $\delta^{18}O_p$ (Kurita et al., 2009).

Many speleothem sites in the monsoon domains and IPWP have seasonal biases, whereby most rainfall occurs during the local monsoon season. As such, changes in $\delta^{18}O_p$ at these sites are often interpreted as changes in the strength or intensity of the local monsoon system, a so-called 'regional' amount effect driven by upstream depletion in the monsoon circulation (Denniston et al., 2013b; Dutt et al., 2015; Konecky et al., 2016; Lewis et al., 2010; Moerman et al., 2013). However, this assumption may be flawed if the site is receiving contributions from multiple source regions with different isotopic compositions (Baker et al., 2015; Griffiths et al., 2009; Li et al., 2016). Source region effects become increasingly challenging at sites with limited seasonality, and instead receiving contributions from multiple

sources throughout the year, which may have changed over time (Cobb et al., 2007; Wurtzel et al., 2018).

There is a need to understand moisture origins in the modern climate system to consider how these might have changed under different background conditions. It is well-established that North Atlantic abrupt events such as the Younger Dryas (YD) and Heinrich Stadial 1 (HS1) had far-reaching effects, influencing hydroclimate not only in the ASM/ISM realm but in the IPWP as well (Dykoski et al., 2005; Gibbons et al., 2014; Mohtadi et al., 2014; Stager et al., 2011; Zhou et al., 2016). However, it is unclear whether the observed changes in the proxy records are a direct result of changes in rainfall amount or rather due to changes in the vapour transport pathways. Furthermore, during the Last Glacial Maximum (LGM), sea level was up to 130 m lower than present and IPWP topography was much different than today (Sathiamurthy and Voris, 2006). The exposure of large continental shelves likely would have played a role in the available sources of moisture to the cave sites (Griffiths et al., 2009).

Wurtzel et al. (2018) (Chapter 2 in this thesis) presented preliminary exploration of this idea at Tangga Cave in Sumatra by comparing modern $\delta^{18}O_p$-rainfall relationships with observed and modelled data, evaluating moisture sources using back-trajectory air parcel modelling, and comparing these results to modelled paleo-moisture source results from an isotope-enabled hosing simulation.

In this chapter, I expand upon the work in Wurtzel et al. (2018) by extending the analysis to include seven additional Indo-Pacific cave sites. I examine the role the 'amount effect' plays at eight Indo-Pacific speleothem sites using output from the spectrally nudged, isotope-enabled general circulation model, IsoGSM (Yoshimura et al., 2008). I explore the seasonal pattern and spatial distribution of rainfall sources using an air parcel back-trajectory model combined with daily gridded rainfall data to estimate the monthly contributions from modern precipitation source regions for each site (Draxler and Hess, 1997). The modern trajectory data is used to validate modelled source regions in the isotope- and water tracer-enabled GCM, NASA-GISS ModelE2-R over the same period as the trajectory

analysis. Finally, preliminary water tracer results from a ModelE-R hosing simulation are presented to address how past precipitation source regions may have changed during the North Atlantic freshwater hosing events.

3.2 Data and methods

3.2.1 Cave sites

Eight cave sites have been chosen for this analysis, all of which have produced decadal to centennial-resolution speleothem records covering at least part of the LGM to present and all spanning the Younger Dryas.

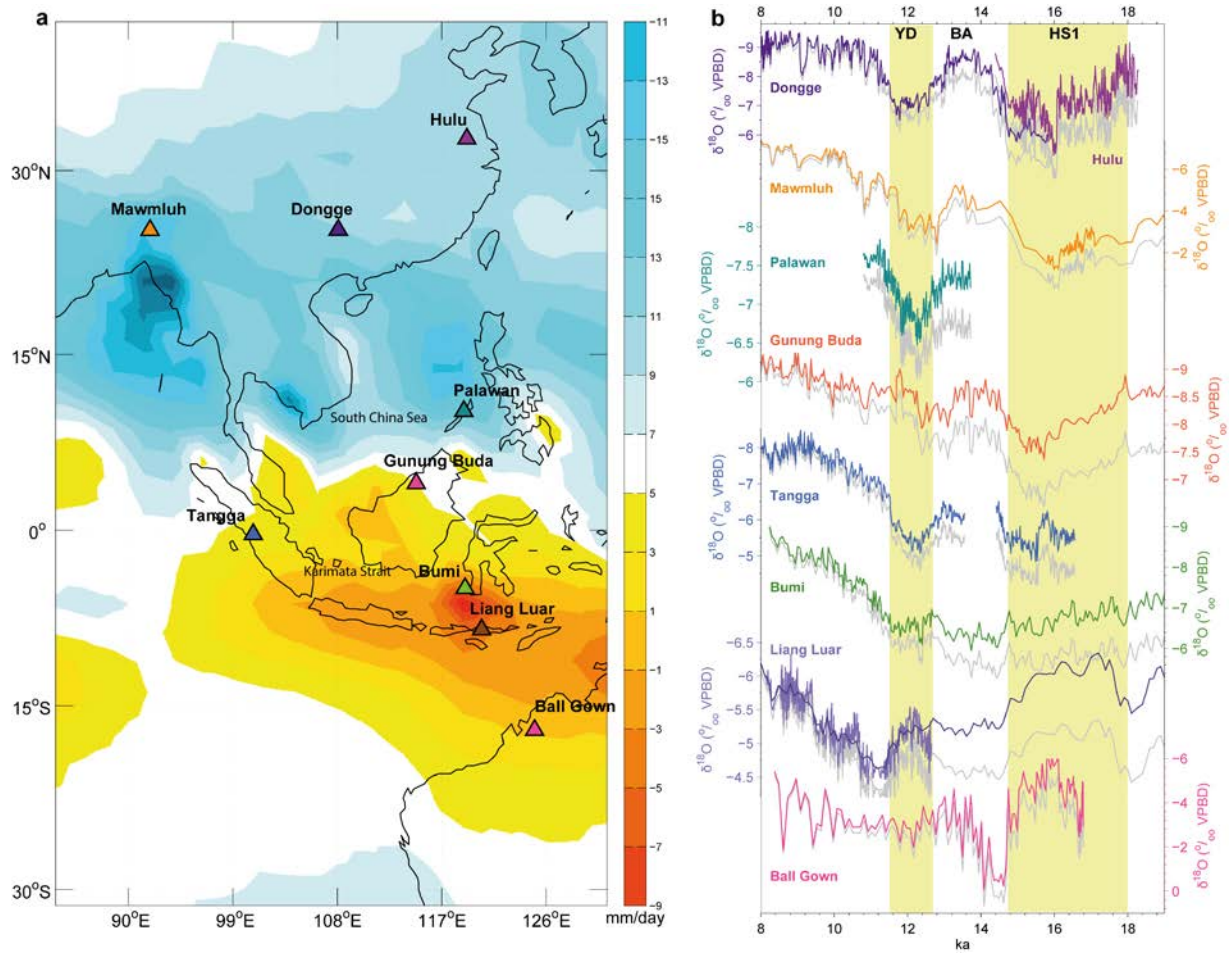

Figure 3.1 – (a) 1979-2015 JJA-DJF precipitation anomaly from CPC Merged Analysis of Precipitation (Xie and Arkin, 1997). Speleothem sites discussed in this study are indicated with triangles. Colors correspond to (b) stacked plot on right. Grey lines depict records uncorrected for ice volume, with the colored lines showing corrected values. Shaded bars indicate timing of Younger Dryas (YD), Bølling-Allerød (BA), and Heinrich Stadial 1 (HS1).

The cave sites span a latitudinal range of 17°S to 25°N and a longitudinal range of 90°E to 120°E, providing excellent spatial coverage across the Australasian monsoon system and the Indo-Pacific Warm Pool (Figure 3.1). All eight sites are subject to the influence of the annual migration of the Intertropical Convergence Zone (ITCZ). The eight sites are described in detail in Section 3.3.

3.2.2 Modern source moisture analysis

The National Oceanic and Atmospheric Administration (NOAA) Air Resources Laboratory's (ARL) HYbrid Single-Particle Lagrangian Integrated Trajectory model (HYSPLIT) is a complete system for computing simple air parcel trajectories and dispersion models (Draxler and Hess, 1997). HYSPLIT traces air particles released from any given height and location backwards to their starting point using a hybrid approach of LaGrangian methodology for the advection of air parcels from their initial location and an Eulerian methodology to compute air pollutants (Stein et al., 2015). HYSPLIT can be initialized with a number of publicly available gridded meteorological datasets with a range of horizontal resolutions, available time periods, and output frequencies (Stein et al., 2015).

In this study, HYSPLIT has been used with NCEP/NCAR Reanalysis data (2.5° latitude-longitude) (Kalnay et al., 1996) to calculate daily back-trajectories for rain-bearing air masses to eight Australasian speleothem sites (Table 3.1). The back-trajectories were calculated for 11 years (2000 – 2010) at 12-hour time steps, tracing back 6 days with a starting height of 500 meters above ground level (magl). The interval 2000-2010 was chosen due to the overlap with available ERA precipitation data and because this interval contains relatively few extreme Indian Ocean Dipole or El Niño-Southern Oscillation events.

Table 3.1 - Speleothem sites and corresponding WMO station and trajectory information.

Cave	Location	Lat	Lon	Elevation (m)	Nearest WMO Station Name (Number)	WMO Station Lat	WMO Station Lon	WMO Station Years	75% threshold (mm/day)	No. of trajectories
Dongge	China	25.28	108.1	680	Hechi (59023)	24.7	108.05	(n=36) 1955-1990	8.7	987
Mawmluh	India	25.26	91.7	1160	Cherrapunji (42515)	25.3	91.7	(n=135) 1872-1959, 1962-1963, 1966-1986, 1988-1989, 1995-2016	11.2	1171
Palawan	Philippines	10.2	118.9	118.9	Pto Princesa (98618)	9.75	118.73	(n=47) 1915-1921, 1923-1927, 1929-1932, 1934-1939, 1951-1975	8.6	1451
Gunung Buda	Borneo	4.03	114.8	120-200	Marudi Airfield (96449.1)	4.17	114.32	(n=13) 1963-1975	8.3	1468
Tangga	Sumatra	-0.36	100.8	600	Payakumbuh (96163.3)	-0.22	100.62	(n=86) 1880-1941, 1951-1975	8.5	2096
Bumi	Sulawesi	-5.02	119.7	40	Mandai Ujung Pandan (97180)	-5.1	119.6	(n=37) 1948-1970, 1972-1984, 2001	8.8	1533
Liang Luar	Flores	-8.5	120.4	550	Ruteng (97284)	-8.6	120.47	(n=55) 1916-1941, 1948-1976	8.9	1012
Ball Gown	NW Australia	-17.03	125	100	Derby (94204.1)	-17.4	124.35	(n=85) 1886-1887, 1891-1892, 1906-1954, 1958-1967, 1969-1976, 1984-1986, 1988-1991, 1994-	5.7	405

ERA daily precipitation data was used rather than NCEP/NCAR daily data due to the higher spatial resolution of the dataset. ERA-interim daily data was compared to the nearest available World Meteorological Organization (WMO) station data for each proxy site by generating annual climatologies using all available station years (varies by site), all available ERA years (1979-2016) and HYSPLIT analysis years (2000-2010) (Figure 3.2).

Rain-bearing trajectories for each site were then run through HYSPLIT's clustering algorithm (Draxler and Hess, 1997), which utilizes the total spatial variance between trajectories to determine clusters. The clustering program includes output for the cluster mean trajectories and cluster assignments for each individual trajectory. Using the trajectory cluster assignments, corresponding ERA daily precipitation amount data was totalled for each month in each cluster, allowing a quantitative assessment of cluster contributions to each proxy site throughout the year.

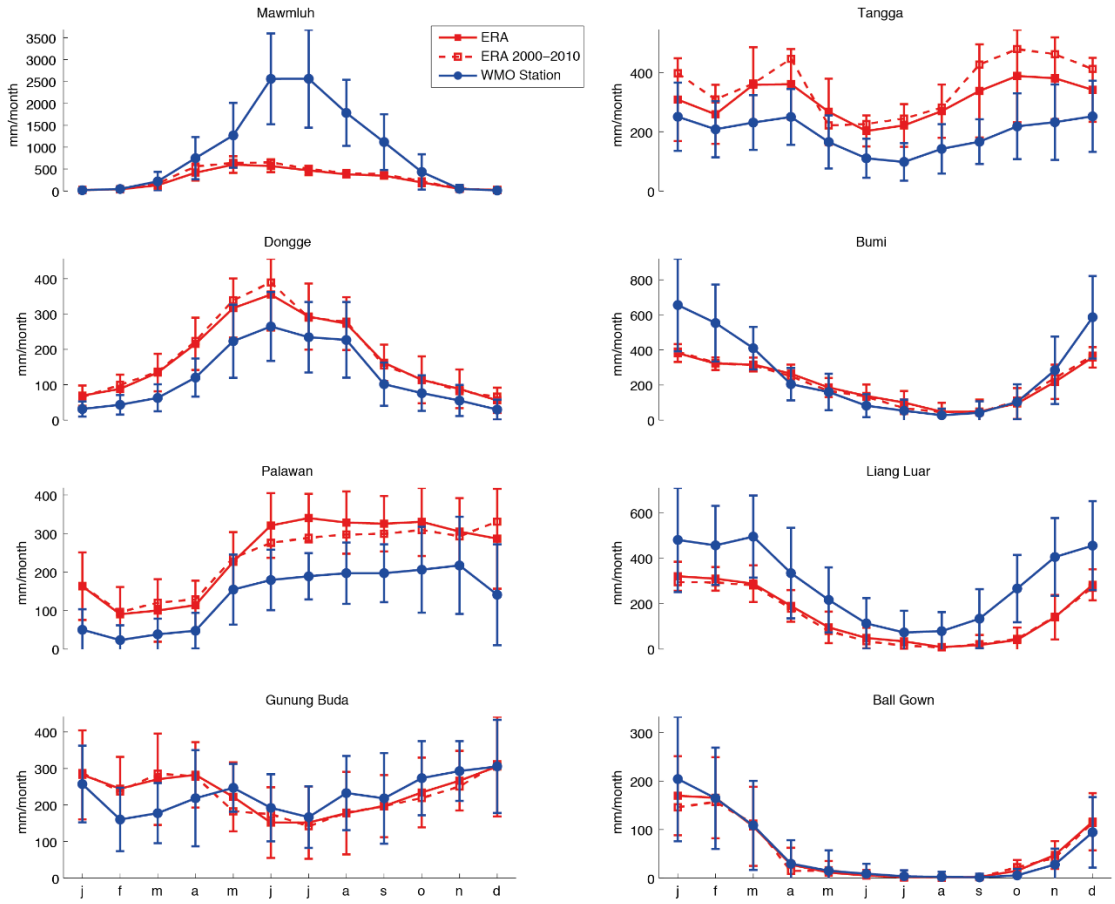

Figure 3.2 – Mean monthly precipitation data for all eight speleothem sites using all ERA years (1979-2015), ERA years overlapping with HYSPLIT analysis (2000-2010), and all available WMO station data (see Table 3.1).

Though NCEP/NCAR data is available from 1948 – present, the number of analysis years included here is limited by the slow work flow involved in trajectory generation when using HYSPLIT for Windows. The PySplit package for Python (Cross, 2015) helps to improve the efficiency of trajectory generation, but is only currently compatible with certain semi-monthly datasets, which do not include NCEP/NCAR reanalysis. Even with the generation of additional trajectories, the limiting factor becomes the time and computing power for running the cluster analysis on trajectory numbers greater than 3000.

To test the sensitivity of the results presented here, HYSPLIT trajectories were regenerated for Sumatra using a higher-resolution meteorological dataset Global Data Assimilation System (GDAS; 0.5° gridded), a higher starting altitude (1100m),

and including a higher percentage of rainfall days (95% of mean annual rainfall). The results of the comparison are discussed in Section 3.4.1.

3.2.3 IsoGSM data

Many speleothem records in the Indo-Pacific attribute a significant proportion of speleothem $\delta^{18}O$ variability to a local, seasonally-biased amount effect. An amount effect interpretation allows speleothem $\delta^{18}O$ to be used as a proxy for changes in paleo-rainfall at these sites. Drip and rainwater monitoring is not feasible at all cave sites and not all sites have GNIP (Global Network for Isotopes in Precipitation) stations within the same climatological region. For the purpose of examining the modern relationship of precipitation $\delta^{18}O_p$ to rainfall at the study site, I use existing monthly output from the spectrally nudged, isotope-enabled general circulation model, IsoGSM (Yoshimura et al., 2008). IsoGSM is run in T63L28 resolution corresponding to approximately 1.875 x 1.875° horizontal grid size with 28 vertical levels. Previous studies have shown that IsoGSM data correlates well with GNIP station data in the ASM/ISM region (Sinha et al., 2015; Yang et al., 2016). IsoGSM also contains output variables for both convective and total precipitation, allowing for a partial assessment of how precipitation type controls $\delta^{18}O_p$ values. Here, I use IsoGSM data to examine the contribution of the amount effect to $\delta^{18}O_p$ at each proxy site, and to consider the processes causing deviation from the amount effect.

3.2.4 GISS ModelE-R vapor source distributions

The Goddard Institute for Space Studies (GISS) ModelE-R is an isotope-enabled coupled atmosphere-ocean model equipped with water vapour source distribution tracers. Two versions of this model are employed in this study.

The older version of the model, referred to herein as "ModelE-R", has 4 x 5° horizontal resolution and 20 vertical atmospheric layers. This version has been used in previous studies to examine global response to large freshwater inputs in the North Atlantic, mimicking Heinrich events (Lewis et al., 2010; Lewis et al., 2013). A freshwater flux of 1 Sv was applied to the North Atlantic for 100 model years using pre-industrial boundary conditions (H1). Water hosing simulations

were run for >500 years to reach quasi-equilibrium. A parallel control (0k) simulation with pre-industrial conditions was run without freshwater perturbation (Lewis et al., 2010).

The newer version of the model, referred to herein as "ModelE2-R", has 2 x 2.5° horizontal resolution and 40 vertical layers (Schmidt et al., 2014). The configuration used in this study, ModelE2.1- NINT, has prescribed CMIP6 SSTs, sea ice, and greenhouse gases, and is nudged with winds from Modern-Era Retrospective analysis for Research and Applications 2 (MERRA2) data for the period 1980 – 2015 (Jesse Nusbaumer, pers. comm.).

Both models incorporate water isotope tracers that are tracked through all stages of the hydrologic cycle (Schmidt et al., 2006). Water vapour source distribution (VSD) tracers are employed using the 'painted water' method in an atmosphere-only simulation driven by surface conditions from the coupled simulation (Lewis et al., 2010). The sources of water vapour are traced back through cloud processes to the site of surface evaporation. The precipitation source distribution (PSD) utilized in this study is a subset of the VSD, defined where vapour condenses to liquid. VSD resolution is ~8x10°. PSDs have been normalized such that the total sum of moisture across the globe is 1. VSD/PSD results are a qualitative tool for examining relative precipitation source changes.

In this study, the MERRA2-forced simulation of ModelE2-R is directly compared to the vapour source distribution results to HYSPLIT trajectory source region results. A deglacial simulation with 1k time slices is currently being run on ModelE2-R by our collaborators at NASA GISS, Allegra LeGrande and Jesse Nusbaumer. In this chapter, I present preliminary VSD results from the hosed pre-industrial simulation of ModelE-R used in Lewis et al., 2010. Although it is beyond the scope of this thesis, it is important to note that we will ultimately examine LGM, H1, YD, and mid-Holocene time slices of the model VSDs in order to test interpretations of previously published speleothem $\delta^{18}O$ records (Wurtzel et al., in prep).

3.3 Site descriptions and mean annual climatology

3.3.1 Mawmluh Cave, India

Mawmluh Cave (25.26°N, 91.71°E, 1160 m) is located in northeast India on the southern fringe of the Meghalaya Plateau near the city of Cherrapunjee (Figure 3.3a [left]) (Breitenbach et al., 2010). Cherrapunjee is famous for being the wettest place on earth (>11,000mm/year) with rainfall primarily arriving between June to September as part of the Indian Summer Monsoon (Figure 3.3a [right])(Murata et al., 2007). The interpretation of speleothem oxygen isotope ($\delta^{18}O$) records from this region is still highly debated, but generally thought to reflect the intensity of the Indian Summer Monsoon.

Previous studies utilizing GNIP stations and boreal summer-only IsoGSM model data indicate that monsoon precipitation amount accounts for up to~30% of the variance in the oxygen isotopic data (Berkelhammer et al., 2013; Berkelhammer et al., 2012; Dutt et al., 2015). On the other hand, a cave monitoring study at Mawmluh shows no empirical amount effect (Breitenbach et al., 2010). Our analysis of all monthly IsoGSM data between 1979-2013 also shows no significant correlation between Mawmluh $\delta^{18}O_p$ and local rainfall amount, confirming results of Yang et al., 2016 suggesting that the local amount effect is not the dominant influence on $\delta^{18}O_p$ (Figure 3.4a). However, other climate processes related to monsoon intensity may well contribute indirectly to $\delta^{18}O_p$. 'Upstream' effects are commonly cited as a control on $\delta^{18}O_p$ variability, referring to the regional depletion caused by rainout along earlier parts of the monsoon transport path, without necessarily changing local rainfall (Yuan et al., 2004). However, peak monsoon rainfall tends to lead $\delta^{18}O_p$ minima at Mawmluh, which led Breitenbach et al., 2010 to suggest that changes in moisture source, source composition (i.e. Bay of Bengal freshening), and transport distance are drivers of local $\delta^{18}O_p$ variability. Increased runoff during the late Indian Summer monsoon leads to freshening (isotopic depletion) of the Bay of Bengal, which is the primary vapour source for Mawmluh. Therefore, rainfall sourced from the Bay of Bengal in the late monsoon season will

continue to be isotopically depleted even as rainfall amount decreases, leading to the seasonal mismatch in amount and $\delta^{18}O_p$ (Figure 3.3a).

Figure 3.3 – (a-h left panel) Topography in region for each cave site. Yellow star indicates location of cave site. Red and green boxes correspond to ERA and IsoGSM grid boxes nearest to cave site. Blue square is the location of the nearest WMO cave site. (a-h right panel) IsoGSM precipitation in mm/day (green diamonds) and IsoGSM $\delta^{18}O_p$ (black triangles on reverse y-scale) in grid box nearest to cave site.

Mawmluh Cave has been the focus of multiple paleoclimate studies, including records spanning the Holocene (Berkelhammer et al., 2012) and Last Glacial Maximum (Dutt et al., 2015). Speleothem $\delta^{18}O$ suggests a dry LGM relative to the Holocene and exhibits a deglacial pattern similar to that of Dongge Cave, including a dry H1/YD and wet BA, interpreted as forcing of the Indian Monsoon by North Atlantic teleconnections.

3.3.2 Dongge Cave, China

Dongge Cave (25.28°N, 108.01°E, 680 m) is located in Guizhou Province in southern inland China (Figure 3.3b [left]). Mean annual precipitation at Dongge Cave is ~1753 mm per year with 80% of rainfall arriving during boreal Asian summer monsoon months (May – Oct) (Figure 3.3b [right]) (Dykoski et al., 2005; Yuan et al., 2004). As with India, controls on $\delta^{18}O_p$ in China are still highly debated (Dayem et al., 2010; Maher and Thompson, 2012). Speleothem $\delta^{18}O$ records from Dongge Cave have classically been interpreted as the change in integrated precipitation to the cave site; that is to say, they reflect the vapour removed from air masses originating in Indo-Pacific waters (Yuan et al., 2004).

More recently, it has been shown that the Indian Ocean contribution to these vapour sources may play a larger role than originally thought (Baker et al., 2015; Yang et al., 2014). Furthermore, it may be changes in source moisture $\delta^{18}O$, or varying source contributions, driving changes in speleothem $\delta^{18}O$ at the site (Maher and Thompson, 2012; Pausata et al., 2011). Though multiple processes may contribute to $\delta^{18}O_p$ variability in China, there is a growing body of evidence that suggests local amount effect is not the dominant process (Dayem et al., 2010; Maher and Thompson, 2012; Wurtzel et al., in prep; Yang et al., 2016).

Our analysis of IsoGSM data demonstrates only a weak monthly amount effect (r^2=0.14), which increases slightly when calculated as an annual amount effect (r^2=0.21), in agreement with the results of Yang et al., 2014 (Figure 3.4b). Furthermore, IsoGSM demonstrates that an additional source of variability is the type of rainfall, whereby stratiform rainfall tends to be lighter than convective rainfall (Aggarwal et al., 2016). Convective rainfall tends to produce higher amounts of rainfall and thus, accounts for a greater proportion of the total rainfall at higher rainfall amounts.

Modelled IsoGSM rainfall shows that at amounts greater than ~9 mm/day, convective rainfall makes up the majority of total rainfall (Figure 3.5a, b). At rainfall amounts less than ~9 mm/day, the fraction of convective rainfall is highly variable.

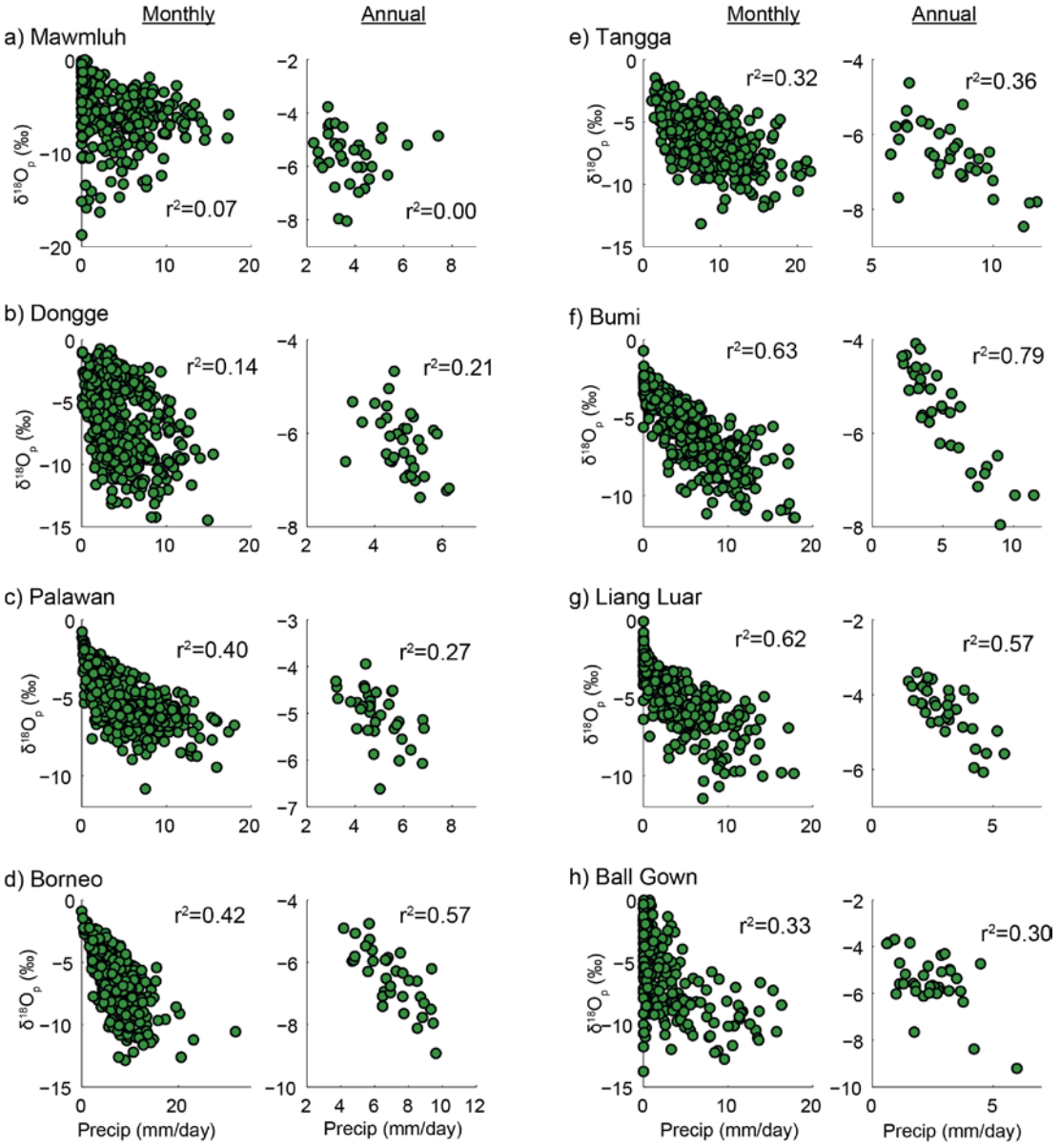

Figure 3.4 – Monthly (left) and annual (right) precipitation amount vs. $\delta^{18}O_p$ at grid point closest to all cave sites for all cave sites (a-h), using IsoGSM data (1979-2013), demonstrating amount effect.

Though convective rainfall is the primary type of rainfall at Dongge, stratiform rainfall becomes far more important at lower rainfall amounts. Because stratiform rainfall is isotopically lighter, it introduces more scatter into the $\delta^{18}O_p$ of low rainfall amounts. As such, the relationship between convective rainfall and $\delta^{18}O_p$ for the Dongge IsoGSM data is stronger (r^2=0.36) than the relationship between total rainfall and $\delta^{18}O_p$ (r^2=0.21). This can be attributed to convective rainfall driving the amount effect (Figure 3.5c).

Stalagmites from Dongge Cave have been used to generate paleoclimate records covering the last interglacial (Yuan et al., 2004) as well as the last deglacial through the Holocene (Dykoski et al., 2005).

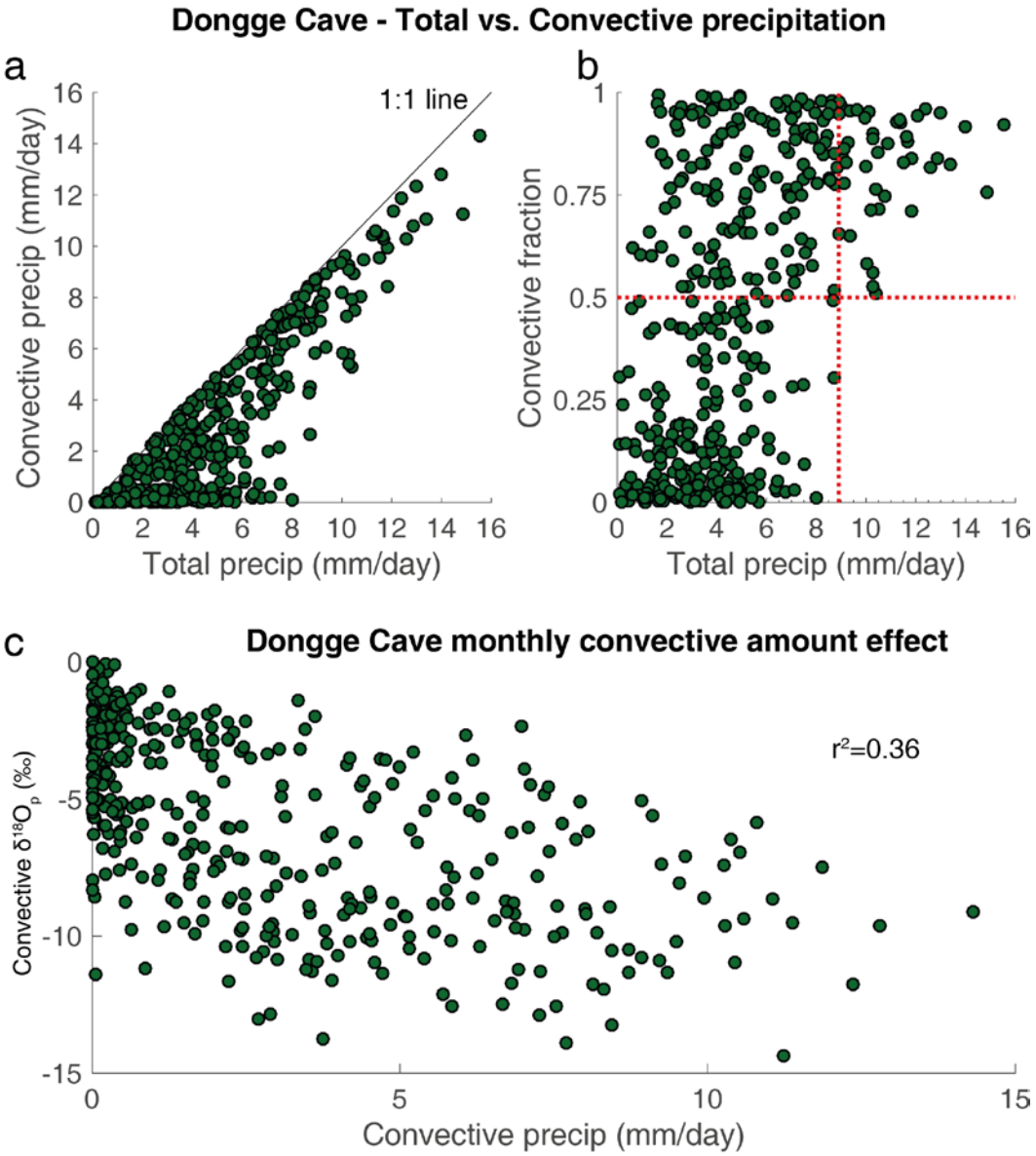

Figure 3.5 - Convective precipitation effects at Dongge Cave, China. (a) IsoGSM total vs. convective rainfall. (b) IsoGSM total rainfall vs. convective fraction of rainfall. Red horizontal line indicates 50% convective rainfall level. Red vertical line indicates amount threshold (~9 mm/day) above which the majority of rainfall is always convective. (c) Convective precipitation-driven amount effect at Dongge Cave.

3.3.3 Palawan, Philippines

Puerto Princesa Subterranean River National Park (10.2°N, 118.9°E, elevation unknown) is located in Palawan, Philippines (Figure 3.3c [left]). The wet season is

reported as running from May-November with 80% of the 2000 mm annual average falling during this period (Partin et al., 2015). ERA and WMO station data suggests a slightly longer rainy season continuing through December (Figure 3.3c). Rainfall $\delta^{18}O$ is thought to dominate the stalagmite $\delta^{18}O$ signal through changes in wet season rainfall via the amount effect, which is a common interpretation for tropical speleothems (Lewis et al., 2010; Moerman et al., 2013). Indeed, IsoGSM data shows that monthly rainfall amounts account for 40% of the variance in $\delta^{18}O_p$, however this drops to 27% when using annual average rainfall, perhaps suggesting that amount is not the dominating influence on longer timescales (Figure 3.4c).

Presently, one stalagmite study exists from Palawan covering the Younger Dryas interval (Partin et al., 2015). Despite the brevity of the record, the positive stalagmite $\delta^{18}O$ excursion is interpreted to reflect dry conditions during the YD, suggesting an important link with the North Atlantic.

3.3.4 Gunung Buda, Borneo

Gunung Buda National Park (4.0°N, 114.8°E, 120-200 m) is a karst system located in northwest Malaysian Borneo (Figure 3.3d) (Cobb et al., 2007). The ITCZ is overhead of Borneo year-round, delivering over 5000 mm of rainfall with little seasonality (Cobb et al., 2007; Partin et al., 2007). ENSO is a dominant influence on rainfall amount in northern Borneo on interannual timescales. Cave drip monitoring studies and analysis of gridded observations have shown that local rainfall $\delta^{18}O$ is representative of regional convective activity more so than local rainfall amount, with local amount only accounting for ~30% of the variance over the 5-year study (Moerman et al., 2013). The longer IsoGSM dataset shows that local amount effect may account for up to 42% (monthly) to 57% (annual) of the variance (Figure 3.4d). In contrast with the lack of seasonality in rainfall amount, a weak seasonal cycle in rainfall $\delta^{18}O$ may be indicative of longer transport pathways and increased Rayleigh fractionation associated with the boreal and austral summer monsoon seasons (Carolin et al., 2016).

Three speleothems from Bukit Assam and Snail Shell Caves in Gunung Buda have been used to generate $\delta^{18}O$ records spanning the last 27,000 years (Partin et al.,

2007). Following enriched isotopic values during the LGM relative to the Holocene, the Gunung Buda speleothem records a $\delta^{18}O$ maximum that coincides with HS1 event in Dongge and Hulu Caves. Surprisingly, this expression of North Atlantic forcing does not extend to the YD event. Rather, the speleothem record exhibits a gradual decline, culminating in minimum $\delta^{18}O$ values at 5 ky BP, which has been interpreted as a response to local September-October-November (SON) insolation maxima and its effect on zonal climate processes across the tropical Pacific Ocean (Carolin et al., 2016).

3.3.5 Tangga Cave, Sumatra

Tangga Cave (0°21'S, 100°45'E, 600 m) is located in the Barisan Mountains of central West Sumatra, Indonesia (Figure 3.3e). Tangga Cave receives high rainfall (>2000 mm) year-round with nearly 70% arriving from the Indian Ocean and the remaining 30% arriving as part of the austral and boreal summer monsoons (Wurtzel et al., 2018). The climatology of the region is largely non-monsoonal, with ITCZ migration dominating the seasonal rainfall pattern (Aldrian and Susanto, 2003; Mohtadi et al., 2014). Data from the spectrally-nudged isotope enabled IsoGSM suggests that the amount effect plays a significant role (>30%) in controlling the $\delta^{18}O$ signal in Sumatra (Figure 3.4e) (Wurtzel et al., 2018). A recently generated stalagmite rainfall record spanning the last 16,000 years demonstrates that central Sumatra is sensitive to North Atlantic forcing, exhibiting a dry YD event of similar timing and magnitude to that displayed at Dongge Cave. The similarities to the Asian monsoon realm are further evidence that the $\delta^{18}O$ signal at Sumatra captures broader regional rainfall changes. The speleothem reconstruction does not extend into the LGM but a nearby seawater oxygen isotope reconstruction suggests that the LGM in this region may have been as wet as the Holocene, exhibiting little glacial-interglacial difference (Mohtadi et al., 2014).

3.3.6 Bumi Cave, Sulawesi

Bumi Cave (5.0°S, 119.7°E, 40 m) is located on the southwest peninsula of Sulawesi near Makassar on the western side of a mountain range (Figure 3.3f). More than 80% of rainfall at the site is brought by the austral summer monsoon between

November and April, as the north-south running mountain range that divides the peninsula blocks southwesterly-sourced boreal monsoon rainfall during the dry season (Krause, 2015). In contrast, on the opposite side of the mountain range near Sinjai, the boreal monsoon dominates rainfall.

Speleothem $\delta^{18}O$ at Bumi Cave is thought to be dominated by the rainfall amount effect on timescales greater than interannual, which is a common interpretation in the deep tropics (Krause, 2015). Indeed, IsoGSM shows that Sulawesi has the highest local amount effect of all the sites considered in this study, with local rainfall amount explaining 67% (monthly) to 79% (annual) of the $\delta^{18}O$ variability (Figure 3.4f). A stalagmite record spanning the last 40,000 years is interpreted as a record of Indo-Australian summer monsoon (IASM/austral summer monsoon) intensity (Krause, 2015). The reconstruction exhibits little to no influence from North Atlantic forcing (no YD or H1) and an isotopically-enriched LGM relative to the Holocene, suggesting that drier conditions prevailed during the LGM, when sea level was lower (Kimbrough, 2016). Increased transport distance over land (continentality) could have acted to deplete the isotopic signature, implying the actual enrichment signal could be stronger.

3.3.7 Liang Luar, Flores

Liang Luar Cave (8.5°S, 120.4°E, 550 m) is located in western Flores, Indonesia (Figure 3.3g) (Griffiths et al., 2009). Mean annual rainfall is 1200 mm/year with 70% falling between December and March during the austral summer monsoon and less than 5% falling during the boreal summer monsoon as a result of orographic features (Figure 3.3g) (Ayliffe et al., 2013; Griffiths et al., 2009). The austral summer monsoon in Flores is dominated by northwesterly convective flow that occurs during the southward migration of the ITCZ.

Moisture source regions at Liang Luar were evaluated using back-trajectory analysis for modelling air parcel paths (Griffiths et al., 2009). Combined with dripwater monitoring, the study demonstrated that the cave site received rainfall from two isotopically distinct sources: isotopically-heavy southwesterly dry season sources and isotopically-light northwesterly wet season sources, with ~70%

of rainfall occurring during the latter. As a result, speleothem $\delta^{18}O$ is interpreted as changes associated with the IASM either via a change in the fraction of the year dominated by austral summer rainfall (seasonality) or the amount of rainfall falling during summer (Griffiths et al., 2009). Subsequent studies at Liang Luar continue to interpret changes in $\delta^{18}O_p$ as regional changes in 'monsoon intensity' or 'regional rainfall amount', but also acknowledge that competing moisture sources could alter the $\delta^{18}O_p$ signal without local precipitation changes (Ayliffe et al., 2013; Griffiths et al., 2016). Results from IsoGSM do suggest that the amount effect has a strong influence on at least modern $\delta^{18}O_p$ (r^2=0.62) (Figure 3.4g).

Multiple speleothem records from Liang Luar spanning different time intervals at varying resolutions have been published (e.g., Ayliffe et al., 2013; Griffiths et al., 2009; Griffiths et al., 2016; Lewis et al., 2011). In contrast to Sulawesi, the Flores speleothem record suggests a relatively wet LGM (Ayliffe et al., 2013) and a sensitivity to North Atlantic forcing in the form of wet YD and HS1 events (Ayliffe et al., 2013; Griffiths et al., 2009). The wet YD and HS1 at Flores have been interpreted as evidence for a southward migration of the ITCZ, with this same southward shift causing drying during these climate intervals at NH sites (e.g., Dongge, Mawmluh).

3.3.8 Ball Gown Cave, Australia

Ball Gown Cave (BGC; 17.0°S, 125.0°E, 100 m) is located in the western Kimberly of northwest Australia with an annual climatology dominated by the Indo-Australian summer monsoon (Figure 3.3h). Approximately 90% of Ball Gown Cave's rainfall arrives between December and March, and annual rainfall decreases sharply with distance south of BGC, emphasizing the sensitivity of the site to IASM extent. Previous studies have used GNIP station data from Darwin to demonstrate a strong amount effect (r^2=0.6) on regional $\delta^{18}O_p$ values (Denniston et al., 2013a; Denniston et al., 2013b). IsoGSM data suggests a substantial, but weaker, amount effect of r^2=0.3 (Figure 3.4h). Darwin is located 900 km to the northeast of BGC (12.5°S, 130.1°E), east of the Timor Sea. These small geographic differences likely result in different climatological patterns. The Kimberly coast is also adjacent to a broad

continental shelf, which when exposed during periods of lower sea level may have added an additional non-climatic component to $\delta^{18}O_p$ changes at Ball Gown Cave, as there would have been increased distance to the coast and no shallow warm water nearby.

A composite rainfall record comprised of six stalagmites from Ball Gown Cave intermittently spans the last 40,000 years. Two of these samples span the late deglacial to early Holocene and exhibit slightly lighter values during the YD and HS1. These intervals are interpreted as wet periods associated with a southward shift of the ITCZ, however, a gap in speleothem coverage between 17 and 19 ka makes it difficult to constrain the climatological conditions during LGM.

3.4 HYSPLIT analysis

3.4.1 HYSPLIT sensitivity test

Two trajectory generation scenarios were run for Tangga Cave, Sumatra, using different meteorological datasets, starting altitudes and rainfall thresholds (Figure 3.6). Both scenarios use 11 years of data, but the GDAS analysis period is for 2006-2016 due to data availability for this period only. The most striking difference between the two scenarios is the spread of the trajectory starting points in the GDAS scenario. In contrast to the NCEP/NCAR scenario, with a starting height of 500 magl (equivalent to ~950 hPa over Sumatra), the GDAS scenario has a starting altitude of 1100 magl (~850 hPa over Sumatra). The latter starting altitude was chosen as the height from which rainfall often originates.

Unsurprisingly, the higher wind speeds at higher levels of the atmosphere result in longer trajectories over the same 6-day period, extending well into the western Indian Ocean. Despite these differences, the cluster analysis still results in very similar sources in both scenarios. GDAS trajectories have approximately the same spread as NCEP/NCAR when limiting the trajectory duration to 4 days (not shown). This analysis does not, however, establish where moisture evaporates along the path and is picked up by the air parcel. As will be seen in Section 3.6.1, GISS

ModelE-R precipitation sources, which do trace moisture back to the point of condensation, are similar to HSYPLIT trajectories for the 6-day/500 magl simulation. The 6-day/500 magl simulation is similar to the 4-day/1100 magl simulation, suggesting that 4 day back-trajectories with starting heights of 1100 magl is likely a suitable estimate for rainfall origination.

An additional major difference in the trajectory analysis is that GDAS shows a much larger contribution from the distal (western to central) Indian Ocean relative to the local Indian Ocean. This could be due to the longer average air parcel paths reaching the western Indian Ocean, or due to the additional 20% of rainfall included in the GDAS test. For example, a study using Tropical Rainfall Measuring Mission (TRMM) precipitation radar data shows that land regions tend to have lower stratiform rain fractions while oceans have higher fractions, and that the central Indian Ocean is subject to these higher stratiform fractions (Schumacher and Houze Jr., 2003). If rainfall derived from the central Indian Ocean is characterized by smaller rainfall amounts associated with stratiform rain, rather than event-driven rainfall, these trajectories would have been excluded in the NCEP/NCAR scenario, due to the >8.6 mm threshold used in screening trajectories.

Additional sensitivity testing was beyond the scope of this research, however, for the qualitative assessment in this paper, we are satisfied by the similarity in source patterns and contributions between the two scenarios.

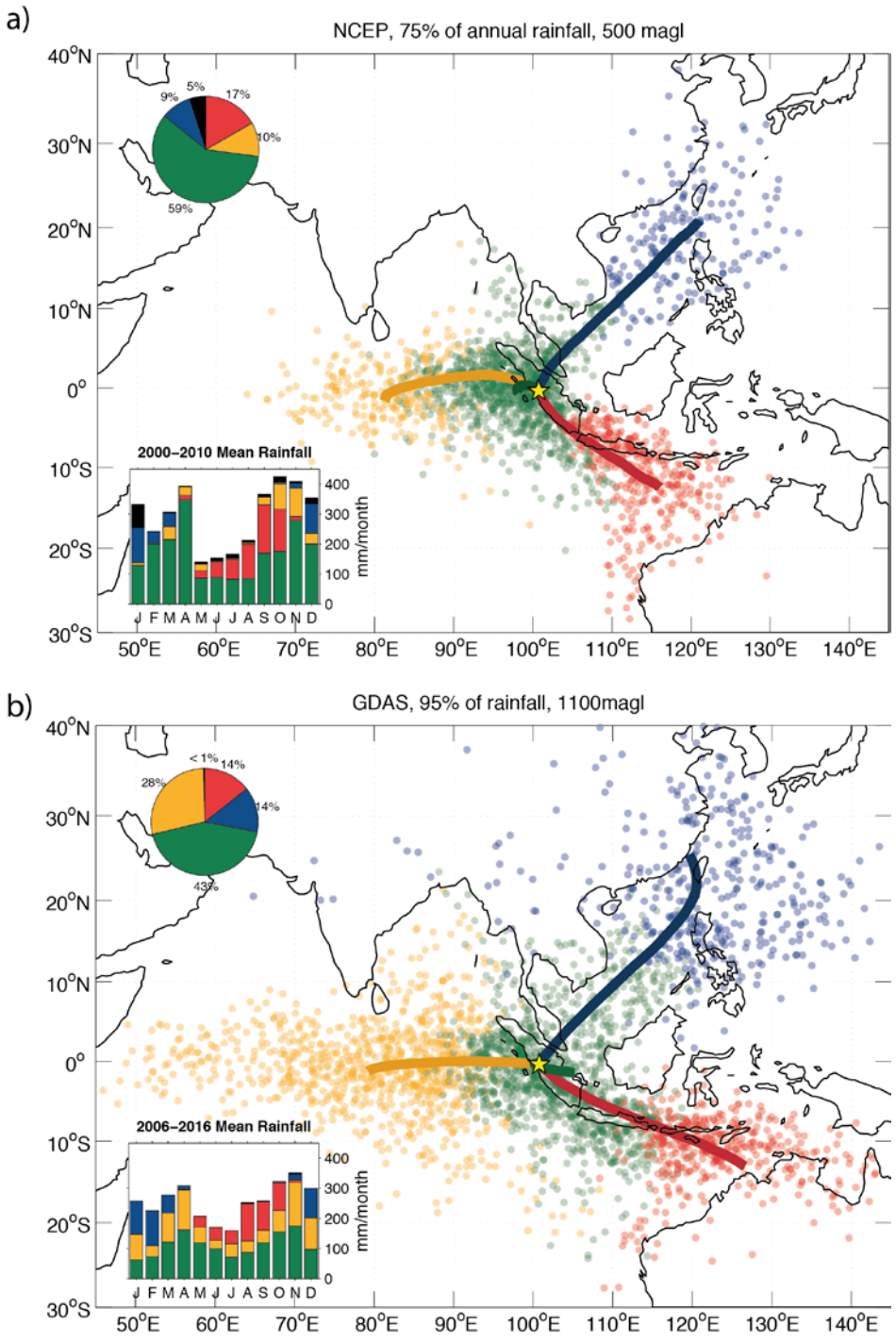

Figure 3.6 - HYSPLIT back trajectory analysis showing four primary paths of source moisture to Tangga Cave using (a) NCEP meteorological data over the period 2000-2010 with a starting height of 500 magl and including 75% of average annual rainfall and (b) using GDAS meteorological data over the period 2006-2016 with a starting height of 1100 magl and including 95% of average annual rainfall. Colored dots represent starting points of 6-day back trajectories of rain bearing masses to sites. Results of HYSPLIT trajectory cluster analysis are plotted as lines indicating the mean trajectory path of each cluster, where colors represent boreal summer (red), austral summer (blue), local (green), and distal/other (yellow) sources. The pie chart represents percent annual rainfall corresponding to each source. Black represents unassigned trajectories. Inset shows average monthly rainfall at site over the analysis period (2000-2010, ERA-interim), where colors correspond to monthly contribution from each source.

3.4.2 HYSPLIT results and discussion

Mawmluh Cave in India ERA-interim data severely underestimates Cherrapunjee station data (Figure 3.2). The Meghalaya Plateau is known to be the wettest place in the world, but is heterogenous within the region due to the highly variable topography (Murata et al., 2007). Cherrapunjee is particularly sensitive to updrafts creating high rainfall. Like the IsoGSM data, the ERA grid box is very large and likely homogenizes the rainfall data across the plateau. The ERA also places the peak monsoon season earlier than station data. In terms of HYSPLIT analysis, we conclude that the trajectories are likely representative of a realistic geographic and temporal distribution, despite the trajectory selection being based on ERA data.

As demonstrated in previous studies, the ERA-interim data for the analysis period 2000-2010 show that the majority of rainfall at Mawmluh Cave falls during the boreal summer monsoon season (May through September) (Figure 3.7a). The HYSPLIT analysis confirms that almost all rainfall is sourced either locally (30%) or from the Indian Ocean (39% Bay of Bengal, 31% Arabian Sea). The largely distal source of precipitation is consistent with interpretations of 'upstream effects' on rainfall $\delta^{18}O$ at the Mawmluh Cave site, and emphasizes the likelihood that Mawmluh Cave may be sensitive to changes in isotopic composition of the Bay of Bengal. Indeed, previous comparisons of local $\delta^{18}O$ with local rainfall amount suggest that the local amount effect only accounts for 30% of the variability in the $\delta^{18}O$ (Berkelhammer et al., 2013; Dutt et al., 2015).

Dongge Cave in China receives the majority of its rainfall during the boreal summer monsoon, based on the analysis period 2000-2010. The site receives year-round contributions from the Yellow and East China Seas (Figure 3.7b). The South China Sea contributes 30% of the total annual rainfall, with increased contributions during the boreal summer monsoon season. Indian Ocean transport contributes 23% of the annual total, occurring almost entirely between May and August. Isotopic mixing of these different sources may contribute to the weak amount effect observed at Dongge Cave.

Palawan in the Philippines receives the majority of its rainfall from the boreal monsoon between May and October. The primary source of this rainfall is the Karimata Strait, accounting for nearly 50% of total annual rainfall (Figure 3.7c). In October, northeasterly sources begin to contribute and by November, the Karimata Strait source is cut off. Rainfall amounts in Palawan remain extremely high during November and December with Pacific sources dominating the contribution. The site receives very little rainfall between January and April. Unlike the other sites in this study, Palawan receives almost no rainfall from local sources. Instead, rainfall at Palawan arrives via long transport pathways. Mixing of non-local moisture sources with very different isotopic values could potentially explain why the amount effect at Palawan decreases with longer temporal averaging. Monthly precipitation from a given source may show a relationship with the isotopic value occurring when that source dominates, but annual average precipitation may not relate well to the average annual isotopic values from two discrete sources. For example, precipitation remains high throughout June to December, but the primary source of precipitation shifts from the Karimata Strait to the Pacific and distal East Asia in November. There may be an 'amount effect' associated with each of these sources, but the relationship between amount and isotopic composition of those sources may not be the same. By averaging the $\delta^{18}O_p$ by month rather than by trajectory, the source-specific signal becomes mixed and we lose the 'amount effect' signal.

Gunung Buda in Borneo receives high rainfall year-round (Figure 3.7d). Around 32% is derived from the distal northeast (Pacific Ocean) primarily between November and April as part of the austral summer monsoon system. An additional 31% derives from south and southwest Karimata Strait and Java Sea between May and October as part of the boreal summer monsoon system. Local rainfall from the northeast (Sulu Sea) contributes 35%, arriving year-round.

Analysis of back-trajectories to Sumatra has been undertaken previously using NCEP/NCAR reanalysis (Wurtzel et al., 2018). Approximately 69% of average annual rainfall is sourced from the equatorial eastern Indian Ocean (59% local, 10%

distal), and arrives throughout the year (Figure 3.7e). From late-April through mid-November, rainfall can also be sourced from the Timor Sea, and this accounts for 17% of the annual average. These trajectories are associated with the southeasterly trades that form during the boreal summer monsoon. From late November through mid-March, this SE trade wind source is cut off and replaced by a long-range South China Sea source. These northeasterly trajectories are associated with circulation patterns of the austral summer monsoon, and contribute 9% of the average annual rainfall to Tangga Cave. Approximately 5% of annual rainfall does not fall into the 3 major trajectory clusters.

Due to the mountain range that restricts southeasterly rainfall, Bumi Cave in Sulawesi receives the majority of its rainfall from the austral summer monsoon between November and April (Figure 3.7f). Approximately 45% is sourced locally from the Makassar Strait and 23% arrives from the Karimata Strait to the west. An additional 19% is sourced from the Pacific. The remaining 10% arrives during the austral winter season; however, this is likely an overestimate due to the coarse resolution of the ERA data, which incorporates part of the southeast side of the dividing mountain range. Indeed, the WMO station data exhibits a stronger seasonality that should bias rainfall contributions more strongly toward the austral summer season.

Liang Luar Cave in Flores receives the majority of rainfall as part of the austral summer monsoon between November and April, with only 10% arriving between April and October from the southeast (Figure 3.7g). Local rainfall contributes 36%, while an additional 33% arrives from the Karimata Strait as part of the austral summer monsoon. Surprisingly, Flores receives a non-trivial contribution of 19% from the southeastern Indian Ocean. These results suggest that thinking of Flores as a two-source system (Griffiths et al., 2009), dominated by northeasterly flow, may be overly simplistic. While southeasterly sources may have always been limited due to the presence of a mountain range, changing proportions of the Indian Ocean source could affect isotopic variability, assuming that the Indian

Ocean source has a different isotopic composition than the austral summer monsoon source.

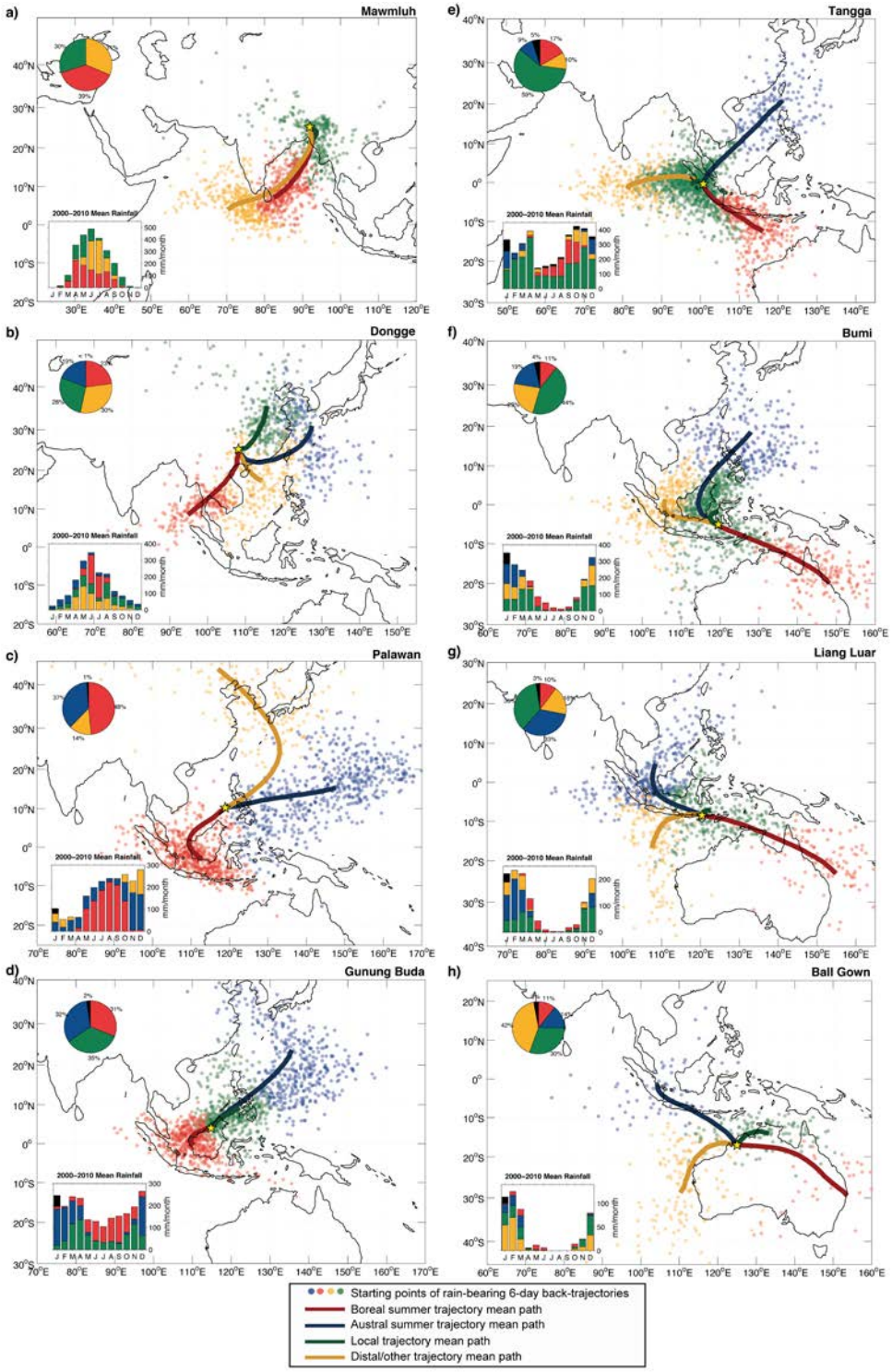

Figure 3.7 - HYSPLIT back-trajectory analysis showing primary paths of source moisture to the eight cave sites using NCEP meteorological data over the period 2000-2010 with a starting height of 500 magl. Colored dots

represent starting points of 6-day back-trajectories of rain bearing masses to sites. Results of HYSPLIT back-trajectory cluster analysis are plotted as lines indicating the mean trajectory path of each cluster, where colors represent boreal summer (red), austral summer (blue), local (green), and distal/other (yellow) sources. The pie chart represents percent annual rainfall corresponding to each source. Black represents unassigned trajectories. Inset shows average monthly rainfall at site over the analysis period (2000-2010, ERA-interim), where colors correspond to monthly contribution from each source.

Ball Gown Cave receives nearly all of its rainfall between December and March during the austral summer monsoon season (Figure 3.7h). Northeasterly rainfall, primarily from the Timor Sea, accounts for 30% and an additional 14% occurs along the northwest branch of the austral summer monsoon. However, nearly 45% arrives from the southeast Indian Ocean, brought by SH westerlies that have been deflected by a heat low that forms over Australia during austral summer. The heat low is a semi-permanent high-temperature, low-pressure system that develops over Pilbara, Australia during the summer months, the intensity of which is related to differential land-sea temperature gradients (Gentilli, 1971). The multiple sources which bring rainfall to BGC during the very short wet season may result in the weaker than expected amount effect. No HYSPLIT analysis was performed for Darwin so we are unable to evaluate whether different moisture sources are response for different amount effects between Darwin and Ball Gown Cave.

3.5 HYSPLIT sources from a paleo-perspective

3.5.1 The Younger Dryas in the Indo-Pacific Warm Pool

The systematic HYSPLIT analysis of all 8 speleothem sites presented in this chapter compliment Chapter 2's discussion of rainfall variability in the Indo-Pacific Warm Pool during the YD (Wurtzel et al., 2018). This approach enables us to better understand Indo-Pacific signals during the YD interval, and their relation to climatic and geographic change.

Speleothem records from China, India, Palawan, and Sumatra all experience ^{18}O enrichment during the Younger Dryas, suggesting a region-wide coherence for this climatic anomaly (Figure 3.1). Despite only a quarter of Dongge Cave's rainfall being sourced from the Indian Ocean, coherence between Chinese and Indian records suggests that the Indian Ocean source dominates variability on timescales

ranging from the interannual to the millennial (Pausata et al., 2011; Yang et al., 2016). Dongge Cave shares a similar deglacial sequence to that of Mawmluh Cave in India (Dutt et al., 2015; Dykoski et al., 2005), which receives all of its rainfall from the Indian Ocean. An ^{18}O-depleted Bølling-Allerød followed by an ^{18}O-enriched YD feature prominently in both records. Freshwater hosing simulations and proxy reconstructions focusing on the western Indian Ocean demonstrate that western Indian Ocean cooling during hosing events results in reduced rainout along the monsoon transport paths and heavier $\delta^{18}O$ values downstream in China and India. However, this mechanism is unlikely to drive enrichment at Sumatra or Palawan, as the western Indian Ocean cooling is not along the moisture transport path to either Sumatra or Palawan.

Another oft-invoked response to North Atlantic freshwater forcing is a southward shift of the ITCZ. A reasonable expectation would be that a more southerly mean ITCZ would result in reduction of northern tropical rainfall, cause little change near the equator, and increase southern tropical rainfall (Stager et al., 2011). In these circumstances, the boreal summer northern ITCZ limit would be restricted, leading to a reduction in ISM/ASM rainfall. In the IPWP, a southward ITCZ shift during the YD is supported by isotopic changes in sites at the northern and southern edges of the IPWP. These include an increase in precipitation recorded by speleothems from Flores (Ayliffe et al., 2013; Griffiths et al., 2009), and rainfall decreases in Palawan in the northern IPWP (Partin et al., 2015). However, the strong drying at Sumatra on the equator, while Borneo records no change at 4°N (between Sumatra and Palawan), suggests that an ITCZ shift alone cannot explain the YD response in the IPWP.

The Palawan HYSPLIT analysis demonstrates that moisture from the Karimata Strait provides nearly 50% of the rainfall to Palawan. Estimates of sea-level change during the YD suggest that it was 55 - 65 m below present, such that the Sunda Shelf in the Karimata Strait was largely exposed, the South China Sea had begun to expand westward, and the Gulf of Thailand had started to flood (Figure

3.8) (Hanebuth et al., 2011). Because the Karimata Strait was still exposed land, a major source of moisture to Palawan would have been cut off.

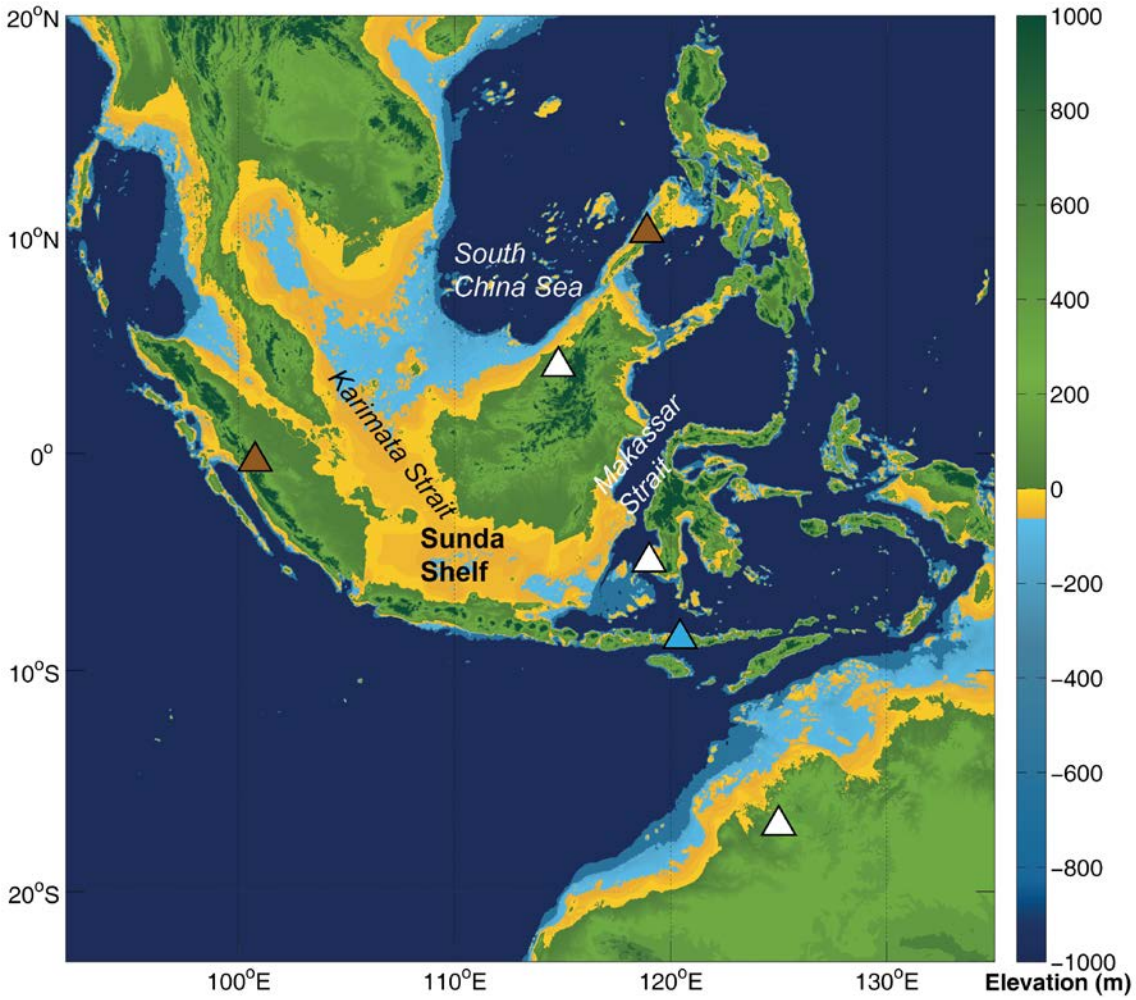

Figure 3.8 – Indo-Pacific topography during the Younger Dryas (~12.7 ka); 60 m below present), with modern land masses (green) and exposed shelves (yellow). Triangles represent location of cave sites and hydroclimate status during the Younger Dryas (brown – dry; white – neutral; blue – wet)

It is perhaps more surprising then that the Borneo speleothem is not as drastically affected by the exposure of the Karimata Strait as Palawan. The longer Borneo speleothem records covering glacial-interglacial timescales (Carolin et al., 2016) demonstrate that Borneo is sensitive to North Atlantic forcing as Heinrich stadials are robustly recorded in the Borneo record. Despite this, the YD does not show up clearly in the record from Gunung Buda. It has been hypothesized that the strong precessional control on Borneo rainfall may have dominated over remote forcing during the last deglaciation (Carolin et al., 2016). However, previous Heinrich

events (i.e., H3, H6) have occurred during periods of increasing insolation (Carolin et al., 2013). Instead, because sea level was rising during the last deglaciation, there may have been more local moisture sources available to Borneo via the expanded South China Sea, Sulu and Sulawesi Seas. Palawan, on the other hand, appears to derive most of its moisture from distal sources, receiving very little from local sources. Without a longer record spanning both the Holocene and the last glacial period, it is challenging to assess whether the Palawan response is due to the change in sea level-driven moisture source, or circulation and convective changes associated with North Atlantic forcing.

In contrast to sites that receive their moisture from the Sunda Shelf, HYSPLIT analysis indicates that Sumatra does not appear directly sensitive to changes in sea level. The majority of Tangga Cave moisture is sourced from the Indian Ocean, with corresponding monsoon pathways contributing during boreal and austral summers. Weakening in monsoon pathways was shown to produce a significant decrease in local rainfall during the Younger Dryas (Wurtzel et al., 2018).

3.5.2 Indo-Australian summer monsoon

Three sites in the southern hemisphere which have been classically interpreted as proxies for the IASM also reveal a more complicated pattern of source moisture that may have changed during the YD and LGM. Highly monsoonal climates dominate the modern climatologies at SW Sulawesi, Flores, and NW Australia, which receive high rainfall during the austral summer monsoon and virtually none during austral winter. As such, changes in speleothem isotopes at these sites have been interpreted as changes in IASM intensity, because they receive the majority of their rainfall from this system. However, examination of the HYSPLIT results demonstrates that such an interpretation is overly simplistic for at least, Flores and NW Australia.

In the case of SW Sulawesi, the mountain range which blocks southerly rainfall is presumed to have done so since at least the LGM, so the majority of rainfall should arrive from the north during the austral summer monsoon season. At least 25% of Bumi Cave's rainfall is sourced from the Karimata Strait, which was at least

partially exposed during the YD. Like Palawan, the exposure of the Sunda Shelf cuts off a major moisture source to the cave site. Yet unlike Palawan, Sulawesi does not record a significant change during the YD. Sulawesi's large contribution of local rainfall may render it less sensitive to the degree of Sunda Shelf exposure during the YD, as the ITCZ would still need to pass overhead. Like Borneo, it is possible that insolation forcing overrides the local decrease in moisture availability.

Unlike Sulawesi, for which orographic restrictions force the majority of rainfall to come from the IASM, Liang Luar and Ball Gown Cave also receive considerable moisture contributions from the southeast Indian Ocean. The Indo-Australian summer monsoon over northwest Australia is a complicated system, deriving rainfall not only from northwesterly convective flow, but also from the south-southwest, where Southern Hemisphere westerlies are deflected around the semi-permanent Pilbara heat low into the monsoon trough (Gentilli, 1971; Wyrwoll and Miller, 2001). Surprisingly, over 40% of modern moisture is sourced from the southwesterly flow, rather than the 'true' northwest IASM.

The Makassar Strait is sensitive to changes in the western Pacific mean state (Linsley et al., 2017). Previous studies have linked October precessional forcing to orbital scale rainfall variations at cave sites in southwest Sulawesi, including Bumi Cave (Kimbrough, 2016; Krause, 2015). The HYSPLIT analysis performed here supports the idea that Pacific forcing could be superimposed on the decreased rainfall dictated by shelf exposure during glacial states, as the source of moisture would likely shift from the exposed Karimata Strait to the Pacific (Figure 3.8).

During the Last Glacial Maximum, the Liang Luar Cave record exhibits relatively depleted isotopic values, suggesting that the LGM may have been as wet as the Holocene. Considering that a major source of rainfall to Flores is the exposed Sunda Shelf, this is somewhat surprising. However, it is possible that the Indian Ocean source played a greater role in delivering rainfall to the cave site. There is also the possibility that seasonality may have changed with increased delivery of winter rainfall relative to present. Previous studies have suggested that summer

insolation drives the Flores signal until sea-level forcings take over when the Sunda shelf flooded (Ayliffe et al., 2013; Griffiths et al., 2009).

3.6 Preliminary paleo-VSD results

3.6.1 HYSPLIT-ModelE2-R PSD validation

For the purpose of exploring paleo-moisture source changes, I will be employing a hosing run of GISS ModelE-R equipped with VSD tracers. Future work will use a VSD-equipped GISS ModelE2-R to evaluate paleo-moisture source changes. First, we must evaluate if GISS ModelE2-R adequately captures the modern-day moisture pathways relevant for each speleothem site. I do so by qualitatively assessing whether a MERRA-forced run of ModelE2-R for the period 2000-2010 exhibits the major precipitation source features observed in the HYSPLIT analysis. ModelE2-R is used for the modern validation in anticipation of running paleo-VSD tracers on the higher resolution model. It is expected that the physics governing both models are reasonably similar, such that validation using the ModelE2-R simulation should be sufficient for interpreting the ModelE-R paleo-VSDs (Jesse Nusbaumer, pers. comm.) The precipitation source distributions (PSDs) described here have been normalized such that the sum of all global moisture equals one. It is important to note that PSDs do not reflect the amount of moisture arriving to a site – only the fractional source of the moisture.

As suggested by HYPSLIT, Mawmluh and Dongge caves have persistent annual local sources from the Bay of Bengal and eastern Pacific Ocean, respectively (Figure 3.9a, c). When examining the boreal summer monsoon season, the Bay of Bengal and Indian Ocean sources increase for both sites, reflecting the dominance of ISM rainfall at the Chinese cave sites during the Asian summer monsoon season (Figure 3.9b, d).

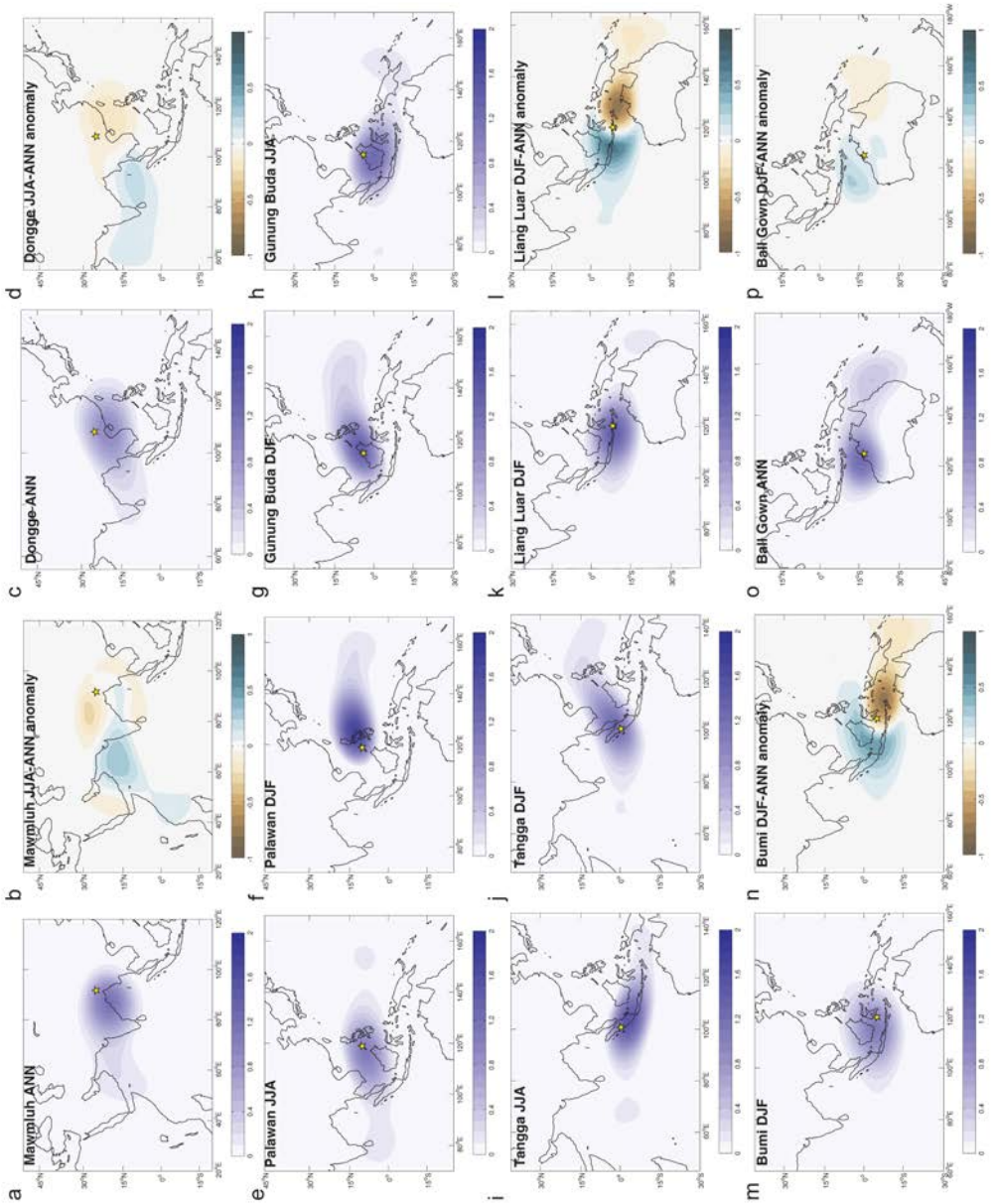

Figure 3.9 - Precipitation source distributions (PSDs) for GISS ModelE2-R MERRA2-nudged simulation. Scale is in percent (%) of global moisture.

The dominance of the Karimata Strait moisture source indicated by HYSPLIT is not as evident in the Palawan JJA PSD though the PSD center is clearly shifted westward relative to DJF, during which the PSD extends well eastward into the Pacific (Figure 3.9e-f). Overall, the PSD shows a predominance of local sources in contrast with the distal sources suggested by the HYSPLIT analysis.

At Borneo, local sources from the South China Sea persist year round, while the PSD center shifts westward toward the Karimata Strait during boreal summer, reflecting the dominant southerly trajectory of the winds in agreement with HYSPLIT data (Figure 3.9g). From December through March, the PSD extends eastward into the Pacific, reflecting the long-range Pacific sources that dominate the HYSPLIT contributions between December and January before tailing off by April (Figure 3.9h).

Sumatra HYSPLIT results have previously been compared to PSDs produced by ModelE-R in Wurtzel et al. (2018). Results from ModelE2-R show largely the same pattern with local sources dominating throughout the year, while additional southeasterly and northeasterly sources appear during boreal summer and austral summer respectively (Figure 3.9i-j).

Neither Sulawesi nor Flores PSDs capture the full range of sources suggested by HYSPLIT during their local rainy season, DJF. Both PSDs suggest highly local sources that don't include contributions from the Pacific or northern Karimata Strait and South China Sea (Figure 3.9k, m). During the rest of the year, the PSDs exhibit strong contributions from the southeast (Figure 3.9l, n). Though these winds do dominate outside of DJF, neither site receives considerable rainfall during the off-season. The DJF PSD for Flores does expand slightly further into the Indian Ocean than during the rest of the year, perhaps meaning that the DJF southwesterly flow as seen in HYSPLIT is an important source of moisture. The mismatch between the HYSPLIT and PSD data for these two sites may reflect the low resolution of the model and the importance of orographic effects at both sites, which the model may not be able to capture.

Ball Gown Cave PSDs shows a similar spatial pattern of moisture sources year-round with local, southwesterly and southeasterly sources always contributing. However, during the only season with rainfall, DJF, the proportion of precipitation sourced from local sources and the Indian Ocean is higher than from the southeast. This agrees with HYSPLIT results; however, the PSD does not reflect any considerable fraction of rainfall sourced from the 'true' northwesterly monsoon Figure 3.9o-p).

GISS ModelE2-R appears to capture all the major features and timings of modern climate at most of the cave sites (Mawmluh, Dongge, Palawan, Borneo, Sumatra). At Ball Gown cave, the PSDs lack the longer trajectories originating from the Karimata Strait, but pick up the zonal sources. Despite capturing the northwesterly trajectory of the austral summer monsoon, the overall pattern of PSDs at Sulawesi and Flores bears only a weak resemblance to the pattern suggested by HYSPLIT analysis.

3.6.2 Preliminary ModelE-R hosing PSDs

In this section, I present preliminary results from a simulation run on GISS ModelE-R in which the control run with pre-industrial boundary conditions was hosed with 1 Sv over 100 years in the North Atlantic. This type of hosing experiment is typically used to explore millennial scale climate events such as the YD. Because neither Flores nor Sulawesi accurately reflected modern sources, we do not attempt to interpret the paleo-PSD results.

Hosing results for Dongge and Mawmluh caves suggest a transition to more local sources during the boreal summer monsoon season (JJA). In the case of Dongge, there is an overall reduction from Indian Ocean sources, while the fraction of western Pacific sourced rainfall increases (Figure 3.10a). Mawmluh sees a reduction of long transport paths from the western Indian Ocean, while the percentage of rainfall arriving from the nearby Bay of Bengal increases (Figure 3.10b). These changes are likely a result of cooling in the western Indian Ocean during North Atlantic freshwater events, reducing moisture availability from that

region (Pausata et al., 2011), and are consistent with the ^{18}O enrichment observed at both sites during the YD.

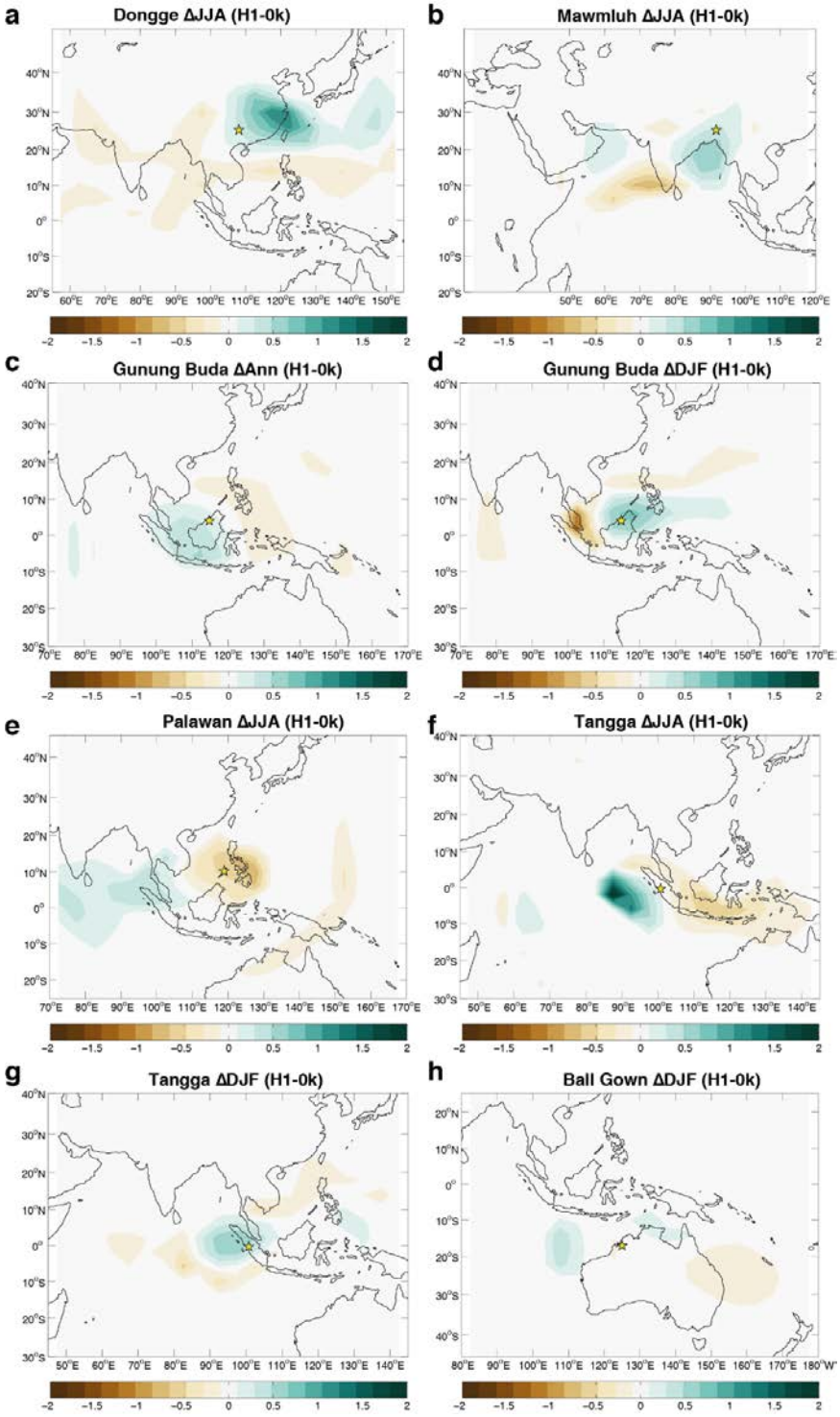

Figure 3.10 – Paleo-PSD anomalies from the hosing ('H1') simulation of ModelE-R. Scale is percent (%) of global moisture.

Borneo indicates an increase in the fraction of moisture being sourced from the Karimata Strait during all seasons except DJF, during which there is a reduction of westerly-sourced precipitation and an increase in local easterly-sourced precipitation (Figure 3.10c-d). Due to the exposure of the Sunda Shelf during the last deglaciation, the increase in moisture from the Karimata Strait is unlikely. The land configuration in the model uses modern sea level and therefore doesn't include an exposed Sunda Shelf. It is likely that during the YD, moisture would have been constrained to Pacific sources if there was restricted moisture availability from the Karimata Strait.

Palawan, which receives very little moisture locally in the modern, shows a further decrease in locally-sourced moisture during JJA and an increase in westerly-sourced moisture from the Gulf of Thailand and the eastern Indian Ocean, though it's unclear if this is an artifact of the modern PSD overestimating the local contributions (Figure 3.10e). The Gulf of Thailand transport path is a modern feature of the Palawan PSD and the hosing PSD anomaly might be reflecting a greater portion of moisture along this pathway. However, because the modern PSDs underestimate the contribution of the Karimata Strait, this change in fraction source may be attributed to the wrong pathway. As with Borneo, even if the change in the source occurred in the Karimata Strait, the model does not accurately reflect the topography during the deglaciation.

Sumatra PSDs reveal a reduction in the fraction of moisture coming from both the DJF northeasterly pathway and JJA southeasterly pathway associated with the migration of the ITCZ (Figure 3.10f-g). The strong YD signal observed at Tangga Cave, Sumatra has been attributed to the reduction of moisture from these pathways (Wurtzel et al., 2018).

Only minor precipitation source anomalies occur because of freshwater forcing during DJF at Ball Gown Cave (Figure 3.10h). These include a slight increase in southeast Indian Ocean sources and decrease in Pacific sources. No YD is observed at BGC. Though this could potentially be due to Indian Ocean sources compensating for lost northerly sourced moisture, it is likely due to the limited

southerly extent of the YD anomaly. Alternatively, expansion of the northwest Australian shelf (Figure 3.8) could reduce moisture sources and offset any increase in the duration of the austral monsoon season. Future simulations looking at the differences between H1, YD, and the LGM may help constrain the effect of precipitation source changes on rainfall amount.

3.7 Conclusions

In this research, I have undertaken a systematic analysis of modern moisture sources for eight monsoon and Indo-Pacific speleothem sites and compared these sources to modelled precipitation sources during an idealized hosing event. Speleothem $\delta^{18}O$ records at these sites have often been interpreted as the change in rainfall intensity/amount from a single system (i.e. Indian/Asian summer monsoon, Indo-Australian summer monsoon). However, analysis of modelled amount effects at each of these sites demonstrates that the amount effect is weak outside of the deep tropics. Even at some sites in the Indo-Pacific Warm Pool (i.e., Palawan, Sumatra), the amount effect explains less than 50% of the variance in $\delta^{18}O_p$. HYSPLIT back-trajectory air parcel analysis demonstrates that of the sites that have classically been interpreted using the amount effect, Sulawesi was the only site to demonstrate a strong amount effect from a single source, while other sites have multiple moisture source regions (e.g., Borneo, Flores, Ball Gown Cave). If the water vapour from these regions has different isotopic compositions, the mixing of these sources can contribute to the variance in the $\delta^{18}O_p$ at the sites. Furthermore, the proportion of contributing source regions may have changed over time.

HYSPLIT results compare well with twentieth century ModelE2-R PSDs at Dongge, Mawmluh, Gunung Buda, Palawan, and Tangga caves, but seem to underestimate the long northerly transport paths associated with the Indo-Australian monsoon at Bumi, Liang Luar, and Ball Gown Caves. Paleo-PSDs from the 0k-hosing run of ModelE-R may not be accurately reflecting source moisture changes at sites that receive modern rainfall from the Sunda Shelf (i.e. Gunung Buda, Palawan).

However, at sites less affected by topography (i.e., Mawmluh, Dongge, Tangga), paleo-PSDs indicate a weakening of monsoon pathways during hosing events, and different proportions of source moisture contributions at Dongge and Tangga Caves.

Mawmluh Cave moisture is dominated by Indian Ocean sources, though the amount effect is very weak at this site, possibly due to a time-lagged response to Bay of Bengal freshening. During hosing events, moisture sources may have become more localized. Dongge Cave displays a weak amount effect with modern moisture sources from the Indian and Pacific Oceans. The Indian source dominates during boreal summer, but during hosing events this source decreases and the Pacific source may have contributed more. Palawan has a relatively weak amount effect for the tropics with rainfall primarily arriving from the Karimata Strait during boreal summer. Pacific contributions increase during November and December. An increase in western-sourced moisture during boreal summer is observed during hosing, however this may not be reflecting changes in the observed modern moisture pathways, which weren't captured well in ModelE2-R. Topography likely played an important role in modulating past moisture pathways as the Karimata Strait would have been exposed during periods of lower sea level. As Palawan remained dry during the YD, it appears Pacific sources did not compensate for reduced Karimata Strait moisture. In contrast, Borneo, which also receives high rainfall from Karimata Strait in the modern day and has a moderately strong amount effect, may have experienced increased local and Pacific moisture compensating during the YD. Sumatra has a weak amount effect likely due to mixed source regions. The proportion of these sources is likely to have changed during hosing, when simulations indicate a reduction in monsoon pathways. Ball Gown Cave has a weak amount effect, receiving modern rainfall from many different sources. The role of past topography is unknown, but the proportion of different moisture sources arriving is likely an important factor in determining local $\delta^{18}O_p$.

Lastly, although we were unable to assess Sulawesi and Flores in the hosing experiment, there is much to infer about local hydroclimate and the amount effect at these sites. Sulawesi has a strong amount effect with the majority of its rainfall either locally or northwesterly-sourced as part of the austral summer monsoon. Past changes were likely affected by topography, but orographic barriers (i.e., mountain ranges) prevent alternate source regions from playing a major role. Flores similarly has a strong amount effect, receives its moisture from the austral summer monsoon, and is sensitive to topography; however, Indian Ocean contributions may provide an important alternate source of moisture.

This work demonstrates that a detailed understanding of modern climatology is crucial in informing paleoclimatic interpretation. It demonstrates that geographically close sites may have different dominating moisture sources. Furthermore, the study highlights changes in moisture sources that may impact $\delta^{18}O_p$ at the cave sites, including changing the transport path length or contributions from different sources. This emphasizes the importance of considering multiple transport pathways and changes in relative importance of these pathways when interpreting $\delta^{18}O$ changes in speleothems.

3.7.1 Future Directions

This work is currently being prepared for publication in *Climate of the Past* in collaboration with Allegra LeGrande and Jesse Nusbaumer at NASA GISS, Nerilie Abram at the Research School of Earth Sciences, ANU, and Sophie Lewis at the Fenner School of the Environment, ANU. In preparation for publication, there are additional changes and analyzes to be made. First, to consolidate the many data sets that have been utilized in this study, I will replace the IsoGSM amount effect analysis with data from the isotope-enabled, MERRA2-forced run of GISS ModelE2-R NINT. This new model will allow for a more direct comparison of the modern precipitation source distributions of each site with their local amount effect.

Additionally, GISS ModelE2-R is currently being run at 1 ky time slices since the Last Glacial Maximum with ice volume and topography configured for those slices. I will be comparing the PSDs and $\delta^{18}O_p$ patterns from LGM (~19 ka), Heinrich

Stadial 1 (~17 ka), and Younger Dryas (~12 ka) time slices. In particular, I am interested if small changes in topography between HS1 and the YD could be responsible for the hydroclimate sensitivity or lack thereof, at sites very near to the exposed Sunda Shelf. Likewise, I would like to compare LGM and YD PSDs to examine how the prevailing circulations in the IPWP were different. There is much debate over whether the LGM was as wet as the Holocene or if glacial aridity prevailed in the IPWP (Konecky et al., 2016).

This study was largely qualitative; HYSPLIT and PSDs allow us to examine moisture origins and relative global abundance but are not conducive to quantifying the fraction and isotopic values of waters arriving at a site from a particular source. The work presented here suggests that considering moisture source and fractionation along the moisture transport path are critical to interpreting isotopic signatures to a paleoproxy site, particularly at sites with complicated seasonality. In our future work, we will use tagged water regions based on the HYSPLIT and PSD results to quantify the isotopic signature of the waters arriving from the identified source regions in both modern and paleo-runs. This will help address assumptions of stationarity in the source regions and the amount effect over time.

References

Aggarwal, P.K., Romatschke, U., Araguas-Araguas, L., Belachew, D., Longstaffe, F.J., Berg, P., Schumacher, C., Funk, A. (2016). Proportions of convective and stratiform precipitation revealed in water isotope ratios. Nature Geoscience 9, 624. http://dx.doi.org/10.1038/Ngeo2739

Aldrian, E., Susanto, R.D. (2003). Identification of three dominant rainfall regions within Indonesia and their relationship to sea surface temperature. International Journal of Climatology 23, 1435-1452. http://dx.doi.org/10.1002/joc.950

Ayliffe, L.K., Gagan, M.K., Zhao, J.-x., Drysdale, R.N., Hellstrom, J.C., Hantoro, W.S., Griffiths, M.L., Scott-Gagan, H., Pierre, E.S., Cowley, J.A., Suwargadi, B.W. (2013). Rapid interhemispheric climate links via the Australasian monsoon during the last deglaciation. Nature Communications 4, 2908. http://dx.doi.org/10.1038/ncomms3908

Baker, A.J., Sodemann, H., Baldini, J.U.L., Breitenbach, S.F.M., Johnson, K.R., van Hunen, J., Zhang, P. (2015). Seasonality of westerly moisture transport in the East Asian summer monsoon and its implications for interpreting

precipitation $\delta^{18}O$. Journal of Geophysical Research: Atmospheres 120, 5850-5862. http://dx.doi.org/10.1002/2014JD022919

Belgaman, H.A., Ichiyanagi, K., Suwarman, R., Tanoue, M., Aldrian, E., Utami, A.I.D., Kusumaningtyas, S.D.A. (2017). Characteristics of seasonal precipitation isotope variability in Indonesia. Hydrological Research Letters 11, 92-98. http://dx.doi.org/10.3178/hrl.11.92

Berkelhammer, M., Sinha, A., Mudelsee, M., Cheng, H., Yoshimura, K., Biswas, J. (2013). On the low frequency component of the ENSO-Indian Monsoon relationship; a paired proxy perspective. Clim. Past Discuss. 9, 3103-3123. http://dx.doi.org/10.5194/cp-10-733-2014

Berkelhammer, M., Sinha, A., Stott, L., Cheng, H., Pausata, F.S.R., Yoshimura, K. (2012). An Abrupt Shift in the Indian Monsoon 4000 Years Ago, Climates, Landscapes, and Civilizations. AGU, Washington, DC, pp. 75-87.

Breitenbach, S.F.M., Adkins, J.F., Meyer, H., Marwan, N., Kumar, K.K., Haug, G.H. (2010). Strong influence of water vapor source dynamics on stable isotopes in precipitation observed in Southern Meghalaya, NE India. Earth and Planetary Science Letters 292, 212-220. http://dx.doi.org/10.1016/j.epsl.2010.01.038

Carolin, S.A., Cobb, K.M., Adkins, J.F., Clark, B., Conroy, J.L., Lejau, S., Malang, J., Tuen, A.A. (2013). Varied response of western Pacific hydrology to climate forcings over the last glacial period. Science 340, 1564-1566. http://dx.doi.org/10.1126/science.1233797

Carolin, S.A., Cobb, K.M., Lynch-Stieglitz, J., Moerman, J.W., Partin, J.W., Lejau, S., Malang, J., Clark, B., Tuen, A.A., Adkins, J.F. (2016). Northern Borneo stalagmite records reveal West Pacific hydroclimate across MIS 5 and 6. Earth and Planetary Science Letters 439, 182-193. http://dx.doi.org/10.1016/j.epsl.2016.01.028

Cobb, K.M., Adkins, J.F., Partin, J.W., Clark, B. (2007). Regional-scale climate influences on temporal variations of rainwater and cave dripwater oxygen isotopes in northern Borneo. Earth and Planetary Science Letters 263, 207-220. http://dx.doi.org/10.1016/j.epsl.2007.08.024

Cross, M. (2015). PySPLIT: a Package for the Generation, Analysis, and Visualization of HYSPLIT Air Parcel Trajectories.

Cruz, F.W., Burns, S.J., Karmann, I., Sharp, W.D., Vuille, M., Cardoso, A.O., Ferrari, J.A., Silva Dias, P.L., Viana, O. (2005). Insolation-driven changes in atmospheric circulation over the past 116,000 years in subtropical Brazil. Nature 434, 63-66. http://dx.doi.org/10.1038/nature03365

Dansgaard, W. (1964). Stable isotopes in precipitation. Tellus 16, 436-468.

Dayem, K.E., Molnar, P., Battisti, D.S., Roe, G.H. (2010). Lessons learned from oxygen isotopes in modern precipitation applied to interpretation of speleothem records of paleoclimate from eastern Asia. Earth and Planetary Science Letters 295, 219-230. http://dx.doi.org/10.1016/j.epsl.2010.04.003

Denniston, R.F., Asmerom, Y., Lachniet, M., Polyak, V.J., Hope, P., An, N., Rodzinyak, K., Humphreys, W.F. (2013a). A Last Glacial Maximum through middle Holocene stalagmite record of coastal Western Australia climate.

Quaternary Science Reviews 77, 101-112. http://dx.doi.org/10.1016/j.quascirev.2013.07.002

Denniston, R.F., Wyrwoll, K.-H., Asmerom, Y., Polyak, V.J., Humphreys, W.F., Cugley, J., Woods, D., LaPointe, Z., Peota, J., Greaves, E. (2013b). North Atlantic forcing of millennial-scale Indo-Australian monsoon dynamics during the Last Glacial period. Quaternary Science Reviews 72, 159-168. http://dx.doi.org/10.1016/j.quascirev.2013.04.012

Draxler, R.R., Hess, G.D. (1997), Description of the HYSPLIT_4 modeling system, NOAA Tech. Memo. ERL ARL-224. NOAA, Silver Spring, MD, p. 24.

Dutt, S., Gupta, A.K., Clemens, S.C., Cheng, H., Singh, R.K., Kathayat, G., Edwards, R.L. (2015). Abrupt changes in Indian summer monsoon strength during 33,800 to 5500 years B.P. Geophysical Research Letters 42, 5526-5532. http://dx.doi.org/10.1029/2012GM001207

Dykoski, C.A., Edwards, R.L., Cheng, H., Yuan, D., Cai, Y., Zhang, M., Lin, Y., Qing, J., An, Z., Revenaugh, J. (2005). A high-resolution, absolute-dated Holocene and deglacial Asian monsoon record from Dongge Cave, China. Earth and Planetary Science Letters 233, 71-86. http://dx.doi.org/10.1016/j.epsl.2005.01.036

Gentilli, J. (1971), Climates of Australia and New Zealand. Elsevier Pub. Co.

Gibbons, F.T., Oppo, D.W., Mohtadi, M., Rosenthal, Y., Cheng, J., Liu, Z., Linsley, B.K. (2014). Deglacial $\delta^{18}O$ and hydrologic variability in the tropical Pacific and Indian Oceans. Earth and Planetary Science Letters 387, 240-251. http://dx.doi.org/10.1016/j.epsl.2013.11.032

Griffiths, M.L., Drysdale, R.N., Gagan, M.K., Zhao, J.-x., Ayliffe, L.K., Hellstrom, J.C., Hantoro, W.S., Frisia, S., Feng, Y.-X., Cartwright, I., St. Pierre, E.J., Fischer, M.J., Suwargadi, B.W. (2009). Increasing Australian-Indonesian monsoon rainfall linked to early Holocene sea-level rise. Nature Geoscience 2, 636-639. http://dx.doi.org/10.1038/Ngeo605

Griffiths, M.L., Kimbrough, A.K., Gagan, M.K., Drysdale, R.N., Cole, J.E., Johnson, K.R., Zhao, J.-X., Cook, B.I., Hellstrom, J.C., Hantoro, W.S. (2016). Western Pacific hydroclimate linked to global climate variability over the past two millennia. Nature Communications 7, 11719. http://dx.doi.org/10.1038/ncomms11719

Hanebuth, T.J.J., Voris, H.K., Yokoyama, Y., Saito, Y., Okuno, J.i. (2011). Formation and fate of sedimentary depocentres on Southeast Asia's Sunda Shelf over the past sea-level cycle and biogeographic implications. Earth-Science Reviews 104, 92-110. http://dx.doi.org/10.1016/j.earscirev.2010.09.006

Hendy, C.H. (1971). The isotopic geochemistry of speleothems—I. The calculation of the effects of different modes of formation on the isotopic composition of speleothems and their applicability as palaeoclimatic indicators. Geochimica et Cosmochimica Acta 35, 801-824.

Kalnay, E., Kanamitsu, M., Kistler, R., Collins, W., Deaven, D., Gandin, L., Iredell, M., Saha, S., White, G., Woollen, J., Zhu, Y., Leetmaa, A., Reynolds, R., Chelliah, M., Ebisuzaki, W., Higgins, W., Janowiak, J., Mo, K.C., Ropelewski, C., Wang, J., Jenne, R., Joseph, D. (1996). The NCEP/NCAR 40-Year Reanalysis Project.

Bulletin of the American Meteorological Society 77, 437-471. http://dx.doi.org/10.1175/1520-0477(1996)077<0437:Tnyrp>2.0.Co;2

Kimbrough, A.K. (2016), The glacial-interglacial monsoon recorded by stalgmites from Southwest Sulawesi, Research School of Earth Sciences. Australian National University.

Konecky, B., Russell, J., Bijaksana, S. (2016). Glacial aridity in central Indonesia coeval with intensified monsoon circulation. Earth and Planetary Science Letters 437, 15-24. http://dx.doi.org/10.1016/j.epsl.2015.12.037

Krause, C.E. (2015), Reconstructing the Australasian monsoon over the last 40,000 years using speleothems and palaeoclimate modelling, Research School of Earth Sciences. Australian National University, Canberra, Australia.

Kurita, N., Ichiyanagi, K., Matsumoto, J., Yamanaka, M.D. (2009). The relationship between the isotopic content of precipitation and the precipitation amount in tropical regions. Journal of geochemical exploration 102, 113-122. http://dx.doi.org/10.1016/j.gexplo.2009.03.002

LeGrande, A.N., Schmidt, G.A. (2006). Global gridded data set of the oxygen isotopic composition in seawater. Geophysical Research Letters 33, L12604. http://dx.doi.org/10.1029/2006gl026011

Lewis, S.C., Gagan, M.K., Ayliffe, L.K., Zhao, J.-x., Hantoro, W.S., Treble, P.C., Hellstrom, J.C., LeGrande, A.N., Kelley, M., Schmidt, G.A., Suwargadi, B.W. (2011). High-resolution stalagmite reconstructions of Australian-Indonesian monsoon rainfall variability during Heinrich stadial 3 and Greenland interstadial 4. Earth and Planetary Science Letters 303, 133-142. http://dx.doi.org/10.1016/j.epsl.2010.12.048

Lewis, S.C., LeGrande, A.N., Kelley, M., Schmidt, G.A. (2010). Water vapour source impacts on oxygen isotope variability in tropical precipitation during Heinrich events. Climate of the Past 6, 325-343. http://dx.doi.org/10.5194/cp-6-325-2010

Lewis, S.C., LeGrande, A.N., Kelley, M., Schmidt, G.A. (2013). Modeling insights into deuterium excess as an indicator of water vapor source conditions. Journal of Geophysical Research: Atmospheres 118, 243-262. http://dx.doi.org/10.1029/2012jd017804

Li, X., Zhou, W., Chen, Y.D. (2016). Detecting the origins of moisture over southeast China: Seasonal variation and heavy rainfall. Advances in Atmospheric Sciences 33, 319-329. http://dx.doi.org/10.1007/s00376-015-4197-5

Linsley, B.K., Wu, H.C., Rixen, T., Charles, C.D., Gordon, A.L., Moore, M.D. (2017). SPCZ zonal events and downstream influence on surface ocean conditions in the Indonesian Throughflow region. Geophysical Research Letters 44, 293-303. http://dx.doi.org/10.1002/2016gl070985

Liu, Z., Wen, X., Brady, E.C., Otto-Bliesner, B., Yu, G., Lu, H., Cheng, H., Wang, Y., Zheng, W., Ding, Y., Edwards, R.L., Cheng, J., Liu, W., Yang, H. (2014). Chinese cave records and the East Asia Summer Monsoon. Quaternary Science Reviews 83, 115-128. http://dx.doi.org/10.1016/j.quascirev.2013.10.021

Maher, B.A., Thompson, R. (2012). Oxygen isotopes from Chinese caves: records not of monsoon rainfall but of circulation regime. Journal of Quaternary Science 27, 615-624. http://dx.doi.org/10.1002/jqs.2553

Moerman, J.W., Cobb, K.M., Adkins, J.F., Sodemann, H., Clark, B., Tuen, A.A. (2013). Diurnal to interannual rainfall $\delta^{18}O$ variations in northern Borneo driven by regional hydrology. Earth and Planetary Science Letters 369–370, 108-119. http://dx.doi.org/10.1016/j.epsl.2013.03.014

Mohtadi, M., Prange, M., Oppo, D.W., De Pol-Holz, R., Merkel, U., Zhang, X., Steinke, S., Luckge, A. (2014). North Atlantic forcing of tropical Indian Ocean climate. Nature 509, 76-80. http://dx.doi.org/10.1038/nature13196

Murata, F., Hayashi, T., Matsumoto, J., Asada, H. (2007). Rainfall on the Meghalaya plateau in northeastern India—one of the rainiest places in the world. Natural Hazards 42, 391-399. http://dx.doi.org/10.1007/s11069-006-9084-z

Partin, J.W., Cobb, K.M., Adkins, J.F., Clark, B., Fernandez, D.P. (2007). Millennial-scale trends in west Pacific warm pool hydrology since the Last Glacial Maximum. Nature 449, 452-455. http://dx.doi.org/10.1038/nature06164

Partin, J.W., Quinn, T.M., Shen, C.C., Okumura, Y., Cardenas, M.B., Siringan, F.P., Banner, J.L., Lin, K., Hu, H.M., Taylor, F.W. (2015). Gradual onset and recovery of the Younger Dryas abrupt climate event in the tropics. Nature Communications 6, 8061. http://dx.doi.org/10.1038/ncomms9061

Pausata, F.S.R., Battisti, D.S., Nisancioglu, K.H., Bitz, C.M. (2011). Chinese stalagmite $\delta^{18}O$ controlled by changes in the Indian monsoon during a simulated Heinrich event. Nature Geoscience 4, 474-480. http://dx.doi.org/10.1038/ngeo1169

Risi, C., Bony, S., Vimeux, F. (2008). Influence of convective processes on the isotopic composition ($\delta^{18}O$ and δD) of precipitation and water vapor in the tropics: 2. Physical interpretation of the amount effect. Journal of Geophysical Research: Atmospheres 113, D19306. http://dx.doi.org/10.1029/2008JD009943

Rozanski, K., Araguás-Araguás, L., Gonfiantini, R. (1993). Isotopic patterns in modern global precipitation, Climate Change in Continental Isotopic Records. American Geophysical Union, pp. 1-36.

Sathiamurthy, E., Voris, H.K. (2006). Maps of Holocene sea level transgression and submerged lakes on the Sunda Shelf. The Natural History Journal of Chulalongkorn University, Supplement 2, 1-43.

Schmidt, G.A., Kelley, M., Nazarenko, L., Ruedy, R., Russell, G.L., Aleinov, I., Bauer, M., Bauer, S.E., Bhat, M.K., Bleck, R., Canuto, V., Chen, Y.-H., Cheng, Y., Clune, T.L., Del Genio, A., de Fainchtein, R., Faluvegi, G., Hansen, J.E., Healy, R.J., Kiang, N.Y., Koch, D., Lacis, A.A., LeGrande, A.N., Lerner, J., Lo, K.K., Matthews, E.E., Menon, S., Miller, R.L., Oinas, V., Oloso, A.O., Perlwitz, J.P., Puma, M.J., Putman, W.M., Rind, D., Romanou, A., Sato, M., Shindell, D.T., Sun, S., Syed, R.A., Tausnev, N., Tsigaridis, K., Unger, N., Voulgarakis, A., Yao, M.-S., Zhang, J. (2014). Configuration and assessment of the GISS ModelE2 contributions to the CMIP5 archive. Journal of Advances in Modeling Earth Systems 6, 141-184. http://dx.doi.org/10.1002/2013ms000265

Schumacher, C., Houze Jr., R.A. (2003). Stratiform rain in the tropics as seen by the TRMM precipitation radar. Journal of Climate 16, 1739-1756. http://dx.doi.org/10.1175/1520-0442(2003)016<1739:Sritta>2.0.Co;2

Shakun, J.D., Burns, S.J., Fleitmann, D., Kramers, J., Matter, A., Al-Subary, A. (2007). A high-resolution, absolute-dated deglacial speleothem record of Indian Ocean climate from Socotra Island, Yemen. Earth and Planetary Science Letters 259, 442-456. http://dx.doi.org/10.1016/j.epsl.2007.05.004

Sinha, A., Kathayat, G., Cheng, H., Breitenbach, S.F.M., Berkelhammer, M., Mudelsee, M., Biswas, J., Edwards, R.L. (2015). Trends and oscillations in the Indian summer monsoon rainfall over the last two millennia. Nature Communications 6, 6309. http://dx.doi.org/10.1038/ncomms7309

Stager, J.C., Ryves, D.B., Chase, B.M., Pausata, F.S.R. (2011). Catastrophic Drought in the Afro-Asian Monsoon Region During Heinrich Event 1. Science 331, 1299-1302. http://dx.doi.org/10.1126/science.1198322

Stein, A.F., Draxler, R.R., Rolph, G.D., Stunder, B.J.B., Cohen, M.D., Ngan, F. (2015). NOAA's HYSPLIT Atmospheric Transport and Dispersion Modeling System. Bulletin of the American Meteorological Society 96, 2059-2077. http://dx.doi.org/10.1175/BAMS-D-14-00110.1

Wang, X., Auler, A.S., Edwards, R.L., Cheng, H., Ito, E., Wang, Y., Kong, X., Solheid, M. (2007). Millennial-scale precipitation changes in southern Brazil over the past 90,000 years. Geophysical Research Letters 34, L23701. http://dx.doi.org/10.1029/2007gl031149

Wurtzel, J.B., Abram, N.J., Lewis, S.C., Bajo, P., Hellstrom, J.C., Troitzsch, U., Heslop, D. (2018). Tropical Indo-Pacific hydroclimate response to North Atlantic forcing during the last deglaciation as recorded by a speleothem from Sumatra, Indonesia. Earth and Planetary Science Letters 492, 264-278. http://dx.doi.org/10.1016/j.epsl.2018.04.001

Wurtzel, J.B., Abram, N.J., Lewis, S.C., Nusbaumer, J., LeGrande, A.N. (in prep). Indo-Pacific moisture source variability from proxies, models and observations. Climate of the Past.

Wyrwoll, K.-H., Miller, G.H. (2001). Initiation of the Australian summer monsoon 14,000 years ago. Quaternary International 83–85, 119-128. http://dx.doi.org/10.1016/S1040-6182(01)00034-9

Xie, P., Arkin, P.A. (1997). Global precipitation: A 17-year monthly analysis based on gauge observations, satellite estimates, and numerical model outputs. Bulletin of the American Meteorological Society 78, 2539-2558. http://dx.doi.org/10.1175/1520-0477(1997)078<2539:Gpayma>2.0.Co;2

Yang, H., Johnson, K.R., Griffiths, M.L., Yoshimura, K. (2016). Interannual controls on oxygen isotope variability in Asian monsoon precipitation and implications for paleoclimate reconstructions. Journal of Geophysical Research: Atmospheres 121, n/a-n/a. http://dx.doi.org/10.1002/2015jd024683

Yang, X., Liu, J., Liang, F., Yuan, D., Yang, Y., Lu, Y., Chen, F. (2014). Holocene stalagmite δ18O records in the East Asian monsoon region and their correlation with those in the Indian monsoon region. The Holocene 24, 1657-1664. http://dx.doi.org/10.1177/0959683614551222

Yoshimura, K., Kanamitsu, M., Noone, D., Oki, T. (2008). Historical isotope simulation using Reanalysis atmospheric data. Journal of Geophysical

Research: Atmospheres 113, n/a-n/a. http://dx.doi.org/10.1029/2008jd010074

Yuan, D., Cheng, H., Edwards, R.L., Dykoski, C.A., Kelly, M.J., Zhang, M., Qing, J., Lin, Y., Wang, Y., Wu, J., Dorale, J.A., An, Z., Cai, Y. (2004). Timing, Duration, and Transitions of the Last Interglacial Asian Monsoon. Science 304, 575-578. http://dx.doi.org/10.1126/science.1091220

Zhou, X., Sun, L., Chu, Y., Xia, Z., Zhou, X., Li, X., Chu, Z., Liu, X., Shao, D., Wang, Y. (2016). Catastrophic drought in East Asian monsoon region during Heinrich event 1. Quaternary Science Reviews 141, 1-8. http://dx.doi.org/10.1016/j.quascirev.2016.03.029

4 Aragonite-calcite speleothem petrography and geochemistry

4.1 Introduction

Speleothems are secondary cave deposits that most commonly precipitate as either calcite or the metastable $CaCO_3$ polymorph, aragonite (Hill and Forti, 1997). Most paleoclimatic reconstructions use calcite stalagmites because aragonite is thermodynamically unstable and therefore subject to variable post-depositional alteration to calcite (Finch et al., 2001; Frisia et al., 2002). U/Th dating and interpretation of isotopes and trace elements becomes ambiguous in secondary calcite because the transformation takes place in an open system (Bajo et al., 2016; Frisia et al., 2002; Lachniet et al., 2012). However, if no diagenetic alteration has taken place, aragonite speleothems can be robust archives for paleoclimatic studies, in part due to their high uranium concentrations, providing the opportunity for excellent age models with small uncertainties (Zhang et al., 2013). As stable aragonite can persist indefinitely, aragonitic speleothems have already been successfully employed in paleo-reconstructions (Cosford et al., 2008; Li et al., 2011a).

Aragonite stalagmites tend to form during slow drip rates and when the aqueous Mg/Ca value is greater than unity (Frisia et al., 2002). As such, aragonite usually precipitates from Mg-rich dolomitic host rocks rather than limestone (Railsback et al., 1994). Because enhanced Mg values often result from dry conditions associated with increased evaporation, it is thought that the presence of aragonite can represent paleoaridity (Frisia et al., 2002). On intra-annual timescales, aragonite-calcite laminae couplets have been shown to correspond to dry and wet seasons, respectively (Railsback et al., 1994). Recent field experiments have shown that aragonite precipitation is favoured by high Mg/Ca ratios in the fluid (>0.5), high fluid pH (>8.2), low calcite saturation (<0.8), and slow drip rates (Riechelmann et al., 2014). When seepage waters contain Mg/Ca ratios on the order of >2.4, aragonite is the only stable carbonate phase.

Studies of the isotopic fractionation offset between calcite and aragonite are limited and based primarily on experimental studies (Kim et al., 2007; Tarutani et al., 1969). At 25 °C under equilibrium conditions, experimental and theoretical studies of synthetic calcite-aragonite transitions have predicted that aragonite should have $\delta^{18}O$ values 0.6 – 0.8 ‰ higher than calcite (Kim et al., 2007; Tarutani et al., 1969). Measured values from aragonitic coralline sponges (Böhm et al., 2000), other biogenic aragonite (Grossman and Ku, 1986), and co-precipitating cave calcite and aragonite (Frisia et al., 2002), indicate a potential fractionation offset range of 0.6 – 1.4 ‰ though offsets less than 1‰ are more commonly reported.

The few climate reconstruction studies featuring both aragonite and calcite speleothems apply a range of $\delta^{18}O$ corrections between 0.6 and 1.0‰ (Denniston et al., 2013; Holmgren et al., 2003; Kotlia et al., 2014). Most of these studies are either comparing separate aragonite and calcite specimens or a single section of aragonite within a calcite speleothem. In one case, the sample contained a mixture of co-precipitated aragonite and calcite as identified by Raman spectroscopy and XRD, and was corrected according to the mineral fraction (Holzkämper et al., 2009). In the case of Wurtzel et al. (2018), aragonite and calcite did not co-precipitate, but interlayering was sufficiently abrupt that the 0.5 mm resolution stable isotope samples could contain material from both phases.

Studies of trace elements in speleothems often focus on trace elements that are incorporated into calcite through substitution for the Ca^{2+} cation in the $CaCO_3$ structure by divalent ions such as Mg^{2+}, Sr^{2+}, and Ba^{2+} (Fairchild and Treble, 2009). Though trace elements can also be incorporated through the occlusion of particulates into the crystal lattice, and by adsorption onto the crystal surface, the method of cation exchange is the most easily quantified (Gascoyne, 1983). The ratio of trace element to calcium in the carbonate (Tr/Ca_{CaCO3}) can be described by the concentration of the trace element in the fluid solution ($Tr/Ca_{solution}$) and the distribution coefficient (D_{Tr})(Gascoyne, 1983; Morse and Bender, 1990), such that:

$$D_{Tr} = \frac{(^{Tr}/_{\mathrm{Ca}})_{\mathrm{CaCO_3}}}{(^{Tr}/_{\mathrm{Ca}})_{\mathrm{solution}}} \quad (1)$$

The relative trace element abundance in the fluid ($Tr/\mathrm{Ca_{solution}}$) can also vary due to environmental parameters (i.e., precipitation, vegetation, prior calcite precipitation) in and above the cave, and D_{Tr} can vary with physical parameters (i.e., temperature, growth rate, mineralogy) (Fairchild and Treble, 2009; Finch et al., 2001).

Calcite partition coefficients are significantly better quantified than those for aragonite. The temperature dependence of D_{Mg} into calcite is well-established. However, annual temperature in the cave environment is relatively constant (McDermott, 2004) and though tropical glacial temperatures may have been 3-4 °C below present (Mohtadi et al., 2014), this temperature change has a negligible effect on D_{Mg} with respect to dripwater concentration (Day and Henderson, 2013). This means that as a general rule, Mg/Ca values in carbonate are principally a function of the Mg concentration of the dripwater solution (Gascoyne, 1983; Johnson et al., 2006). Mechanisms proposed to explain Mg variations in cave dripwaters include increased residence time for dolomite dissolution and prior calcite precipitation (PCP), which would also affect Sr and Ba ratios, because all three have partition coefficients << 1 for calcite. Prior calcite precipitation refers to the precipitation of calcite prior to the dripwater reaching the speleothem, and its enhanced occurrence has oft been linked to drier conditions (Fairchild et al., 2000; Johnson et al., 2006; McMillan et al., 2005).

Mineralogical effects become extremely important when working with a calcite-aragonite speleothem. The major difference between calcite and aragonite is within their crystallographic structures (trigonal versus orthorhombic); the difference in the D_{Tr} between aragonite and calcite can be described in terms of ionic theory (Finch et al., 2001). While aragonite tends to form from solutions with high Mg/Ca concentrations, little Mg^{2+} is included in aragonite because its ionic radius is much smaller than the Ca^{2+}cation site in aragonite (Fairchild and Baker, 2012). Accordingly, Mg^{2+} is more stable in the calcite structure, while Ba^{2+} and Sr^{2+},

which have larger ionic radii than Ca^{2+}, are more stable within the aragonite lattice (Finch et al., 2001). This relationship emphasizes the importance of considering prior aragonite precipitation (PAP) as a potential controlling factor on elemental concentrations, since D_{Sr} and D_{Ba} are much closer to unity in aragonite (Fairchild and Treble, 2009). Whereas the effect of PCP on trace element concentrations has been the subject of multiple studies (Huang and Fairchild, 2001; Johnson et al., 2006; Sinclair et al., 2012), PAP has only recently been formally documented (Wassenburg et al., 2012; Wassenburg et al., 2013).

Interpreting the relationship between climate variability and trace element concentrations in speleothems relies on understanding the environmental controls on dripwater concentrations, and the thermodynamic and kinetic controls on distribution coefficients between the dripwater and speleothems. Attempts to quantify $D_{Tr(Cc)}$ over the previous few decades have used karst analogue laboratory experiments (Gascoyne, 1983; Huang and Fairchild, 2001; Tesoriero and Pankow, 1996), however only recently have attempts been made to quantify $D_{Tr(Ar)}$ in a natural karst setting (Jamieson et al., 2016; Wassenburg et al., 2016).

In addition to the substitution of divalent ions, elements may also be incorporated into carbonate by occlusion of particulates in between growing crystals or by adsorption onto the surface of growing crystals (Gascoyne, 1983). These processes are not as well-studied as substitution, and their incorporation into calcite speleothems is still being deciphered, with aragonite lagging even further behind. Phosphorous (P), for example, is thought to enter the speleothem through adsorption of the phosphate ion (PO_4^{3-}) onto the carbonate surface (Fairchild and Treble, 2009; Meyer, 1984). The source of the phosphate may be from vegetation decay at the surface or soil processes (Huang et al., 2001; Treble et al., 2003). Uranium (U), like P, may also be incorporated by scavenging from solution, possibly due to the strong affinity between phosphate and uranyl ions (UO_2^{2+}) (Johnson et al., 2006). U enters solution as large uranyl ions, which are relatively more stable within aragonite's orthorhombic crystal lattice, leading to preferential uptake by aragonite (Ortega et al., 2005). It is unclear whether the mechanism of

incorporation is by adsorption, occlusion, or direct substitution of non-divalent ions (Reeder et al., 2000). Sodium (Na), on the other hand, is likely incorporated via occlusion into crystal defect sites, and may be related to fluid salinity (Fairchild et al., 2001). Likewise, manganese (Mn) and aluminum (Al) may enter the speleothem through occlusion as particles or colloids in the dripwater and increase with increased filtration (Zhou et al., 2008). Divalent manganese (Mn^{2+}) can also substitute into the crystal lattice, but covariance with Al suggests a particulate source (Zhou et al., 2008).

This chapter will present multiproxy data from a unique speleothem specimen containing frequent transitions between primary aragonite and primary calcite that occur on timescales greater than seasonal. I compare this record to a second speleothem sample principally composed of calcite, which grew concurrently in the same cave. The replicate record is used to estimate the oxygen isotope fractionation offset between aragonite and calcite. High-resolution trace element data is used to estimate aragonite distribution coefficients for four commonly used trace elements and I discuss controls on trace element variability from an environmental hydrology context. Bedrock analysis, trace elements, and thin section petrography suggest that bio-mediation and karst hydrology are the main controls on the precipitation of aragonite or calcite.

4.2 Setting

4.2.1 Tangga Cave

Tangga Cave is located in the Barisan Mountains of central West Sumatra, Indonesia (0°21'S, 100°45'E, 600 m). The caves in this region lie within a Lower Carboniferous to Mid-Permian limestone member of the Kuantan Formation (Barber et al., 2005) (Figure 4.1). The limestone-dominated formation is interbedded with quartzites, slates, phyllites, and siliceous shales (Silitonga and Kastowo, 1995). The limestone member overlies a shale and phyllite member, containing intercalations of quartzite, siltstone, chert and lava flows. Though not specifically documented, the presence of aragonite suggests dolomite may be

present (Railsback et al., 1994). The entrance to Tangga Cave is at the base of a sinkhole covered with jungle vegetation. The cave narrows considerably ~50m from the entrance, and descends steeply to a lower level with an underground river passage (Figure 4.2).

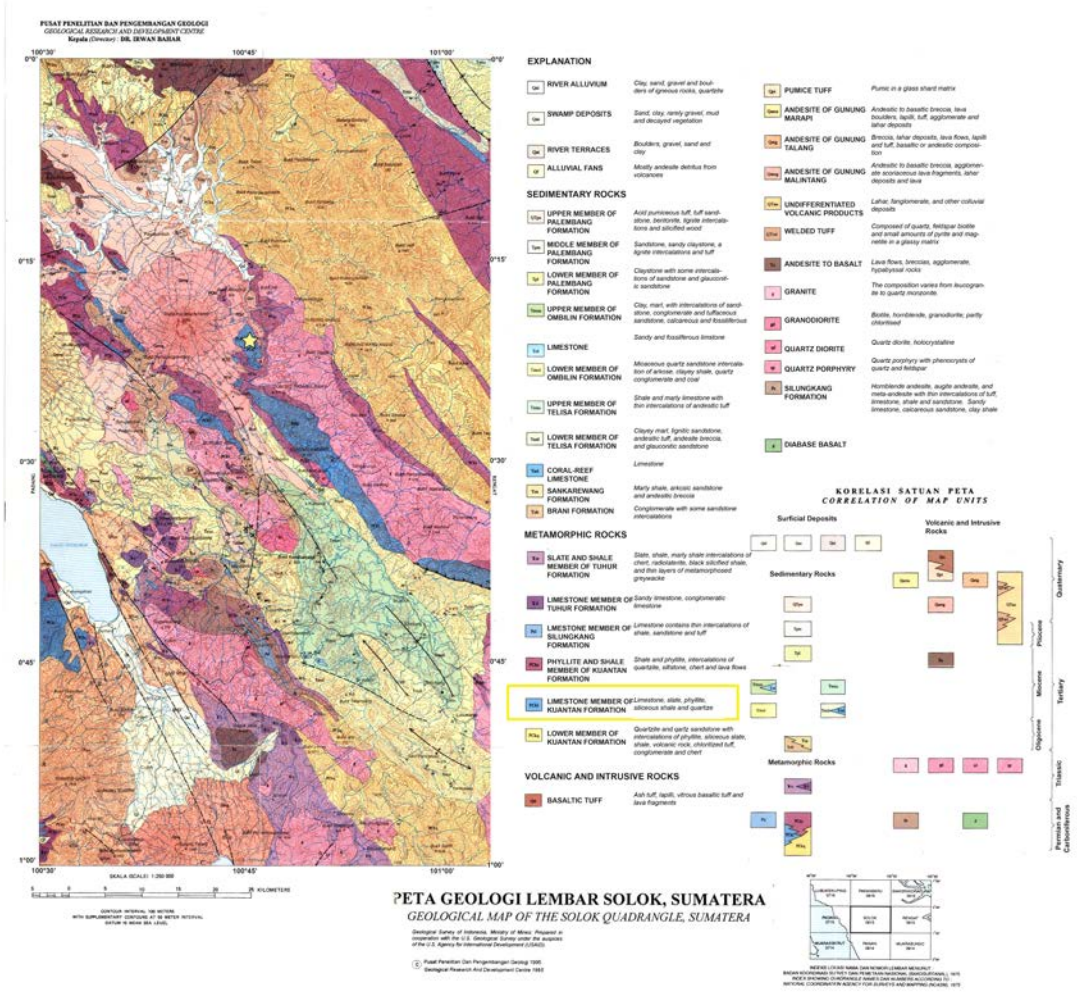

Figure 4.1 – Geologic map of Solok Quadrangle, Sumatra. Cave site is marked by star and lies within the Limestone Member of the Kuantan formation (yellow rectangle). Modified from Silitonga and Kastowo, 1995.

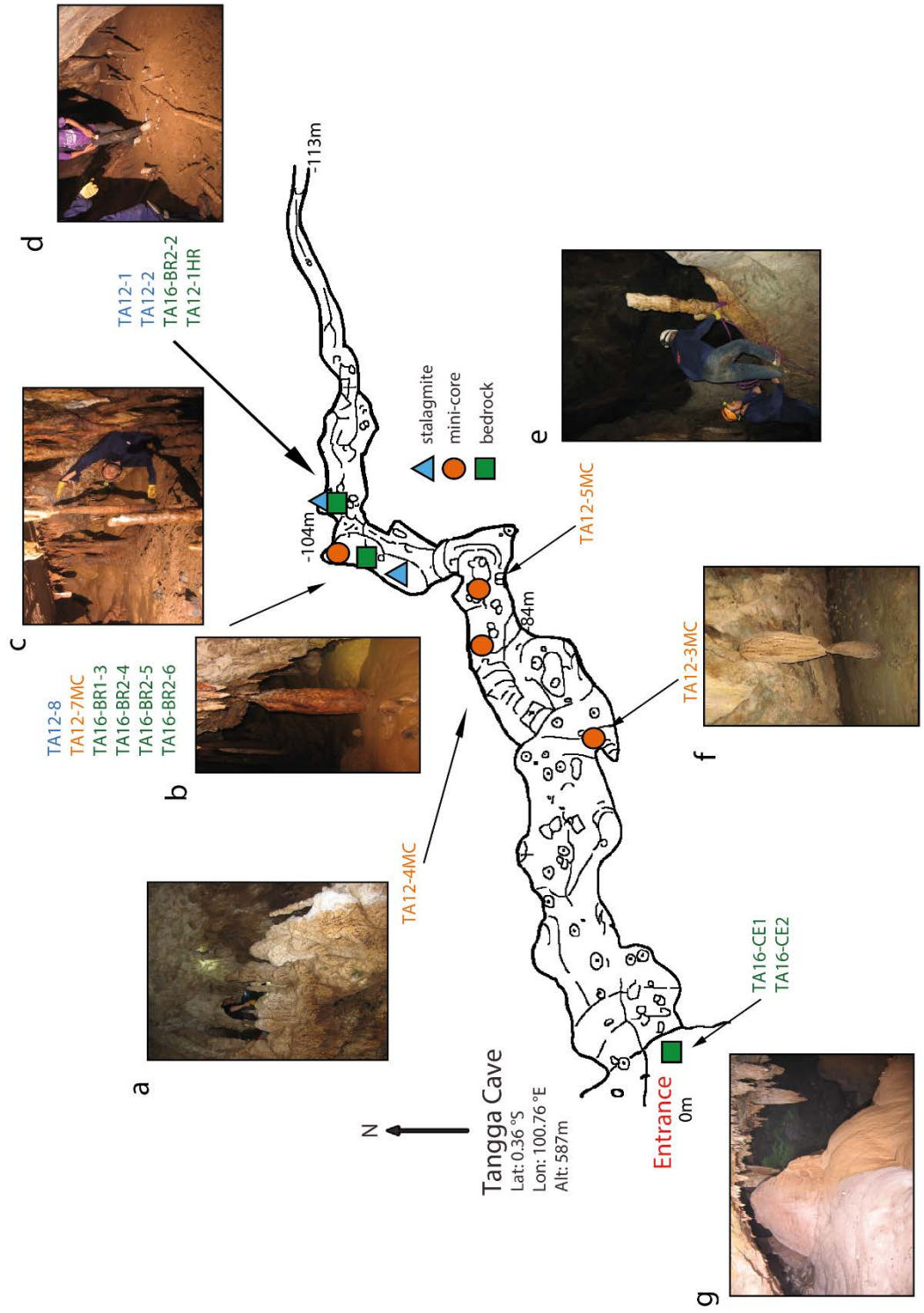

Figure 4.2 – Cave map with photographs (a-g) taken from different sections of the cave. Symbols indicate the position of collection sites for samples. (a) Location of ledge where minicore 4MC was collected; (b) Stalagmite from which 7MC was collected; (c) chamber where TA12-8 was found toppled; (d) chamber where TA12-1 and TA12-2 were found toppled; (e) stalagmite from which 5MC was collected; (f) stalagmite from which 3MC was collected (g) cave entrance looking outwards from inside of cave

4.2.2 Samples

Three stalagmites were used for this study, along with eight bedrock samples and four mini-cores collected from inside Tangga Cave, using methods described in Scroxton et al. (2016) (Figure 4.2). Mini-cores TA12-3MC, 4MC, and 5MC were collected from stalagmites ~60, 86, and 90 m into Tangga Cave. TA12-8 was found in a low passage way above the river ~95 m into the cave. TA12-7MC was collected from a stalagmite further into this same chamber. Stalagmites TA12-1 and TA12-2 were collected from a small chamber located ~105 m from the cave entrance. Both stalagmites were found toppled, and TA12-1 was found in 7 pieces. Two bedrock samples were collected from the cave entrance, an additional four bedrock samples are from the same chamber as TA12-8, and one sample is from the same chamber as TA12-1 and TA12-2. Bedrock samples were collected as loose rocks from the ground or chiseled from the wall and ceiling of the cave chambers.

4.3 Methods

4.3.1 XRD

X-ray diffraction (XRD) was performed on speleothem and bedrock samples to determine composition and calcite Mg-content (Table 4.1). XRD was carried out at the Australian National University using a SIEMENS D501 Bragg-Brentano diffractometer using CuKα radiation and a SIEMENS D5005 Bragg-Brentano diffractometer using CoKα radiation. Both instruments are equipped with a graphite monochromator and scintillation detector. On the D501, the scan range was up to 2 to 70° 2θ, at a step width of 0.02°, and a scan speed of 1° per 60 s. On the D5005, the scan range was 4 to 84° 2θ, at a step width of 0.04°, and a scan speed of 1° per 100 s.

Table 4.1 - List of samples analyzed by XRD

Sample ID	Location in cave	Sample description	Composition[+]	Calcite Unit cell length[^]	$MgCaCO_3$ mol%
Stalagmites					
TA12-1-7	106 m	Scraped from central axis to outside	Aragonite small amount of 6mol% Mg-calcite		
TA12-2g-calc	106 m	used motorized drill to create groove in calcite layer	100% 6.4mol% Mg-calcite	unit a:4.9731 unit c: 16.9825	3.2±0.5 mol% $MgCaCO_3$
TA12-8-lB3	95 m	Low-res (1cm bulk) powder	100% 6.4% Mg-calcite	unit a:4.9732 unit c: 16.9925	3.2±0.2 mol% $MgCaCO_3$
Minicores					
TA12-3MC-4	60 m	scraped outside of inner most piece of mini core	99.8% 2mol% Mg-calcite 0.2% aragonite	unit a: 4.983 unit c: 17.0361	1.3±0.2 mol% $MgCaCO_3$
TA12-4MC-2	86 m	scraped outside of inner most piece of mini core	100% calcite	unit a: 4.9869 unit c: 17.0544	0.5±0.1 mol% $MgCaCO_3$
TA12-5MC-2	90 m	scraped outside of inner most piece of mini core	92.6% calcite 7.4% aragonite	unit a:4.9818 unit c: 17.0254	1.6±0.3 mol% $MgCaCO_3$
TA12-7MC-2	100 m	scraped outside of inner most piece of mini core	100% calcite	unit a:4.9765 unit c: 17.0099	2.4±0.2 mol% $MgCaCO_3$
Hostrock					
TA12-1HR		scraped dark patch from base of TA12-1-7	Quartz, clinochlore (chlorite), 6.4mol% Mg-calcite, fluorapatite		
TA16-BR1-3	Same room as TA12-8	black rock from ceiling	Quartz, mica (illite, biotite, muscovite), clays (chlorite), biotite, microcline (K-feldspar), trace amounts of plagioclase		
TA16-BR2-2	Same room as TA12-1/2	Grey with red veins from ceiling	Dolomite, some quartz, trace calcite		

Table 4.1 (con't) - List of samples analyzed by XRD

Sample ID	Location in cave	Sample description	Composition[+]	Calcite Unit cell length[^]	$MgCaCO_3$ mol%
TA16-BR2-4	Same room as TA12-8	Grey, powdery material from ceiling	Talc, quartz		
TA16-BR2-5	Same room as TA12-8	Black, rusty-looking from ceiling	Quartz, clinochlore		
TA16-BR2-6	Same room as TA12-8	White with large crystals and black coating (only white portion analysed)	Quartz, anatase		
TA16-CE1	Cave entrance	White-ish low density rock, loose from ground	Calcite, vermiculite, tremolite		
TA16-CE2	Cave entrance	Grey rock, loose from ground	Dolomite, trace quartz		
Other					
TA12-2g-mud	106 m	scraped various parts of mud coating from offcut of TA12-2g	Quartz, kaolinite, sandinine, calcite, dolomite, illite, magnetite, hydroxyl-apatite (up to 10%)		

+Qualitative composition from mineral identification software package Diffrac*plus* Eva
^Modeled unit cell length and mineral quantification using program Siroquant 3.0
*estimate of Mg-calcite mol% based on Bischoff Mg-cell unit curve

An XRD sample for stalagmite TA12-8 was prepared from a bulk 1 cm transect milled powder. XRD samples for all mini-cores and stalagmite TA12-1 were generated by scraping powder lengthwise from the side of a mini-core or scraping perpendicular to the growth axis from the center to the outside of the stalagmite. This method precludes identification of alternating layers or co-precipitation, but provides a qualitative estimate of what mineral phases precipitated in different parts of the cave. The mineralogy for TA12-2 was primarily established using Raman spectroscopy in a previous study, but here a calcite layer was targeted for determining Mg content and sampled with a motorized hand-held drill.

Stalagmite and mini-core samples were ground by hand in an agate mortar with acetone and suspended on a quartz low-background sample holder. Bedrock samples were milled in a McCrone micronizing mill in ethanol, and filled in a side-packed sample holder. Results were interpreted using the SIEMENS software package Diffrac*plus* Eva (2000) for mineral identification, and the program Siroquant 3.0 for mineral quantification.

Bischoff et al. (1983) determined the relationship between unit cell parameters of synthetic Ca-Mg carbonate and Mg-content experimentally by performing high-PT syntheses of various compositions and refining the unit cell parameters based on XRD data. A three-dimensional polynomial was fitted to the data of Bischoff et al. (1983) to determine the Mg-content in calcite for the unit cell parameters that resulted from the refinements of our XRD data with the program Siroquant 3.0.

4.3.2 Geochronology

Age control for the TA12-8 sample is based on ten uranium-thorium (U/Th) dates generated at the University of Melbourne on a Nu Instruments Plasma multi-collector ICP-MS using the methods of Hellstrom (2003). The U-Th dating results are summarized in Table 4.2. Ages are given in thousands of years before present (ky BP; where “present” is defined as 1950 A.D.).

All ten U-series dates for TA12-8 fall in stratigraphic order (within error). The uranium concentrations in the sample range from 3.2 – 5.7 ppm, an order of

magnitude higher than typical calcite values. Ages were corrected for the initial ^{230}Th concentration using the stratigraphical constraint model of Hellstrom (2006), an initial [$^{230}Th/^{232}Th$] of 1.5 ± 1.5 and the U and Th decay constants of Cheng et al. (2013).

Table 4.2 - U/Th dates for stalagmite TA12-8

Sample ID	Depth (mm)	^{238}U (ppb) ±2σ	[$^{230}Th/^{232}Th$]	[$^{230}Th/^{238}U$]	[$^{234}U/^{238}U$]	Uncorrected Age[#] (ky BP)	Corrected Age[#] (ky BP)	Corr. Initial [$^{234}U/^{238}U$]
U4	5	3478 ±262	208.2	0.0322 ±0.0003	1.2793 ±0.0040	2.711±0.028	2.691 ±0.034	1.2815 ±0.0040
U38	40	4421 ±333	40.0	0.0558 ±0.0005	1.3583 ±0.0044	4.499±0.044	4.331 ±0.175	1.3628 ±0.0044
U120	124.1	3922 ±297	440.0	0.0677 ±0.0006	1.3604 ±0.0044	5.488±0.054	5.469 ±0.057	1.3661 ±0.0044
U190	191.8	4656 ±352	789.2	0.0687 ±0.0006	1.3238 ±0.0042	5.732±0.055	5.722 ±0.056	1.3291 ±0.0042
U252	252	5718 ±433	221.2	0.0685 ±0.0004	1.2553 ±0.0040	6.041±0.042	6.001 ±0.058	1.2597 ±0.0041
U338	333	5013 ±379	653.8	0.0833 ±0.0007	1.3467 ±0.0044	6.878±0.065	6.863 ±0.067	1.3535 ±0.0045
U404	404	3243 ±244	237.0	0.0853 ±0.0009	1.3545 ±0.0040	7.007±0.080	6.964 ±0.091	1.3616 ±0.0041
U474	474.6	3725 ±281	239.4	0.0840 ±0.0011	1.2914 ±0.0041	7.249±0.102	7.205 ±0.110	1.2974 ±0.0042
U519	519.2	4795 ±363	469.3	0.0869 ±0.0009	1.3108 ±0.0040	7.393±0.083	7.371 ±0.086	1.3174 ±0.0041
U636	636.2	4916 ±370	2490.8	0.0890 ±0.0006	1.2793 ±0.0041	7.777±0.061	7.772 ±0.061	1.2856 ±0.0042

[#]Age in ky BP; thousands of years before present where present is defined as 1950 A.D. Ages are calculated using decay constants specified in Cheng *et al.* (2013).
All ratios [bracketed] are reported as activities. The uncertainty is reported as 2σ error. Corrected ages use an initial [$^{230}Th/^{232}Th$] of 1.5 ± 1.5 for the detrital component.

A rapid change in growth rate suggests a hiatus occurred between the first and second dates, which I identify as a dark lamina at 10 mm depth (Figure 4.3). The age-depth model for the speleothem was constructed using dates only below the hiatus using a Bayesian Monte Carlo approach with the statistical software package, Bacon, for R (Blaauw and Christen, 2011).

4.3.3 Laser-ablation ICP-MS trace element analysis

Trace element measurements for TA12-2 were made at the Australian National University using an ArF Excimer laser ablation system (193 nm; Lambda Physik LPX120i) coupled with a single collector Varian 820 quadrupole inductively coupled plasma mass spectrometer (ICP-MS). All sample tracks were pre-ablated using a 265 μm spot size at 10 Hz moving at 200 μm/s in order to pre-clean the trace element analysis track.

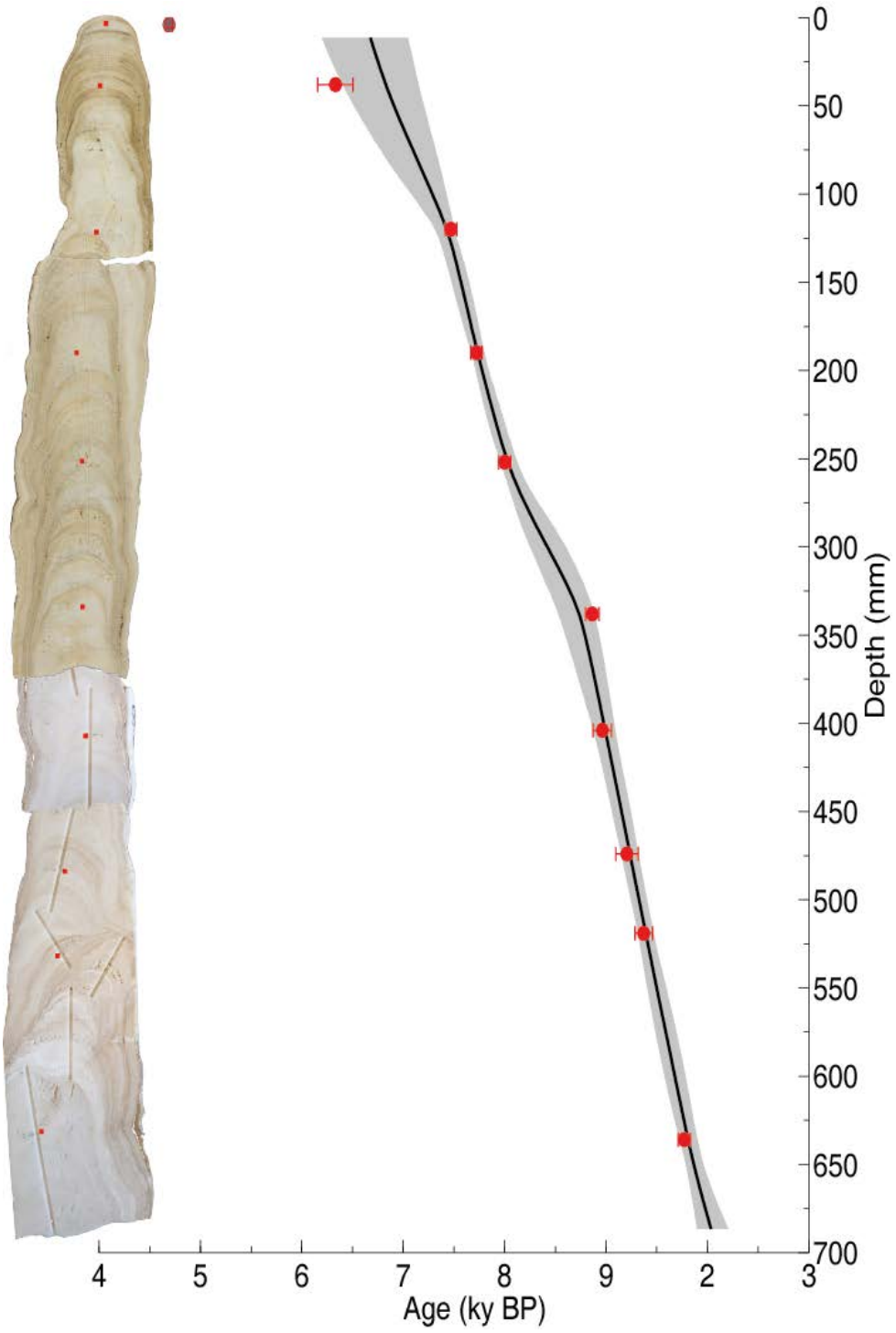

Figure 4.3 – Image of TA12-8 next to U/Th age-depth model for TA12-8. Red circles (with 2σ error) indicate where date was taken. Black line is age-depth model. 2σ confidence interval is marked in grey. Age model and uncertainties were generated in Bacon software for R (Blaauw and Christen, 2011). Groove on image shows milling transect for $\delta^{18}O$ samples. Top date (black) was not included in age model.

Analyses were conducted by pulsing the laser at 5Hz with a 40 μm round ablation spot moving at 40 μm/s. Twenty elemental masses (^{11}B, ^{23}Na, ^{24}Mg, ^{25}Mg, ^{27}Al, ^{31}P, ^{43}Ca, ^{44}Ca, ^{47}Ti, ^{55}Mn, ^{66}Zn, ^{86}Sr, ^{88}Sr, ^{89}Y, ^{137}Ba, ^{138}Ba, ^{139}La, ^{208}Pb, ^{232}Th, ^{238}U) were measured for transects running along the growth axis of TA12-2. Analysis was also performed on three standards (NIST612, NIST610, in-house coral NEP 3B) and for background counts. The standards and background were measured before and after each analysis transect to correct for drift. All data was corrected relative to the NIST612 glass standard, and normalized to ^{43}Ca, using a MATLAB script written by me. Calcite and aragonite phases are identifiable in the variable Sr and Mg content of the speleothem.

4.3.4 Raman spectroscopy

Raman spectroscopy is a non-destructive method that can be used to identify the relative amounts of mineral phases using the vibrational modes of different crystal lattices. In the case of carbonate, the different crystal structures of aragonite and calcite produce distinct Raman spectra, despite sharing the same $CaCO_3$ composition (White, 2006). Raman analysis was performed on TA12-2 only, along the same analysis track as the trace element laser ablation analysis. Raman analysis was carried out at the ANU's Research School of Physics on a Renishaw InVin Raman spectrometer, using a 632 nm red laser at 50% power with 1200 mm^{-1} grating. A 20x objective lens with a 1.93 μm diameter spot size was used in conjunction with a 1 second acquisition time. Spectra were collected in a broad spectral frequency range from 120-1974 cm^{-1}, but the low frequency range between 150-300 cm^{-1} was used for identifying the diagnostic peaks for calcite (280 cm^{-1}) and aragonite (206 cm^{-1}).

4.3.5 Thin section petrography

Thin sections were created for TA12-2 only, from the same offcut slab pieces used for trace element analysis. These pieces were further reduced in size to create a full 13-piece transect of 2x1" thin sections. The unpolished thin sections were prepared at the ANU and photographed at high magnification using a Leica Power Mosaic at the Research School of Earth Sciences, ANU. Thin sections were used to

verify the mineralogical classifications inferred from trace element analysis and Raman spectroscopy. Further identification of mineralogy and diagenetic features was performed at the School of Environmental and Life Sciences at the University of Newcastle. Micro-fluorescence was also performed at the University of Newcastle using a Zeiss Axioplan microscope.

4.4 Results and Discussion

4.4.1 Bedrock composition

Eight bedrock samples from various parts of the cave (Figure 4.2 and Table 4.1) were analyzed with XRD. The samples exhibit a wide range of physical characteristics and suggest a high level of heterogeneity in the bedrock. XRD analysis shows a mineralogy dominated by quartz, in addition to mica (muscovite) and K-feldspars (potentially from granitic rocks), clay minerals (illite and kaolinite), titanium oxide (anatase), chlorite (clinochlore), talc, tremolite, and trace amounts of plagioclase. Two samples were primarily dolomite; one of these was found in the chamber where aragonitic speleothems TA12-1 and TA12-2 precipitated. Neither dolomite nor limestone were identified in the chamber with TA12-8, however, talc and tremolite are commonly associated with the metamorphism of siliceous dolomites, providing further evidence for the dolomitic nature of the host rocks of Tangga Cave (Deer et al., 2013).

4.4.2 Thin section petrography

Thin section petrography reveals sharp transitions between aragonite and calcite throughout TA12-2. Elongated aragonite needle crystals dominate the lowest portion of the speleothem between 370 and 440 mm, corresponding to the Younger Dryas stadial. Though porous, there are no signs of replacement. Rather, pure acicular aragonite prevails as 'ideal' clean uniform growth (Figure 4.4d).

In contrast, upper parts of the speleothem between 45 and 125 mm also grew continuously as aragonite (Figure 4.4a), but the crystal growth is erratic, apparently disrupted by the presence of detrital material. These two different

aragonite fabrics likely indicate two different hydrologic regimes, with the dripwaters feeding the cleaner aragonite being more filtered in the karst than the later aragonite. Pollen records from inland mountain lake Danau di Atas, 85 km south of Tangga Cave, show an abrupt shift in pollen assemblages ca. 12.4 ka, suggesting a change in vegetation and soil profile could be responsible for the change for the change in filtration regimes (Stuijts et al., 1988).

The middle section of the speleothem (176 to 370 mm) is characterized by frequent oscillations between aragonite and calcite. Thin dark layers appear to separate most transitions between calcite and aragonite, suggesting that these layers may play a role in mediating phase changes (Figure 4.4b-c). It is hypothesized that these layers may be microbial mats, which cap the aragonite and prevent it from growing, while allowing calcite to nucleate (Silvia Frisia, pers. comm.). One of these layers caps the clean, acicular calcite in the lower section of the speleothem.

Examination of the dark layers under micro-fluorescence reveals the presence of organics (Figure 4.4e-f). Lack of organic matter within the YD section also meant there was no decay of organic matter to induce mineral corrosion by acidic waters. Younger sections of the speleothem contain aragonite that was partially corroded by aggressive waters, though there is no presence of organics *within* the aragonite crystal structure. The extra-lattice organics do however play a role in forcing aragonite needle growth in erratic directions. In contrast, the presence of organics within calcite suggests that these were crucial in the nucleation of calcite crystals.

The majority of observed fabrics were primary in nature with no aragonitic needle relics observed within calcite crystals. Micro-replacement of individual crystals was occasionally observed, usually triggered by the corrosion of aragonite and input of organic matter.

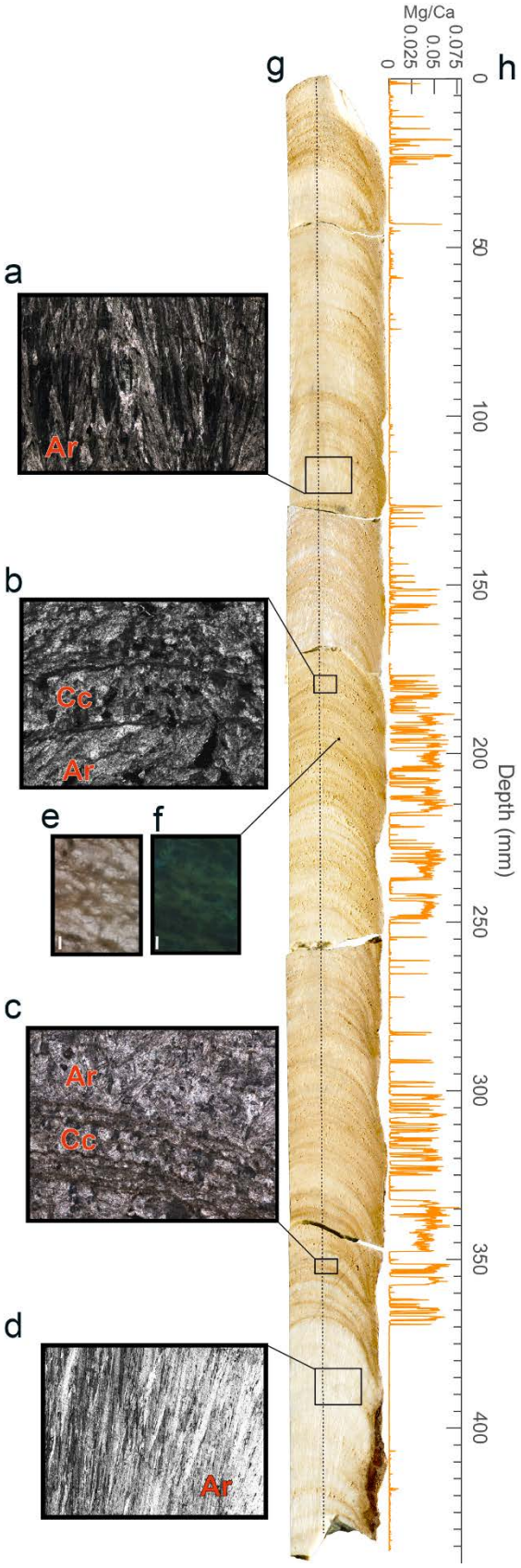

Figure 4.4 – (a-d) Aragonite (Ar) and calcite (Cc) thin section petrography in cross-polarized light, (e) transmitted light, (f) microfluorescence photos of organic layers and (g) reflected light photography of offcut slab of TA12-2 with (h) LA-ICP-MS Mg/Ca concentrations plotted as a reference for calcite/aragonite phases. (a) Erratic aragonite crystal growth disrupted by detrital material. (b-c) CC-Ar and Ar-Cc transitions separated by thin dark layers, potentially microbial mats that allow calcite to nucleate. (d) 'Ideal' clean acicular aragonite growth during Younger Dryas era, neatly oriented in same growth direction. (e) Transmitted light microphotograph of thin, dark layers separating calcite growth. Scale bar in lower left corner is 100 μm. (f) Same region as (e) but under blue-green fluorescence excited at the 365 nm band, demonstrating the presence of organics in dark layers. (g) Offcut slabs of TA12-2 on which laser-ablation trace element and petrographic analysis was performed. Dashed line shows laser ablation track. Rectangles indicate where thin section microphotos were taken. (g) Laser-ablation Mg/Ca concentrations. High values indicate the presence of calcite.

4.4.3 Correction for isotopic fractionation differences

Chapter 2 has already successfully applied a $\delta^{18}O$ correction to account for differences in oxygen isotope fractionation between aragonite and calcite. The offset used in that study to correct from calcite to aragonite (+1‰) was chosen based on qualitative assessment; a +1‰ correction rendered calcite values roughly equivalent to adjacent aragonite values. Here I revisit the correction using a newly presented speleothem, TA12-8, from the same cave, which precipitated calcite concurrently with TA12-2's aragonite growth. I compare fractionation offsets between coevally growing calcite and aragonite and compare these values to minimum and maximum fractionation offsets from the published literature.

TA12-8 had much higher average growth rates than TA12-2 (~250 mm/ky), therefore TA12-8 oxygen values were interpolated to the TA12-2 age model using nearest-neighbour interpolation (Figure 4.5a). Both data sets were then smoothed with a 7-point running mean. There is large point to point variability between the two datasets that is likely due to a combination of different drip paths, unrefined age models, and kinetic effects.

Smoothing allows a better assessment of the mean oxygen values in either carbonate phase, however, it does erode certain offsets that are likely real (e.g., calcite spike within aragonite section of TA12-8). This is a necessary sacrifice for calculating the oxygen offset between the two pieces, though it creates median values that do not cleanly fall into the expected offset ranges. The plotted difference between the two smoothed records does not demonstrate a clear picture of oxygen isotopic fractionation between calcite and aragonite (Figure 4.5b).

Several sections are close to the 1‰ offset used in Wurtzel et al. (2018) (i.e., at ~5 ky BP, between 7.2 and 7.4 ky BP, between 7.7 and 7.8 ky BP), and several more are close to 0‰, indicating where the same phase precipitated simultaneously (i.e., at ~5.7 ky BP, 6.4 ky BP, 7 ky BP), but many values fall in between or outside of these expected values. A histogram of the offsets reveals peaks at 0‰, 0.35‰, 0.65‰, and 1‰ (Figure 4.5c). The peak at 0‰ is expected where the same phase

is precipitating simultaneously but mostly occurs due to the smoothing process. It is possible that the peak at 0.35‰ may be indicative of a constant fractionation offset between fractionation in the two cave chambers, although it is possible that it is a smoothing artifact. Peaks at 0.65‰ and 1‰ both fall within the published ranges of fractionation differences between aragonite and calcite and occur with similar frequency.

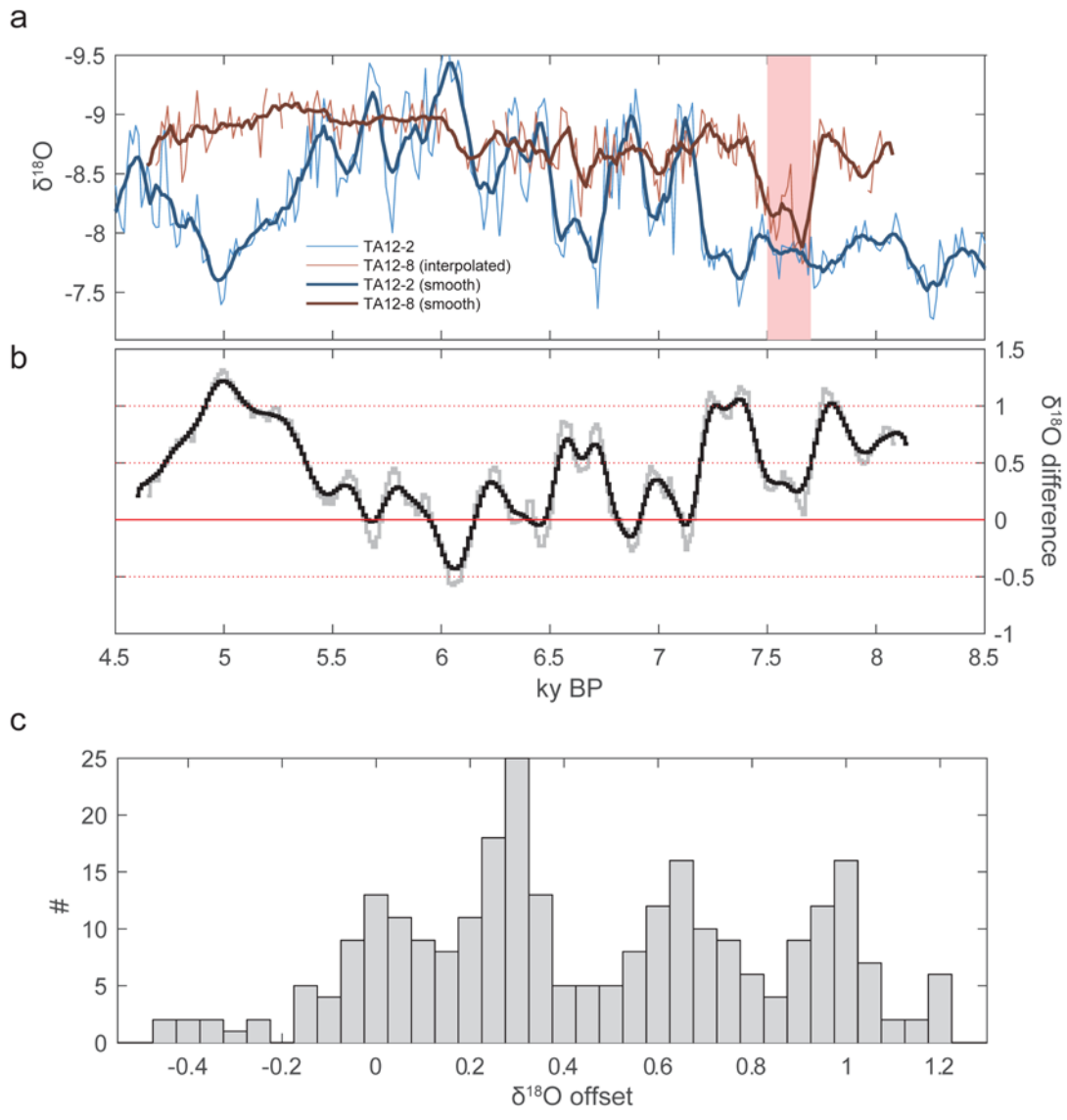

Figure 4.5 – (a) Comparison of $\delta^{18}O$ in stalagmites TA12-2 (blue) and TA12-8 interpolated to TA12-2 age scale (red). 7-point smooths are in thick, dark lines. Red vertical bar represents aragonitic interval in TA12-8. TA12-8 is otherwise assumed to be calcite. (b) Difference between TA12-2 $\delta^{18}O$ and TA12-8 $\delta^{18}O$ (grey) and 9-point smooth (black). (c) Histogram (0.05 ‰ bins) of $\delta^{18}O$ differences in (b).

There are several caveats to this analysis. First, more age control in both samples is required to ensure that we are comparing co-precipitating intervals. TA12-8 has visually uneven growth lamina, indicating that the growth rate may have changed multiple times throughout its lifetime (Figure 4.3). Secondly, unlike TA12-2, TA12-8 has not been evaluated for mineralogy at high-resolution using either laser-ablation trace element analysis or Raman spectroscopy. Bulk XRD analysis of a sample near the top of the speleothem indicated no aragonite, however, isotopic values between 7.5 and 7.7 ky BP become abruptly enriched by ~0.8‰, likely indicating a phase change to aragonite. This raises the possibility of both additional aragonite phases or co-precipitation of the two minerals during intervals that were not examined with XRD. Even small amounts of aragonite in the TA12-8 isotope samples could cause the calculated isotopic difference between calcite and aragonite to be underestimated and inconsistent.

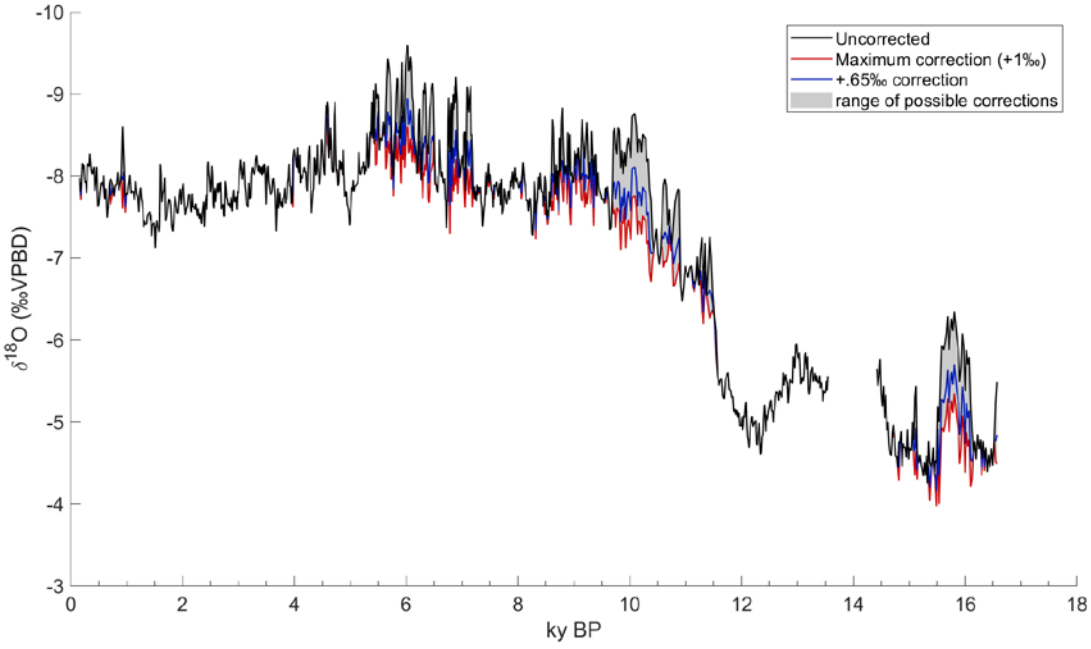

Figure 4.6 – Range of oxygen isotope fractionation corrections for TA12-2. The three curves represent the uncorrected $\delta^{18}O$ data (black), the maximum fractionation correction of +1‰ used in Wurtzel et al., 2018 (red), and the low-end correction of +0.65‰ (blue). The curves are adjusted by a fraction of the correction value based on the percent of calcite contained in the isotope sample. Grey shading indicates the range of possible corrections between 0 and 1‰. Where there is no shading or secondary curves, the speleothem sample is 100% aragonite.

Because this analysis did not provide a clear singular offset, I revisited the isotopic correction TA12-2 using the low-end 0.65‰ offset for $\delta^{18}O$ fractionation differences between aragonite and calcite (Figure 4.6). The 0.65‰ offset does not bring calcite values in line with adjacent values, such that the transition out of the Younger Dryas is not smooth, but punctuated by stepwise wet intervals. This is not unreasonable considering that a change in environmental conditions (such as enhanced filtration due to increased rainfall) is necessary to trigger changes in mineralogy, however there is little evidence to suggest the stepwise transition is a regional signal rather than an artifact of cave hydrology. That said, the 0.35‰ difference between the two corrections is also quite small with regards to the natural centennial- to millennial-scale variability in the record.

4.4.4 Calculation of distribution coefficients

As with isotopic fractionation, mineralogy can have a significant impact on trace element distribution coefficients. The many, rapid transitions between aragonite and calcite in TA12-2 offer a unique opportunity to a) examine the thresholds in Mg concentration which lead to a phase change from aragonite to calcite and from calcite to aragonite and b) back-calculate aragonite distribution coefficients using the known distribution coefficients for speleothem calcite.

I employed methods similar to that of Wassenburg et al., 2016 (herein referred to as W16) and Jamieson et al., 2016, however, I did not make an excess Ca^{2+} correction for Rayleigh distillation. First, Bayesian change point analysis (Ruggieri and Lawrence, 2014) was used to identify change points along the LA-ICP-MS Sr transects with greater than 95% solution confidence (Figure 4.7). Twelve data points on either side of the transition were extracted corresponding to transition lengths of 0.41 to 1.35 mm and transition durations of 0.926 to 70.215 years. Transitions were manually screened using Sr, U, and Mg data to ensure that there were no major jumps or outliers on either side of the transition that might indicate co-precipitation of aragonite and calcite. All the retained transitions are shown in Figure 4.8 with the data points used in the calculation. Trace element

concentrations in calcite and aragonite ($Tr/Ca_{(Cc)}$ and of $Tr/Ca_{(Ar)}$, respectively) were calculated by averaging the twelve points on each side of the transition.

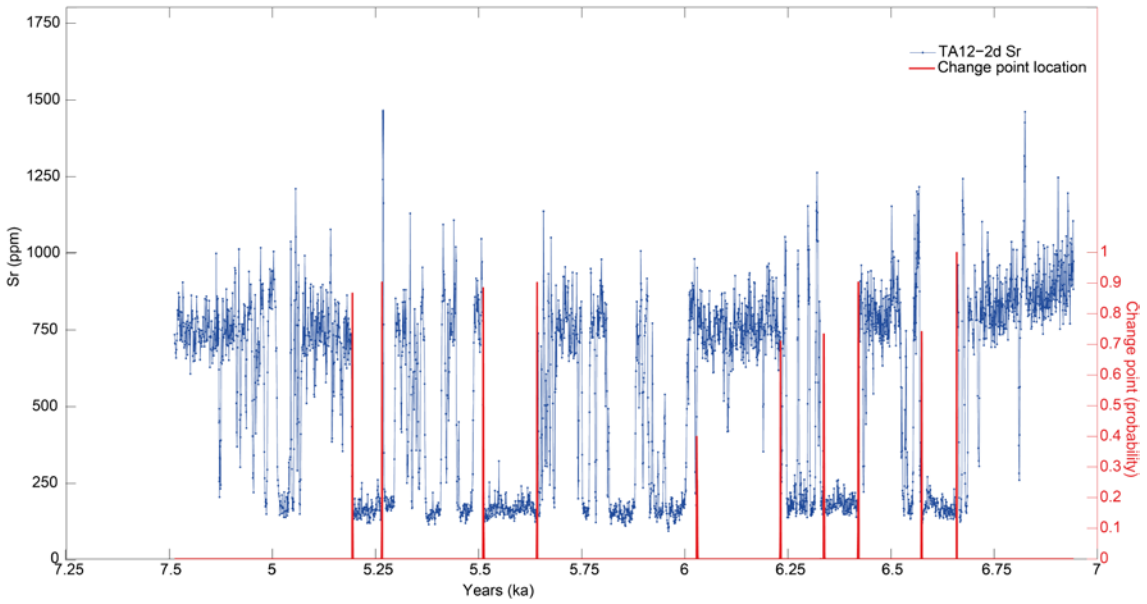

Figure 4.7 – Example of Bayesian change point analysis prior to manual screening of transitions as it was applied to Sr concentrations (blue) in TA12-2-transect D. The same analysis was applied to all seven laser-ablation trace element transects. Red spikes represent likely locations of change points.

In order to calculate $D_{Tr(Ar)}$, I used the following series of equations, propagating the standard error of the mean trace element to Ca ratios. First, I calculate the concentration of the element in the dripwater by rearranging Equation 1 using the laser-ablation measured value of $Tr/Ca_{(Cc)}$:

$$\left({}^{Tr}/_{Ca}\right)_{dw} = \frac{({}^{Tr}/_{Ca})_{Cc}}{D_{Tr(Cc)}} \quad (2)$$

I used the temperature-dependent equations of Day and Henderson (2013) to calculate $D_{Mg(Cc)}$:

$$D_{Mg(Cc)} = 0.01e^{0.02T} \quad (3)$$

where T=24°C, the assumed annual average temperature of Tangga Cave, resulting in $D_{Mg(Cc)}$ of 0.0162. For $D_{Sr(Cc)}$, $D_{U(Cc)}$, $D_{Ba(Cc)}$, which have no significant temperature dependence (Day and Henderson, 2013), I used the same values as W16, corresponding to $D_{Sr(Cc)}$=0.12 $D_{U(Cc)}$=0.12, and $D_{Ba(Cc)}$=0.11, respectively.

I then substituted in the measured value of the element in aragonite with the calculated value of the dripwater to estimate $D_{Tr(\mathrm{Ar})}$:

$$D_{Tr(\mathrm{Ar})} = \frac{(^{Tr}/_{\mathrm{Ca}})_{Ar}}{(^{Tr}/_{\mathrm{Ca}})_{\mathrm{dw}}} \tag{4}$$

This process was repeated for twenty transitions total; eleven aragonite-to-calcite and nine calcite-to-aragonite.

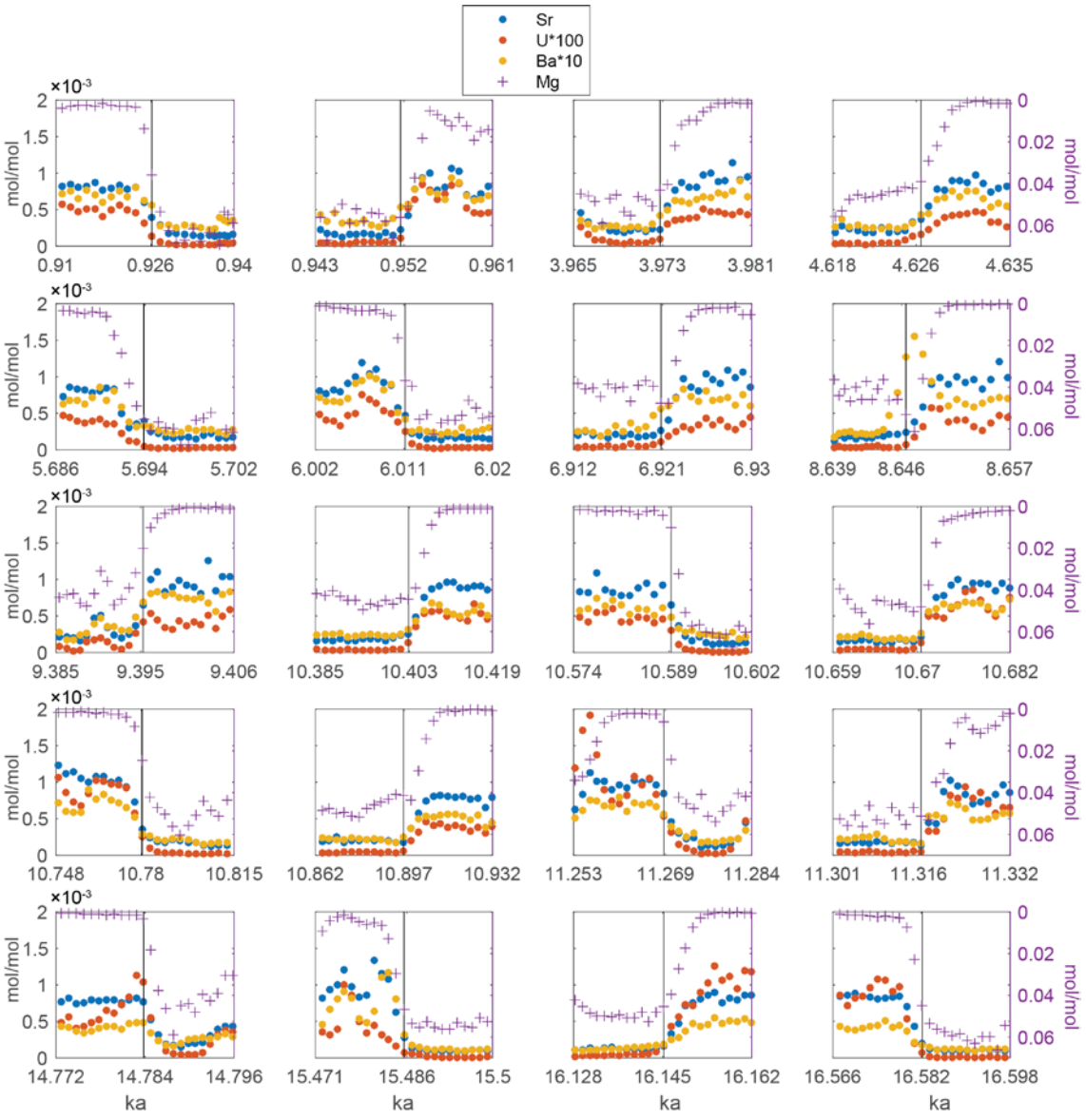

Figure 4.8 – Twenty transitions used in this analysis after retaining only transitions with >95% solution confidence and manually screening for element spikes. In all graphs, Sr (blue), U (red) and Ba (yellow) correspond to the y-axis on the left. U and Ba have been scaled for plotting purposes. Mg (purple cross) corresponds to y-axis on right.

One underlying assumption in this process is that the concentration of the dripwater does not undergo major changes at the transition between calcite and aragonite. As a change in dripwater chemistry of pH, Mg/Ca concentration or calcite saturation state is usually implied to trigger a change in carbonate phase, this assumption is flawed. However, I assume here that the dripwater chemistry change is instantaneous over the transition and that the changes in chemistry required to force a phase change will be accounted for in the propagated error (Wassenburg et al., 2016).

As expected, average Mg concentrations in calcite are an order of magnitude higher than in aragonite, while Sr, Ba, and U are all lower in calcite than in aragonite by up to an order of magnitude (Table 4.3). Calculated $D_{Tr(Ar)}$ for Ba and Sr show the smallest variability, while U and Mg $D_{Tr(Ar)}$ demonstrate a wide range of values (Figure 4.9). Only $D_{U(Ar)}$ fall within the expected range of values based on previous studies of partitioning into aragonite.

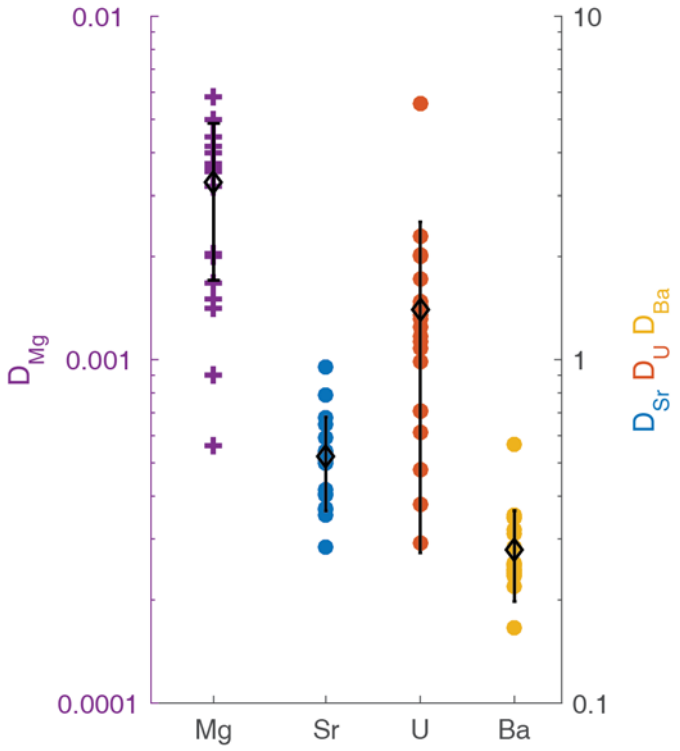

Figure 4.9 – Comparison of speleothem aragonite distribution coefficients for Mg, Sr, U, and Ba calculated from the studied transitions. Open black diamond indicates mean value across all transitions with 1σ errors.

The average calculated Mg/Ca dripwater value across all twenty transitions is 3.02±0.42 (1σ), with a slightly higher average of 3.17±0.51 when only considering calcite-to-aragonite transitions. Though such a high value is consistent with the high concentrations needed to precipitate aragonite, the calculated aragonite-to-calcite dripwater value of 2.89±0.30 is also well above the threshold at which aragonite should continue precipitating (Riechelmann et al., 2014). Even using the highest experimental values of $D_{Mg(Cc)}$ (~.029) from Day and Henderson (2013), average calculated dripwater ratios would be greater than 1.1.

Using the original mean value of 3.02 in the dripwater, solving Equation 4 for $D_{Mg(Ar)}$ yields a mean value of 0.00329±0.00158, two orders of magnitude higher than the majority of values reported in W16. Assuming that the $D_{Mg(Cc)}$ is correct, since the calculated dripwater values are not off by orders of magnitude, the other source of error may be in the measured values of Mg/Ca in aragonite. At two orders of magnitude higher than W16, this may very well explain the mismatch between the calculated $D_{Mg(Ar)}$ values. The source of the high Mg in aragonite could be particle-bound Mg at intercrystalline boundaries (Belli et al., 2017).

The measured concentrations of Sr/Ca in both aragonite and calcite were highly consistent across all transitions, regardless of transition direction. As a results dripwater values were also consistent. The mean values in the calcite were 2.03E-04±6.19E-05 (1σ), while aragonite values were 8.13E-04±8.61E-05. The calculated $D_{Sr(Ar)}$ is 0.52±0.16. This is lower than the expected value of >1, however not by orders of magnitude. The very consistent values across transitions suggest that the error may lie with the choice of $D_{Sr(Cc)}$, rather than the presence of detrital material.

Experimental work has demonstrated a possible range for $D_{Sr(Cc)}$ between 0.08 and 0.3 (Day and Henderson, 2013) (Huang and Fairchild, 2001). I used the relatively conservative value of 0.12 used by W16 for replication purposes. However, previous work has demonstrated links between $D_{Sr(Cc)}$ and growth rate (Treble et al., 2005) and Mg concentration in the fluid (Mucci and Morse, 1983).

Table 4.3 - Measured and calculated trace element ratios in calcite (Cc), aragonite (Ar), and dripwater (dw), and estimate of aragonite partitioning coefficients for each transition, transition type means, and mean of all transitions

Mg	Transition Age (ky)	Transition Depth (mm)	Duration (years)	Length (mm)	$Mg/Ca_{(Cc)}$	1 SE	$Mg/Ca_{(Ar)}$	1 SE	$Mg/Ca_{(dw)}$	1 SE	$D_{Mg(Ar)}$	1 SE
Cc-Ar	0.93	22.48	30.078	0.693	6.00E-02	9.12E-03	6.22E-03	9.46E-03	3.72	0.56	1.67E-03	2.56E-03
	5.69	188.18	17.848	0.411	6.03E-02	5.76E-03	1.66E-02	1.90E-02	3.73	0.36	4.44E-03	5.10E-03
	6.01	199.12	15.615	0.611	5.19E-02	7.14E-03	6.56E-03	9.94E-03	3.21	0.44	2.04E-03	3.11E-03
	10.59	351.33	17.858	0.617	5.31E-02	1.55E-02	2.98E-03	2.25E-03	3.29	0.96	9.06E-04	7.34E-04
	10.78	355.13	15.969	0.559	4.77E-02	8.81E-03	4.15E-03	6.49E-03	2.95	0.55	1.41E-03	2.22E-03
	11.27	364.29	17.316	0.599	4.03E-02	1.28E-02	1.04E-02	1.20E-02	2.49	0.79	4.17E-03	5.00E-03
	14.78	10.18	18.167	0.865	3.73E-02	1.42E-02	1.30E-03	7.71E-04	2.31	0.88	5.63E-04	3.97E-04
	15.49	28.31	17.666	0.597	5.26E-02	4.40E-03	1.19E-02	1.34E-02	3.26	0.27	3.64E-03	4.12E-03
	16.58	49.65	20.114	0.534	5.79E-02	5.26E-03	7.19E-03	1.27E-02	3.58	0.33	2.01E-03	3.55E-03
Ar-Cc	0.95	23.07	33.958	0.682	5.69E-02	4.99E-03	2.05E-02	1.68E-02	3.52	0.31	5.81E-03	4.80E-03
	3.97	126.90	28.382	0.567	4.75E-02	6.79E-03	1.17E-02	1.45E-02	2.94	0.42	4.00E-03	4.97E-03
	4.63	151.72	23.164	0.465	4.67E-02	5.30E-03	9.20E-03	1.28E-02	2.89	0.33	3.19E-03	4.46E-03
	6.92	236.73	67.524	1.324	4.09E-02	3.36E-03	1.26E-02	1.71E-02	2.53	0.21	4.99E-03	6.76E-03
	8.65	302.49	70.215	1.350	4.30E-02	4.93E-03	1.33E-02	2.19E-02	2.66	0.30	5.00E-03	8.24E-03
	9.40	325.02	30.970	0.564	3.94E-02	7.91E-03	3.67E-03	5.62E-03	2.44	0.49	1.50E-03	2.32E-03
	10.40	347.59	31.033	0.564	4.47E-02	2.49E-03	9.71E-03	1.55E-02	2.77	0.15	3.51E-03	5.61E-03
	10.67	352.94	24.004	0.638	4.73E-02	4.11E-03	1.08E-02	1.49E-02	2.92	0.25	3.69E-03	5.10E-03
	10.90	357.39	29.474	0.638	4.70E-02	3.61E-03	1.08E-02	1.64E-02	2.91	0.22	3.71E-03	5.65E-03
	11.32	365.16	33.754	0.638	5.13E-02	3.74E-03	1.85E-02	1.79E-02	3.18	0.23	5.83E-03	5.66E-03
	16.15	41.25	32.608	0.638	4.86E-02	2.78E-03	1.11E-02	1.62E-02	3.01	0.17	3.68E-03	5.39E-03
				Mean	$Mg/Ca_{(Cc)}$	**1σ**	$Mg/Ca_{(Ar)}$	**1σ**	$Mg/Ca_{(dw)}$	**1σ**	$D_{Mg(Ar)}$	**1σ**
				Cc-Ar	5.12E-02	8.19E-03	7.47E-03	4.78E-03	3.17	0.51	2.32E-03	1.42E-03
				Ar-Cc	4.67E-02	4.85E-03	1.20E-02	4.50E-03	2.89	0.30	4.08E-03	1.26E-03
				All	4.87E-02	6.79E-03	9.96E-03	5.06E-03	3.02	0.42	3.29E-03	1.58E-03

Table 4.3 (con't) – Measured and calculated trace element ratios in calcite (Cc), aragonite (Ar), and dripwater (dw), and estimate of aragonite partitioning coefficients for each transition, transition type means, and mean of all transitions

Sr	Transition Age (ky)	Transition Depth (mm)	Duration (years)	Length (mm)	$Sr/Ca_{(Cc)}$	1 SE	$Sr/Ca_{(Ar)}$	1 SE	$Sr/Ca_{(dw)}$	1 SE	$D_{Sr(Ar)}$	1 SE
Cc-Ar	0.93	22.48	30.078	0.693	1.81E-04	7.65E-05	7.70E-04	1.31E-04	1.51E-03	6.37E-04	0.51	0.23
	5.69	188.18	17.848	0.411	2.02E-04	6.63E-05	6.81E-04	2.11E-04	1.68E-03	5.53E-04	0.41	0.18
	6.01	199.12	15.615	0.611	1.93E-04	8.75E-05	8.69E-04	1.99E-04	1.61E-03	7.29E-04	0.54	0.27
	10.59	351.33	17.858	0.617	2.03E-04	1.53E-04	8.45E-04	1.04E-04	1.69E-03	1.28E-03	0.50	0.38
	10.78	355.13	15.969	0.559	1.83E-04	6.28E-05	9.88E-04	2.24E-04	1.52E-03	5.24E-04	0.65	0.27
	11.27	364.29	17.316	0.599	3.07E-04	2.23E-04	9.43E-04	1.24E-04	2.56E-03	1.86E-03	0.37	0.27
	14.78	10.18	18.167	0.865	3.29E-04	1.77E-04	7.80E-04	2.63E-05	2.74E-03	1.47E-03	0.28	0.15
	15.49	28.31	17.666	0.597	1.13E-04	5.00E-05	8.99E-04	2.83E-04	9.43E-04	4.17E-04	0.95	0.52
	16.58	49.65	20.114	0.534	1.14E-04	2.65E-05	7.51E-04	2.04E-04	9.48E-04	2.21E-04	0.79	0.28
Ar-Cc	0.95	23.07	33.958	0.682	1.75E-04	3.16E-05	7.63E-04	2.36E-04	1.46E-03	2.64E-04	0.52	0.19
	3.97	126.90	28.382	0.567	2.83E-04	1.25E-04	8.30E-04	2.29E-04	2.35E-03	1.05E-03	0.35	0.18
	4.63	151.72	23.164	0.465	2.33E-04	5.96E-05	7.81E-04	1.61E-04	1.94E-03	4.96E-04	0.40	0.13
	6.92	236.73	67.524	1.324	2.02E-04	2.74E-05	8.42E-04	2.52E-04	1.68E-03	2.28E-04	0.50	0.16
	8.65	302.49	70.215	1.350	1.85E-04	3.08E-05	8.36E-04	2.71E-04	1.54E-03	2.57E-04	0.54	0.20
	9.40	325.02	30.970	0.564	3.09E-04	1.51E-04	9.43E-04	1.52E-04	2.58E-03	1.25E-03	0.37	0.19
	10.40	347.59	31.033	0.564	1.86E-04	2.80E-05	8.10E-04	2.08E-04	1.55E-03	2.33E-04	0.52	0.16
	10.67	352.94	24.004	0.638	1.65E-04	2.19E-05	8.12E-04	2.20E-04	1.37E-03	1.82E-04	0.59	0.18
	10.90	357.39	29.474	0.638	1.97E-04	1.97E-05	6.85E-04	2.00E-04	1.64E-03	1.64E-04	0.42	0.13
	11.32	365.16	33.754	0.638	1.70E-04	1.40E-05	7.34E-04	2.53E-04	1.41E-03	1.17E-04	0.52	0.18
	16.15	41.25	32.608	0.638	1.23E-04	1.71E-05	6.99E-04	2.30E-04	1.03E-03	1.43E-04	0.68	0.24
				Mean	$Sr/Ca_{(Cc)}$	**1σ**	$Sr/Ca_{(Ar)}$	**1σ**	$Sr/Ca_{(dw)}$	**1σ**	$D_{Sr(Ar)}$	**1σ**
				Cc-Ar	2.03E-04	7.41E-05	8.36E-04	9.90E-05	1.69E-03	6.17E-04	0.56	0.21
				Ar-Cc	2.02E-04	5.37E-05	7.94E-04	7.33E-05	1.69E-03	4.47E-04	0.49	0.10
				All	2.03E-04	6.19E-05	8.13E-04	8.61E-05	1.69E-03	5.15E-04	0.52	0.16

Table 4.3 (con't) – Measured and calculated trace element ratios in calcite (Cc), aragonite (Ar), and dripwater (dw), and estimate of aragonite partitioning coefficients for each transition, transition type means, and mean of all transitions

U	Transition Age (ky)	Transition Depth (mm)	Duration (years)	Length (mm)	$U/Ca_{(Cc)}$	1 SE	$U/Ca_{(Ar)}$	1 SE	$U/Ca_{(dw)}$	1 SE	$D_{U(Ar)}$	1 SE
Cc-Ar	0.93	22.48	30.078	0.693	4.05E-07	3.20E-07	4.58E-06	1.17E-06	3.38E-06	2.67E-06	1.35	1.12
	5.69	188.18	17.848	0.411	2.96E-07	6.74E-08	3.24E-06	1.52E-06	2.47E-06	5.62E-07	1.31	0.68
	6.01	199.12	15.615	0.611	5.17E-07	6.10E-07	4.86E-06	1.44E-06	4.31E-06	5.09E-06	1.13	1.37
	10.59	351.33	17.858	0.617	4.77E-07	8.31E-07	4.65E-06	7.53E-07	3.97E-06	6.93E-06	1.17	2.05
	10.78	355.13	15.969	0.559	4.96E-07	6.29E-07	8.36E-06	2.31E-06	4.14E-06	5.24E-06	2.02	2.62
	11.27	364.29	17.316	0.599	2.07E-06	2.19E-06	1.06E-05	4.02E-06	1.73E-05	1.82E-05	0.62	0.69
	14.78	10.18	18.167	0.865	2.62E-06	2.83E-06	6.38E-06	2.36E-06	2.18E-05	2.35E-05	0.29	0.33
	15.49	28.31	17.666	0.597	2.20E-07	2.19E-07	4.19E-06	2.55E-06	1.84E-06	1.82E-06	2.28	2.66
	16.58	49.65	20.114	0.534	1.62E-07	1.56E-07	7.48E-06	3.12E-06	1.35E-06	1.30E-06	5.56	5.84
Ar-Cc	0.95	23.07	33.958	0.682	4.88E-07	2.02E-07	6.01E-06	2.12E-06	4.07E-06	1.68E-06	1.48	0.80
	3.97	126.90	28.382	0.567	9.92E-07	8.09E-07	3.96E-06	1.06E-06	8.27E-06	6.74E-06	0.48	0.41
	4.63	151.72	23.164	0.465	5.88E-07	4.32E-07	3.47E-06	9.81E-07	4.90E-06	3.60E-06	0.71	0.56
	6.92	236.73	67.524	1.324	5.28E-07	2.19E-07	3.12E-06	9.54E-07	4.40E-06	1.82E-06	0.71	0.37
	8.65	302.49	70.215	1.350	4.05E-07	1.17E-07	3.65E-06	1.42E-06	3.37E-06	9.78E-07	1.08	0.52
	9.40	325.02	30.970	0.564	1.35E-06	1.12E-06	4.29E-06	8.49E-07	1.13E-05	9.30E-06	0.38	0.32
	10.40	347.59	31.033	0.564	4.56E-07	2.88E-07	4.74E-06	1.28E-06	3.80E-06	2.40E-06	1.25	0.86
	10.67	352.94	24.004	0.638	4.95E-07	2.54E-07	5.90E-06	1.89E-06	4.12E-06	2.12E-06	1.43	0.87
	10.90	357.39	29.474	0.638	4.17E-07	1.02E-07	3.42E-06	1.07E-06	3.48E-06	8.46E-07	0.98	0.39
	11.32	365.16	33.754	0.638	4.26E-07	7.44E-08	6.11E-06	2.55E-06	3.55E-06	6.20E-07	1.72	0.78
	16.15	41.25	32.608	0.638	5.21E-07	3.96E-07	8.68E-06	3.29E-06	4.34E-06	3.30E-06	2.00	1.70
				Mean	$U/Ca_{(Cc)}$	**1σ**	$U/Ca_{(Ar)}$	**1σ**	$U/Ca_{(dw)}$	**1σ**	$D_{U(Ar)}$	**1σ**
				Cc-Ar	8.07E-07	8.91E-07	6.04E-06	2.38E-06	6.72E-06	7.42E-06	1.75	1.55
				Ar-Cc	6.06E-07	2.97E-07	4.85E-06	1.68E-06	5.05E-06	2.47E-06	1.11	0.52
				All	6.97E-07	6.25E-07	5.39E-06	2.06E-06	5.81E-06	5.21E-06	1.40	1.12

Table 4.3 (con't) – Measured and calculated trace element ratios in calcite (Cc), aragonite (Ar), and dripwater (dw), and estimate of aragonite partitioning coefficients for each transition, transition type means, and mean of all transitions

Ba	Transition Age (ky)	Transition Depth (mm)	Duration (years)	Length (mm)	$Ba/Ca_{(Cc)}$	1 SE	$Ba/Ca_{(Ar)}$	1 SE	$Ba/Ca_{(dw)}$	1 SE	$D_{Ba(Ar)}$	1 SE
Cc-Ar	0.93	22.48	30.078	0.693	3.17E-05	8.93E-06	6.92E-05	7.07E-06	2.88E-04	8.12E-05	0.24	0.07
	5.69	188.18	17.848	0.411	2.64E-05	3.33E-06	6.07E-05	1.71E-05	2.40E-04	3.03E-05	0.25	0.08
	6.01	199.12	15.615	0.611	2.69E-05	5.26E-06	7.59E-05	1.82E-05	2.44E-04	4.78E-05	0.31	0.10
	10.59	351.33	17.858	0.617	2.67E-05	7.45E-06	6.06E-05	7.49E-06	2.42E-04	6.78E-05	0.25	0.08
	10.78	355.13	15.969	0.559	2.07E-05	4.05E-06	6.62E-05	1.53E-05	1.88E-04	3.68E-05	0.35	0.11
	11.27	364.29	17.316	0.599	2.89E-05	1.20E-05	6.70E-05	7.94E-06	2.63E-04	1.09E-04	0.26	0.11
	14.78	10.18	18.167	0.865	2.74E-05	8.15E-06	4.14E-05	4.75E-06	2.49E-04	7.40E-05	0.17	0.05
	15.49	28.31	17.666	0.597	1.35E-05	5.86E-06	6.95E-05	2.69E-05	1.23E-04	5.32E-05	0.57	0.33
	16.58	49.65	20.114	0.534	1.24E-05	1.87E-06	3.91E-05	9.43E-06	1.13E-04	1.70E-05	0.35	0.10
Ar-Cc	0.95	23.07	33.958	0.682	3.64E-05	7.51E-06	7.21E-05	1.28E-05	3.30E-04	6.83E-05	0.22	0.06
	3.97	126.90	28.382	0.567	2.93E-05	6.45E-06	6.53E-05	1.16E-05	2.67E-04	5.86E-05	0.24	0.07
	4.63	151.72	23.164	0.465	2.86E-05	5.55E-06	6.12E-05	1.11E-05	2.60E-04	5.04E-05	0.24	0.06
	6.92	236.73	67.524	1.324	3.08E-05	1.04E-05	6.87E-05	8.15E-06	2.80E-04	9.43E-05	0.25	0.09
	8.65	302.49	70.215	1.350	3.70E-05	3.17E-05	8.52E-05	3.20E-05	3.36E-04	2.88E-04	0.25	0.24
	9.40	325.02	30.970	0.564	3.44E-05	1.44E-05	7.51E-05	7.35E-06	3.13E-04	1.31E-04	0.24	0.10
	10.40	347.59	31.033	0.564	2.45E-05	2.56E-06	5.40E-05	9.63E-06	2.22E-04	2.33E-05	0.24	0.05
	10.67	352.94	24.004	0.638	2.08E-05	2.91E-06	6.05E-05	1.15E-05	1.89E-04	2.64E-05	0.32	0.08
	10.90	357.39	29.474	0.638	2.24E-05	2.57E-06	4.79E-05	9.38E-06	2.04E-04	2.34E-05	0.24	0.05
	11.32	365.16	33.754	0.638	2.07E-05	4.15E-06	5.36E-05	1.35E-05	1.88E-04	3.77E-05	0.28	0.09
	16.15	41.25	32.608	0.638	1.35E-05	2.65E-06	4.22E-05	1.16E-05	1.22E-04	2.41E-05	0.34	0.12
				Mean	$Ba/Ca_{(Cc)}$	**1σ**	$Ba/Ca_{(Ar)}$	**1σ**	$Ba/Ca_{(dw)}$	**1σ**	$D_{Ba(Ar)}$	**1σ**
				Cc-Ar	2.38E-05	6.80E-06	6.11E-05	1.27E-05	2.17E-04	6.19E-05	0.30	0.11
				Ar-Cc	2.71E-05	7.43E-06	6.24E-05	1.26E-05	2.47E-04	6.75E-05	0.26	0.04
				All	2.56E-05	7.17E-06	6.18E-05	1.23E-05	2.33E-04	6.51E-05	0.28	0.08

Though the experiments of Mucci and Morse (1983) were for marine analogues, the positive covariation between $D_{Sr(Cc)}$ and $\%MgCO_3$ provides compelling evidence for a Mg-content control on $D_{Sr(Cc)}$. The mechanism is not known, but incorporation of small Mg^{2+} ions into the larger Ca^{2+} cation site may distort the calcite crystal lattice such that it induces larger adjacent cation sites suitable for incorporation of Sr^{2+} (Mucci and Morse, 1983). Indeed, using their equation, $D_{Sr(Cc)}=0.146 + 1.833 * mol\%MgCO_3$, and the 3.2% $MgCO_3$ indicated by XRD on the calcite layers of TA12-2, yields a $D_{Sr(Cc)}$ of 0.2047. Applying this value to our back-calculations results in a mean $D_{Sr(Ar)}$ value of 0.8885±0.2706, much closer to the expected value of 1 indicating the preference of Sr towards aragonite.

Calculated mean $D_{U(Ar)}$ values are quite close to the expected values of ~1 though there is considerable spread in the data ($D_{U(Ar)}$ =1.4±1.12). This value is on par with studies of biogenic-precipitated aragonite from corals estimated in studies between 1963 and 1982, but lower than the recently calculated values for speleothems (Jamieson et al., 2016; Wassenburg et al., 2016), which range up to nearly 10. The large spread of data seems to stem from the initial concentration measurements, which are the least consistent across transitions of the four elements evaluated here, having the largest errors.

Calculated mean $D_{Ba(Ar)}$ values are, like $D_{Sr(Ar)}$ values, lower than expected, but highly consistent across transitions, yielding a mean value of 0.28±0.08. Ba and Sr both have ionic radii larger than Ca, leading to their preferential corporation into the aragonite lattice. As such, it is expected that $D_{Ba(Ar)}$ should be greater than 1, however, W16 also calculated $D_{Ba(Ar)}$ to be <1. The consistency of Ba/Ca between transitions suggests that the issue is not due to excess Ba through detrital input, but rather with the choice for $D_{Ba(Cc)}$. Our choice of $D_{Ba(Cc)}$=0.12 falls within the lower range of experimental values between 0.11 and 0.28 (Day and Henderson, 2013), which are of similar magnitude to cultured benthic foraminifera experiments (Havach et al., 2001), but an order of magnitude higher inorganic calcite precipitation experiments (Pingitore and Eastman, 1984; Tesoriero and Pankow, 1996; Yoshida et al., 2008). In order to achieve $D_{Ba(Ar)}$ values of >1, $D_{Ba(Cc)}$

must be larger than the published values (>0.3). Due to the similarities between Sr and Ba in terms of ionic radius, it is possible that a similar Mg-dependent mechanism distorts the calcite lattice to allow more Ba to be incorporated into the Ca sites. This would result in a higher $D_{Ba(Cc)}$ than has been previously published; however, inorganic karst analogue culturing experiments would be required to test the sensitivity of Ba concentrations to Mg content.

4.4.5 Aragonite-calcite mechanisms

An important question to ask is why aragonite is forming at all in this system. Previous studies using aragonite speleothems suggest that stable aragonite tends to precipitate from dolomite ($CaMg(CO_3)_2$) bedrock (Cosford et al., 2008; Li et al., 2011b; Wassenburg et al., 2013). Dry conditions have also been cited as a possible formation mechanism (Railsback et al., 1994), however, this explanation seems unlikely near Tangga Cave, which is relatively wet year-round. This provides a strong case for TA12-2 having been precipitated from dolomitic karst, which is supported by the XRD analysis of multiple bedrock samples from the cave. Some field experiments have shown that the host rock is the dominant control on the fluid Mg/Ca ratio (Riechelmann et al., 2014), while other studies on semi-arid sites have demonstrated significant contribution from soils (Rutlidge et al., 2014).

The higher Mg ion concentrations in the dripwater that result from dolomite dissolution inhibit calcite growth by adsorbing onto the surface of the calcite nuclei (Davis et al., 2000). At Mg/Ca ratios greater than 1.1, this allows aragonite nuclei to outcompete calcite formation (De Choudens-Sánchez and González, 2009; Frisia et al., 2002). Despite dry conditions not being prevalent in Sumatra, relatively drier periods can lead to increased residence times in the dolomite host rock, causing enhanced Mg-leaching into the dripwater, and further preventing calcite nucleation (Fairchild et al., 2000). In order for calcite to form, it would require the dripwater solution to be supersaturated in calcite or for dripwater Mg concentrations to decrease (De Choudens-Sánchez and González, 2009). As calcite did precipitate at times in the formation of the TA12-2 record, one or both of these two conditions must have been met in Tangga Cave. The latter condition could be

met with a high influx of low-Mg dripwater, which could decrease the dolomite residence time, and dilute the dripwater solution.

Though dilution of the high Mg karst reservoir must be a precursor to calcite formation, dilution events may not necessary occur during the wettest climatic intervals. Clusters of calcite layers appear in approximately three different locations on TA12-2; the mid-Holocene (~7.2 – 5.5 ky BP), the late deglacial (~11.5 – 8.5 ky BP), and towards the end of the Heinrich Stadial 1 (~16.3 – 15.5 ky BP). The mid-Holocene is thought to be a warmer, wetter period globally (Renssen et al., 2009). The deglaciation coincides with a regional increase in precipitation in the Indo-Pacific and Asian realms (Cheng et al., 2012) but is not as wet as the mid-Holocene. This suggests that the control on Mg dilution may be related to filtration rates, rather than rainfall amount; that is to say, drip water Mg concentration and subsequent phase changes may be more directly related to karst hydrology than regional precipitation patterns. Invoking a similar mechanism as suggested by Bar-Matthews et al. (1991), it is possible that floodwaters with low Mg concentration seeped into the cave quickly, decreasing residence time of the reservoir and diluting the Mg/Ca ratio of the dripwater solution, thus allowing calcite to form, and this increased filtration need not be related to higher-than-average annual rainfall (Figure 4.10).

The distribution of aragonite and calcite speleothems is variable within the cave. TA12-1 and TA12-2 grew principally as aragonite, however, TA12-8 grew principally as 3.2% Mg-calcite, switching to aragonite once during its tenure. Furthermore, TA12-8's calcite and TA12-1 and 2's aragonite precipitated simultaneously, demonstrating that cave hydrology was not homogenous. The geochemical characteristics of the drips feeding calcitic TA12-8 and aragonitic TA12-2 must have been different in saturation state, pH, or Mg content.

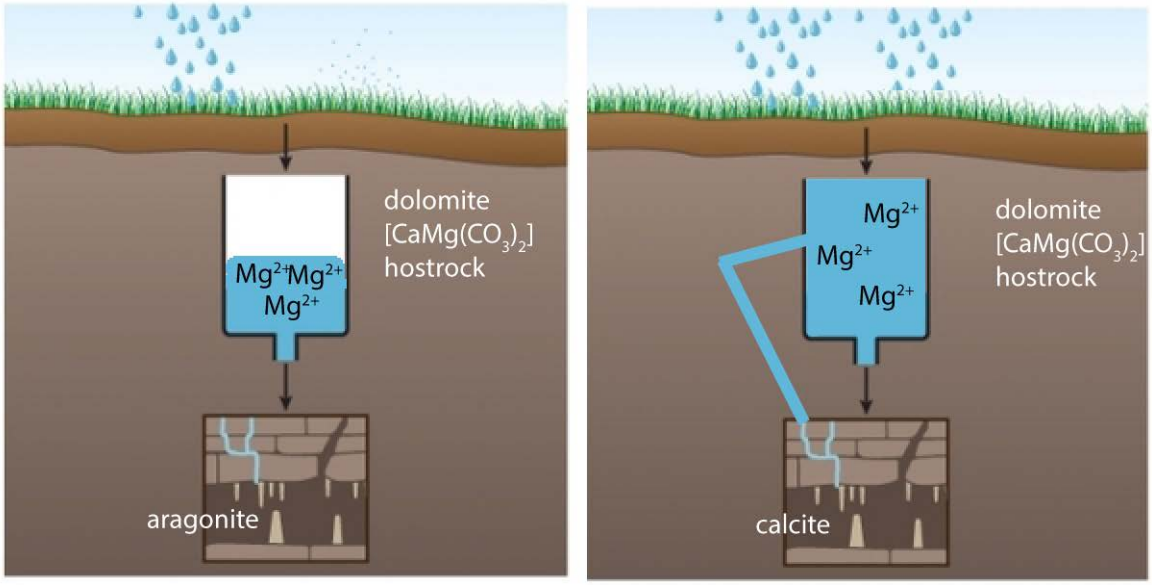

Figure 4.10 - Conditions for formation of aragonite vs. calcite in Tangga Cave. (left) Low filtration rates and long residence times allow Mg to leach from dolomite bedrock and cause high Mg concentrations in dripwater that inhibit calcite formation. (right) During high filtration events, the reservoir may fill, diluting the Mg concentration. Shorter residence times and, potentially, new flow paths, allow low-Mg water to reach the cave and calcite to form. Modified from Baker and Fairchild (2012).

4.4.6 Trace element environmental variability

Strontium, barium, uranium and magnesium trace element variability in TA12-2 is dominated by the crystallographic differences between aragonite and calcite, which lead to preferential incorporation of the former three into aragonite and magnesium into calcite. To examine environmental controls, rather than mineralogical controls, I examine how these elements change within the aragonite phase only. It might be expected that the extremely low incorporation into aragonite would obscure the environmental Mg signal, however, Mg shows extensive covariation with $\delta^{18}O$ for much of the record, including throughout the YD (Figure 4.11). Surprisingly, Mg is positively covarying with rainfall (interpreted from corrected $\delta^{18}O$ curve), in contrast with the majority of prior studies of Mg incorporation (e.g., Fairchild and Treble, 2009; Johnson et al., 2006; Sinclair et al., 2012; Treble et al., 2003).

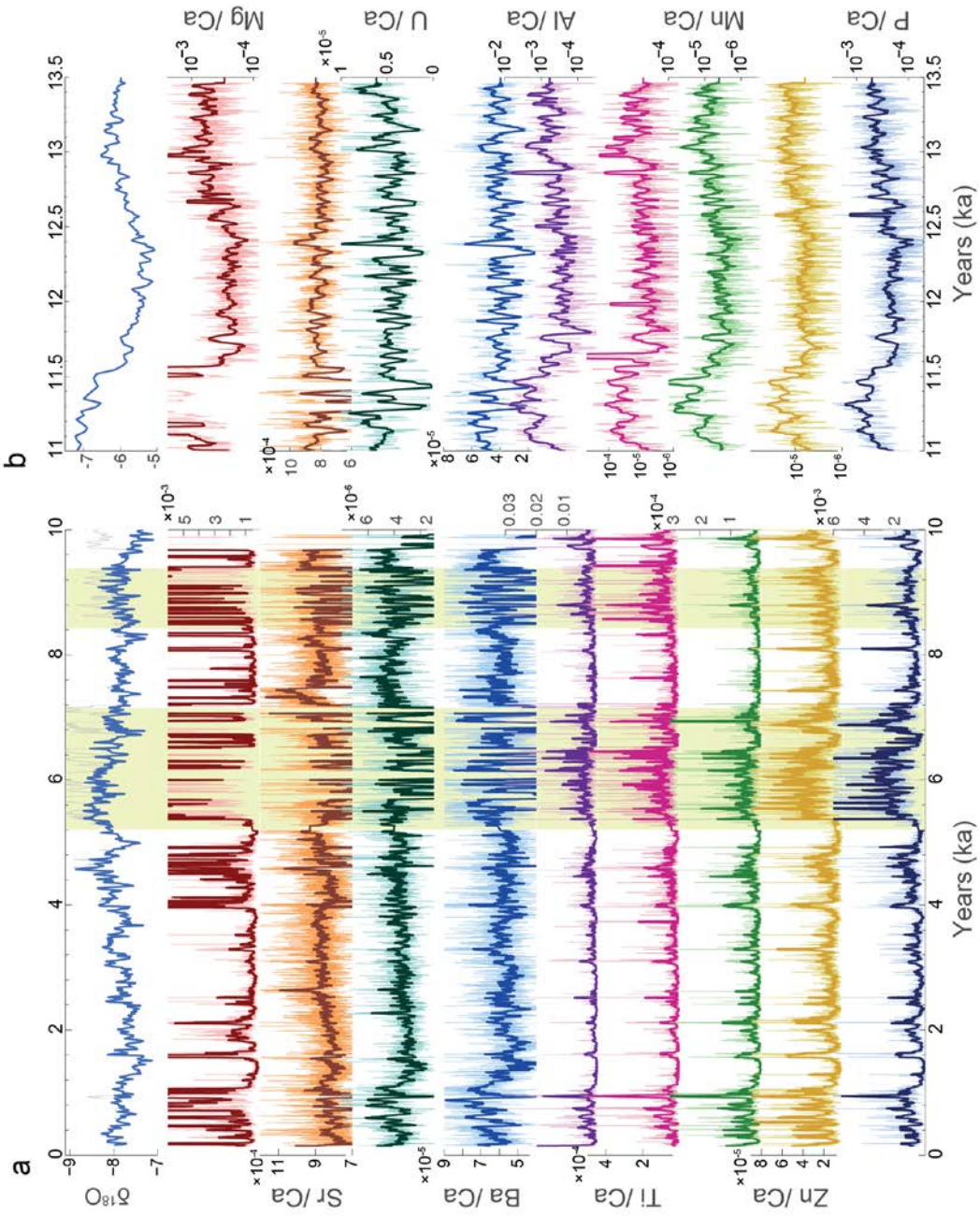

Figure 4.11 – Trace element variability during (a) the Holocene, and (b) Younger Dryas. Light colors are raw data, dark colors are 25-point smooth. Note that (a) and (b) are plotted on different y-scales. Y-axis is scaled to maximize trace element variability within aragonite phases. Vertical shading denotes clustering of spikes in particulate-bound elements.

Most studies of Mg incorporation describe an inverse relationship with rainfall; this includes studies from subannual to millennial time scales, and for both aragonitic and calcitic speleothems (Finch et al., 2001; Johnson et al., 2006; McMillan et al., 2005; Wassenburg et al., 2013). The most commonly proposed mechanism is PCP, in which dry periods promote the occurrence of prior degassing and precipitation of calcite earlier on the flow pathway, increasing Mg, Sr and Ba ratios and enriching $\delta^{13}C$ in the dripwater before it reaches the speleothem (Fairchild et al., 2000). If this were the case in TA12-2, we would expect to see high covariance between Mg, Sr, and Ba due to all having distribution coefficients <<1 (Sinclair et al., 2012). This is not apparent in the TA12-2 record. If aragonite, rather than calcite, were to prematurely precipitate (i.e., PAP), it could explain why Ba and Sr don't covary with Mg (i.e., $K_{Sr,Ba}$ are close to unity), but residual Mg concentrations in the drip water would be even higher when $\delta^{18}O$ is higher (Wassenburg et al., 2013), which, again, is the opposite of what is observed in TA12-2. Another mechanism used to explain changes in Mg concentration is increased residence time in a dolomite aquifer, allowing for increased leaching of Mg (Fairchild et al., 2000) Again, in this instance, we would expect higher Mg/Ca ratios in drier periods, which is not the case.

One possible explanation for the positive covariation between Mg and rainfall could be that Mg is entering the speleothem as a particulate in clay minerals and adsorbing onto the aragonite crystal surface (Wassenburg et al., 2013). This hypothesis would likely require a rapid growth rate to 'capture' the Mg that has bound to the surface (Watson, 1996). The entry-by-particulate theory is supported by similar profiles in other colloidal and particulate clay mineral elements, such as Al, Mn, and Zn, which would also increase with enhanced filtration (Yang et al., 2015).

Aside from the divalent cations, most other elements exhibit a coherent pattern within TA12-2. Al, P, Ti, Zn, and Mn all have generally low background concentrations with clusters of 'spikes' (Figure 4.11). The spike clusters appear to roughly correspond to the darkest layers of the speleothem, while values return to

near zero in whiter, cleaner-looking layers. This strongly suggests that these elements are tied to increased detrital input. Though not necessarily associated with higher rainfall, the detrital layers and element spikes are most likely associated with increased filtration into the cave, or regular flooding of Tangga cave from the river that today passes through the lower levels.

4.5 Conclusions

Aragonite speleothems can potentially serve as robust archives for paleoclimatic reconstruction if understanding of the constraints on their trace element and isotope geochemistry can be improved. This study used a unique aragonitic speleothem with intermittent calcite layers to evaluate oxygen isotope fractionation differences between aragonite and calcite, estimate distribution coefficients of major trace elements into aragonite, and assess environmental controls on trace element variability and aragonite-calcite precipitation.

I was unable to resolve the oxygen fractionation offset between aragonite and calcite likely due to a combination of kinetic effects on subdecadal timescales and dating uncertainties for TA12-8. However, the difference in $\delta^{18}O$ values inferred from the simultaneous growth of TA12-2 and TA12-8 are in the range of 0.6-1.0‰. Furthermore, a correction closer to 1‰ is required to bring TA12-2 calcite $\delta^{18}O$ values in line with adjacent aragonite $\delta^{18}O$ values.

Our estimate of mean aragonite distribution coefficients for Mg ($D_{Mg(Ar)}$= 0.00329±0.00158), Sr ($D_{Sr(Ar)}$= 0.52±0.16), U ($D_{U(Ar)}$= 1.40±1.12), and Ba ($D_{Sr(Ar)}$= 0.28±0.08), do not generally replicate the values produced by W16. $D_{Mg(Ar)}$ is two orders of magnitude higher than that estimated by W16, possibly related to excess particulate Mg. $D_{Sr(Ar)}$ is less than the 1 predicted by ionic theory, but could potentially closer to 1 if a $D_{Sr(Cc)}$ accounting for Mg mol% were used. $D_{Ba(Ar)}$ may be subject to similar effects as $D_{Sr(Ar)}$. $D_{U(Ar)}$ is close to the expected value of 1, but significantly lower than 4-9 range estimated by W16.

Our calculated partition coefficients are in poor agreement with previous studies, and with ionic theory, leading us to conclude that excess element concentrations in detrital material being measured by laser-ablation are likely interfering with our calculation of the coefficients. Alternatively, poor constraints on calcite partition coefficients may also lead to inaccurate quantification of aragonite partition coefficients. Additional karst analogue and natural karst studies are required to refine our understanding of Mg content on partition coefficients in both carbonate phases.

The presence of detrital Mg is further supported by the similar patterns with trace elements that typically become mobile by adsorption onto colloidal particles (e.g., Mn, Al, Th) (Fairchild and Treble, 2009). Spikes in these elements are likely related to increased filtration into the cave. The presence of these spikes is often, though not always, associated with the appearance of calcite in the speleothem. From this, we deduce that calcite precipitation is initiated by high filtration into the cave, and dilution of the Mg concentration in the karst reservoir.

4.5.1 Future work

There were multiple limitations on the quantification of oxygen isotope fractionation offsets between aragonite and calcite. First, a point-to-point comparison of TA12-2 and TA12-8 requires a more refined age model due to natural variability of the samples and the frequent transitions between calcite and aragonite in TA12-2. Secondly, TA12-8 has only been tested for mineralogy through bulk XRD analysis. The interval of ^{18}O enrichment at the base of TA12-8 demonstrates that aragonite is present for at least part of the growth period. Raman spectroscopy and thin section petrography should be used to confirm TA12-8 mineralogy throughout its length to rule out co-precipitation of phases. This will also be important for correcting the TA12-8 $\delta^{18}O$ record for use in future climate reconstructions.

In addition to better constraints on TA12-8's chronology and mineralogy, high-resolution $\delta^{18}O$ analysis across calcite-aragonite transitions in TA12-2 could be used to quantify the isotopic difference immediately at the transition. Though this

resolution is not achievable by isotope ratio mass spectrometry, ANU is home to the Sensitive High Resolution Ion Microprobe for Stable Isotopes (SHRIMP SI), which is capable of resolving oxygen isotopic differences of 0.1‰ at spatial scales of 10-30 μm.

There is still much room for improvement on the calculation of the distribution coefficients in aragonite. The calculation of the mean element concentrations in aragonite and calcite was determined by using 12 points on either side of the changepoint transition. This method includes one or two transitional points on either side of the transition, such that error is introduced into the mean. Eliminating several points from either side of the change point would promote greater accuracy. Calculation of excess calcium, as was performed in W16, may also improve the final estimates. Furthermore, the current method of error propagation only includes the error on the mean of the twelve trace element measurements for each carbonate phase. Future work should improve this by including the error on the choice of $D_{Tr(Cc)}$ as well as the analytical error on the laser ablation trace elements. This method may benefit from a Monte Carlo approach to error propagation.

However, the primary source of error is likely due to extra-lattice detritus. Detrital material likely contributes to excess concentrations of trace elements in both the aragonite and calcite. It may be possible to remove some of the extra-lattice detrital material through ultrasonication of gently crushed samples (Kaufman et al., 1998). Trace element concentrations could then be measured by ICP-AES. Ultrasonication of thin section surfaces and subsequent measurement by LA-ICP-MS could also be attempted. However, the best approach, in lieu of paleo-dripwater measurements, may be to calculate the "speleothem enrichment factor" by comparing the concentration of trace elements in the host rock with the concentration in the speleothem (Frisia et al., 2012). As the dripwater should primarily reflect the host rock composition, differences between the host rock concentration and speleothem concentration can be informative about other

sources of trace element. Additional bedrock and soil samples from the cave site would also aid in constraining trace element contributions from these sources.

Discussion with the authors of the original $D_{Tr(Ar)}$ study, Jasper Wassenberg et al., will also provide valuable feedback moving forward towards a journal-ready publication and dialogue was initiated with first author Jasper Wassenberg (University of Mainz) at the Karst Record 7 conference in Melbourne in 2014 and with second author Denis Scholz at Karst Record 8 in Austin in 2017.

The aragonite-calcite speleothem featured in this thesis is a truly unique sample that may yet yield more information about the roles of karst hydrology and biomediation in the precipitation of carbonate phases and fabrics. Future work with Silvia Frisia (University of Newcastle), expert in speleothem petrography, could target specific transitions in the speleothem with micro-fluorescence to expand upon our initial observations of microbial mats. There is a growing body of literature on the occurrence and function of microbial mats and biofilms in cave settings (e.g., Jones, 2011; Northup and Lavoie, 2001; Northup et al., 2011). Scanning electron microscopy (SEM) and transmission electron microscopy (TEM) will be powerful tools in determining the origin and formation of the dark, organic lamina observed in TA12-2.

This study would also benefit from developing a conceptual model for speleothem growth in the Tangga Cave system, which may ultimately be broadly relevant in the field as aragonite speleothem reconstructions become more common. Pauline Treble (ANSTO) is an expert in karst hydrology, groundwater interactions, and speleothem trace elements and isotopes, who may be able to assist in this endeavor.

References

Bajo, P., Hellstrom, J., Frisia, S., Drysdale, R., Black, J., Woodhead, J., Borsato, A., Zanchetta, G., Wallace, M.W., Regattieri, E., Haese, R. (2016). "Cryptic" diagenesis and its implications for speleothem geochronologies. Quaternary Science Reviews 148, 17-28. http://dx.doi.org/10.1016/j.quascirev.2016.06.020

Baker, A., Fairchild, I. (2012), Drip water hydrology and speleothems. Nature Education Knowledge.

Bar-Matthews, M., Matthews, A., Ayalon, A. (1991). Environmental controls of speleothem mineralogy in a karstic dolomitic terrain (Soreq Cave, Israel). The Journal of Geology 99, 189-207.

Barber, A.J., Crow, M.J., Milsom, J. (2005), Sumatra: geology, resources and tectonic evolution. Geological Society of London.

Belli, R., Borsato, A., Frisia, S., Drysdale, R., Maas, R., Greig, A. (2017). Investigating the hydrological significance of stalagmite geochemistry (Mg, Sr) using Sr isotope and particulate element records across the Late Glacial-to-Holocene transition. Geochimica et Cosmochimica Acta 199, 247-263. http://dx.doi.org/10.1016/j.gca.2016.10.024

Bischoff, W.D., Bishop, F.C., Mackenzie, F.T. (1983). Biogenically produced magnesian calcite: inhomogeneities in chemical and physical properties: comparison with synthetic phases. American Mineralogist 68, 1183-1188.

Blaauw, M., Christen, J.A. (2011). Flexible paleoclimate age-depth models using an autoregressive gamma process. Bayesian Analysis 6, 457-474. http://dx.doi.org/10.1214/11-Ba618

Böhm, F., Joachimski, M.M., Dullo, W.-C., Eisenhauer, A., Lehnert, H., Reitner, J., Wörheide, G. (2000). Oxygen isotope fractionation in marine aragonite of coralline sponges. Geochimica et Cosmochimica Acta 64, 1695-1703. http://dx.doi.org/10.1016/S0016-7037(99)00408-1

Cheng, H., Lawrence Edwards, R., Shen, C.-C., Polyak, V.J., Asmerom, Y., Woodhead, J., Hellstrom, J.C., Wang, Y., Kong, X., Spötl, C., Wang, X., Calvin Alexander Jr, E. (2013). Improvements in ^{230}Th dating, ^{230}Th and ^{234}U half-life values, and U–Th isotopic measurements by multi-collector inductively coupled plasma mass spectrometry. Earth and Planetary Science Letters 371–372, 82-91. http://dx.doi.org/10.1016/j.epsl.2013.04.006

Cheng, H., Sinha, A., Wang, X., Cruz, F.W., Edwards, R.L. (2012). The Global Paleomonsoon as seen through speleothem records from Asia and the Americas. Climate Dynamics 39, 1045-1062. http://dx.doi.org/10.1007/s00382-012-1363-7

Cosford, J., Qing, H., Eglington, B., Mattey, D., Yuan, D., Zhang, M., Cheng, H. (2008). East Asian monsoon variability since the Mid-Holocene recorded in a high-resolution, absolute-dated aragonite speleothem from eastern China. Earth and Planetary Science Letters 275, 296-307. http://dx.doi.org/10.1016/j.epsl.2008.08.018

Davis, K.J., Dove, P.M., De Yoreo, J.J. (2000). The Role of Mg^{2+} as an Impurity in Calcite Growth. Science 290, 1134-1137. http://dx.doi.org/10.1126/science.290.5494.1134

Day, C.C., Henderson, G.M. (2013). Controls on trace-element partitioning in cave-analogue calcite. Geochimica et Cosmochimica Acta 120, 612-627. http://dx.doi.org/10.1016/j.gca.2013.05.044

De Choudens-Sánchez, V., González, L.A. (2009). Calcite and aragonite precipitation under controlled instantaneous supersaturation: Elucidating the role of $CaCO_3$ saturation state and Mg/Ca ratio on calcium carbonate

polymorphism. Journal of Sedimentary Research 79, 363-376. http://dx.doi.org/10.2110/jsr.2009.043

Deer, W.A., Howie, R.A., Zussman, J. (2013), An Introduction to the Rock-Forming Minerals, 3rd ed. The Mineralogical Society, London.

Denniston, R.F., Wyrwoll, K.-H., Polyak, V.J., Brown, J.R., Asmerom, Y., Wanamaker Jr, A.D., LaPointe, Z., Ellerbroek, R., Barthelmes, M., Cleary, D., Cugley, J., Woods, D., Humphreys, W.F. (2013). A stalagmite record of Holocene Indonesian–Australian summer monsoon variability from the Australian tropics. Quaternary Science Reviews 78, 155-168. http://dx.doi.org/10.1016/j.quascirev.2013.08.004

Fairchild, I.J., Baker, A. (2012), Speleothem science: from process to past environments. Wiley-Blackwell.

Fairchild, I.J., Baker, A., Borsato, A., Frisia, S., Hinton, R.W., McDermott, F., Tooth, A.F. (2001). Annual to sub-annual resolution of multiple trace-element trends in speleothems. Journal of the Geological Society 158, 831-841. http://dx.doi.org/10.1144/jgs.158.5.831

Fairchild, I.J., Borsato, A., Tooth, A.F., Frisia, S., Hawkesworth, C.J., Huang, Y., McDermott, F., Spiro, B. (2000). Controls on trace element (Sr–Mg) compositions of carbonate cave waters: implications for speleothem climatic records. Chemical Geology 166, 255-269. http://dx.doi.org/10.1016/S0009-2541(99)00216-8

Fairchild, I.J., Treble, P.C. (2009). Trace elements in speleothems as recorders of environmental change. Quaternary Science Reviews 28, 449-468. http://dx.doi.org/10.1016/j.quascirev.2008.11.007

Finch, A.A., Shaw, P.A., Weedon, G.P., Holmgren, K. (2001). Trace element variation in speleothem aragonite: potential for palaeoenvironmental reconstruction. Earth and Planetary Science Letters 186, 255-267. http://dx.doi.org/10.1016/S0012-821x(01)00253-9

Frisia, S., Borsato, A., Drysdale, R.N., Paul, B., Greig, A., Cotte, M. (2012). A re-evaluation of the palaeoclimatic significance of phosphorus variability in speleothems revealed by high-resolution synchrotron micro XRF mapping. Climate of the Past 8, 2039-2051. http://dx.doi.org/10.5194/cp-8-2039-2012

Frisia, S., Borsato, A., Fairchild, I.J., McDermott, F., Selmo, E.M. (2002). Aragonite-calcite relationships in speleothems (Grotte De Clamouse, France): Environment, fabrics, and carbonate geochemistry. Journal of Sedimentary Research 72, 687-699. http://dx.doi.org/10.1306/020702720687

Gascoyne, M. (1983). Trace-element partition coefficients in the calcite-water system and their paleoclimatic significance in cave studies. Journal of Hydrology 61, 213-222. http://dx.doi.org/10.1016/0022-1694(83)90249-4

Grossman, E.L., Ku, T.-L. (1986). Oxygen and carbon isotope fractionation in biogenic aragonite: Temperature effects. Chemical Geology: Isotope Geoscience section 59, 59-74. http://dx.doi.org/10.1016/0168-9622(86)90057-6

Havach, S.M., Chandler, G.T., Wilson-Finelli, A., Shaw, T.J. (2001). Experimental determination of trace element partition coefficients in cultured benthic

foraminifera. Geochimica et Cosmochimica Acta 65, 1277-1283. http://dx.doi.org/10.1016/S0016-7037(00)00563-9

Hellstrom, J. (2003). Rapid and accurate U/Th dating using parallel ion-counting multi-collector ICP-MS. Journal of Analytical Atomic Spectrometry 18, 1346-1351. http://dx.doi.org/10.1039/b308781f

Hellstrom, J.C. (2006). U–Th dating of speleothems with high initial ^{230}Th using stratigraphical constraint. Quaternary Geochronology 1, 289-295. http://dx.doi.org/10.1016/j.quageo.2007.01.004

Hill, C.A., Forti, P. (1997), Cave minerals of the world. National speleological society.

Holmgren, K., Lee-Thorp, J.A., Cooper, G.R.J., Lundblad, K., Partridge, T.C., Scott, L., Sithaldeen, R., Siep Talma, A., Tyson, P.D. (2003). Persistent millennial-scale climatic variability over the past 25,000 years in Southern Africa. Quaternary Science Reviews 22, 2311-2326. http://dx.doi.org/10.1016/S0277-3791(03)00204-X

Holzkämper, S., Holmgren, K., Lee-Thorp, J., Talma, S., Mangini, A., Partridge, T. (2009). Late Pleistocene stalagmite growth in Wolkberg Cave, South Africa. Earth and Planetary Science Letters 282, 212-221. http://dx.doi.org/10.1016/j.epsl.2009.03.016

Huang, Y., Fairchild, I.J. (2001). Partitioning of Sr^{2+} and Mg^{2+} into calcite under karst-analogue experimental conditions. Geochimica et Cosmochimica Acta 65, 47-62. http://dx.doi.org/10.1016/S0016-7037(00)00513-5

Huang, Y., Fairchild, I.J., Borsato, A., Frisia, S., Cassidy, N.J., McDermott, F., Hawkesworth, C.J. (2001). Seasonal variations in Sr, Mg and P in modern speleothems (Grotta di Ernesto, Italy). Chemical Geology 175, 429-448. http://dx.doi.org/10.1016/S0009-2541(00)00337-5

Jamieson, R.A., Baldini, J.U.L., Brett, M.J., Taylor, J., Ridley, H.E., Ottley, C.J., Prufer, K.M., Wassenburg, J.A., Scholz, D., Breitenbach, S.F.M. (2016). Intra- and inter-annual uranium concentration variability in a Belizean stalagmite controlled by prior aragonite precipitation: a new tool for reconstructing hydro-climate using aragonitic speleothems. Geochimica et Cosmochimica Acta 190, 332-346. http://dx.doi.org/10.1016/j.gca.2016.06.037

Johnson, K.R., Hu, C., Belshaw, N.S., Henderson, G.M. (2006). Seasonal trace-element and stable-isotope variations in a Chinese speleothem: The potential for high-resolution paleomonsoon reconstruction. Earth and Planetary Science Letters 244, 394-407. http://dx.doi.org/10.1016/j.epsl.2006.01.064

Jones, B. (2011). Stalactite Growth Mediated by Biofilms: Example from Nani Cave, Cayman Brac, British West Indies. Journal of Sedimentary Research 81, 322-338. http://dx.doi.org/10.2110/jsr.2011.28

Kaufman, A., Wasserburg, G.J., Porcelli, D., Bar-Matthews, M., Ayalon, A., Halicz, L. (1998). U-Th isotope systematics from the Soreq cave, Israel and climatic correlations. Earth and Planetary Science Letters 156, 141-155. http://dx.doi.org/10.1016/S0012-821x(98)00002-8

Kim, S.-T., O'Neil, J.R., Hillaire-Marcel, C., Mucci, A. (2007). Oxygen isotope fractionation between synthetic aragonite and water: Influence of temperature and Mg^{2+} concentration. Geochimica et Cosmochimica Acta 71, 4704-4715. http://dx.doi.org/10.1016/j.gca.2007.04.019

Kotlia, B.S., Singh, A.K., Joshi, L.M., Dhaila, B.S. (2014). Precipitation variability in the Indian Central Himalaya during last ca. 4,000 years inferred from a speleothem record: Impact of Indian Summer Monsoon (ISM) and Westerlies. Quaternary International. http://dx.doi.org/10.1016/j.quaint.2014.10.066

Lachniet, M.S., Bernal, J.P., Asmerom, Y., Polyak, V. (2012). Uranium loss and aragonite–calcite age discordance in a calcitized aragonite stalagmite. Quaternary Geochronology 14, 26-37. http://dx.doi.org/10.1016/j.quageo.2012.08.003

Li, H.-C., Lee, Z.-H., Wan, N.-J., Shen, C.-C., Li, T.-Y., Yuan, D.-X., Chen, Y.-H. (2011a). The $\delta^{18}O$ and $\delta^{13}C$ records in an aragonite stalagmite from Furong Cave, Chongqing, China: A-2000-year record of monsoonal climate. Journal of Asian Earth Sciences 40, 1121-1130. http://dx.doi.org/10.1016/j.jseaes.2010.06.011

Li, T.-Y., Shen, C.-C., Li, H.-C., Li, J.-Y., Chiang, H.-W., Song, S.-R., Yuan, D.-X., Lin, C.D.J., Gao, P., Zhou, L., Wang, J.-L., Ye, M.-Y., Tang, L.-L., Xie, S.-Y. (2011b). Oxygen and carbon isotopic systematics of aragonite speleothems and water in Furong Cave, Chongqing, China. Geochimica et Cosmochimica Acta 75, 4140-4156. http://dx.doi.org/10.1016/j.gca.2011.04.003

McDermott, F. (2004). Palaeo-climate reconstruction from stable isotope variations in speleothems: a review. Quaternary Science Reviews 23, 901-918. http://dx.doi.org/10.1016/j.quascirev.2003.06.021

McMillan, E.A., Fairchild, I.J., Frisia, S., Borsato, A., McDermott, F. (2005). Annual trace element cycles in calcite–aragonite speleothems: evidence of drought in the western Mediterranean 1200–1100 yr BP. Journal of Quaternary Science 20, 423-433. http://dx.doi.org/10.1002/jqs.943

Meyer, H.J. (1984). The influence of impurities on the growth rate of calcite. Journal of Crystal Growth 66, 639-646. http://dx.doi.org/10.1016/0022-0248(84)90164-7

Mohtadi, M., Prange, M., Oppo, D.W., De Pol-Holz, R., Merkel, U., Zhang, X., Steinke, S., Luckge, A. (2014). North Atlantic forcing of tropical Indian Ocean climate. Nature 509, 76-80. http://dx.doi.org/10.1038/nature13196

Morse, J.W., Bender, M.L. (1990). Partition coefficients in calcite: Examination of factors influencing the validity of experimental results and their application to natural systems. Chemical Geology 82, 265-277. http://dx.doi.org/10.1016/0009-2541(90)90085-L

Mucci, A., Morse, J.W. (1983). The incorporation of Mg^{2+} and Sr^{2+} into calcite overgrowths: influences of growth rate and solution composition. Geochimica et Cosmochimica Acta 47, 217-233. http://dx.doi.org/10.1016/0016-7037(83)90135-7

Northup, D.E., Lavoie, K.H. (2001). Geomicrobiology of caves: A review. Geomicrobiology Journal 18, 199-222. http://dx.doi.org/10.1080/01490450152467750

Northup, D.E., Melim, L.A., Spilde, M.N., Hathaway, J.J., Garcia, M.G., Moya, M., Stone, F.D., Boston, P.J., Dapkevicius, M.L., Riquelme, C. (2011). Lava cave microbial communities within mats and secondary mineral deposits: implications for

life detection on other planets. Astrobiology 11, 601-618. http://dx.doi.org/10.1089/ast.2010.0562

Ortega, R., Maire, R., Devès, G., Quinif, Y. (2005). High-resolution mapping of uranium and other trace elements in recrystallized aragonite–calcite speleothems from caves in the Pyrenees (France): Implication for U-series dating. Earth and Planetary Science Letters 237, 911-923. http://dx.doi.org/10.1016/j.epsl.2005.06.045

Pingitore, N.E., Eastman, M.P. (1984). The experimental partitioning of Ba^{2+} into calcite. Chemical Geology 45, 113-120. http://dx.doi.org/10.1016/0009-2541(84)90118-9

Railsback, L.B., Brook, G.A., Chen, J., Kalin, R., Fleisher, C.J. (1994). Environmental controls on the petrology of a late Holocene speleothem from Botswana with annual layers of aragonite and calcite. Journal of Sedimentary Research 64, 147-155. http://dx.doi.org/10.1306/D4267D39-2B26-11D7-8648000102C1865D

Reeder, R.J., Nugent, M., Lamble, G.M., Tait, C.D., Morris, D.E. (2000). Uranyl incorporation into calcite and aragonite: XAFS and luminescence studies. Environmental Science & Technology 34, 638-644. http://dx.doi.org/10.1021/es990981j

Renssen, H., Seppa, H., Heiri, O., Roche, D.M., Goosse, H., Fichefet, T. (2009). The spatial and temporal complexity of the Holocene thermal maximum. Nature Geoscience 2, 411-414. http://dx.doi.org/10.1038/Ngeo513

Riechelmann, S., Schröder-Ritzrau, A., Wassenburg, J.A., Schreuer, J., Richter, D.K., Riechelmann, D.F.C., Terente, M., Constantin, S., Mangini, A., Immenhauser, A. (2014). Physicochemical characteristics of drip waters: Influence on mineralogy and crystal morphology of recent cave carbonate precipitates. Geochimica et Cosmochimica Acta 145, 13-29. http://dx.doi.org/10.1016/j.gca.2014.09.019

Ruggieri, E., Lawrence, C.E. (2014). The Bayesian Change Point and Variable Selection Algorithm: Application to the $\delta^{18}O$ Proxy Record of the Plio-Pleistocene. Journal of Computational and Graphical Statistics 23, 87-110. http://dx.doi.org/10.1080/10618600.2012.707852

Rutlidge, H., Baker, A., Marjo, C.E., Andersen, M.S., Graham, P.W., Cuthbert, M.O., Rau, G.C., Roshan, H., Markowska, M., Mariethoz, G., Jex, C.N. (2014). Dripwater organic matter and trace element geochemistry in a semi-arid karst environment: Implications for speleothem paleoclimatology. Geochimica et Cosmochimica Acta 135, 217-230. http://dx.doi.org/10.1016/j.gca.2014.03.036

Scroxton, N., Gagan, M.K., Dunbar, G.B., Ayliffe, L.K., Hantoro, W.S., Shen, C.-C., Hellstrom, J.C., Zhao, J.-x., Cheng, H., Edwards, R.L., Sun, H., Rifai, H. (2016). Natural attrition and growth frequency variations of stalagmites in southwest Sulawesi over the past 530,000 years. Palaeogeography, Palaeoclimatology, Palaeoecology 441, 823-833. http://dx.doi.org/10.1016/j.palaeo.2015.10.030

Silitonga, P.H., Kastowo (1995), Geologic Map of the Solok Quadrangle, Sumatra, in: Ratman, N. (Ed.), 2 ed. Pusat Penelitian Dan Pengembangan Geologi, Bandung.

Sinclair, D.J., Banner, J.L., Taylor, F.W., Partin, J., Jenson, J., Mylroie, J., Goddard, E., Quinn, T., Jocson, J., Miklavič, B. (2012). Magnesium and strontium systematics in tropical speleothems from the Western Pacific. Chemical Geology 294–295, 1-17. http://dx.doi.org/10.1016/j.chemgeo.2011.10.008

Stuijts, I., Newsome, J.C., Flenley, J.R. (1988). Evidence for late quaternary vegetational change in the Sumatran and Javan highlands. Review of Palaeobotany and Palynology 55, 207-216. http://dx.doi.org/10.1016/0034-6667(88)90086-3

Tarutani, T., Clayton, R.N., Mayeda, T.K. (1969). The effect of polymorphism and magnesium substitution on oxygen isotope fractionation between calcium carbonate and water. Geochimica et Cosmochimica Acta 33, 987-996. http://dx.doi.org/10.1016/0016-7037(69)90108-2

Tesoriero, A.J., Pankow, J.F. (1996). Solid solution partitioning of Sr^{2+}, Ba^{2+}, and Cd^{2+} to calcite. Geochimica et Cosmochimica Acta 60, 1053-1063. http://dx.doi.org/10.1016/0016-7037(95)00449-1

Treble, P., Shelley, J.M.G., Chappell, J. (2003). Comparison of high resolution sub-annual records of trace elements in a modern (1911–1992) speleothem with instrumental climate data from southwest Australia. Earth and Planetary Science Letters 216, 141-153. http://dx.doi.org/10.1016/S0012-821x(03)00504-1

Treble, P.C., Chappell, J., Shelley, J.M.G. (2005). Complex speleothem growth processes revealed by trace element mapping and scanning electron microscopy of annual layers. Geochimica et Cosmochimica Acta 69, 4855-4863. http://dx.doi.org/10.1016/j.gca.2005.06.008

Wassenburg, J.A., Immenhauser, A., Richter, D.K., Jochum, K.P., Fietzke, J., Deininger, M., Goos, M., Scholz, D., Sabaoui, A. (2012). Climate and cave control on Pleistocene/Holocene calcite-to-aragonite transitions in speleothems from Morocco: Elemental and isotopic evidence. Geochimica et Cosmochimica Acta 92, 23-47. http://dx.doi.org/10.1016/j.gca.2012.06.002

Wassenburg, J.A., Immenhauser, A., Richter, D.K., Niedermayr, A., Riechelmann, S., Fietzke, J., Scholz, D., Jochum, K.P., Fohlmeister, J., Schröder-Ritzrau, A., Sabaoui, A., Riechelmann, D.F.C., Schneider, L., Esper, J. (2013). Moroccan speleothem and tree ring records suggest a variable positive state of the North Atlantic Oscillation during the Medieval Warm Period. Earth and Planetary Science Letters 375, 291-302. http://dx.doi.org/10.1016/j.epsl.2013.05.048

Wassenburg, J.A., Scholz, D., Jochum, K.P., Cheng, H., Oster, J., Immenhauser, A., Richter, D.K., Häger, T., Jamieson, R.A., Baldini, J.U.L., Hoffmann, D., Breitenbach, S.F.M. (2016). Determination of aragonite trace element distribution coefficients from speleothem calcite-aragonite transitions. Geochimica et Cosmochimica Acta 190, 347-367. http://dx.doi.org/10.1016/j.gca.2016.06.036

Watson, E.B. (1996). Surface enrichment and trace-element uptake during crystal growth. Geochimica et Cosmochimica Acta 60, 5013-5020. http://dx.doi.org/10.1016/S0016-7037(96)00299-2

White, W.B. (2006). Identification of cave minerals by Raman spectroscopy: new technology for non-destructive analysis. International Journal of Speleology 35, 103-107.

Wurtzel, J.B., Abram, N.J., Lewis, S.C., Bajo, P., Hellstrom, J.C., Troitzsch, U., Heslop, D. (2018). Tropical Indo-Pacific hydroclimate response to North Atlantic forcing during the last deglaciation as recorded by a speleothem from Sumatra, Indonesia. Earth and Planetary Science Letters 492, 264-278. http://dx.doi.org/10.1016/j.epsl.2018.04.001

Yang, Q., Scholz, D., Jochum, K.P., Hoffmann, D.L., Stoll, B., Weis, U., Schwager, B., Andreae, M.O. (2015). Lead isotope variability in speleothems—A promising new proxy for hydrological change? First results from a stalagmite from western Germany. Chemical Geology 396, 143-151. http://dx.doi.org/10.1016/j.chemgeo.2014.12.028

Yoshida, Y., Yoshikawa, H., Nakanishi, T. (2008). Partition coefficients of Ra and Ba in calcite. GEOCHEMICAL JOURNAL 42, 295-304. http://dx.doi.org/10.2343/geochemj.42.295

Zhang, H.-L., Yu, K.-F., Zhao, J.-X., Feng, Y.-X., Lin, Y.-S., Zhou, W., Liu, G.-H. (2013). East Asian Summer Monsoon variations in the past 12.5ka: High-resolution $\delta^{18}O$ record from a precisely dated aragonite stalagmite in central China. Journal of Asian Earth Sciences 73, 162-175. http://dx.doi.org/10.1016/j.jseaes.2013.04.015

Zhou, H., Chi, B., Lawrence, M., Zhao, J., Yan, J., Greig, A., Feng, Y. (2008). High-resolution and precisely dated record of weathering and hydrological dynamics recorded by manganese and rare-earth elements in a stalagmite from Central China. Quaternary Research 69, 438-446. http://dx.doi.org/10.1016/j.yqres.2008.02.005

5 Conclusions

5.1 Revisiting the Research Objectives

1) **What was the state of hydroclimate in the Indo-Pacific Warm Pool during the last deglaciation, particularly during the Younger Dryas? How do North Atlantic abrupt events manifest in the IPWP?**

Chapter 2 presented a new deglacial stalagmite record from Sumatra, Indonesia. The Sumatran speleothem demonstrates a clear deglacial structure that includes ^{18}O enrichment during the Younger Dryas and ^{18}O depletion during the Bølling-Allerød, similar to the pattern seen in speleothems of the Asian and Indian monsoon realms. The speleothem $\delta^{18}O$ changes at this site are best explained by changes in rainfall amount and changes in the contributions from different moisture pathways. Reduced rainfall in Sumatra during the Younger Dryas is most likely driven by reductions in convection along the northern or southern monsoon transport pathways to Sumatra. Considered with other regional proxies, the record from Sumatra suggests the response of the IPWP to North Atlantic freshwater forcing is not solely driven by southward shifts of the ITCZ, but also weakened Hadley cell convection.

2) **What are the major sources of moisture to Indo-Pacific speleothem sites and how have these sources changed over time? How might these sources contribute to the variability in rainfall $\delta^{18}O$?**

Chapter 3 used isotope-enabled models and back-trajectory air parcel analysis to evaluate moisture source regions at eight key Indo-Pacific sites. Mawmluh Cave moisture is dominated by Indian Ocean sources, though the amount effect is very weak at this site, possibly due to a time-lagged response to Bay of Bengal freshening. During hosing, moisture sources may have become more localized. Dongge Cave displays a weak amount effect with modern moisture sources from the Indian and Pacific Oceans. The Indian source dominates during boreal summer but during hosing events, this source decreases and the Pacific source may have contributed more. Palawan has a relatively weak amount effect for the tropics

with rainfall primarily arriving from the Karimata Strait during boreal summer. Pacific contributions become high during November and December. Topography likely played an important role in modulating past moisture pathways as the Karimata Strait would have been exposed during periods of lower sea level. As Palawan remained dry during the YD, it appears Pacific sources did not compensate for reduced Karimata moisture. In contrast, Borneo, which also receives high rainfall from Karimata in the modern, may exhibit increased local and Pacific moisture compensating during the YD. Sumatra has a weak amount effect likely due to mixed source regions. The proportion of these sources is likely to have changed during hosing, when simulations indicate a reduction in monsoon pathways. Sulawesi has a strong amount effect with the majority of its rainfall either locally or northwesterly-sourced as part of the austral summer monsoon. Past changes were likely affected by topography, but orographic barriers prevent alternate source regions from playing a major role. Flores similarly has a strong amount effect, receives its moisture from the austral summer monsoon, and is sensitive to topography, however, Indian Ocean contributions may provide an important alternate source of moisture. Lastly, Ball Gown Cave has a weak amount effect, receiving modern rainfall from many different sources. The role of past topography is unknown, but the proportion of different moisture sources arriving is likely an important factor in determining local $\delta^{18}O_p$.

3) **What can we learn about aragonite-calcite systematics in the karst system? What are the aragonite distribution coefficients for trace elements of interest? What are the hydrologic controls on aragonite-calcite precipitation?**

Chapter 4 calculated isotopic fractionation offsets between aragonite and calcite, estimated aragonite partitioning coefficients, and used thin section petrography and trace element analysis to explore karst hydrology. I was unable to resolve a precise oxygen fractionation offset between aragonite and calcite due to a combination of kinetic effects on subdecadal timescales and dating uncertainties. However, the range of offset values inferred from the two stalagmites presented in this study lies between 0.6-1.0‰.

I estimated mean aragonite distribution coefficients for Mg ($D_{Mg(Ar)}$= 0.00329±0.00158), Sr ($D_{Sr(Ar)}$= 0.52±0.16), U ($D_{U(Ar)}$= 1.40±1.12), and Ba ($D_{Sr(Ar)}$= 0.28±0.08). $D_{Mg(Ar)}$ is two orders of magnitude higher than previous studies, possibly related to excess particulate Mg in the crystal lattice. $D_{Sr(Ar)}$ is less than the 1 predicted by ionic theory, but could potentially closer to 1 if a $D_{Sr(Cc)}$ accounting for Mg mol% were used. $D_{Ba(Ar)}$ may be subject to similar effects as $D_{Sr(Ar)}$. $D_{U(Ar)}$ is close to the expected value of 1.

The presence of detrital Mg is further supported by the similar patterns with trace elements that typically become mobile by adsorption onto colloidal particles. Spikes in these elements are likely related to increased filtration into the cave and are associated with the appearance of calcite in the speleothem. Calcite precipitation is initiated by high filtration into the cave, and dilution of the Mg concentration in the karst reservoir. In petrographic microphotographs, thin, dark layers, thought to be microbial mats, are often a precursor to calcite nucleation. Future SEM and TEM work may prove valuable in supporting this interpretation.

5.2 Summary

In this thesis, I presented a precisely-dated, high-resolution record of eastern Indian Ocean hydroclimate variability spanning the last 16 ky (thousand years) from $\delta^{18}O$ measurements in an aragonite-calcite speleothem from central Sumatra. This work focuses on the late deglacial period (~17 – 10 ka) and represents the western-most speleothem record from the IPWP region. I have undertaken a systematic analysis of modern moisture sources for eight monsoon and Indo-Pacific speleothem sites and compared these sources to modelled precipitation sources during an idealized hosing event. Finally, I used a unique aragonitic speleothem with intermittent calcite layers to evaluate oxygen isotope fractionation differences between aragonite and calcite, estimate distribution coefficients of major trace elements into aragonite, and assess environmental controls on trace element variability and aragonite-calcite precipitation.

Together, this research establishes a robust basis for interpreting the climatic history retained in the 16,500-year long speleothem $\delta^{18}O$ record for Tangga Cave and provides context relative to other speleothem records from the Indo-Pacific Warm Pool region. This work demonstrates the extended reach of North Atlantic abrupt forcing into the eastern tropical Indian Ocean, supporting this conclusion with systematic analysis of the modern hydroclimate system through use of isotope enabled climate models and back-trajectory air parcel analysis.

5.3 Future Work

In addition to future work identified within Chapters 2-4 of this thesis, there are several additional avenues of research to be pursued within the framework of this study.

5.3.1 U/Th laser ablation multi-collector inductively coupled plasma mass spectrometry

Laser ablation MC-ICP-MS methods offer several advantages over solution MC-ICP-MS: (a) it measures U-series related isotopes (^{238}U, ^{234}U, ^{230}Th) at very high spatial resolution (10-100μm); (b) it is non-destructive to samples; (c) it is cheaper than solution U/Th dating; and (d) the analysis speed is very fast, on the order of hours (Eggins et al., 2005). However, there are also a number of limitations with regards to using the method on speleothems including reduced sensitivity and precision in comparison to conventional solution MC-ICP-MS. Previous studies have shown that precise laser ablation measurements require uranium concentrations of at least 1ppm, whereas most speleothems have concentrations less than 0.2ppm (Eggins et al., 2005).

In the course of this research, I generated a U/Th LA-MC-ICP-MS transect on aragonitic stalagmite TA12-2 (Figure 5.1). Comparison between the solution chemistry and laser-ablation data shows promising agreement, which indicates that further development of this novel approach could be beneficial. Minor offsets in the youngest part of the speleothem suggest that using this method will require an assessment of the accuracy and parameterization of the laser ablation

technique as compared to solution chemistry. Nonetheless, development of this technique will likely lead to long-term cost and time savings, as LA-MC-ICP-MS is both less costly at ~$2500 versus $400/sample (less if internal), and more time efficient; laser ablation U/Th isotopes on 50 cm TA12-2 were measured in three days and required no pre-preparation of the sample.

While LA-MC-ICP-MS dating is not a feasible solution for generating precise age models, there are multiple reasons to perform an initial LA-MC-ICP-MS scan of speleothem samples. First, LA-MC-ICP-MS provides rapid preliminary estimates of uranium and thorium concentrations, which can be used to target and prepare suitable samples for U-Th solution chemistry. Likewise, the uranium concentrations would be indicative of aragonite and calcite phases. Second, in speleothems that do have U-concentrations higher than 1ppm, such as those with an aragonite composition, LA-MC-ICP-MS dating is capable of providing relatively accurate initial dates.

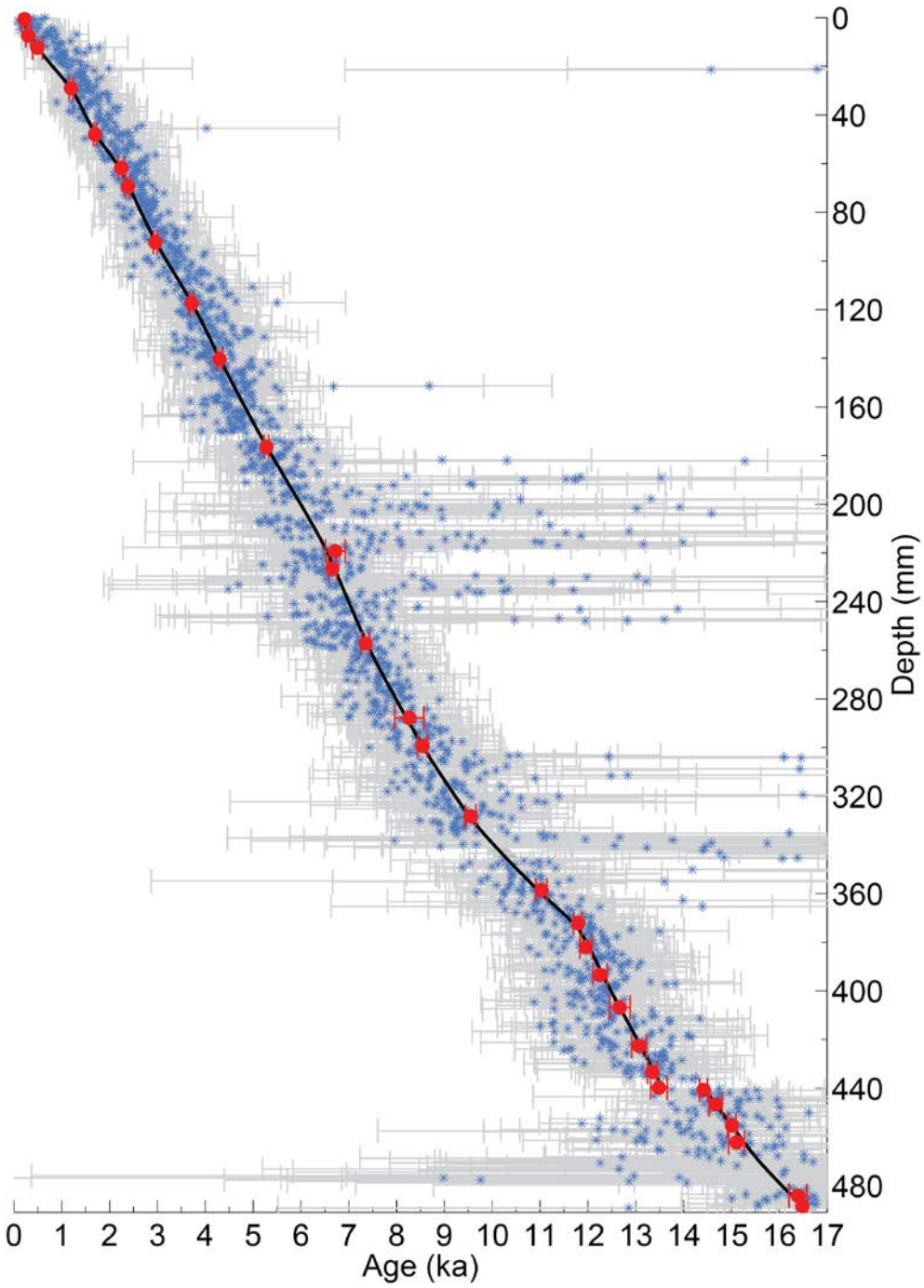

Figure 5.1 - TA12-2 age-depth model for U-Th solution dates and corresponding error bars (red), and U-Th laser-ablation transect ages (blue) and corresponding error bars (grey). Laser data is binned to approximate stable isotope measurement resolution. Anomalous ages are expected to be associated with calcite portions of the speleothem, which contain U/Th values below the detection limits of the LA method.

5.3.2 Additional HYSPLIT analysis

When I initially started working with HYSPLIT trajectories, trajectory generation was a tedious and time-consuming process. Due to the slow workflow, I focused on generating 10-year climatologies for the eight sites that were presented in Chapter 2. With the release of the PySPLIT package for Python in 2015, trajectory generation is now far more streamlined, and opens the potential for additional analysis. In particular, it would be rewarding to examine moisture source changes at the proxy sites during ENSO and IOD years. Similarly, we can also examine moisture source changes during the wettest and driest years on record. I did a preliminary exploration of the latter for Tangga Cave, Sumatra. Using daily ERA data for 1979-2015, I isolated the five wettest and five driest years at Tangga Cave and generated HYSPLIT clusters for trajectories in those years. Because these years did not necessarily correspond to the indices of important climate modes (IOD/ENSO), I started to look at the anomalies in common climate variables (e.g., SST, winds) during those years. Preliminary results of this work show that SST anomalies may be important in controlling precipitation amounts over Sumatra, and that SST anomalies may affect source moisture transport length and pathways.

This would be a valuable analysis to extend to the other speleothem sites, some of which are highly sensitive to ENSO state. Furthermore, these results could be compared to VSD-enabled, ENSO-forced simulations of GISS ModelE2-R (Lewis et al., 2014).

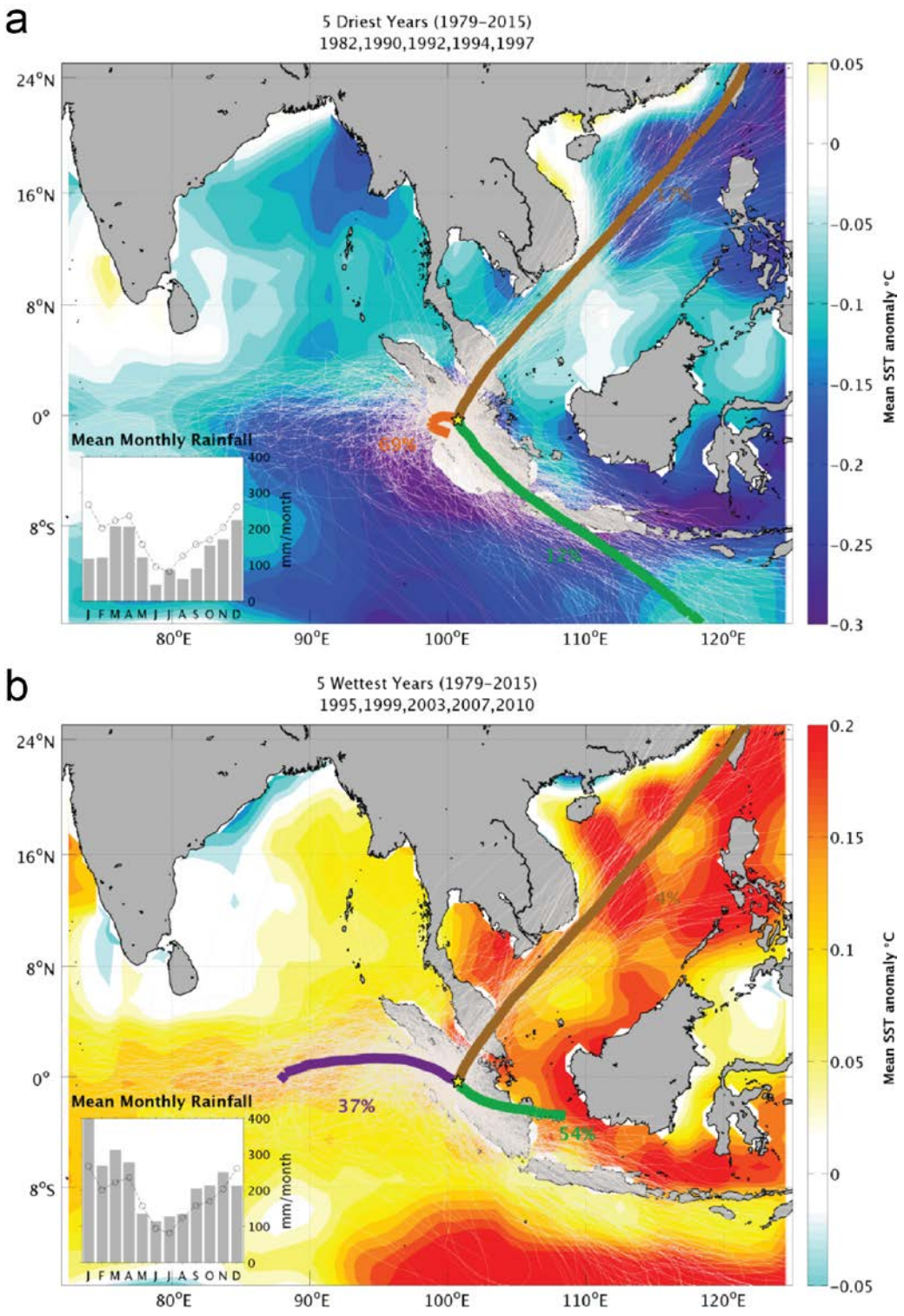

Figure 5.2 – HYSPLIT analysis for the (a) five driest and (b) five wettest years at Tangga Cave between 1979-2015. Grey lines show all trajectories for rain-bearing days in the targeted years. Colored lines are results of cluster analysis. Insets show average climatology for the targeted years (grey bars) and mean 1979-2015 climatology (dotted line/markers). Contours reflect SST anomalies for targeted years (relative to the 1980-2010 mean).

5.3.3 Stable carbon isotopes

Stable carbon isotopes (d13C) of speleothems are an often under-utilized proxy in paleoclimate due to the difficulty in interpreting $\delta^{13}C$ (Fairchild and Baker, 2012). The contribution of atmospheric CO_2 is often negligible in controlling the carbon isotopic value of a speleothem (Cosford et al., 2009; Hendy, 1971). Rather, biological processes in the soil, such as plant respiration and organic matter decomposition, and bedrock dissolution are the main components of the $\delta^{13}C$ signal (Fairchild et al., 2006; Lambert and Aharon, 2011). The two main interpretations of the biological $\delta^{13}C$ signal in the speleothem are as variations in either type of vegetation (C_3:C_4) above the cave (Dorale et al., 1992; Passey et al., 2009) or overall vegetation density above the cave (Baldini et al., 2005; Cosford et al., 2009), both of which are indirectly related to changes in climate. Within the cave environment, prior calcite precipitation (PCP) and mineralogy may lead to further alteration of the $\delta^{13}C$ signal within the speleothem. PCP generally occurs in relatively drier conditions, when CO_2 may degas and cause calcite to precipitate upflow of the speleothem. This may cause early fractionation of $\delta^{13}C$, leaving the residual dripwater enriched when it reaches the speleothem (Baker et al., 1997; Oster et al., 2010).

The $\delta^{13}C$ data for speleothem TA12-2 was generated simultaneously with $\delta^{18}O$ data, but further investigation of the $\delta^{13}C$ data was beyond the scope of this thesis. As with the $\delta^{18}O$ data, the $\delta^{13}C$ data would have required an isotopic correction for mineralogical effects on the stable isotope fraction. Fractionation of $\delta^{13}C$ in aragonite is poorly studied, but early research on isotopic fractionation in synthetic aragonite suggests that the $\delta^{13}C$ is enriched by approximately 1.7‰ relative to calcite (Romanek et al., 1992). More recently, an enrichment of 2.5‰ was observed in an aragonite layer of a calcite speleothem (McMillan et al., 2005) though other studies have suggested values up to 3.4‰ (Frisia et al., 2002). A preliminary correction of +2% was applied to the TA12-2 record, as this appeared to bring calcite values in line with aragonite values (Figure 5.3).

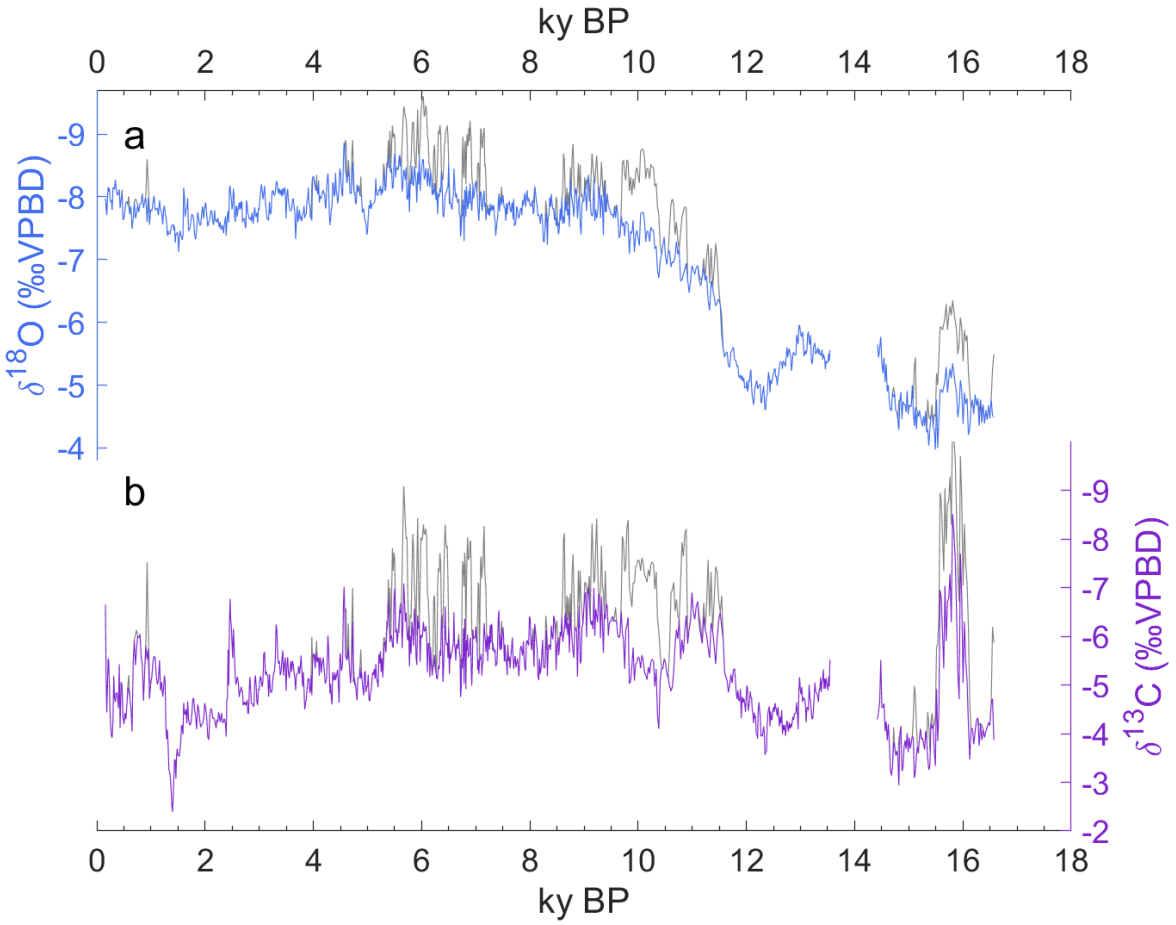

Figure 5.3 – (a) Uncorrected (grey) and corrected (blue) oxygen isotope record with an applied fractionation offset of +1‰. (b) Uncorrected (grey) and corrected (purple) carbon isotope record with an applied fractionation offset of +2‰. The corrected curve is a function of the percentage of calcite in each stable isotope measurement such that $\delta_{corrected} = \delta_{uncorrected}$ + (fractionation offset * calcite fraction).

In the corrected record, carbon isotopic values are enriched (~-4‰) between 13.5-11.5 ky BP, slightly leading the similarly-timed oxygen enrichment. These are not the heaviest values of the record, which occur as a ~500 year event centered at 1.3 ky BP (~-2.4‰). This event is not accompanied by a corresponding excursion in the oxygen record. Though such an enrichment could be caused by PCP, the trace element data do not support this mechanism, as no PCP-like covariation is observed between the $\delta^{13}C$ and trace elements (i.e., Mg and Sr), leaving vegetative productivity a likely source of $\delta^{13}C$ variations to be explored. Unfortunately, there do not appear to be any sufficiently high-resolution pollen records available in the region to explore this further at present.

Another striking feature in the record is the depletion event between 16 and 15 ky BP, which is echoed to a smaller degree in the oxygen isotopes, and occurs in a calcite section of the speleothem. Even applying the maximum possible correction (~3.4‰) would not bring the $\delta^{13}C$ values in line with the surrounding aragonite values. There are no major climatic events associated within this interval, however, a shift of this magnitude in stable isotopes and mineralogy necessitates an environmental shift, and merits further investigation as to the regional extent of this phenomenon.

5.3.4 The Holocene

This thesis has focused on the climate of the last deglaciation. In addition to this work, there are still 10,000 years of Holocene data to be interpreted. Unlike ASM/ISM $\delta^{18}O$ records that weaken with boreal summer insolation over the Holocene (Dykoski et al., 2005; Fleitmann et al., 2003) and Indo-Pacific $\delta^{18}O$ records that appear to have links to rising equatorial SON insolation or sea-level rise (Carolin et al., 2013; Griffiths et al., 2009; Kimbrough, 2016), the $\delta^{18}O$ record from Tangga Cave remains relatively stable over the Holocene (Figure 5.4). The Tangga Cave record does exhibit the mysterious ^{18}O reversal over the last 2000 years observed in many ASM records (Zhao et al., 2013), that is in opposition to the decreasing trend of boreal summer insolation.

There is also great interest in the state of the Indian Ocean during the mid-Holocene (Abram et al., 2007; de Boer et al., 2014; Kuhnert et al., 2014; Tierney et al., 2013). Positive Indian Ocean Dipole events have been linked to catastrophic flooding in East African countries (Black, 2003; Clark et al., 2003) and devastating droughts in Australia and Indonesia (Abram et al., 2003; Ummenhofer et al., 2009). Recent studies have shown there has been an increase in positive IOD events over the twentieth century (Abram et al., 2008). Furthermore, this trend may continue in the future due to greenhouse warming (Cai et al., 2014).

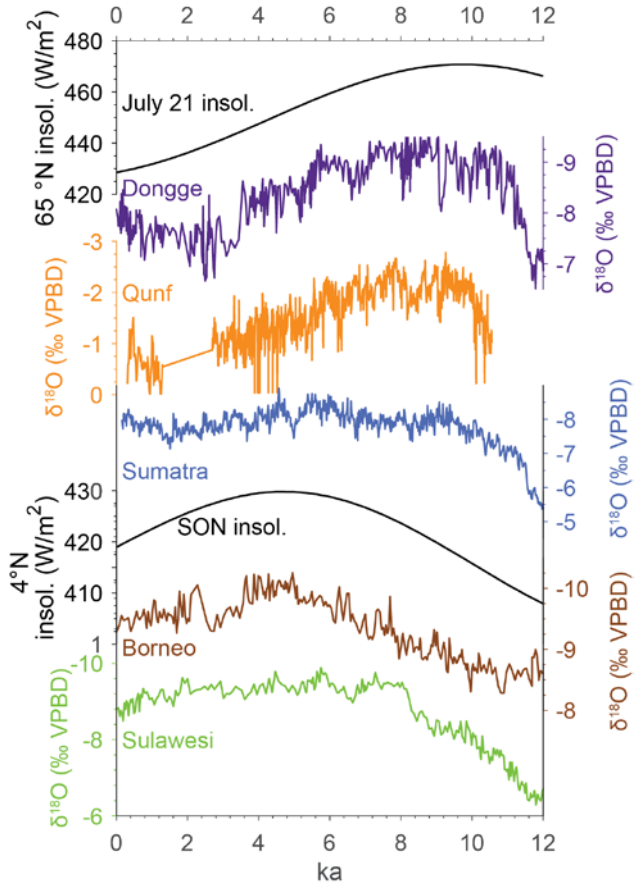

Figure 5.4 – Speleothem records from the ASM domain (Dongge and Qunf Caves) that weaken with boreal summer insolation over the Holocene, the Sumatran speleothem, and speleothem records with influences from equatorial September-October-November insolation and sea level change (Borneo and Sulawesi speleothems).

Some paleo-studies support a dipole-like mode in SSTs and precipitation across the Indian Ocean during the mid-Holocene (Figure 5.5) (Kuhnert et al., 2014; Niedermeyer et al., 2014; Tierney et al., 2012). However, these records are either low-resolution marine or lake sediment cores, or short-lived corals.

The Sumatran speleothem offers a new perspective on both Asian monsoon and Indian Ocean dynamics during the Holocene epoch. Because Sumatra shows both similarities to Chinese speleothems (during North Atlantic abrupt events, last 2000-year trend) and differences (Holocene trends), it may be possible to deconvolve some of the mechanisms influencing different parts of the Indian Ocean rim. Furthermore, the Sumatran record is the first high-resolution terrestrial record of rainfall from the eastern Indian Ocean, and provides an atmospheric counterpart to SST records from nearby (Mohtadi et al., 2014). This is

important in examining whether there was always an associated hydrologic response to ocean temperature anomalies in the eastern Indian Ocean.

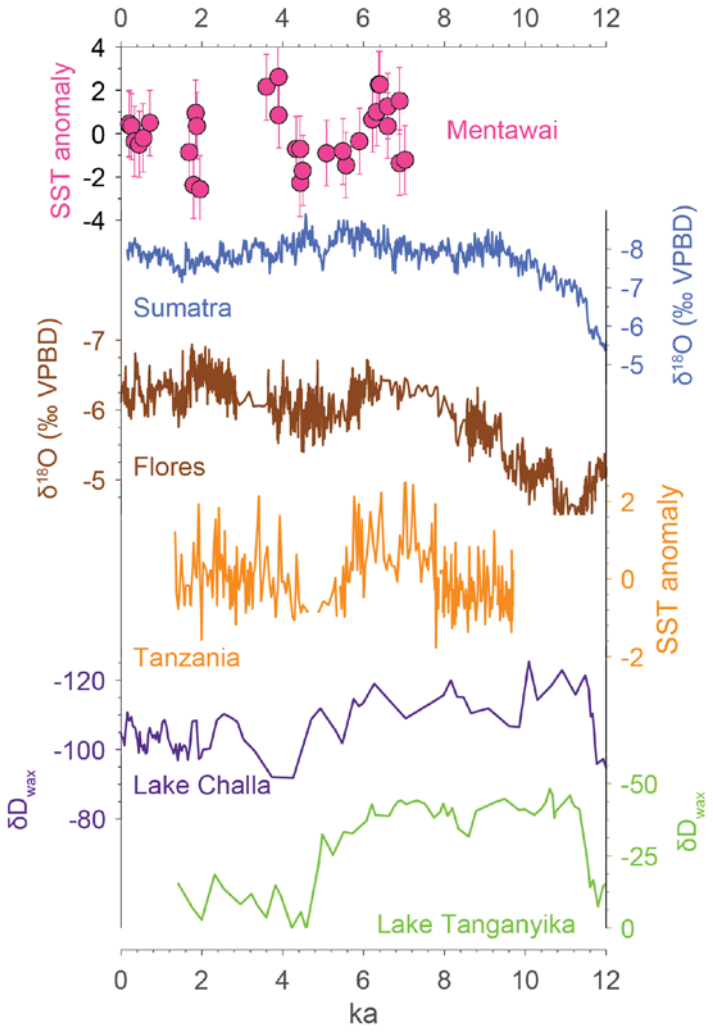

Figure 5.5 – Records of precipitation and SST from the eastern Indian Ocean (Mentawai coral Sr/Ca-SST, Sumatra speleothem $\delta^{18}O$, Flores speleothem $\delta^{18}O$) and western Indian Ocean (Tanzania sediment core Mg/Ca-SST, Lake Challa and Lake Tanganyika δD leaf wax).

References

Abram, N.J., Gagan, M.K., Cole, J.E., Hantoro, W.S., Mudelsee, M. (2008). Recent intensification of tropical climate variability in the Indian Ocean. Nature Geoscience 1, 849-853. http://dx.doi.org/10.1038/ngeo357

Abram, N.J., Gagan, M.K., Liu, Z., Hantoro, W.S., McCulloch, M.T., Suwargadi, B.W. (2007). Seasonal characteristics of the Indian Ocean Dipole during the Holocene epoch. Nature 445, 299-302. http://dx.doi.org/10.1038/nature05477

Abram, N.J., Gagan, M.K., McCulloch, M.T., Chappell, J., Hantoro, W.S. (2003). Coral reef death during the 1997 Indian Ocean Dipole linked to Indonesian wildfires. Science 301, 952-955. http://dx.doi.org/10.1126/science.1083841

Baker, A., Ito, E., Smart, P.L., McEwan, R.F. (1997). Elevated and variable values of ^{13}C in speleothems in a British cave system. Chemical Geology 136, 263-270. http://dx.doi.org/10.1016/S0009-2541(96)00129-5

Baldini, J.U.L., McDermott, F., Baker, A., Baldini, L.M., Mattey, D.P., Railsback, L.B. (2005). Biomass effects on stalagmite growth and isotope ratios: A 20th century analogue from Wiltshire, England. Earth and Planetary Science Letters 240, 486-494. http://dx.doi.org/10.1016/j.epsl.2005.09.022

Black, E. (2003). The impact of Indian and Pacific Ocean processes on the East African short rains. CLIVAR Exchanges 8, 40-42.

Cai, W., Santoso, A., Wang, G., Weller, E., Wu, L., Ashok, K., Masumoto, Y., Yamagata, T. (2014). Increased frequency of extreme Indian Ocean Dipole events due to greenhouse warming. Nature 510, 254-258. http://dx.doi.org/10.1038/nature13327

Carolin, S.A., Cobb, K.M., Adkins, J.F., Clark, B., Conroy, J.L., Lejau, S., Malang, J., Tuen, A.A. (2013). Varied response of western Pacific hydrology to climate forcings over the last glacial period. Science 340, 1564-1566. http://dx.doi.org/10.1126/science.1233797

Clark, C.O., Webster, P.J., Cole, J.E. (2003). Interdecadal variability of the relationship between the Indian Ocean zonal mode and East African coastal rainfall anomalies. Journal of Climate 16, 548-554. http://dx.doi.org/10.1175/1520-0442(2003)016<0548:Ivotrb>2.0.Co;2

Cosford, J., Qing, H., Mattey, D., Eglington, B., Zhang, M. (2009). Climatic and local effects on stalagmite $\delta^{13}C$ values at Lianhua Cave, China. Palaeogeography, Palaeoclimatology, Palaeoecology 280, 235-244. http://dx.doi.org/10.1016/j.palaeo.2009.05.020

de Boer, E.J., Tjallingii, R., Vélez, M.I., Rijsdijk, K.F., Vlug, A., Reichart, G.-J., Prendergast, A.L., de Louw, P.G.B., Florens, F.B.V., Baider, C., Hooghiemstra, H. (2014). Climate variability in the SW Indian Ocean from an 8000-yr long multi-proxy record in the Mauritian lowlands shows a middle to late Holocene shift from negative IOD-state to ENSO-state. Quaternary Science Reviews 86, 175-189.

Dorale, J.A., González, L.A., Reagan, M.K., Pickett, D.A., Murrell, M.T., Baker, R.G. (1992). A high-resolution record of Holocene climate change in speleothem calcite from Cold Water Cave, Northeast Iowa. Science 258, 1626-1630. http://dx.doi.org/10.2307/2882065

Dykoski, C.A., Edwards, R.L., Cheng, H., Yuan, D., Cai, Y., Zhang, M., Lin, Y., Qing, J., An, Z., Revenaugh, J. (2005). A high-resolution, absolute-dated Holocene and deglacial Asian monsoon record from Dongge Cave, China. Earth and Planetary Science Letters 233, 71-86. http://dx.doi.org/10.1016/j.epsl.2005.01.036

Eggins, S.M., Grün, R., McCulloch, M.T., Pike, A.W.G., Chappell, J., Kinsley, L., Mortimer, G., Shelley, M., Murray-Wallace, C.V., Spötl, C., Taylor, L. (2005). In

situ U-series dating by laser-ablation multi-collector ICPMS: new prospects for Quaternary geochronology. Quaternary Science Reviews 24, 2523-2538. http://dx.doi.org/10.1016/j.quascirev.2005.07.006

Fairchild, I.J., Baker, A. (2012), Speleothem science: from process to past environments. Wiley-Blackwell.

Fairchild, I.J., Smith, C.L., Baker, A., Fuller, L., Spötl, C., Mattey, D., McDermott, F., E.I.M.F. (2006). Modification and preservation of environmental signals in speleothems. Earth-Science Reviews 75, 105-153. http://dx.doi.org/10.1016/j.earscirev.2005.08.003

Fleitmann, D., Burns, S.J., Mudelsee, M., Neff, U., Kramers, J., Mangini, A., Matter, A. (2003). Holocene Forcing of the Indian Monsoon Recorded in a Stalagmite from Southern Oman. Science 300, 1737-1739. http://dx.doi.org/10.1126/science.1083130

Frisia, S., Borsato, A., Fairchild, I.J., McDermott, F., Selmo, E.M. (2002). Aragonite-calcite relationships in speleothems (Grotte De Clamouse, France): Environment, fabrics, and carbonate geochemistry. Journal of Sedimentary Research 72, 687-699. http://dx.doi.org/10.1306/020702720687

Griffiths, M.L., Drysdale, R.N., Gagan, M.K., Zhao, J.-x., Ayliffe, L.K., Hellstrom, J.C., Hantoro, W.S., Frisia, S., Feng, Y.-X., Cartwright, I., St. Pierre, E.J., Fischer, M.J., Suwargadi, B.W. (2009). Increasing Australian-Indonesian monsoon rainfall linked to early Holocene sea-level rise. Nature Geoscience 2, 636-639. http://dx.doi.org/10.1038/Ngeo605

Hendy, C.H. (1971). The isotopic geochemistry of speleothems—I. The calculation of the effects of different modes of formation on the isotopic composition of speleothems and their applicability as palaeoclimatic indicators. Geochimica et Cosmochimica Acta 35, 801-824.

Kimbrough, A.K. (2016), The glacial-interglacial monsoon recorded by stalgmites from Southwest Sulawesi, Research School of Earth Sciences. Australian National University.

Kuhnert, H., Kuhlmann, H., Mohtadi, M., Meggers, H., Baumann, K.-H., Pätzold, J. (2014). Holocene tropical Western Indian Ocean sea surface temperatures in covariation with climatic changes in the Indonesian region. Paleoceanography 29, 2013PA002555. http://dx.doi.org/10.1002/2013pa002555

Lambert, W.J., Aharon, P. (2011). Controls on dissolved inorganic carbon and $\delta^{13}C$ in cave waters from DeSoto Caverns: Implications for speleothem $\delta^{13}C$ assessments. Geochimica et Cosmochimica Acta 75, 753-768. http://dx.doi.org/10.1016/j.gca.2010.11.006

Lewis, S.C., LeGrande, A.N., Schmidt, G.A., Kelley, M. (2014). Comparison of forced ENSO-like hydrological expressions in simulations of the preindustrial and mid-Holocene. Journal of Geophysical Research: Atmospheres 119, 7064-7082. http://dx.doi.org/10.1002/2013jd020961

McMillan, E.A., Fairchild, I.J., Frisia, S., Borsato, A., McDermott, F. (2005). Annual trace element cycles in calcite–aragonite speleothems: evidence of drought in the western Mediterranean 1200–1100 yr BP. Journal of Quaternary Science 20, 423-433. http://dx.doi.org/10.1002/jqs.943

Mohtadi, M., Prange, M., Oppo, D.W., De Pol-Holz, R., Merkel, U., Zhang, X., Steinke, S., Luckge, A. (2014). North Atlantic forcing of tropical Indian Ocean climate. Nature 509, 76-80. http://dx.doi.org/10.1038/nature13196

Niedermeyer, E.M., Sessions, A.L., Feakins, S.J., Mohtadi, M. (2014). Hydroclimate of the western Indo-Pacific Warm Pool during the past 24,000 years. Proceedings of the National Academy of Sciences 111, 9402-9406. http://dx.doi.org/10.1073/pnas.1323585111

Oster, J.L., Montañez, I.P., Guilderson, T.P., Sharp, W.D., Banner, J.L. (2010). Modeling speleothem $\delta^{13}C$ variability in a central Sierra Nevada cave using ^{14}C and $^{87}Sr/^{86}Sr$. Geochimica et Cosmochimica Acta 74, 5228-5242. http://dx.doi.org/10.1016/j.gca.2010.06.030

Passey, B.H., Ayliffe, L.K., Kaakinen, A., Zhang, Z., Eronen, J.T., Zhu, Y., Zhou, L., Cerling, T.E., Fortelius, M. (2009). Strengthened East Asian summer monsoons during a period of high-latitude warmth? Isotopic evidence from Mio-Pliocene fossil mammals and soil carbonates from northern China. Earth and Planetary Science Letters 277, 443-452. http://dx.doi.org/10.1016/j.epsl.2008.11.008

Romanek, C.S., Grossman, E.L., Morse, J.W. (1992). Carbon isotopic fractionation in synthetic aragonite and calcite: Effects of temperature and precipitation rate. Geochimica et Cosmochimica Acta 56, 419-430. http://dx.doi.org/10.1016/0016-7037(92)90142-6

Tierney, J.E., Oppo, D.W., LeGrande, A.N., Huang, Y., Rosenthal, Y., Linsley, B.K. (2012). The influence of Indian Ocean atmospheric circulation on Warm Pool hydroclimate during the Holocene epoch. Journal of Geophysical Research: Atmospheres 117. http://dx.doi.org/10.1029/2012jd018060

Tierney, J.E., Smerdon, J.E., Anchukaitis, K.J., Seager, R. (2013). Multidecadal variability in East African hydroclimate controlled by the Indian Ocean. Nature 493, 389-392. http://dx.doi.org/10.1038/nature11785

Ummenhofer, C.C., England, M.H., McIntosh, P.C., Meyers, G.A., Pook, M.J., Risbey, J.S., Gupta, A.S., Taschetto, A.S. (2009). What causes southeast Australia's worst droughts? Geophysical Research Letters 36, L04706. http://dx.doi.org/10.1029/2008GL036801

Zhao, C., Chang, Y.-P., Chen, M.-T., Liu, Z. (2013). Possible reverse trend in Asian summer monsoon strength during the late Holocene. Journal of Asian Earth Sciences 69, 102-112. http://dx.doi.org/10.1016/j.jseaes.2012.09.028

Appendix

This appendix contains:

A1) TA12-2 stable isotope data

A2) TA12-8 stable isotope data

A3)* TA12-2 Raman spectroscopy

A4)* TA12-2 LA-ICP-MS trace element analysis

A5)* LA-MC-ICP-MS U/Th analysis

*Appendices A3-A5 are included as electronic appendices only (see attached USB drive)

Appendix 1

A1 – TA12-2 stable isotope data. Note that "δ^{18}O-arag" refers to δ^{18}O values which have been corrected for mineralogy to aragonite-equivalent values. "δ^{18}O-corr" refers to the ice volume corrected δ18O values. Where applicable, isotope values shown equal the mean of replicate measurements. Age is reported in ky BP where present is 1950.

Sample ID	Depth (mm)	Age (ky BP)	δ^{18}O-raw (‰VPDB)	δ^{18}O-arag (‰VPDB)	δ^{18}O-corr (‰VPDB)	δ^{13}C-raw (‰VPDB)
TA12-2-1	0.25	0.159	-7.98	-7.98	-7.99	-6.650
TA12-2-2	0.75	0.172	-7.82	-7.82	-7.83	-5.149
TA12-2-3	1.25	0.184	-7.87	-7.71	-7.72	-4.433
TA12-2-4	1.75	0.196	-7.94	-7.94	-7.96	-4.969
TA12-2-5	2.25	0.209	-8.16	-8.16	-8.17	-5.543
TA12-2-6	2.75	0.221	-8.08	-8.08	-8.10	-5.481
TA12-2-7	3.25	0.233	-8.14	-8.14	-8.15	-4.924
TA12-2-8	3.75	0.246	-7.98	-7.98	-7.99	-4.425
TA12-2-9	4.25	0.258	-7.91	-7.91	-7.93	-4.097
TA12-2-10	4.75	0.271	-7.94	-7.94	-7.96	-3.943
TA12-2-11	5.25	0.284	-7.79	-7.79	-7.80	-3.919
TA12-2-12	5.75	0.299	-8.15	-8.15	-8.16	-4.262
TA12-2-13	6.25	0.313	-8.15	-8.15	-8.17	-5.183
TA12-2-14	6.75	0.327	-8.12	-8.12	-8.13	-4.739
TA12-2-15	7.25	0.342	-8.27	-8.27	-8.29	-4.649
TA12-2-16	7.75	0.356	-8.14	-8.14	-8.16	-4.836
TA12-2-17	8.25	0.371	-8.05	-8.05	-8.07	-4.840
TA12-2-18	8.75	0.385	-8.02	-8.02	-8.04	-4.714
TA12-2-19	9.25	0.400	-8.07	-8.07	-8.09	-4.524
TA12-2-20	9.75	0.414	-8.12	-8.12	-8.13	-5.426
TA12-2-21	10.25	0.430	-7.82	-7.82	-7.83	-4.113
TA12-2-22	10.75	0.448	-7.95	-7.95	-7.97	-5.063
TA12-2-23	11.25	0.466	-8.11	-8.07	-8.08	-4.906
TA12-2-24	11.75	0.484	-7.63	-7.63	-7.65	-4.330
TA12-2-25	12.25	0.502	-7.65	-7.65	-7.66	-4.194
TA12-2-26	12.75	0.519	-7.79	-7.79	-7.80	-4.422
TA12-2-27	13.25	0.537	-7.90	-7.90	-7.92	-4.292
TA12-2-28	13.75	0.555	-7.93	-7.93	-7.94	-4.580
TA12-2-29	14.25	0.573	-7.88	-7.88	-7.89	-4.956
TA12-2-30	14.75	0.590	-8.01	-7.85	-7.86	-4.885
TA12-2-31	15.25	0.610	-7.72	-7.72	-7.74	-4.733
TA12-2-32	15.75	0.631	-7.85	-7.85	-7.86	-4.523
TA12-2-33	16.25	0.651	-7.49	-7.49	-7.50	-4.045
TA12-2-34	16.75	0.672	-7.64	-7.64	-7.66	-5.485
TA12-2-35	17.25	0.693	-7.92	-7.92	-7.94	-5.918
TA12-2-36	17.75	0.714	-7.97	-7.65	-7.67	-5.405
TA12-2-37	18.25	0.734	-7.93	-7.73	-7.75	-5.727
TA12-2-38	18.75	0.755	-7.87	-7.87	-7.89	-5.999

Sample ID	Depth (mm)	Age (ky BP)	$\delta^{18}O$-raw (‰VPDB)	$\delta^{18}O$-arag (‰VPDB)	$\delta^{18}O$-corr (‰VPDB)	$\delta^{13}C$-raw (‰VPDB)
TA12-2-39	19.25	0.776	-7.75	-7.75	-7.77	-5.968
TA12-2-40	19.75	0.797	-7.89	-7.89	-7.91	-6.042
TA12-2-41	20.25	0.818	-7.89	-7.89	-7.90	-5.596
TA12-2-42	20.75	0.840	-8.05	-8.05	-8.07	-5.415
TA12-2-43	21.25	0.863	-7.82	-7.82	-7.84	-4.676
TA12-2-44	21.75	0.885	-7.92	-7.92	-7.94	-5.313
TA12-2-45	22.25	0.907	-8.04	-7.97	-7.99	-5.792
TA12-2-46	22.75	0.929	-8.60	-7.60	-7.62	-5.521
TA12-2-47	23.25	0.951	-8.19	-7.99	-8.00	-5.742
TA12-2-48	23.75	0.973	-7.76	-7.55	-7.57	-4.712
TA12-2-49	24.25	0.995	-7.79	-7.79	-7.81	-5.021
TA12-2-50	24.75	1.017	-7.77	-7.77	-7.79	-5.176
TA12-2-51	25.25	1.038	-7.91	-7.91	-7.92	-5.489
TA12-2-52	25.75	1.058	-8.02	-8.02	-8.03	-5.588
TA12-2-53	26.25	1.078	-7.79	-7.79	-7.80	-5.561
TA12-2-54	26.75	1.098	-7.81	-7.81	-7.83	-5.170
TA12-2-55	27.25	1.118	-7.82	-7.82	-7.83	-5.009
TA12-2-56	27.75	1.138	-7.71	-7.71	-7.72	-5.098
TA12-2-57	28.25	1.158	-7.94	-7.94	-7.96	-5.506
TA12-2-58	28.75	1.178	-7.79	-7.79	-7.81	-4.885
TA12-2-59	29.25	1.198	-7.75	-7.75	-7.77	-5.059
TA12-2-60	29.75	1.218	-7.56	-7.56	-7.58	-4.755
TA12-2-61	30.25	1.235	-7.81	-7.81	-7.83	-4.928
TA12-2-62	30.75	1.249	-7.86	-7.86	-7.88	-5.194
TA12-2-63	31.25	1.263	-7.73	-7.73	-7.75	-5.072
TA12-2-64	31.75	1.276	-7.68	-7.68	-7.70	-4.109
TA12-2-65	32.25	1.290	-7.59	-7.59	-7.60	-3.886
TA12-2-66	32.75	1.304	-7.38	-7.38	-7.39	-4.084
TA12-2-67	33.25	1.318	-7.46	-7.46	-7.48	-3.741
TA12-2-68	33.75	1.332	-7.41	-7.41	-7.43	-3.260
TA12-2-69	34.25	1.346	-7.41	-7.41	-7.42	-3.219
TA12-2-70	34.75	1.360	-7.43	-7.43	-7.45	-3.079
TA12-2-71	35.25	1.373	-7.52	-7.52	-7.54	-2.843
TA12-2-72	35.75	1.386	-7.54	-7.54	-7.56	-2.534
TA12-2-73	36.25	1.398	-7.54	-7.54	-7.56	-2.390
TA12-2-74	36.75	1.411	-7.57	-7.57	-7.58	-2.682
TA12-2-75	37.25	1.423	-7.46	-7.46	-7.48	-3.092
TA12-2-76	37.75	1.436	-7.53	-7.53	-7.55	-3.473
TA12-2-77	38.25	1.448	-7.27	-7.27	-7.28	-3.460
TA12-2-78	38.75	1.461	-7.41	-7.41	-7.43	-3.075
TA12-2-79	39.25	1.473	-7.40	-7.40	-7.42	-3.539
TA12-2-80	39.75	1.486	-7.44	-7.44	-7.46	-3.692
TA12-2-81	40.25	1.499	-7.36	-7.36	-7.38	-3.566
TA12-2-82	40.75	1.512	-7.12	-7.12	-7.14	-3.534

Sample ID	Depth (mm)	Age (ky BP)	$\delta^{18}O$-raw (‰VPDB)	$\delta^{18}O$-arag (‰VPDB)	$\delta^{18}O$-corr (‰VPDB)	$\delta^{13}C$-raw (‰VPDB)
TA12-2-83	41.25	1.525	-7.37	-7.37	-7.39	-3.535
TA12-2-84	41.75	1.539	-7.46	-7.46	-7.48	-3.681
TA12-2-85	42.25	1.552	-7.38	-7.38	-7.40	-3.866
TA12-2-86	42.75	1.565	-7.37	-7.37	-7.39	-4.176
TA12-2-87	43.25	1.578	-7.31	-7.31	-7.33	-4.140
TA12-2-88	43.75	1.592	-7.39	-7.39	-7.41	-3.981
TA12-2-89	44.25	1.605	-8.15	-8.15	-8.17	-4.631
TA12-2-90	44.75	1.618	-8.02	-8.02	-8.04	-4.433
TA12-2-91	45.25	1.632	-7.68	-7.68	-7.70	-4.385
TA12-2-92	45.75	1.648	-7.80	-7.80	-7.82	-4.501
TA12-2-93	46.25	1.663	-7.81	-7.81	-7.83	-4.210
TA12-2-94	46.75	1.679	-7.98	-7.98	-8.00	-4.664
TA12-2-95	47.25	1.694	-7.46	-7.46	-7.48	-4.311
TA12-2-96	47.75	1.710	-7.48	-7.48	-7.50	-4.199
TA12-2-97	48.25	1.725	-7.53	-7.53	-7.55	-4.172
TA12-2-98	48.75	1.741	-7.64	-7.64	-7.66	-4.224
TA12-2-99	49.25	1.756	-7.72	-7.72	-7.74	-4.406
TA12-2-100	49.75	1.772	-7.71	-7.71	-7.73	-4.696
TA12-2-101	50.25	1.789	-7.64	-7.64	-7.66	-4.731
TA12-2-102	50.75	1.807	-7.38	-7.38	-7.40	-4.482
TA12-2-103	51.25	1.826	-7.32	-7.32	-7.35	-4.337
TA12-2-104	51.75	1.844	-7.48	-7.48	-7.50	-4.090
TA12-2-105	52.25	1.863	-7.75	-7.75	-7.78	-4.599
TA12-2-106	52.75	1.882	-7.66	-7.66	-7.68	-4.496
TA12-2-107	53.25	1.900	-7.55	-7.55	-7.57	-4.287
TA12-2-108	53.75	1.919	-7.55	-7.55	-7.57	-4.132
TA12-2-109	54.25	1.937	-7.73	-7.73	-7.75	-4.184
TA12-2-110	54.75	1.956	-7.85	-7.85	-7.87	-4.209
TA12-2-111	55.25	1.974	-7.65	-7.65	-7.68	-4.312
TA12-2-112	55.75	1.993	-7.83	-7.83	-7.85	-4.628
TA12-2-113	56.25	2.012	-7.91	-7.91	-7.93	-4.500
TA12-2-114	56.75	2.031	-7.71	-7.71	-7.73	-4.317
TA12-2-115	57.25	2.050	-7.53	-7.53	-7.55	-3.929
TA12-2-116	57.75	2.069	-7.60	-7.60	-7.62	-3.872
TA12-2-117	58.25	2.087	-7.64	-7.64	-7.66	-4.373
TA12-2-118	58.75	2.106	-7.78	-7.78	-7.80	-4.517
TA12-2-119	59.25	2.125	-7.77	-7.77	-7.80	-4.480
TA12-2-120	59.75	2.143	-7.59	-7.59	-7.61	-4.309
TA12-2-121	60.25	2.160	-7.56	-7.56	-7.58	-4.328
TA12-2-122	60.75	2.175	-7.78	-7.78	-7.81	-4.289
TA12-2-123	61.25	2.190	-7.61	-7.61	-7.64	-4.196
TA12-2-124	61.75	2.205	-7.63	-7.63	-7.65	-4.111
TA12-2-125	62.25	2.219	-7.59	-7.59	-7.61	-4.285
TA12-2-126	62.75	2.234	-7.67	-7.67	-7.69	-4.232

Sample ID	Depth (mm)	Age (ky BP)	$\delta^{18}O$-raw (‰VPDB)	$\delta^{18}O$-arag (‰VPDB)	$\delta^{18}O$-corr (‰VPDB)	$\delta^{13}C$-raw (‰VPDB)
TA12-2-127	63.25	2.249	-7.58	-7.58	-7.61	-4.440
TA12-2-128	63.75	2.264	-7.51	-7.51	-7.54	-4.360
TA12-2-129	64.25	2.278	-7.60	-7.60	-7.63	-4.238
TA12-2-130	64.75	2.293	-7.48	-7.48	-7.50	-4.357
TA12-2-131	65.25	2.306	-7.49	-7.49	-7.52	-4.419
TA12-2-132	65.75	2.318	-7.55	-7.55	-7.57	-4.228
TA12-2-133	66.25	2.330	-7.48	-7.48	-7.50	-4.224
TA12-2-134	66.75	2.342	-7.42	-7.42	-7.44	-4.252
TA12-2-135	67.25	2.354	-7.55	-7.55	-7.57	-4.307
TA12-2-136	67.75	2.366	-7.62	-7.62	-7.64	-4.270
TA12-2-137	68.25	2.378	-7.69	-7.69	-7.71	-4.181
TA12-2-138	68.75	2.389	-7.38	-7.38	-7.40	-3.939
TA12-2-139	69.25	2.401	-7.58	-7.58	-7.60	-4.671
TA12-2-140	69.75	2.413	-7.70	-7.70	-7.73	-4.745
TA12-2-141	70.25	2.425	-7.77	-7.77	-7.80	-5.725
TA12-2-142	70.75	2.437	-7.59	-7.59	-7.61	-4.989
TA12-2-143	71.25	2.450	-8.12	-8.12	-8.14	-6.232
TA12-2-144	71.75	2.462	-8.18	-8.18	-8.20	-6.771
TA12-2-145	72.25	2.474	-8.03	-8.03	-8.06	-6.340
TA12-2-146	72.75	2.486	-7.96	-7.96	-7.98	-6.170
TA12-2-147	73.25	2.498	-7.80	-7.80	-7.82	-5.843
TA12-2-148	73.75	2.510	-7.87	-7.87	-7.90	-5.551
TA12-2-149	74.25	2.523	-8.13	-8.13	-8.15	-6.151
TA12-2-150	74.75	2.535	-8.02	-8.02	-8.05	-5.853
TA12-2-151	75.25	2.547	-7.65	-7.65	-7.68	-5.449
TA12-2-152	75.75	2.559	-7.60	-7.60	-7.63	-5.128
TA12-2-153	76.25	2.571	-7.83	-7.83	-7.85	-5.004
TA12-2-154	76.75	2.583	-7.86	-7.86	-7.89	-5.074
TA12-2-155	77.25	2.595	-7.68	-7.68	-7.71	-5.165
TA12-2-156	77.75	2.607	-7.80	-7.80	-7.82	-5.109
TA12-2-157	78.25	2.619	-7.84	-7.84	-7.87	-4.964
TA12-2-158	78.75	2.631	-7.91	-7.91	-7.94	-4.751
TA12-2-159	79.25	2.643	-7.79	-7.79	-7.82	-4.831
TA12-2-160	79.75	2.655	-7.92	-7.92	-7.95	-4.884
TA12-2-161	80.25	2.667	-7.81	-7.81	-7.84	-4.967
TA12-2-162	80.75	2.679	-7.93	-7.93	-7.96	-4.865
TA12-2-163	81.25	2.692	-7.59	-7.59	-7.62	-4.884
TA12-2-164	81.75	2.704	-7.65	-7.65	-7.67	-4.577
TA12-2-165	82.25	2.716	-7.63	-7.63	-7.65	-4.651
TA12-2-166	82.75	2.728	-7.66	-7.66	-7.69	-4.600
TA12-2-167	83.25	2.741	-7.53	-7.53	-7.56	-4.644
TA12-2-168	83.75	2.753	-7.50	-7.50	-7.53	-4.578
TA12-2-169	84.25	2.765	-7.94	-7.94	-7.97	-4.614
TA12-2-170	84.75	2.777	-7.88	-7.88	-7.90	-4.693

Sample ID	Depth (mm)	Age (ky BP)	$\delta^{18}O$-raw (‰VPDB)	$\delta^{18}O$-arag (‰VPDB)	$\delta^{18}O$-corr (‰VPDB)	$\delta^{13}C$-raw (‰VPDB)
TA12-2-171	85.25	2.790	-7.74	-7.74	-7.76	-4.419
TA12-2-172	85.75	2.802	-7.72	-7.72	-7.75	-4.404
TA12-2-173	86.25	2.815	-7.64	-7.64	-7.67	-4.853
TA12-2-174	86.75	2.828	-7.65	-7.65	-7.68	-5.161
TA12-2-175	87.25	2.840	-7.67	-7.67	-7.70	-4.945
TA12-2-176	87.75	2.853	-7.61	-7.61	-7.63	-4.643
TA12-2-177	88.25	2.866	-7.75	-7.75	-7.77	-4.603
TA12-2-178	88.75	2.878	-7.66	-7.66	-7.69	-4.622
TA12-2-179	89.25	2.891	-7.57	-7.57	-7.60	-4.552
TA12-2-180	89.75	2.903	-7.73	-7.73	-7.76	-4.566
TA12-2-181	90.25	2.917	-7.83	-7.83	-7.86	-5.063
TA12-2-182	90.75	2.930	-7.69	-7.69	-7.71	-5.197
TA12-2-183	91.25	2.944	-7.68	-7.68	-7.71	-4.968
TA12-2-184	91.75	2.958	-7.75	-7.75	-7.78	-4.640
TA12-2-185	92.25	2.971	-7.59	-7.59	-7.62	-4.590
TA12-2-186	92.75	2.985	-7.82	-7.82	-7.85	-4.919
TA12-2-187	93.25	2.999	-7.79	-7.79	-7.82	-4.896
TA12-2-188	93.75	3.012	-7.97	-7.97	-8.00	-5.104
TA12-2-189	94.25	3.026	-8.08	-8.08	-8.11	-5.184
TA12-2-190	94.75	3.040	-8.20	-8.20	-8.23	-5.089
TA12-2-191	95.25	3.054	-8.10	-8.10	-8.13	-4.958
TA12-2-192	95.75	3.069	-7.96	-7.96	-7.99	-5.077
TA12-2-193	96.25	3.084	-8.05	-8.05	-8.08	-5.644
TA12-2-194	96.75	3.099	-8.17	-8.17	-8.20	-5.678
TA12-2-195	97.25	3.114	-7.90	-7.90	-7.93	-5.210
TA12-2-196	97.75	3.129	-7.81	-7.81	-7.84	-5.281
TA12-2-197	98.25	3.144	-7.64	-7.64	-7.67	-5.197
TA12-2-198	98.75	3.159	-7.65	-7.65	-7.68	-5.196
TA12-2-199	99.25	3.174	-7.62	-7.62	-7.65	-4.757
TA12-2-200	99.75	3.189	-7.92	-7.92	-7.95	-5.220
TA12-2-201	100.25	3.204	-7.72	-7.72	-7.75	-4.893
TA12-2-202	100.75	3.219	-7.74	-7.74	-7.77	-4.837
TA12-2-203	101.25	3.235	-8.05	-8.05	-8.08	-4.877
TA12-2-204	101.75	3.250	-8.11	-8.11	-8.14	-5.096
TA12-2-205	102.25	3.266	-8.06	-8.06	-8.09	-5.229
TA12-2-206	102.75	3.281	-8.02	-8.02	-8.05	-5.278
TA12-2-207	103.25	3.296	-8.07	-8.07	-8.10	-5.514
TA12-2-208	103.75	3.312	-8.21	-8.21	-8.24	-6.239
TA12-2-209	104.25	3.327	-8.25	-8.25	-8.29	-6.128
TA12-2-210	104.75	3.342	-8.12	-8.12	-8.15	-5.586
TA12-2-211	105.25	3.358	-8.05	-8.05	-8.09	-5.435
TA12-2-212	105.75	3.373	-8.14	-8.14	-8.17	-5.492
TA12-2-213	106.25	3.389	-8.03	-8.03	-8.06	-5.201
TA12-2-214	106.75	3.404	-8.12	-8.12	-8.15	-5.270

Sample ID	Depth (mm)	Age (ky BP)	$\delta^{18}O$-raw (‰VPDB)	$\delta^{18}O$-arag (‰VPDB)	$\delta^{18}O$-corr (‰VPDB)	$\delta^{13}C$-raw (‰VPDB)
TA12-2-215	107.25	3.419	-8.00	-8.00	-8.04	-5.510
TA12-2-216	107.75	3.435	-8.13	-8.13	-8.17	-5.709
TA12-2-217	108.25	3.450	-8.03	-8.03	-8.06	-5.191
TA12-2-218	108.75	3.465	-8.15	-8.15	-8.18	-5.414
TA12-2-219	109.25	3.481	-8.10	-8.10	-8.13	-5.564
TA12-2-220	109.75	3.496	-7.65	-7.65	-7.69	-4.880
TA12-2-221	110.25	3.511	-8.01	-8.01	-8.05	-5.371
TA12-2-222	110.75	3.526	-8.13	-8.13	-8.16	-5.568
TA12-2-223	111.25	3.541	-7.93	-7.93	-7.96	-5.234
TA12-2-224	111.75	3.555	-7.85	-7.85	-7.88	-5.140
TA12-2-225	112.25	3.570	-7.78	-7.78	-7.81	-5.306
TA12-2-226	112.75	3.585	-7.78	-7.78	-7.81	-5.489
TA12-2-227	113.25	3.600	-7.80	-7.80	-7.84	-5.273
TA12-2-228	113.75	3.615	-7.96	-7.96	-7.99	-5.493
TA12-2-229	114.25	3.629	-7.97	-7.97	-8.01	-5.418
TA12-2-230	114.75	3.644	-7.85	-7.85	-7.89	-5.254
TA12-2-231	115.25	3.659	-7.74	-7.74	-7.77	-5.131
TA12-2-232	115.75	3.673	-7.33	-7.33	-7.36	-4.891
TA12-2-233	116.25	3.687	-7.60	-7.60	-7.64	-5.209
TA12-2-234	116.75	3.702	-7.85	-7.85	-7.89	-5.239
TA12-2-235	117.25	3.716	-7.60	-7.60	-7.64	-5.240
TA12-2-236	117.75	3.730	-7.69	-7.69	-7.73	-5.387
TA12-2-237	118.25	3.744	-7.80	-7.80	-7.83	-5.226
TA12-2-238	118.75	3.758	-7.64	-7.64	-7.67	-5.375
TA12-2-239	119.25	3.773	-7.69	-7.69	-7.72	-5.602
TA12-2-240	119.75	3.787	-7.61	-7.61	-7.65	-5.300
TA12-2-241	120.25	3.801	-7.74	-7.74	-7.77	-4.967
TA12-2-242	120.75	3.814	-7.75	-7.75	-7.78	-5.267
TA12-2-243	121.25	3.828	-7.86	-7.86	-7.89	-4.930
TA12-2-244	121.75	3.841	-7.66	-7.66	-7.70	-4.495
TA12-2-245	122.25	3.854	-7.72	-7.72	-7.76	-4.616
TA12-2-246	122.75	3.868	-7.72	-7.72	-7.75	-4.675
TA12-2-247	123.25	3.881	-7.93	-7.93	-7.96	-4.886
TA12-2-248	123.75	3.895	-7.97	-7.97	-8.01	-5.057
TA12-2-249	124.25	3.908	-8.15	-8.15	-8.19	-5.138
TA12-2-250	124.75	3.921	-7.87	-7.87	-7.91	-5.102
TA12-2-251	125.25	3.934	-7.88	-7.88	-7.91	-4.835
TA12-2-252	125.75	3.947	-7.66	-7.66	-7.70	-4.886
TA12-2-253	126.25	3.960	-7.69	-7.69	-7.72	-5.204
TA12-2-254	126.75	3.972	-8.22	-7.62	-7.66	-4.793
TA12-2-255	127.25	3.985	-8.29	-8.29	-8.33	-5.443
TA12-2-256	127.75	3.998	-8.33	-8.33	-8.37	-5.623
TA12-2-257	128.25	4.010	-8.29	-8.29	-8.32	-5.643
TA12-2-258	128.75	4.023	-8.26	-8.21	-8.24	-5.509

Sample ID	Depth (mm)	Age (ky BP)	$\delta^{18}O$-raw (‰VPDB)	$\delta^{18}O$-arag (‰VPDB)	$\delta^{18}O$-corr (‰VPDB)	$\delta^{13}C$-raw (‰VPDB)
TA12-2-259	129.25	4.036	-8.16	-8.16	-8.19	-5.343
TA12-2-260	129.75	4.048	-8.10	-8.10	-8.14	-5.663
TA12-2-261	130.25	4.061	-8.35	-8.16	-8.20	-5.533
TA12-2-262	130.75	4.073	-8.08	-8.08	-8.12	-5.461
TA12-2-263	131.25	4.085	-8.04	-8.04	-8.08	-5.567
TA12-2-264	131.75	4.097	-8.26	-8.26	-8.30	-5.553
TA12-2-265	132.25	4.109	-7.91	-7.91	-7.95	-5.189
TA12-2-266	132.75	4.122	-8.02	-8.02	-8.05	-5.565
TA12-2-267	133.25	4.134	-7.97	-7.97	-8.01	-5.526
TA12-2-268	133.75	4.146	-7.98	-7.98	-8.02	-5.247
TA12-2-269	134.25	4.158	-8.05	-8.05	-8.09	-5.414
TA12-2-270	134.75	4.170	-8.07	-8.07	-8.11	-5.473
TA12-2-271	135.25	4.183	-8.11	-8.11	-8.15	-5.565
TA12-2-272	135.75	4.195	-8.04	-8.04	-8.08	-5.362
TA12-2-273	136.25	4.207	-8.06	-8.06	-8.10	-5.211
TA12-2-274	136.75	4.220	-7.87	-7.87	-7.90	-5.025
TA12-2-275	137.25	4.232	-7.81	-7.81	-7.85	-5.073
TA12-2-276	137.75	4.245	-8.09	-8.09	-8.13	-5.136
TA12-2-277	138.25	4.257	-8.28	-8.28	-8.32	-5.539
TA12-2-278	138.75	4.269	-8.37	-8.37	-8.41	-6.016
TA12-2-279	139.25	4.282	-8.20	-8.20	-8.24	-5.728
TA12-2-280	139.75	4.294	-7.76	-7.76	-7.80	-5.276
TA12-2-281	140.25	4.307	-7.55	-7.55	-7.59	-4.820
TA12-2-282	140.75	4.320	-7.66	-7.66	-7.70	-5.025
TA12-2-283	141.25	4.332	-7.80	-7.80	-7.84	-4.721
TA12-2-284	141.75	4.345	-7.85	-7.85	-7.89	-4.597
TA12-2-285	142.25	4.358	-8.23	-8.23	-8.27	-5.266
TA12-2-286	142.75	4.371	-8.19	-8.19	-8.23	-5.120
TA12-2-287	143.25	4.384	-8.01	-8.01	-8.05	-5.096
TA12-2-288	143.75	4.397	-8.04	-8.04	-8.08	-5.257
TA12-2-289	144.25	4.410	-8.38	-8.38	-8.42	-5.099
TA12-2-290	144.75	4.423	-8.10	-8.10	-8.14	-5.167
TA12-2-291	145.25	4.436	-8.03	-8.03	-8.07	-5.250
TA12-2-292	145.75	4.449	-7.89	-7.89	-7.93	-5.311
TA12-2-293	146.25	4.463	-7.99	-7.99	-8.03	-4.977
TA12-2-294	146.75	4.476	-8.20	-8.20	-8.24	-4.637
TA12-2-295	147.25	4.489	-8.45	-8.45	-8.49	-5.545
TA12-2-296	147.75	4.502	-8.39	-8.39	-8.43	-5.653
TA12-2-297	148.25	4.515	-8.19	-8.19	-8.23	-5.290
TA12-2-298	148.75	4.528	-8.05	-8.05	-8.10	-5.328
TA12-2-299	149.25	4.541	-8.01	-8.01	-8.05	-5.486
TA12-2-300	149.75	4.554	-8.55	-8.55	-8.59	-6.608
TA12-2-301	150.25	4.568	-8.86	-8.86	-8.91	-7.013
TA12-2-302	150.75	4.581	-8.75	-8.75	-8.79	-6.467

Sample ID	Depth (mm)	Age (ky BP)	$\delta^{18}O$-raw (‰VPDB)	$\delta^{18}O$-arag (‰VPDB)	$\delta^{18}O$-corr (‰VPDB)	$\delta^{13}C$-raw (‰VPDB)
TA12-2-303	151.25	4.594	-8.91	-8.41	-8.45	-5.574
TA12-2-304	151.75	4.607	-8.83	-8.35	-8.40	-5.564
TA12-2-305	152.25	4.621	-8.22	-8.22	-8.26	-5.506
TA12-2-306	152.75	4.634	-8.33	-8.33	-8.37	-5.579
TA12-2-307	153.25	4.647	-8.59	-8.32	-8.37	-5.735
TA12-2-308	153.75	4.660	-8.43	-8.43	-8.47	-5.475
TA12-2-309	154.25	4.674	-8.09	-8.09	-8.13	-5.265
TA12-2-310	154.75	4.687	-8.05	-8.05	-8.09	-5.035
TA12-2-311	155.25	4.700	-8.05	-8.05	-8.10	-5.279
TA12-2-312	155.75	4.714	-8.72	-8.41	-8.45	-5.745
TA12-2-313	156.25	4.727	-8.90	-8.55	-8.60	-6.294
TA12-2-314	156.75	4.741	-8.39	-8.20	-8.24	-5.059
TA12-2-315	157.25	4.754	-8.06	-8.06	-8.11	-5.145
TA12-2-316	157.75	4.768	-8.08	-8.03	-8.08	-4.988
TA12-2-317	158.25	4.781	-7.88	-7.88	-7.92	-5.011
TA12-2-318	158.75	4.795	-7.91	-7.91	-7.96	-4.821
TA12-2-319	159.25	4.808	-8.19	-8.19	-8.24	-4.685
TA12-2-320	159.75	4.822	-8.08	-8.08	-8.12	-5.151
TA12-2-321	160.25	4.835	-8.18	-8.18	-8.22	-5.144
TA12-2-322	160.75	4.849	-8.10	-8.10	-8.15	-5.146
TA12-2-323	161.25	4.863	-8.01	-8.01	-8.06	-5.369
TA12-2-324	161.75	4.877	-8.32	-8.02	-8.07	-5.132
TA12-2-325	162.25	4.890	-8.00	-8.00	-8.05	-5.254
TA12-2-326	162.75	4.904	-7.75	-7.75	-7.79	-5.056
TA12-2-327	163.25	4.918	-7.78	-7.78	-7.82	-4.901
TA12-2-328	163.75	4.932	-7.81	-7.81	-7.86	-4.787
TA12-2-329	164.25	4.946	-7.66	-7.66	-7.70	-5.257
TA12-2-330	164.75	4.959	-7.63	-7.63	-7.67	-5.284
TA12-2-331	165.25	4.973	-7.57	-7.57	-7.62	-4.849
TA12-2-332	165.75	4.987	-7.40	-7.40	-7.44	-4.968
TA12-2-333	166.25	5.001	-7.45	-7.45	-7.49	-4.967
TA12-2-334	166.75	5.015	-7.69	-7.69	-7.73	-5.210
TA12-2-335	167.25	5.028	-7.86	-7.86	-7.91	-4.692
TA12-2-336	167.75	5.042	-7.81	-7.81	-7.86	-4.668
TA12-2-337	168.25	5.056	-7.95	-7.95	-8.00	-4.848
TA12-2-338	168.75	5.070	-7.81	-7.81	-7.86	-4.895
TA12-2-339	169.25	5.084	-7.88	-7.88	-7.93	-5.105
TA12-2-340	169.75	5.097	-7.88	-7.88	-7.93	-5.263
TA12-2-341	170.25	5.111	-7.89	-7.89	-7.94	-5.211
TA12-2-342	170.75	5.125	-7.90	-7.90	-7.95	-5.325
TA12-2-343	171.25	5.140	-7.95	-7.95	-8.00	-5.131
TA12-2-344	171.75	5.154	-8.29	-8.29	-8.34	-5.431
TA12-2-345	172.25	5.168	-8.06	-8.06	-8.11	-5.130
TA12-2-346	172.75	5.182	-8.02	-8.02	-8.07	-5.062

Sample ID	Depth (mm)	Age (ky BP)	$\delta^{18}O$-raw (‰VPDB)	$\delta^{18}O$-arag (‰VPDB)	$\delta^{18}O$-corr (‰VPDB)	$\delta^{13}C$-raw (‰VPDB)
TA12-2-347	173.25	5.197	-8.04	-8.04	-8.09	-4.956
TA12-2-348	173.75	5.211	-8.12	-8.12	-8.17	-5.631
TA12-2-349	174.25	5.225	-8.09	-8.09	-8.15	-5.442
TA12-2-350	174.75	5.239	-8.18	-8.18	-8.23	-5.691
TA12-2-351	175.25	5.253	-8.02	-8.02	-8.07	-5.268
TA12-2-352	175.75	5.268	-8.13	-8.13	-8.18	-5.548
TA12-2-353	176.25	5.283	-8.06	-8.06	-8.11	-5.153
TA12-2-354	176.75	5.297	-8.53	-8.31	-8.36	-5.499
TA12-2-355	177.25	5.312	-8.45	-8.40	-8.46	-5.877
TA12-2-356	177.75	5.326	-8.09	-8.09	-8.15	-5.868
TA12-2-357	178.25	5.341	-8.20	-8.15	-8.20	-5.668
TA12-2-358	178.75	5.356	-8.54	-8.44	-8.49	-6.108
TA12-2-359	179.25	5.370	-8.50	-8.50	-8.56	-6.236
TA12-2-360	179.75	5.385	-8.90	-8.68	-8.73	-6.722
TA12-2-361	180.25	5.400	-8.46	-8.46	-8.51	-6.390
TA12-2-362	180.75	5.415	-9.05	-8.49	-8.55	-5.886
TA12-2-363	181.25	5.430	-8.38	-8.38	-8.44	-5.965
TA12-2-364	181.75	5.445	-8.83	-8.45	-8.50	-6.020
TA12-2-365	182.25	5.460	-9.13	-8.13	-8.19	-5.812
TA12-2-366	182.75	5.475	-8.94	-8.15	-8.21	-5.762
TA12-2-367	183.25	5.490	-9.00	-8.54	-8.60	-6.795
TA12-2-368	183.75	5.505	-8.96	-8.69	-8.75	-6.990
TA12-2-369	184.25	5.520	-8.31	-8.31	-8.37	-6.077
TA12-2-370	184.75	5.535	-8.46	-8.46	-8.52	-6.153
TA12-2-371	185.25	5.550	-8.46	-8.46	-8.52	-5.843
TA12-2-372	185.75	5.565	-8.43	-8.43	-8.49	-6.095
TA12-2-373	186.25	5.580	-8.60	-8.50	-8.56	-6.068
TA12-2-374	186.75	5.595	-8.67	-8.67	-8.72	-6.550
TA12-2-375	187.25	5.610	-8.59	-8.48	-8.54	-6.470
TA12-2-376	187.75	5.625	-8.50	-8.50	-8.56	-6.657
TA12-2-377	188.25	5.640	-8.84	-8.08	-8.14	-5.753
TA12-2-378	188.75	5.655	-9.17	-8.17	-8.23	-6.242
TA12-2-379	189.25	5.670	-9.43	-8.43	-8.49	-7.086
TA12-2-380	189.75	5.685	-9.38	-8.38	-8.44	-6.727
TA12-2-381	190.25	5.700	-9.27	-8.27	-8.33	-6.298
TA12-2-382	190.75	5.715	-9.23	-8.47	-8.53	-6.486
TA12-2-383	191.25	5.730	-8.96	-7.96	-8.02	-6.037
TA12-2-384	191.75	5.745	-8.39	-7.96	-8.02	-5.917
TA12-2-385	192.25	5.760	-8.24	-8.24	-8.30	-6.212
TA12-2-386	192.75	5.775	-8.00	-7.75	-7.82	-5.378
TA12-2-387	193.25	5.790	-8.47	-8.26	-8.33	-6.014
TA12-2-388	193.75	5.805	-8.57	-8.20	-8.26	-5.639
TA12-2-389	194.25	5.821	-8.97	-8.49	-8.56	-6.302
TA12-2-390	194.75	5.836	-9.19	-8.19	-8.26	-6.100

Sample ID	Depth (mm)	Age (ky BP)	$\delta^{18}O$-raw (‰VPDB)	$\delta^{18}O$-arag (‰VPDB)	$\delta^{18}O$-corr (‰VPDB)	$\delta^{13}C$-raw (‰VPDB)
TA12-2-391	195.25	5.851	-9.18	-8.18	-8.24	-5.802
TA12-2-392	195.75	5.866	-8.71	-8.49	-8.55	-6.568
TA12-2-393	196.25	5.881	-8.54	-8.37	-8.43	-6.317
TA12-2-394	196.75	5.897	-8.45	-8.23	-8.30	-5.587
TA12-2-395	197.25	5.912	-8.91	-7.91	-7.97	-5.411
TA12-2-396	197.75	5.927	-9.39	-8.39	-8.45	-6.427
TA12-2-397	198.25	5.942	-8.70	-8.20	-8.26	-6.150
TA12-2-398	198.75	5.957	-8.65	-8.65	-8.72	-6.301
TA12-2-399	199.25	5.973	-8.90	-8.10	-8.16	-5.478
TA12-2-400	199.75	5.988	-9.33	-8.33	-8.39	-6.031
TA12-2-401	200.25	6.003	-9.46	-8.46	-8.53	-5.964
TA12-2-402	200.75	6.018	-9.60	-8.60	-8.66	-6.044
TA12-2-403	201.25	6.033	-9.59	-8.59	-8.66	-6.294
TA12-2-404	201.75	6.048	-9.28	-8.28	-8.34	-6.102
TA12-2-405	202.25	6.063	-9.31	-8.31	-8.38	-6.108
TA12-2-406	202.75	6.078	-9.46	-8.46	-8.53	-6.208
TA12-2-407	203.25	6.093	-9.34	-8.34	-8.41	-6.009
TA12-2-408	203.75	6.107	-8.97	-8.17	-8.24	-5.258
TA12-2-409	204.25	6.122	-8.90	-8.45	-8.52	-5.864
TA12-2-410	204.75	6.137	-8.52	-8.28	-8.35	-5.842
TA12-2-411	205.25	6.152	-8.46	-8.16	-8.23	-5.165
TA12-2-412	205.75	6.166	-8.40	-8.40	-8.47	-5.777
TA12-2-413	206.25	6.181	-8.30	-8.30	-8.38	-5.419
TA12-2-414	206.75	6.195	-8.03	-8.03	-8.10	-5.195
TA12-2-415	207.25	6.210	-8.22	-8.12	-8.19	-5.371
TA12-2-416	207.75	6.224	-8.73	-8.03	-8.11	-5.388
TA12-2-417	208.25	6.239	-8.83	-8.22	-8.29	-5.617
TA12-2-418	208.75	6.253	-8.36	-8.07	-8.14	-5.315
TA12-2-419	209.25	6.268	-7.95	-7.95	-8.02	-5.243
TA12-2-420	209.75	6.282	-8.27	-8.07	-8.15	-5.114
TA12-2-421	210.25	6.297	-8.68	-7.73	-7.80	-5.168
TA12-2-422	210.75	6.311	-9.05	-8.05	-8.12	-5.397
TA12-2-423	211.25	6.324	-9.00	-8.00	-8.07	-5.325
TA12-2-424	211.75	6.338	-9.14	-8.14	-8.22	-5.709
TA12-2-425	212.25	6.352	-9.02	-8.07	-8.14	-5.598
TA12-2-426	212.75	6.366	-8.42	-8.42	-8.49	-6.391
TA12-2-427	213.25	6.380	-8.32	-8.16	-8.24	-6.115
TA12-2-428	213.75	6.394	-8.26	-7.71	-7.79	-5.061
TA12-2-429	214.25	6.408	-8.52	-7.67	-7.75	-5.402
TA12-2-430	214.75	6.422	-8.83	-7.83	-7.91	-5.848
TA12-2-431	215.25	6.435	-8.88	-8.04	-8.12	-6.613
TA12-2-432	215.75	6.448	-9.06	-8.06	-8.13	-5.937
TA12-2-433	216.25	6.461	-9.08	-8.08	-8.16	-5.819
TA12-2-434	216.75	6.474	-9.14	-8.14	-8.21	-5.856

Sample ID	Depth (mm)	Age (ky BP)	$\delta^{18}O$-raw (‰VPDB)	$\delta^{18}O$-arag (‰VPDB)	$\delta^{18}O$-corr (‰VPDB)	$\delta^{13}C$-raw (‰VPDB)
TA12-2-435	217.25	6.487	-8.95	-8.16	-8.24	-5.552
TA12-2-436	217.75	6.500	-8.54	-8.54	-8.61	-6.161
TA12-2-437	218.25	6.513	-8.15	-7.89	-7.97	-5.228
TA12-2-438	218.75	6.526	-7.91	-7.91	-7.99	-5.634
TA12-2-439	219.25	6.539	-7.90	-7.90	-7.97	-5.537
TA12-2-440	219.75	6.551	-7.82	-7.82	-7.90	-5.649
TA12-2-441	220.25	6.563	-7.80	-7.80	-7.88	-5.694
TA12-2-442	220.75	6.575	-8.00	-8.00	-8.08	-5.786
TA12-2-443	221.25	6.586	-8.00	-8.00	-8.08	-5.853
TA12-2-444	221.75	6.597	-8.45	-8.45	-8.53	-6.493
TA12-2-445	222.25	6.609	-8.26	-8.26	-8.34	-5.822
TA12-2-446	222.75	6.620	-8.07	-8.07	-8.15	-5.731
TA12-2-447	223.25	6.631	-7.99	-7.99	-8.07	-5.498
TA12-2-448	223.75	6.643	-8.05	-8.05	-8.13	-5.796
TA12-2-449	224.25	6.654	-7.97	-7.97	-8.05	-5.841
TA12-2-450	224.75	6.666	-7.91	-7.91	-7.99	-5.743
TA12-2-451	225.25	6.677	-7.91	-7.91	-7.99	-5.934
TA12-2-452	225.75	6.687	-7.97	-7.92	-8.00	-5.944
TA12-2-453	226.25	6.698	-7.71	-7.71	-7.79	-5.685
TA12-2-454	226.75	6.709	-7.70	-7.70	-7.78	-5.586
TA12-2-455	227.25	6.720	-7.37	-7.37	-7.45	-4.750
TA12-2-456	227.75	6.731	-7.74	-7.47	-7.55	-4.914
TA12-2-457	228.25	6.741	-7.93	-7.72	-7.81	-5.552
TA12-2-458	228.75	6.752	-8.68	-7.68	-7.77	-5.336
TA12-2-459	229.25	6.763	-8.96	-7.96	-8.04	-5.540
TA12-2-460	229.75	6.774	-8.39	-7.81	-7.89	-6.156
TA12-2-461	230.25	6.785	-8.29	-7.29	-7.38	-5.020
TA12-2-462	230.75	6.796	-8.79	-8.11	-8.19	-6.357
TA12-2-463	231.25	6.807	-8.89	-8.09	-8.18	-5.863
TA12-2-464	231.75	6.817	-8.20	-7.68	-7.77	-4.914
TA12-2-465	232.25	6.828	-8.67	-8.17	-8.25	-5.932
TA12-2-466	232.75	6.839	-9.00	-8.00	-8.08	-5.708
TA12-2-467	233.25	6.850	-8.81	-7.81	-7.89	-6.035
TA12-2-468	233.75	6.861	-8.86	-7.86	-7.95	-5.561
TA12-2-469	234.25	6.872	-9.09	-8.09	-8.18	-5.646
TA12-2-470	234.75	6.882	-8.89	-7.89	-7.97	-5.607
TA12-2-471	235.25	6.893	-9.21	-8.21	-8.30	-5.922
TA12-2-472	235.75	6.904	-9.05	-8.05	-8.13	-5.966
TA12-2-473	236.25	6.915	-8.91	-7.91	-7.99	-5.410
TA12-2-474	236.75	6.926	-8.35	-7.78	-7.87	-4.986
TA12-2-475	237.25	6.937	-8.22	-7.95	-8.04	-5.414
TA12-2-476	237.75	6.948	-8.20	-8.20	-8.28	-6.135
TA12-2-477	238.25	6.959	-7.98	-7.98	-8.06	-5.938
TA12-2-478	238.75	6.970	-8.04	-8.04	-8.12	-5.994

Sample ID	Depth (mm)	Age (ky BP)	$\delta^{18}O$-raw (‰VPDB)	$\delta^{18}O$-arag (‰VPDB)	$\delta^{18}O$-corr (‰VPDB)	$\delta^{13}C$-raw (‰VPDB)
TA12-2-479	239.25	6.981	-8.11	-8.11	-8.20	-5.967
TA12-2-480	239.75	6.992	-8.21	-8.21	-8.29	-6.002
TA12-2-481	240.25	7.003	-8.25	-8.25	-8.34	-6.201
TA12-2-482	240.75	7.013	-8.16	-8.16	-8.25	-5.871
TA12-2-483	241.25	7.024	-8.07	-8.07	-8.15	-5.987
TA12-2-484	241.75	7.035	-8.50	-7.90	-7.99	-5.310
TA12-2-485	242.25	7.046	-8.54	-7.75	-7.84	-5.523
TA12-2-486	242.75	7.057	-8.53	-7.61	-7.70	-5.224
TA12-2-487	243.25	7.068	-7.82	-7.82	-7.91	-5.453
TA12-2-488	243.75	7.079	-8.49	-7.99	-8.08	-5.572
TA12-2-489	244.25	7.090	-9.09	-8.09	-8.18	-5.526
TA12-2-490	244.75	7.101	-9.06	-8.06	-8.15	-5.638
TA12-2-491	245.25	7.112	-8.83	-7.83	-7.92	-5.190
TA12-2-492	245.75	7.123	-8.77	-7.77	-7.86	-5.421
TA12-2-493	246.25	7.134	-8.94	-7.94	-8.03	-5.446
TA12-2-494	246.75	7.145	-9.01	-8.01	-8.10	-5.953
TA12-2-495	247.25	7.155	-9.10	-8.10	-8.19	-6.270
TA12-2-496	247.75	7.167	-8.49	-7.84	-7.93	-6.067
TA12-2-497	248.25	7.177	-8.52	-7.90	-8.00	-5.893
TA12-2-498	248.75	7.188	-8.27	-7.62	-7.71	-5.674
TA12-2-499	249.25	7.199	-7.86	-7.79	-7.88	-5.906
TA12-2-500	249.75	7.210	-7.77	-7.77	-7.86	-6.035
TA12-2-501	250.25	7.221	-7.87	-7.74	-7.83	-5.487
TA12-2-502	250.75	7.232	-7.72	-7.72	-7.81	-5.952
TA12-2-503	251.25	7.244	-7.82	-7.82	-7.91	-6.005
TA12-2-504	251.75	7.255	-7.69	-7.69	-7.78	-5.725
TA12-2-505	252.25	7.266	-7.89	-7.89	-7.99	-6.228
TA12-2-506	252.75	7.277	-7.76	-7.76	-7.86	-5.860
TA12-2-507	253.25	7.288	-7.82	-7.82	-7.91	-6.254
TA12-2-508	253.75	7.300	-7.87	-7.87	-7.96	-6.203
TA12-2-509	254.25	7.311	-7.83	-7.78	-7.88	-5.710
TA12-2-510	254.75	7.322	-7.84	-7.79	-7.88	-5.758
TA12-2-511	255.25	7.333	-7.87	-7.87	-7.96	-5.740
TA12-2-512	255.75	7.345	-7.68	-7.68	-7.77	-5.667
TA12-2-513	256.25	7.357	-7.63	-7.63	-7.73	-5.723
TA12-2-514	256.75	7.369	-7.38	-7.38	-7.48	-5.386
TA12-2-515	257.25	7.380	-7.49	-7.49	-7.58	-5.403
TA12-2-516	257.75	7.392	-7.60	-7.60	-7.70	-5.464
TA12-2-517	258.25	7.404	-7.66	-7.66	-7.75	-5.823
TA12-2-518	258.75	7.416	-7.88	-7.88	-7.98	-6.359
TA12-2-519	259.25	7.427	-8.05	-8.05	-8.15	-6.528
TA12-2-520	259.75	7.439	-7.77	-7.77	-7.87	-5.798
TA12-2-521	260.25	7.451	-7.96	-7.96	-8.06	-5.714
TA12-2-522	260.75	7.464	-8.01	-8.01	-8.11	-6.035

Sample ID	Depth (mm)	Age (ky BP)	$\delta^{18}O$-raw (‰VPDB)	$\delta^{18}O$-arag (‰VPDB)	$\delta^{18}O$-corr (‰VPDB)	$\delta^{13}C$-raw (‰VPDB)
TA12-2-523	261.25	7.477	-8.16	-7.87	-7.96	-5.731
TA12-2-524	261.75	7.490	-7.93	-7.93	-8.02	-6.042
TA12-2-525	262.25	7.503	-8.03	-8.03	-8.13	-6.181
TA12-2-526	262.75	7.515	-7.90	-7.90	-8.00	-5.957
TA12-2-527	263.25	7.528	-7.82	-7.82	-7.92	-5.483
TA12-2-528	263.75	7.541	-7.82	-7.82	-7.92	-5.828
TA12-2-529	264.25	7.554	-7.61	-7.61	-7.71	-5.482
TA12-2-530	264.75	7.567	-7.90	-7.90	-8.00	-5.492
TA12-2-531	265.25	7.580	-7.89	-7.72	-7.82	-5.201
TA12-2-532	265.75	7.594	-7.88	-7.88	-7.98	-5.825
TA12-2-533	266.25	7.607	-7.88	-7.88	-7.98	-5.492
TA12-2-534	266.75	7.621	-7.93	-7.93	-8.03	-5.579
TA12-2-535	267.25	7.634	-7.82	-7.82	-7.92	-5.342
TA12-2-536	267.75	7.648	-7.75	-7.75	-7.85	-5.574
TA12-2-537	268.25	7.662	-7.84	-7.84	-7.94	-5.742
TA12-2-538	268.75	7.675	-7.91	-7.91	-8.01	-5.974
TA12-2-539	269.25	7.688	-7.65	-7.65	-7.75	-5.624
TA12-2-540	269.75	7.701	-7.97	-7.97	-8.07	-5.328
TA12-2-541	270.25	7.715	-7.54	-7.54	-7.64	-5.502
TA12-2-542	270.75	7.729	-7.56	-7.56	-7.66	-5.594
TA12-2-543	271.25	7.743	-7.60	-7.60	-7.71	-5.356
TA12-2-544	271.75	7.756	-7.85	-7.85	-7.95	-5.448
TA12-2-545	272.25	7.770	-7.80	-7.80	-7.91	-5.542
TA12-2-546	272.75	7.784	-7.70	-7.70	-7.81	-5.385
TA12-2-547	273.25	7.797	-7.66	-7.66	-7.76	-5.177
TA12-2-548	273.75	7.811	-7.72	-7.72	-7.82	-5.507
TA12-2-549	274.25	7.825	-7.82	-7.82	-7.92	-5.740
TA12-2-550	274.75	7.838	-7.82	-7.82	-7.93	-5.803
TA12-2-551	275.25	7.852	-7.71	-7.71	-7.82	-5.708
TA12-2-552	275.75	7.866	-7.95	-7.95	-8.06	-5.601
TA12-2-553	276.25	7.880	-7.86	-7.86	-7.97	-5.898
TA12-2-554	276.75	7.894	-7.97	-7.97	-8.08	-5.551
TA12-2-555	277.25	7.908	-8.06	-8.06	-8.17	-5.348
TA12-2-556	277.75	7.922	-7.84	-7.84	-7.95	-5.289
TA12-2-557	278.25	7.936	-7.99	-7.99	-8.10	-5.867
TA12-2-558	278.75	7.949	-8.10	-8.10	-8.21	-5.921
TA12-2-559	279.25	7.963	-7.93	-7.93	-8.04	-5.859
TA12-2-560	279.75	7.977	-7.98	-7.98	-8.09	-5.809
TA12-2-561	280.25	7.991	-7.91	-7.91	-8.02	-6.408
TA12-2-562	280.75	8.005	-7.87	-7.87	-7.98	-6.359
TA12-2-563	281.25	8.020	-7.85	-7.85	-7.96	-5.889
TA12-2-564	281.75	8.034	-7.89	-7.89	-8.01	-5.715
TA12-2-565	282.25	8.048	-7.94	-7.94	-8.05	-6.017
TA12-2-566	282.75	8.062	-7.91	-7.72	-7.83	-5.794

Sample ID	Depth (mm)	Age (ky BP)	$\delta^{18}O$-raw (‰VPDB)	$\delta^{18}O$-arag (‰VPDB)	$\delta^{18}O$-corr (‰VPDB)	$\delta^{13}C$-raw (‰VPDB)
TA12-2-567	283.25	8.077	-8.03	-7.78	-7.89	-5.372
TA12-2-568	283.75	8.091	-8.17	-8.17	-8.28	-6.257
TA12-2-569	284.25	8.105	-8.07	-8.07	-8.18	-6.095
TA12-2-570	284.75	8.119	-7.94	-7.94	-8.05	-5.911
TA12-2-571	285.25	8.134	-7.86	-7.86	-7.98	-5.746
TA12-2-572	285.75	8.148	-7.70	-7.70	-7.81	-5.195
TA12-2-573	286.25	8.163	-7.72	-7.72	-7.83	-5.095
TA12-2-574	286.75	8.177	-7.69	-7.69	-7.81	-5.535
TA12-2-575	287.25	8.192	-7.57	-7.57	-7.69	-5.229
TA12-2-576	287.75	8.206	-7.71	-7.71	-7.83	-5.325
TA12-2-577	288.25	8.221	-7.73	-7.73	-7.85	-5.620
TA12-2-578	288.75	8.235	-7.58	-7.58	-7.70	-5.926
TA12-2-579	289.25	8.250	-7.29	-7.29	-7.41	-5.372
TA12-2-580	289.75	8.264	-7.27	-7.27	-7.39	-5.342
TA12-2-581	290.25	8.279	-7.46	-7.46	-7.58	-5.359
TA12-2-582	290.75	8.293	-7.94	-7.63	-7.75	-5.795
TA12-2-583	291.25	8.308	-7.82	-7.76	-7.88	-6.127
TA12-2-584	291.75	8.323	-7.55	-7.23	-7.35	-5.185
TA12-2-585	292.25	8.337	-7.66	-7.66	-7.78	-5.691
TA12-2-586	292.75	8.352	-7.73	-7.73	-7.85	-5.826
TA12-2-587	293.25	8.367	-7.99	-7.99	-8.11	-5.827
TA12-2-588	293.75	8.381	-7.84	-7.84	-7.96	-5.714
TA12-2-589	294.25	8.396	-8.04	-8.04	-8.17	-6.215
TA12-2-590	294.75	8.411	-7.88	-7.88	-8.01	-6.013
TA12-2-591	295.25	8.425	-7.80	-7.80	-7.92	-5.937
TA12-2-592	295.75	8.440	-7.81	-7.81	-7.94	-6.421
TA12-2-593	296.25	8.455	-7.63	-7.63	-7.76	-6.357
TA12-2-594	296.75	8.470	-7.77	-7.77	-7.89	-6.017
TA12-2-595	297.25	8.485	-8.00	-7.53	-7.66	-5.300
TA12-2-596	297.75	8.500	-7.93	-7.67	-7.79	-5.803
TA12-2-597	298.25	8.515	-7.51	-7.51	-7.64	-5.926
TA12-2-598	298.75	8.530	-7.59	-7.40	-7.53	-5.611
TA12-2-599	299.25	8.545	-7.50	-7.50	-7.63	-5.757
TA12-2-600	299.75	8.560	-7.81	-7.81	-7.94	-6.089
TA12-2-601	300.25	8.575	-7.63	-7.63	-7.76	-5.997
TA12-2-602	300.75	8.590	-7.98	-7.98	-8.11	-6.389
TA12-2-603	301.25	8.606	-8.05	-7.57	-7.70	-5.885
TA12-2-604	301.75	8.622	-8.69	-7.69	-7.82	-6.006
TA12-2-605	302.25	8.637	-8.58	-7.58	-7.71	-6.118
TA12-2-606	302.75	8.652	-8.07	-8.01	-8.14	-6.473
TA12-2-607	303.25	8.668	-7.77	-7.77	-7.91	-6.148
TA12-2-608	303.75	8.683	-8.14	-7.92	-8.05	-6.394
TA12-2-609	304.25	8.699	-7.85	-7.70	-7.84	-6.029
TA12-2-610	304.75	8.714	-8.07	-7.81	-7.94	-6.265

Sample ID	Depth (mm)	Age (ky BP)	$\delta^{18}O$-raw (‰VPDB)	$\delta^{18}O$-arag (‰VPDB)	$\delta^{18}O$-corr (‰VPDB)	$\delta^{13}C$-raw (‰VPDB)
TA12-2-611	305.25	8.730	-7.67	-7.52	-7.66	-5.664
TA12-2-612	305.75	8.747	-8.47	-8.27	-8.41	-6.477
TA12-2-613	306.25	8.764	-8.05	-8.05	-8.19	-6.178
TA12-2-614	306.75	8.780	-8.65	-7.95	-8.09	-5.907
TA12-2-615	307.25	8.797	-8.84	-7.84	-7.98	-5.685
TA12-2-616	307.75	8.813	-8.35	-7.68	-7.82	-5.558
TA12-2-617	308.25	8.830	-8.03	-8.03	-8.17	-6.204
TA12-2-618	308.75	8.846	-8.13	-8.13	-8.27	-6.123
TA12-2-619	309.25	8.863	-8.01	-8.01	-8.15	-6.141
TA12-2-620	309.75	8.879	-8.18	-7.66	-7.80	-5.173
TA12-2-621	310.25	8.896	-8.54	-7.93	-8.07	-6.135
TA12-2-622	310.75	8.913	-8.02	-8.02	-8.16	-6.622
TA12-2-623	311.25	8.930	-8.51	-7.56	-7.71	-5.440
TA12-2-624	311.75	8.946	-8.00	-7.40	-7.55	-5.497
TA12-2-625	312.25	8.963	-8.05	-7.90	-8.05	-6.208
TA12-2-626	312.75	8.980	-7.93	-7.93	-8.08	-6.243
TA12-2-627	313.25	8.997	-7.92	-7.92	-8.07	-6.563
TA12-2-628	313.75	9.013	-8.31	-8.16	-8.31	-6.806
TA12-2-629	314.25	9.030	-8.13	-8.03	-8.18	-6.903
TA12-2-630	314.75	9.047	-8.27	-7.77	-7.93	-5.980
TA12-2-631	315.25	9.064	-8.22	-8.22	-8.37	-6.848
TA12-2-632	315.75	9.081	-8.35	-8.35	-8.50	-7.021
TA12-2-633	316.25	9.098	-8.18	-7.93	-8.08	-6.739
TA12-2-634	316.75	9.115	-7.96	-7.96	-8.12	-6.363
TA12-2-635	317.25	9.132	-8.37	-7.72	-7.88	-6.235
TA12-2-636	317.75	9.149	-8.69	-7.69	-7.85	-6.316
TA12-2-637	318.25	9.166	-8.48	-7.73	-7.89	-6.147
TA12-2-638	318.75	9.183	-8.33	-8.28	-8.44	-6.994
TA12-2-639	319.25	9.200	-8.21	-7.61	-7.77	-6.003
TA12-2-640	319.75	9.216	-8.45	-7.80	-7.96	-6.562
TA12-2-641	320.25	9.234	-8.66	-7.66	-7.82	-6.421
TA12-2-642	320.75	9.252	-8.35	-7.75	-7.92	-6.288
TA12-2-643	321.25	9.269	-7.97	-7.97	-8.13	-6.864
TA12-2-644	321.75	9.287	-8.17	-8.17	-8.33	-6.804
TA12-2-645	322.25	9.304	-8.16	-7.66	-7.83	-5.960
TA12-2-646	322.75	9.322	-8.55	-8.03	-8.20	-6.816
TA12-2-647	323.25	9.340	-8.25	-7.88	-8.05	-6.302
TA12-2-648	323.75	9.358	-8.00	-7.39	-7.56	-5.660
TA12-2-649	324.25	9.375	-8.25	-8.25	-8.42	-6.468
TA12-2-650	324.75	9.393	-8.27	-7.77	-7.94	-6.349
TA12-2-651	325.25	9.411	-7.76	-7.76	-7.93	-6.672
TA12-2-652	325.75	9.430	-8.05	-8.05	-8.22	-6.616
TA12-2-653	326.25	9.449	-7.88	-7.88	-8.05	-6.013
TA12-2-654	326.75	9.468	-7.81	-7.81	-7.98	-6.284

Sample ID	Depth (mm)	Age (ky BP)	$\delta^{18}O$-raw (‰VPDB)	$\delta^{18}O$-arag (‰VPDB)	$\delta^{18}O$-corr (‰VPDB)	$\delta^{13}C$-raw (‰VPDB)
TA12-2-655	327.25	9.487	-7.77	-7.77	-7.95	-6.288
TA12-2-656	327.75	9.507	-7.71	-7.71	-7.89	-6.347
TA12-2-657	328.25	9.525	-7.73	-7.73	-7.91	-6.411
TA12-2-658	328.75	9.545	-7.66	-7.66	-7.85	-6.300
TA12-2-659	329.25	9.564	-7.86	-7.81	-8.00	-6.326
TA12-2-660	329.75	9.583	-7.80	-7.66	-7.85	-6.322
TA12-2-661	330.25	9.603	-7.87	-7.87	-8.06	-6.277
TA12-2-662	330.75	9.624	-7.72	-7.72	-7.91	-6.014
TA12-2-663	331.25	9.645	-7.35	-7.35	-7.53	-5.966
TA12-2-664	331.75	9.666	-7.37	-7.37	-7.56	-6.038
TA12-2-665	332.25	9.687	-7.78	-7.69	-7.89	-6.517
TA12-2-666	332.75	9.708	-8.54	-7.54	-7.73	-6.059
TA12-2-667	333.25	9.730	-8.59	-7.59	-7.78	-5.928
TA12-2-668	333.75	9.750	-8.37	-7.37	-7.57	-5.330
TA12-2-669	334.25	9.771	-8.26	-7.61	-7.81	-6.141
TA12-2-670	334.75	9.792	-8.59	-7.59	-7.79	-6.228
TA12-2-671	335.25	9.814	-8.56	-7.56	-7.76	-6.389
TA12-2-672	335.75	9.838	-8.09	-7.09	-7.30	-5.024
TA12-2-673	336.25	9.861	-8.32	-7.45	-7.65	-5.082
TA12-2-674	336.75	9.884	-8.03	-7.42	-7.62	-5.381
TA12-2-675	337.25	9.907	-8.29	-7.63	-7.83	-5.769
TA12-2-676	337.75	9.930	-8.12	-7.12	-7.33	-5.088
TA12-2-677	338.25	9.953	-8.38	-7.38	-7.59	-5.412
TA12-2-678	338.75	9.976	-8.47	-7.47	-7.68	-5.466
TA12-2-679	339.25	9.999	-8.34	-7.34	-7.55	-5.574
TA12-2-680	339.75	10.022	-8.22	-7.22	-7.44	-5.545
TA12-2-681	340.25	10.045	-8.73	-7.73	-7.95	-5.343
TA12-2-682	340.75	10.069	-8.75	-7.75	-7.97	-5.613
TA12-2-683	341.25	10.093	-8.76	-7.76	-7.98	-5.500
TA12-2-684	341.75	10.117	-8.63	-7.63	-7.85	-5.262
TA12-2-685	342.25	10.141	-8.28	-7.28	-7.51	-5.204
TA12-2-686	342.75	10.164	-8.46	-7.46	-7.68	-5.109
TA12-2-687	343.25	10.188	-8.44	-7.44	-7.66	-5.367
TA12-2-688	343.75	10.212	-8.29	-7.29	-7.51	-5.231
TA12-2-689	344.25	10.236	-8.52	-7.52	-7.75	-5.473
TA12-2-690	344.75	10.259	-8.47	-7.47	-7.70	-5.530
TA12-2-691	345.25	10.283	-8.47	-7.47	-7.70	-5.476
TA12-2-692	345.75	10.308	-8.17	-7.17	-7.40	-4.970
TA12-2-693	346.25	10.333	-8.21	-7.21	-7.45	-5.326
TA12-2-694	346.75	10.357	-7.83	-6.83	-7.07	-4.367
TA12-2-695	347.25	10.382	-7.71	-6.71	-6.94	-4.097
TA12-2-696	347.75	10.407	-7.24	-6.97	-7.21	-5.098
TA12-2-697	348.25	10.431	-7.08	-7.08	-7.32	-5.339
TA12-2-698	348.75	10.456	-7.22	-7.22	-7.46	-5.328

Sample ID	Depth (mm)	Age (ky BP)	$\delta^{18}O$-raw (‰VPDB)	$\delta^{18}O$-arag (‰VPDB)	$\delta^{18}O$-corr (‰VPDB)	$\delta^{13}C$-raw (‰VPDB)
TA12-2-699	349.25	10.480	-7.36	-7.36	-7.61	-5.542
TA12-2-700	349.75	10.505	-7.05	-7.05	-7.30	-5.459
TA12-2-701	350.25	10.530	-6.92	-6.92	-7.17	-5.231
TA12-2-702	350.75	10.555	-7.11	-7.11	-7.36	-5.143
TA12-2-703	351.25	10.581	-7.52	-7.14	-7.39	-4.984
TA12-2-704	351.75	10.606	-7.88	-6.88	-7.14	-4.874
TA12-2-705	352.25	10.632	-7.97	-6.97	-7.23	-4.954
TA12-2-706	352.75	10.657	-7.87	-6.95	-7.21	-5.270
TA12-2-707	353.25	10.682	-7.40	-7.05	-7.31	-5.823
TA12-2-708	353.75	10.707	-7.59	-7.29	-7.55	-6.138
TA12-2-709	354.25	10.733	-7.31	-7.08	-7.35	-5.946
TA12-2-710	354.75	10.758	-7.17	-7.17	-7.44	-6.348
TA12-2-711	355.25	10.784	-7.43	-6.66	-6.93	-5.525
TA12-2-712	355.75	10.810	-7.67	-6.67	-6.95	-5.930
TA12-2-713	356.25	10.836	-7.77	-6.77	-7.05	-5.645
TA12-2-714	356.75	10.862	-7.84	-6.84	-7.12	-6.123
TA12-2-715	357.25	10.888	-7.83	-6.94	-7.23	-6.421
TA12-2-716	357.75	10.915	-6.68	-6.68	-6.97	-5.846
TA12-2-717	358.25	10.941	-6.47	-6.47	-6.76	-6.137
TA12-2-718	358.75	10.967	-6.65	-6.65	-6.94	-6.319
TA12-2-719	359.25	10.993	-6.90	-6.90	-7.20	-6.900
TA12-2-720	359.75	11.019	-6.83	-6.83	-7.13	-6.513
TA12-2-721	360.25	11.046	-6.76	-6.76	-7.06	-6.345
TA12-2-722	360.75	11.074	-6.88	-6.88	-7.18	-6.622
TA12-2-723	361.25	11.101	-6.91	-6.91	-7.21	-6.715
TA12-2-724	361.75	11.129	-6.75	-6.66	-6.97	-6.214
TA12-2-725	362.25	11.156	-6.68	-6.58	-6.89	-6.032
TA12-2-726	362.75	11.183	-6.71	-6.71	-7.03	-5.849
TA12-2-727	363.25	11.211	-7.02	-6.88	-7.19	-6.400
TA12-2-728	363.75	11.238	-6.67	-6.67	-6.99	-6.142
TA12-2-729	364.25	11.265	-7.07	-6.73	-7.06	-6.020
TA12-2-730	364.75	11.293	-7.25	-6.34	-6.67	-5.752
TA12-2-731	365.25	11.320	-6.62	-6.19	-6.52	-5.554
TA12-2-732	365.75	11.348	-7.18	-6.66	-6.99	-6.273
TA12-2-733	366.25	11.376	-6.54	-6.54	-6.88	-6.114
TA12-2-734	366.75	11.404	-6.87	-6.40	-6.74	-5.801
TA12-2-735	367.25	11.432	-7.26	-6.26	-6.60	-5.429
TA12-2-736	367.75	11.460	-7.01	-6.32	-6.67	-5.949
TA12-2-737	368.25	11.488	-6.58	-6.37	-6.72	-6.325
TA12-2-738	368.75	11.516	-6.28	-6.28	-6.64	-6.494
TA12-2-739	369.25	11.543	-6.11	-5.79	-6.15	-6.201
TA12-2-740	369.75	11.571	-5.58	-5.58	-5.94	-5.943
TA12-2-741	370.25	11.597	-5.45	-5.45	-5.81	-5.270
TA12-2-742	370.75	11.620	-5.52	-5.52	-5.88	-5.164

Sample ID	Depth (mm)	Age (ky BP)	$\delta^{18}O$-raw (‰VPDB)	$\delta^{18}O$-arag (‰VPDB)	$\delta^{18}O$-corr (‰VPDB)	$\delta^{13}C$-raw (‰VPDB)
TA12-2-743	371.25	11.643	-5.53	-5.53	-5.90	-5.088
TA12-2-744	371.75	11.667	-5.31	-5.31	-5.69	-4.849
TA12-2-745	372.25	11.690	-5.28	-5.28	-5.66	-4.996
TA12-2-746	372.75	11.714	-5.52	-5.52	-5.90	-5.216
TA12-2-747	373.25	11.737	-5.57	-5.57	-5.95	-5.038
TA12-2-748	373.75	11.760	-5.61	-5.61	-5.99	-5.318
TA12-2-749	374.25	11.784	-5.39	-5.39	-5.78	-5.331
TA12-2-750	374.75	11.807	-5.39	-5.39	-5.78	-4.911
TA12-2-751	375.25	11.826	-5.29	-5.29	-5.69	-4.712
TA12-2-752	375.75	11.842	-5.31	-5.31	-5.71	-4.887
TA12-2-753	376.25	11.858	-5.14	-5.14	-5.54	-4.675
TA12-2-754	376.75	11.874	-5.12	-5.12	-5.52	-4.675
TA12-2-755	377.25	11.889	-5.17	-5.17	-5.57	-4.922
TA12-2-756	377.75	11.905	-5.09	-5.09	-5.49	-4.319
TA12-2-757	378.25	11.921	-5.15	-5.15	-5.56	-4.760
TA12-2-758	378.75	11.937	-5.06	-5.06	-5.47	-4.633
TA12-2-759	379.25	11.953	-5.11	-5.11	-5.53	-4.723
TA12-2-760	379.75	11.968	-4.95	-4.95	-5.37	-4.612
TA12-2-761	380.25	11.983	-4.96	-4.96	-5.38	-4.444
TA12-2-762	380.75	11.995	-4.95	-4.95	-5.37	-4.728
TA12-2-763	381.25	12.008	-5.07	-5.07	-5.49	-4.988
TA12-2-764	381.75	12.020	-4.90	-4.90	-5.32	-4.927
TA12-2-765	382.25	12.033	-4.95	-4.95	-5.37	-4.468
TA12-2-766	382.75	12.045	-5.08	-5.08	-5.51	-4.575
TA12-2-767	383.25	12.058	-5.06	-5.06	-5.48	-4.641
TA12-2-768	383.75	12.070	-5.19	-5.19	-5.62	-4.866
TA12-2-769	384.25	12.083	-5.25	-5.25	-5.68	-4.736
TA12-2-770	384.75	12.095	-4.98	-4.98	-5.41	-4.743
TA12-2-771	385.25	12.108	-4.82	-4.82	-5.25	-4.486
TA12-2-772	385.75	12.120	-4.77	-4.77	-5.21	-4.396
TA12-2-773	386.25	12.133	-4.69	-4.69	-5.12	-4.214
TA12-2-774	386.75	12.145	-4.79	-4.79	-5.22	-4.432
TA12-2-775	387.25	12.157	-4.97	-4.97	-5.40	-4.315
TA12-2-776	387.75	12.170	-4.99	-4.99	-5.43	-4.362
TA12-2-777	388.25	12.182	-5.05	-5.05	-5.49	-3.991
TA12-2-778	388.75	12.194	-5.07	-5.07	-5.52	-3.987
TA12-2-779	389.25	12.206	-4.94	-4.94	-5.39	-3.898
TA12-2-780	389.75	12.219	-4.97	-4.97	-5.41	-4.493
TA12-2-781	390.25	12.231	-5.00	-5.00	-5.45	-4.642
TA12-2-782	390.75	12.243	-5.00	-5.00	-5.45	-4.490
TA12-2-783	391.25	12.256	-5.02	-5.02	-5.47	-4.353
TA12-2-784	391.75	12.269	-4.73	-4.73	-5.19	-3.945
TA12-2-785	392.25	12.281	-4.71	-4.71	-5.17	-3.974
TA12-2-786	392.75	12.294	-4.84	-4.84	-5.30	-3.940

Sample ID	Depth (mm)	Age (ky BP)	$\delta^{18}O$-raw (‰VPDB)	$\delta^{18}O$-arag (‰VPDB)	$\delta^{18}O$-corr (‰VPDB)	$\delta^{13}C$-raw (‰VPDB)
TA12-2-787	393.25	12.306	-4.92	-4.92	-5.37	-4.047
TA12-2-788	393.75	12.319	-4.99	-4.99	-5.45	-4.144
TA12-2-789	394.25	12.331	-4.76	-4.76	-5.22	-4.002
TA12-2-790	394.75	12.344	-4.60	-4.60	-5.07	-3.563
TA12-2-791	395.25	12.357	-4.64	-4.64	-5.10	-3.634
TA12-2-792	395.75	12.370	-4.83	-4.83	-5.29	-3.624
TA12-2-793	396.25	12.383	-4.83	-4.83	-5.30	-4.121
TA12-2-794	396.75	12.396	-5.06	-5.06	-5.53	-4.420
TA12-2-795	397.25	12.409	-5.21	-5.21	-5.68	-4.500
TA12-2-796	397.75	12.422	-5.11	-5.11	-5.59	-4.556
TA12-2-797	398.25	12.435	-4.88	-4.88	-5.36	-4.147
TA12-2-798	398.75	12.448	-5.08	-5.08	-5.56	-4.460
TA12-2-799	399.25	12.461	-5.02	-5.02	-5.50	-4.279
TA12-2-800	399.75	12.474	-5.07	-5.07	-5.55	-4.288
TA12-2-801	400.25	12.487	-5.15	-5.15	-5.63	-4.445
TA12-2-802	400.75	12.501	-5.18	-5.18	-5.66	-4.543
TA12-2-803	401.25	12.515	-5.25	-5.25	-5.73	-4.447
TA12-2-804	401.75	12.529	-5.27	-5.27	-5.76	-4.627
TA12-2-805	402.25	12.542	-5.13	-5.13	-5.62	-4.533
TA12-2-806	402.75	12.556	-5.14	-5.14	-5.63	-4.492
TA12-2-807	403.25	12.569	-5.00	-5.00	-5.49	-4.363
TA12-2-808	403.75	12.583	-5.13	-5.13	-5.62	-4.544
TA12-2-809	404.25	12.596	-5.18	-5.18	-5.67	-4.338
TA12-2-810	404.75	12.610	-5.30	-5.30	-5.80	-4.144
TA12-2-811	405.25	12.624	-5.38	-5.38	-5.88	-4.348
TA12-2-812	405.75	12.638	-5.36	-5.36	-5.87	-4.211
TA12-2-813	406.25	12.651	-5.36	-5.36	-5.86	-4.483
TA12-2-814	406.75	12.665	-5.26	-5.26	-5.77	-3.988
TA12-2-815	407.25	12.679	-5.39	-5.39	-5.90	-4.181
TA12-2-816	407.75	12.693	-5.37	-5.37	-5.88	-4.069
TA12-2-817	408.25	12.707	-5.33	-5.33	-5.84	-4.177
TA12-2-818	408.75	12.721	-5.30	-5.30	-5.81	-3.954
TA12-2-819	409.25	12.735	-5.46	-5.46	-5.98	-4.108
TA12-2-820	409.75	12.749	-5.60	-5.60	-6.12	-4.267
TA12-2-821	410.25	12.763	-5.45	-5.45	-5.97	-4.156
TA12-2-822	410.75	12.777	-5.53	-5.53	-6.05	-4.039
TA12-2-823	411.25	12.790	-5.58	-5.58	-6.11	-4.235
TA12-2-824	411.75	12.804	-5.51	-5.51	-6.04	-4.100
TA12-2-825	412.25	12.818	-5.47	-5.47	-6.00	-4.196
TA12-2-826	412.75	12.832	-5.23	-5.23	-5.76	-4.131
TA12-2-827	413.25	12.846	-5.34	-5.34	-5.87	-4.243
TA12-2-828	413.75	12.860	-5.50	-5.50	-6.04	-4.345
TA12-2-829	414.25	12.874	-5.52	-5.52	-6.06	-4.280
TA12-2-830	414.75	12.887	-5.48	-5.48	-6.02	-4.418

Sample ID	Depth (mm)	Age (ky BP)	$\delta^{18}O$-raw (‰VPDB)	$\delta^{18}O$-arag (‰VPDB)	$\delta^{18}O$-corr (‰VPDB)	$\delta^{13}C$-raw (‰VPDB)
TA12-2-831	415.25	12.901	-5.49	-5.49	-6.04	-4.408
TA12-2-832	415.75	12.915	-5.47	-5.47	-6.02	-4.435
TA12-2-833	416.25	12.928	-5.80	-5.80	-6.35	-4.640
TA12-2-834	416.75	12.942	-5.73	-5.73	-6.27	-4.411
TA12-2-835	417.25	12.955	-5.66	-5.66	-6.21	-4.086
TA12-2-836	417.75	12.969	-5.95	-5.95	-6.50	-4.858
TA12-2-837	418.25	12.982	-5.96	-5.96	-6.51	-5.160
TA12-2-838	418.75	12.996	-5.86	-5.86	-6.41	-4.892
TA12-2-839	419.25	13.010	-5.79	-5.79	-6.35	-4.809
TA12-2-840	419.75	13.023	-5.77	-5.77	-6.33	-4.957
TA12-2-841	420.25	13.036	-5.85	-5.85	-6.41	-4.646
TA12-2-842	420.75	13.050	-5.70	-5.70	-6.26	-4.743
TA12-2-843	421.25	13.064	-5.46	-5.46	-6.03	-4.700
TA12-2-844	421.75	13.077	-5.50	-5.50	-6.06	-4.717
TA12-2-845	422.25	13.091	-5.55	-5.55	-6.12	-4.583
TA12-2-846	422.75	13.104	-5.50	-5.50	-6.07	-4.230
TA12-2-847	423.25	13.118	-5.57	-5.57	-6.14	-4.541
TA12-2-848	423.75	13.131	-5.81	-5.81	-6.38	-4.533
TA12-2-849	424.25	13.145	-5.85	-5.85	-6.43	-4.475
TA12-2-850	424.75	13.158	-5.70	-5.70	-6.28	-5.003
TA12-2-851	425.25	13.172	-5.64	-5.64	-6.22	-4.749
TA12-2-852	425.75	13.185	-5.80	-5.80	-6.38	-4.670
TA12-2-853	426.25	13.198	-5.40	-5.40	-5.98	-4.425
TA12-2-854	426.75	13.212	-5.34	-5.34	-5.92	-4.303
TA12-2-855	427.25	13.225	-5.41	-5.41	-6.00	-4.305
TA12-2-856	427.75	13.239	-5.60	-5.60	-6.19	-4.509
TA12-2-857	428.25	13.252	-5.64	-5.64	-6.23	-4.747
TA12-2-858	428.75	13.265	-5.67	-5.67	-6.27	-5.046
TA12-2-859	429.25	13.279	-5.49	-5.49	-6.09	-4.865
TA12-2-860	429.75	13.292	-5.52	-5.52	-6.12	-4.840
TA12-2-861	430.25	13.305	-5.55	-5.55	-6.15	-4.815
TA12-2-862	430.75	13.318	-5.60	-5.60	-6.20	-4.752
TA12-2-863	431.25	13.331	-5.50	-5.50	-6.10	-4.652
TA12-2-864	431.75	13.344	-5.57	-5.57	-6.17	-4.916
TA12-2-865	432.25	13.357	-5.50	-5.50	-6.10	-4.895
TA12-2-866	432.75	13.370	-5.48	-5.48	-6.08	-5.156
TA12-2-867	433.25	13.383	-5.48	-5.48	-6.09	-4.854
TA12-2-868	433.75	13.396	-5.57	-5.57	-6.18	-5.061
TA12-2-869	434.25	13.409	-5.41	-5.41	-6.02	-5.105
TA12-2-870	434.75	13.422	-5.49	-5.49	-6.10	-5.318
TA12-2-871	435.25	13.435	-5.46	-5.46	-6.08	-4.921
TA12-2-872	435.75	13.447	-5.40	-5.40	-6.02	-5.128
TA12-2-873	436.25	13.459	-5.25	-5.25	-5.87	-4.923
TA12-2-874	436.75	13.471	-5.39	-5.39	-6.01	-5.140

Sample ID	Depth (mm)	Age (ky BP)	$\delta^{18}O$-raw (‰VPDB)	$\delta^{18}O$-arag (‰VPDB)	$\delta^{18}O$-corr (‰VPDB)	$\delta^{13}C$-raw (‰VPDB)
TA12-2-875	437.25	13.483	-5.36	-5.36	-5.98	-5.043
TA12-2-876	437.75	13.495	-5.36	-5.36	-5.99	-4.975
TA12-2-877	438.25	13.507	-5.37	-5.37	-5.99	-4.890
TA12-2-878	438.75	13.519	-5.50	-5.50	-6.13	-5.175
TA12-2-879	439.25	13.531	-5.39	-5.39	-6.01	-4.971
TA12-2-880	439.75	13.543	-5.56	-5.56	-6.19	-5.521
TA12-2G-881	440.45	14.421	-5.65	-5.65	-6.39	-4.29
TA12-2G-882	440.95	14.441	-5.44	-5.44	-6.18	-4.45
TA12-2G-883	441.45	14.462	-5.58	-5.58	-6.32	-4.64
TA12-2G-884	441.95	14.482	-5.77	-5.77	-6.52	-5.51
TA12-2G-885	442.45	14.502	-5.35	-5.35	-6.10	-4.53
TA12-2G-886	442.95	14.522	-5.19	-5.19	-5.94	-4.54
TA12-2G-887	443.45	14.542	-5.44	-5.44	-6.19	-4.62
TA12-2G-888	443.95	14.562	-5.05	-5.05	-5.81	-4.05
TA12-2G-889	444.45	14.582	-5.33	-5.33	-6.09	-4.25
TA12-2G-890	444.95	14.602	-4.90	-4.90	-5.66	-3.86
TA12-2G-891	445.45	14.621	-5.00	-5.00	-5.76	-4.20
TA12-2G-892	445.95	14.641	-4.73	-4.73	-5.50	-3.80
TA12-2G-893	446.45	14.661	-4.61	-4.61	-5.38	-3.25
TA12-2G-894	446.95	14.680	-4.59	-4.59	-5.36	-3.14
TA12-2G-895	447.45	14.700	-4.88	-4.88	-5.65	-3.33
TA12-2G-896	447.95	14.719	-4.97	-4.81	-5.59	-4.13
TA12-2G-897	448.45	14.739	-4.86	-4.86	-5.64	-3.74
TA12-2G-898	448.95	14.758	-4.59	-4.59	-5.37	-3.55
TA12-2G-899	449.45	14.778	-4.58	-4.58	-5.36	-3.64
TA12-2G-900	449.95	14.797	-4.45	-4.45	-5.23	-3.53
TA12-2G-	450.45	14.816	-4.76	-4.29	-5.07	-3.88

Sample ID	Depth (mm)	Age (ky BP)	$\delta^{18}O$-raw (‰VPDB)	$\delta^{18}O$-arag (‰VPDB)	$\delta^{18}O$-corr (‰VPDB)	$\delta^{13}C$-raw (‰VPDB)
TA12-2G-901						
TA12-2G-902	450.95	14.835	-4.76	-4.76	-5.55	-4.00
TA12-2G-903	451.45	14.854	-4.89	-4.89	-5.68	-4.16
TA12-2G-904	451.95	14.874	-4.46	-4.46	-5.25	-3.23
TA12-2G-905	452.45	14.893	-4.74	-4.74	-5.54	-3.31
TA12-2G-906	452.95	14.912	-4.69	-4.69	-5.49	-3.71
TA12-2G-907	453.45	14.931	-4.69	-4.69	-5.49	-3.86
TA12-2G-908	453.95	14.950	-4.57	-4.57	-5.37	-3.69
TA12-2G-909	454.45	14.969	-4.91	-4.91	-5.71	-4.01
TA12-2G-910	454.95	14.988	-4.54	-4.54	-5.35	-3.62
TA12-2G-911	455.45	15.007	-4.69	-4.69	-5.50	-3.92
TA12-2G-912	455.95	15.026	-4.66	-4.66	-5.47	-3.69
TA12-2G-913	456.45	15.045	-4.66	-4.66	-5.47	-3.81
TA12-2G-914	456.95	15.064	-5.00	-5.00	-5.81	-3.95
TA12-2G-915	457.45	15.083	-4.78	-4.57	-5.39	-4.33
TA12-2G-916	457.95	15.102	-5.30	-4.35	-5.17	-4.98
TA12-2G-917	458.45	15.121	-5.44	-4.65	-5.47	-4.79
TA12-2G-918	458.95	15.140	-4.63	-4.30	-5.12	-4.19
TA12-2G-919	459.45	15.159	-4.57	-4.57	-5.40	-3.73
TA12-2G-920	459.95	15.177	-4.50	-4.50	-5.33	-3.60
TA12-2G-921	460.45	15.196	-4.60	-4.60	-5.43	-3.92
TA12-2G-922	460.95	15.215	-4.49	-4.49	-5.32	-4.10
TA12-2G-923	461.45	15.234	-4.42	-4.42	-5.25	-3.88
TA12-2G-924	461.95	15.253	-4.34	-4.34	-5.18	-3.91

Sample ID	Depth (mm)	Age (ky BP)	$\delta^{18}O$-raw (‰VPDB)	$\delta^{18}O$-arag (‰VPDB)	$\delta^{18}O$-corr (‰VPDB)	$\delta^{13}C$-raw (‰VPDB)
TA12-2G-925	462.45	15.272	-4.51	-4.51	-5.35	-3.79
TA12-2G-926	462.95	15.292	-4.35	-4.35	-5.19	-3.67
TA12-2G-927	463.45	15.311	-4.59	-4.59	-5.43	-4.05
TA12-2G-928	463.95	15.330	-4.25	-4.25	-5.09	-3.86
TA12-2G-929	464.45	15.350	-4.77	-4.30	-5.14	-4.44
TA12-2G-930	464.95	15.370	-4.51	-4.04	-4.88	-4.20
TA12-2G-931	465.45	15.389	-4.46	-4.30	-5.15	-3.65
TA12-2G-932	465.95	15.409	-4.52	-4.52	-5.37	-4.23
TA12-2G-933	466.45	15.429	-4.69	-4.53	-5.39	-4.42
TA12-2G-934	466.95	15.450	-4.35	-4.35	-5.21	-4.17
TA12-2G-935	467.45	15.470	-4.53	-4.27	-5.12	-4.16
TA12-2G-936	467.95	15.491	-4.50	-3.97	-4.83	-4.39
TA12-2G-937	468.45	15.512	-5.19	-4.77	-5.63	-5.76
TA12-2G-938	468.95	15.534	-5.00	-4.00	-4.86	-5.85
TA12-2G-939	469.45	15.556	-5.46	-4.46	-5.33	-6.43
TA12-2G-940	469.95	15.577	-5.93	-4.93	-5.80	-8.95
TA12-2G-941	470.45	15.600	-5.92	-4.92	-5.79	-8.77
TA12-2G-942	470.95	15.622	-5.88	-4.88	-5.75	-8.08
TA12-2G-943	471.45	15.645	-5.97	-4.97	-5.85	-7.34
TA12-2G-944	471.95	15.668	-6.08	-5.08	-5.96	-9.04
TA12-2G-945	472.45	15.691	-6.29	-5.29	-6.17	-7.90
TA12-2G-946	472.95	15.714	-5.88	-4.88	-5.76	-8.71
TA12-2G-947	473.45	15.737	-6.09	-5.09	-5.97	-8.78
TA12-2G-948	473.95	15.761	-6.26	-5.26	-6.15	-9.28

Sample ID	Depth (mm)	Age (ky BP)	$\delta^{18}O$-raw (‰VPDB)	$\delta^{18}O$-arag (‰VPDB)	$\delta^{18}O$-corr (‰VPDB)	$\delta^{13}C$-raw (‰VPDB)
TA12-2G-949	474.45	15.784	-6.11	-5.11	-6.00	-8.29
TA12-2G-950	474.95	15.809	-6.35	-5.35	-6.24	-10.51
TA12-2G-951	475.45	15.833	-6.19	-5.19	-6.08	-10.13
TA12-2G-952	475.95	15.857	-6.02	-5.02	-5.92	-9.62
TA12-2G-953	476.45	15.881	-5.89	-4.89	-5.79	-8.56
TA12-2G-954	476.95	15.905	-5.49	-4.49	-5.39	-7.27
TA12-2G-955	477.45	15.929	-5.66	-4.66	-5.56	-6.71
TA12-2G-956	477.95	15.953	-6.08	-5.08	-5.99	-9.70
TA12-2G-957	478.45	15.978	-5.91	-4.91	-5.82	-8.81
TA12-2G-958	478.95	16.002	-5.38	-4.38	-5.29	-7.04
TA12-2G-959	479.45	16.027	-5.88	-4.88	-5.79	-8.30
TA12-2G-960	479.95	16.051	-5.70	-4.70	-5.61	-7.50
TA12-2G-961	480.45	16.076	-5.79	-4.79	-5.71	-7.09
TA12-2G-962	480.95	16.101	-5.21	-4.21	-5.13	-6.19
TA12-2G-963	481.45	16.125	-4.89	-4.31	-5.23	-4.63
TA12-2G-964	481.95	16.150	-4.63	-4.63	-5.55	-4.09
TA12-2G-965	482.45	16.175	-4.77	-4.77	-5.69	-4.11
TA12-2G-966	482.95	16.200	-4.54	-4.54	-5.47	-3.78
TA12-2G-967	483.45	16.225	-4.85	-4.85	-5.78	-4.05
TA12-2G-968	483.95	16.250	-4.67	-4.67	-5.60	-4.28
TA12-2G-969	484.45	16.275	-4.79	-4.79	-5.72	-4.32
TA12-2G-970	484.95	16.300	-4.56	-4.35	-5.28	-4.17
TA12-2G-971	485.45	16.324	-4.77	-4.77	-5.71	-4.21
TA12-2G-972	485.95	16.349	-4.56	-4.40	-5.34	-4.18

Sample ID	Depth (mm)	Age (ky BP)	$\delta^{18}O$-raw (‰VPDB)	$\delta^{18}O$-arag (‰VPDB)	$\delta^{18}O$-corr (‰VPDB)	$\delta^{13}C$-raw (‰VPDB)
TA12-2G-973	486.45	16.373	-4.69	-4.69	-5.63	-4.09
TA12-2G-974	486.95	16.398	-4.39	-4.39	-5.33	-3.92
TA12-2G-975	487.45	16.423	-4.60	-4.60	-5.54	-4.04
TA12-2G-976	487.95	16.448	-4.45	-4.45	-5.39	-4.14
TA12-2G-977	488.45	16.472	-4.68	-4.68	-5.63	-4.23
TA12-2G-978	488.95	16.497	-4.47	-4.47	-5.42	-4.16
TA12-2G-979	489.45	16.522	-4.78	-4.78	-5.73	-4.60
TA12-2G-980	489.95	16.546	-5.25	-4.51	-5.46	-6.19
TA12-2G-981	490.45	16.571	-5.49	-4.49	-5.44	-5.87

Appendix 2

A2 – TA12-8 stable isotope data. Where applicable, isotope values shown equal the mean of replicate measurements. Age is reported in ky BP where present is 1950.

Sample ID	Depth (mm)	Age (ky BP)	δ^{18}O-raw (‰VPDB)	δ^{13}C-raw (‰VPDB)
TA12-8-A1	0.6	NaN	-8.29	-6.77
TA12-8-A2	1.8	NaN	-8.30	-7.13
TA12-8-A3	3	NaN	-8.42	-6.15
TA12-8-A4	4.2	NaN	-8.31	-6.60
TA12-8-A5	5.4	NaN	-8.51	-7.08
TA12-8-A6	6.6	NaN	-8.41	-6.88
TA12-8-A7	7.8	NaN	-8.70	-7.58
TA12-8-A8	9	NaN	-8.86	-7.70
TA12-8-A9	10.2	NaN	-8.83	-7.71
TA12-8-A10	11.4	4.676	-8.80	-7.84
TA12-8-A11	12.6	4.682	-8.99	-8.34
TA12-8-A12	13.8	4.689	-8.57	-7.83
TA12-8-A13	15	4.695	-8.74	-8.13
TA12-8-A14	16.2	4.702	-8.61	-7.90
TA12-8-A15	17.4	4.708	-8.71	-8.05
TA12-8-A16	18.6	4.715	-8.94	-8.22
TA12-8-A17	19.8	4.721	-8.78	-7.29
TA12-8-A18	21	4.728	-8.87	-8.15
TA12-8-A19	22.2	4.735	-8.97	-8.57
TA12-8-A20	23.4	4.742	-9.07	-7.94
TA12-8-A21	24.6	4.749	-8.90	-8.25
TA12-8-A22	25.8	4.755	-8.72	-7.55
TA12-8-A23	27	4.762	-8.88	-7.64
TA12-8-A24	28.2	4.769	-8.92	-8.17
TA12-8-A25	29.4	4.776	-8.68	-8.47
TA12-8-A26	30.6	4.783	-8.80	-8.35
TA12-8-A27	31.8	4.791	-9.14	-8.88
TA12-8-A28	33	4.798	-9.02	-8.52
TA12-8-A29	34.2	4.805	-8.90	-8.26
TA12-8-A30	35.4	4.812	-8.43	-7.63
TA12-8-A31	36.6	4.820	-8.75	-8.83
TA12-8-A32	37.8	4.827	-8.54	-7.80
TA12-8-A33	39	4.834	-8.51	-7.51
TA12-8-A34	40.2	4.842	-8.84	-7.28
TA12-8-A35	41.4	4.850	-8.91	-6.84
TA12-8-A36	42.6	4.858	-8.65	-7.12
TA12-8-A37	43.8	4.866	-8.91	-6.86
TA12-8-A38	45	4.874	-8.95	-7.54
TA12-8-A39	46.2	4.882	-9.20	-8.62

Sample ID	Depth (mm)	Age (ky BP)	$\delta^{18}O$-raw (‰VPDB)	$\delta^{13}C$-raw (‰VPDB)
TA12-8-A40	47.4	4.890	-8.89	-8.38
TA12-8-A41	48.6	4.899	-9.09	-8.38
TA12-8-A42	49.8	4.907	-8.91	-8.41
TA12-8-A43	51	4.916	-8.94	-8.23
TA12-8-A44	52.2	4.924	-8.68	-7.85
TA12-8-A45	53.4	4.933	-8.75	-8.88
TA12-8-A46	54.6	4.942	-8.97	-9.57
TA12-8-A47	55.8	4.951	-8.81	-9.13
TA12-8-A48	57	4.959	-8.99	-9.50
TA12-8-A49	58.2	4.968	-9.05	-9.25
TA12-8-A50	59.4	4.977	-8.89	-8.58
TA12-8-A51	60.6	4.986	-8.81	-8.85
TA12-8-A52	61.65	4.994	-8.87	-8.04
TA12-8-A53	62.7	5.002	-8.90	-8.14
TA12-8-A54	63.9	5.011	-8.94	-7.88
TA12-8-A55	65.1	5.020	-8.88	-8.46
TA12-8-A56	66.3	5.029	-9.06	-8.87
TA12-8-A57	67.5	5.038	-9.06	-9.12
TA12-8-A58	68.7	5.047	-8.80	-8.43
TA12-8-A59	69.9	5.056	-8.91	-8.30
TA12-8-A60	71.1	5.066	-9.03	-8.85
TA12-8-A61	72.3	5.075	-8.98	-9.01
TA12-8-A62	73.5	5.084	-8.82	-8.95
TA12-8-A63	74.7	5.093	NaN	NaN
TA12-8-A64	75.9	5.102	NaN	NaN
TA12-8-A65	77.1	5.112	NaN	NaN
TA12-8-A66	78.3	5.121	-8.78	-8.79
TA12-8-A67	79.5	5.130	-8.95	-9.04
TA12-8-A68	80.7	5.139	NaN	NaN
TA12-8-A69	81.9	5.148	-9.01	-9.07
TA12-8-A70	83.1	5.157	-8.99	-8.99
TA12-8-A71	84.3	5.167	-8.86	-8.72
TA12-8-A72	85.5	5.176	-8.64	-9.05
TA12-8-A73	86.7	5.185	-9.07	-9.74
TA12-8-A74	87.9	5.194	-8.99	-9.74
TA12-8-A75	89.1	5.204	-9.22	-10.27
TA12-8-A76	90.3	5.213	NaN	NaN
TA12-8-A77	91.5	5.222	-9.13	-9.81
TA12-8-A78	92.7	5.231	-9.00	-9.73
TA12-8-A79	93.9	5.240	NaN	NaN
TA12-8-A80	95.1	5.249	NaN	NaN
TA12-8-A81	96.3	5.259	-9.18	-9.98
TA12-8-A82	97.5	5.268	-9.10	-9.69
TA12-8-A83	98.7	5.277	-8.88	-9.05

Sample ID	Depth (mm)	Age (ky BP)	$\delta^{18}O$-raw (‰VPDB)	$\delta^{13}C$-raw (‰VPDB)
TA12-8-A84	99.9	5.286	NaN	NaN
TA12-8-A85	101.1	5.295	-9.17	-9.78
TA12-8-A86	102.3	5.304	-9.10	-9.63
TA12-8-A87	103.5	5.313	-9.19	-9.77
TA12-8-A88	104.7	5.321	NaN	NaN
TA12-8-A89	105.9	5.330	-9.08	-9.49
TA12-8-A90	107.1	5.339	-9.05	-9.51
TA12-8-A91	108.3	5.348	-9.05	-9.19
TA12-8-A92	109.5	5.357	NaN	NaN
TA12-8-A93	110.7	5.365	-8.90	-9.23
TA12-8-A94	111.9	5.374	-9.03	-9.89
TA12-8-A95	113.1	5.382	-9.00	-9.43
TA12-8-A96	114.3	5.390	-9.11	-9.52
TA12-8-A97	115.5	5.398	-8.97	-9.34
TA12-8-A98	116.7	5.406	-8.76	-8.98
TA12-8-A99	117.9	5.414	-9.12	-9.75
TA12-8-A100	119.1	5.422	-9.09	-9.48
TA12-8-A101	120.3	5.430	-9.20	-9.68
TA12-8-A102	121.5	5.436	-9.10	-9.63
TA12-8-A103	122.7	5.443	-9.14	-9.70
TA12-8-A104	123.9	5.450	-9.03	-9.30
TA12-8-A105	125.1	5.456	-8.87	-8.64
TA12-8-A106	126.3	5.463	-8.97	-8.06
TA12-8-A107	127.5	5.469	-9.19	-8.70
TA12-8-A108	128.7	5.476	-9.02	-9.17
TA12-8-A109	129.9	5.482	-9.07	-9.53
TA12-8-A110	131.1	5.488	-8.86	-8.80
TA12-8-A111	132.3	5.493	-9.12	-9.19
TA12-8-A112	133.5	5.498	-9.03	-8.76
TA12-8-A113	134.95	5.505	-8.86	-8.57
TA12-8-B1	136.4	5.511	-9.11	-8.29
TA12-8-B2	137.6	5.517	-8.75	-7.96
TA12-8-B3	138.8	5.522	-8.90	-8.68
TA12-8-B4	140	5.528	-8.87	-9.21
TA12-8-B5	141.2	5.533	-8.93	-9.44
TA12-8-B6	142.4	5.538	-8.71	-8.61
TA12-8-B7	143.6	5.542	-8.75	-8.55
TA12-8-B8	144.8	5.548	-8.97	-8.95
TA12-8-B9	146	5.552	-9.05	-8.82
TA12-8-B10	147.2	5.557	-8.87	-8.28
TA12-8-B11	148.4	5.563	-8.89	-8.21
TA12-8-B12	149.6	5.568	-8.95	-8.34
TA12-8-B13	150.8	5.572	-8.92	-8.30
TA12-8-B14	152	5.577	-8.69	-7.83

Sample ID	Depth (mm)	Age (ky BP)	$\delta^{18}O$-raw (‰VPDB)	$\delta^{13}C$-raw (‰VPDB)
TA12-8-B15	153.2	5.582	-8.91	-8.29
TA12-8-B16	154.4	5.587	-8.76	-8.41
TA12-8-B17	155.6	5.592	-8.94	-8.67
TA12-8-B18	156.8	5.597	-9.08	-8.90
TA12-8-B19	158	5.602	-8.98	-8.71
TA12-8-B20	159.2	5.607	-8.77	-7.54
TA12-8-B21	160.4	5.612	-8.90	-8.48
TA12-8-B22	161.6	5.617	-8.82	-8.66
TA12-8-B23	162.8	5.622	-8.79	-8.68
TA12-8-B24	164	5.626	-8.77	-7.89
TA12-8-B25	165.2	5.631	-8.92	-7.98
TA12-8-B26	166.4	5.636	-8.87	-7.76
TA12-8-B27	167.6	5.641	-8.90	-7.65
TA12-8-B28	168.8	5.646	-8.99	-8.64
TA12-8-B29	170	5.651	-9.03	-8.87
TA12-8-B30	171.2	5.656	-9.05	-8.80
TA12-8-B31	172.4	5.661	-8.90	-8.65
TA12-8-B32	173.6	5.666	-8.94	-8.72
TA12-8-B33	174.8	5.670	-8.86	-8.41
TA12-8-B34	176	5.675	-8.97	-8.74
TA12-8-B35	177.2	5.680	-8.93	-8.82
TA12-8-B36	178.4	5.685	-8.99	-8.83
TA12-8-B37	179.6	5.690	-8.72	-8.92
TA12-8-B38	180.8	5.695	-8.86	-9.19
TA12-8-B39	182	5.700	-8.95	-9.58
TA12-8-B40	183.2	5.705	-8.94	-9.53
TA12-8-B41	184.4	5.710	-9.02	-9.30
TA12-8-B42	185.6	5.715	-8.97	-9.25
TA12-8-B43	186.8	5.720	-8.67	-8.48
TA12-8-B44	188	5.725	-8.67	-8.93
TA12-8-B45	189.2	5.730	-8.89	-9.25
TA12-8-B46	190.4	5.735	-8.98	-9.47
TA12-8-B47	191.6	5.741	-9.16	-9.40
TA12-8-B48	192.8	5.746	-9.06	-9.02
TA12-8-B49	194	5.751	-9.11	-8.87
TA12-8-B50	195.2	5.757	-8.94	-8.59
TA12-8-B51	196.4	5.762	-9.08	-8.92
TA12-8-B52	197.6	5.767	-9.02	-9.42
TA12-8-B53	198.8	5.772	-9.21	-9.70
TA12-8-B54	199.7	5.776	-8.98	-8.51
TA12-8-B55	200.6	5.780	-9.03	-8.49
TA12-8-B56	201.8	5.786	-8.85	-8.75
TA12-8-B57	203	5.791	-8.84	-8.53
TA12-8-B58	204.2	5.796	-8.78	-8.61

Sample ID	Depth (mm)	Age (ky BP)	$\delta^{18}O$-raw (‰VPDB)	$\delta^{13}C$-raw (‰VPDB)
TA12-8-B59	205.4	5.802	-8.72	-8.28
TA12-8-B60	206.6	5.807	-8.94	-7.90
TA12-8-B61	207.8	5.813	-8.76	-7.51
TA12-8-B62	209	5.818	-8.86	-7.74
TA12-8-B63	210.2	5.824	-8.97	-8.08
TA12-8-B64	211.4	5.829	-9.02	-8.06
TA12-8-B65	212.6	5.835	-8.91	-7.87
TA12-8-B66	213.8	5.840	-8.85	-7.88
TA12-8-B67	215	5.846	-8.97	-7.94
TA12-8-B68	216.2	5.851	-8.97	-8.21
TA12-8-B69	217.4	5.857	-9.01	-7.83
TA12-8-B70	218.6	5.862	-9.00	-7.67
TA12-8-B71	219.8	5.868	-9.09	-7.93
TA12-8-B72	221	5.874	-8.98	-7.81
TA12-8-B73	222.2	5.879	-9.00	-8.09
TA12-8-B74	223.4	5.885	-8.94	-8.02
TA12-8-B75	224.6	5.891	-9.02	-8.30
TA12-8-B76	225.8	5.896	NaN	NaN
TA12-8-B77	227	5.902	-8.87	-7.75
TA12-8-B78	228.2	5.908	-8.89	-8.07
TA12-8-B79	229.4	5.913	-9.12	-8.71
TA12-8-B80	230.6	5.919	-8.95	-8.43
TA12-8-B81	231.8	5.925	-8.98	-7.88
TA12-8-B82	233	5.931	-8.84	-8.13
TA12-8-B83	234.2	5.937	-8.98	-8.46
TA12-8-B84	235.4	5.943	-8.97	-8.58
TA12-8-B85	236.6	5.949	-8.91	-7.86
TA12-8-B86	237.8	5.955	-8.94	-7.80
TA12-8-B87	239	5.961	-9.05	-7.60
TA12-8-B88	240.2	5.967	-9.00	-8.23
TA12-8-B89	241.4	5.973	-9.09	-8.65
TA12-8-B90	242.6	5.980	-8.69	-8.04
TA12-8-B91	243.8	5.986	-8.71	-8.05
TA12-8-B92	245	5.993	-8.76	-8.18
TA12-8-B93	246.2	5.999	-8.85	-8.30
TA12-8-B94	247.4	6.006	-9.01	-8.51
TA12-8-B95	248.6	6.012	NaN	NaN
TA12-8-B96	249.8	6.019	-9.05	-8.44
TA12-8-B97	251	6.026	-8.92	-7.97
TA12-8-B98	252.2	6.034	-8.87	-8.24
TA12-8-B99	253.4	6.041	-9.06	-8.49
TA12-8-B100	254.6	6.049	NaN	NaN
TA12-8-B101	255.8	6.056	-9.04	-6.82
TA12-8-B102	257	6.064	-8.84	-6.65

Sample ID	Depth (mm)	Age (ky BP)	$\delta^{18}O$-raw (‰VPDB)	$\delta^{13}C$-raw (‰VPDB)
TA12-8-B103	258.2	6.071	-8.31	-5.93
TA12-8-B104	259.4	6.079	-8.71	-6.79
TA12-8-B105	260.6	6.087	-8.89	-7.24
TA12-8-B106	261.8	6.096	-8.68	-6.79
TA12-8-B107	263	6.105	-8.75	-6.84
TA12-8-B108	264.2	6.114	-8.73	-6.77
TA12-8-B109	265.4	6.123	-8.54	-6.44
TA12-8-B110	266.6	6.132	-8.65	-7.35
TA12-8-B111	267.8	6.141	-8.69	-7.52
TA12-8-B112	269	6.150	-8.60	-7.28
TA12-8-B113	270.2	6.159	-8.57	-6.51
TA12-8-B114	271.4	6.169	-8.52	-6.72
TA12-8-B115	272.6	6.179	-8.65	-7.68
TA12-8-B116	273.8	6.189	-8.68	-7.54
TA12-8-B117	275	6.199	-8.74	-7.57
TA12-8-B118	276.2	6.209	-8.75	-7.74
TA12-8-B119	277.4	6.219	-8.80	-7.82
TA12-8-B120	278.6	6.228	NaN	NaN
TA12-8-B121	279.8	6.238	NaN	NaN
TA12-8-B122	281	6.249	-8.95	-8.35
TA12-8-B123	282.2	6.259	-8.78	-7.98
TA12-8-B124	283.4	6.270	-8.74	-7.36
TA12-8-B125	284.6	6.281	-8.79	-7.27
TA12-8-B126	285.8	6.291	NaN	NaN
TA12-8-B127	287	6.302	-9.02	-7.30
TA12-8-B128	288.2	6.313	-8.75	-7.09
TA12-8-B129	289.4	6.323	-8.55	-6.97
TA12-8-B130	290.6	6.334	-8.69	-7.87
TA12-8-B131	291.8	6.345	-8.50	-7.51
TA12-8-B132	293	6.356	-8.71	-8.27
TA12-8-B133	294.2	6.368	-8.94	-8.51
TA12-8-B134	295.4	6.379	-8.88	-8.41
TA12-8-B135	296.6	6.390	-8.87	-8.42
TA12-8-B136	297.8	6.401	-8.68	-8.39
TA12-8-B137	299	6.412	-8.51	-8.12
TA12-8-B138	300.2	6.423	-8.66	-8.43
TA12-8-B139	301.4	6.434	-8.60	-8.28
TA12-8-B140	302.6	6.445	-9.02	-9.15
TA12-8-B141	303.8	6.456	-8.76	-8.01
TA12-8-B142	305	6.467	-8.55	-7.70
TA12-8-B143	306.2	6.478	-8.54	-7.82
TA12-8-B144	307.4	6.489	-8.81	-8.80
TA12-8-B145	308.6	6.500	-8.53	-8.21
TA12-8-B146	309.8	6.511	-8.49	-8.31

Sample ID	Depth (mm)	Age (ky BP)	$\delta^{18}O$-raw (‰VPDB)	$\delta^{13}C$-raw (‰VPDB)
TA12-8-B147	311	6.522	-8.59	-8.33
TA12-8-B148	312.2	6.533	-8.55	-8.35
TA12-8-B149	313.4	6.543	-8.54	-8.50
TA12-8-B150	314.6	6.554	-9.06	-9.05
TA12-8-B151	315.8	6.564	-9.03	-9.22
TA12-8-B152	317	6.575	-9.02	-9.13
TA12-8-B153	318.2	6.586	NaN	NaN
TA12-8-B154	319.4	6.596	-8.82	-8.52
TA12-8-B155	320.6	6.606	-8.81	-7.68
TA12-8-B156	321.8	6.616	-8.68	-6.76
TA12-8-B157	323	6.626	-8.80	-6.97
TA12-8-B158	324.2	6.635	-8.31	-6.89
TA12-8-B159	325.4	6.645	-8.14	-7.41
TA12-8-B160	326.6	6.654	-8.55	-8.23
TA12-8-B161	327.8	6.664	-8.51	-8.13
TA12-8-B162	329	6.674	-8.39	-7.95
TA12-8-B163	330.2	6.683	-8.41	-8.10
TA12-8-B164	331.4	6.691	-8.38	-7.71
TA12-8-B165	332.6	6.699	-8.56	-8.11
TA12-8-B166	333.8	6.706	-8.73	-8.51
TA12-8-B167	335	6.714	-8.90	-8.93
TA12-8-B168	336.2	6.722	-8.71	-8.38
TA12-8-B169	337.4	6.730	-8.63	-8.23
TA12-8-B170	338.6	6.737	-8.59	-7.62
TA12-8-B171	339.8	6.745	-8.64	-8.35
TA12-8-B172	341	6.751	-8.56	-8.19
TA12-8-B173	342.2	6.757	-8.89	-8.70
TA12-8-B174	343.4	6.762	-8.90	-9.14
TA12-8-B175	344.6	6.767	-8.65	-9.03
TA12-8-B176	345.8	6.773	-8.72	-9.12
TA12-8-B177	347	6.778	-8.30	-8.37
TA12-8-B178	348.2	6.784	-8.64	-8.70
TA12-8-B179	349.4	6.789	-8.63	-8.72
TA12-8-B180	350.6	6.794	-8.60	-8.76
TA12-8-B181	351.8	6.799	-8.83	-9.02
TA12-8-B182	353	6.804	-8.68	-8.59
TA12-8-B183	354.2	6.809	-8.51	-8.39
TA12-8-B184	355.4	6.814	-8.80	-8.77
TA12-8-B185	356.6	6.819	-8.69	-8.49
TA12-8-B186	357.8	6.824	-8.51	-7.96
TA12-8-B187	359	6.828	-8.61	-8.49
TA12-8-B188	360.2	6.833	-8.59	-8.55
TA12-8-B189	361.4	6.838	-8.75	-9.12
TA12-8-B190	362.6	6.842	-8.49	-8.37

Sample ID	Depth (mm)	Age (ky BP)	$\delta^{18}O$-raw (‰VPDB)	$\delta^{13}C$-raw (‰VPDB)
TA12-8-B191	363.8	6.847	-8.89	-9.12
TA12-8-C001	365	6.851	-8.93	-9.23
TA12-8-C002	366.2	6.856	-8.87	-9.19
TA12-8-C003	367.4	6.860	-8.82	-8.33
TA12-8-C004	368.6	6.865	-8.62	-7.99
TA12-8-C005	369.8	6.869	-8.77	-8.81
TA12-8-C006	371	6.873	-8.84	-9.43
TA12-8-C007	372.2	6.878	-8.71	-9.06
TA12-8-C008	373.4	6.882	-8.64	-9.14
TA12-8-C009	374.6	6.887	-8.73	-9.32
TA12-8-C010	375.8	6.891	-8.77	-9.55
TA12-8-C011	377	6.895	-8.69	-9.34
TA12-8-C012	378.2	6.900	-8.60	-8.98
TA12-8-C013	379.4	6.904	-8.69	-9.18
TA12-8-C014	380.6	6.909	-8.60	-9.12
TA12-8-C015	381.8	6.913	-8.62	-9.00
TA12-8-C016	383	6.917	-8.65	-9.18
TA12-8-C017	384.2	6.922	-8.59	-9.01
TA12-8-C018	385.4	6.926	-8.49	-8.92
TA12-8-C019	386.6	6.930	-8.65	-8.79
TA12-8-C020	387.8	6.934	-8.64	-8.75
TA12-8-C021	389	6.939	-8.73	-9.05
TA12-8-C022	390.2	6.943	-8.76	-9.19
TA12-8-C023	391.4	6.947	-8.61	-8.66
TA12-8-C024	392.6	6.951	-8.77	-9.19
TA12-8-C025	393.8	6.956	-8.67	-8.93
TA12-8-C026	395	6.960	-8.70	-8.96
TA12-8-C027	396.2	6.964	-8.75	-8.93
TA12-8-C028	397.4	6.969	-8.68	-8.68
TA12-8-C029	398.6	6.973	-8.66	-8.94
TA12-8-C030	399.8	6.977	-8.68	-9.26
TA12-8-C031	401	6.981	-8.40	-8.98
TA12-8-C032	402.2	6.986	-8.45	-8.97
TA12-8-C033	403.4	6.990	-8.43	-8.85
TA12-8-C034	404.6	6.994	-8.45	-8.74
TA12-8-C035	405.8	6.998	-8.40	-8.61
TA12-8-C036	407	7.003	-8.27	-8.53
TA12-8-C037	408.2	7.007	-8.19	-8.23
TA12-8-C038	409.4	7.011	-8.23	-8.36
TA12-8-C039	410.6	7.015	-8.56	-8.88
TA12-8-C040	411.8	7.020	-8.52	-8.76
TA12-8-C041	413	7.024	-8.76	-9.38
TA12-8-C042	414.2	7.028	-8.48	-9.02
TA12-8-C043	415.4	7.032	-8.56	-9.13

Sample ID	Depth (mm)	Age (ky BP)	$\delta^{18}O$-raw (‰VPDB)	$\delta^{13}C$-raw (‰VPDB)
TA12-8-C044	416.6	7.036	-8.69	-9.36
TA12-8-C045	417.8	7.041	-8.66	-8.95
TA12-8-C046	419	7.045	-8.59	-8.92
TA12-8-C047	420.2	7.049	-8.71	-8.93
TA12-8-C048	421.4	7.053	-8.62	-9.05
TA12-8-C049	422.6	7.057	-8.49	-8.55
TA12-8-C050	423.8	7.062	-8.89	-9.24
TA12-8-C051	425	7.066	-8.96	-9.43
TA12-8-C052	426.2	7.070	-8.78	-9.15
TA12-8-C053	427.4	7.074	-8.79	-9.21
TA12-8-C054	428.6	7.078	-8.84	-9.27
TA12-8-C055	429.8	7.083	-8.96	-9.26
TA12-8-C056	431	7.087	-9.06	-9.61
TA12-8-C057	432.2	7.091	-8.69	-8.32
TA12-8-C058	433.4	7.095	-8.77	-9.07
TA12-8-C059	434.6	7.099	-8.77	-8.59
TA12-8-C060	435.8	7.104	-8.82	-8.95
TA12-8-C061	437	7.108	-9.03	-9.60
TA12-8-C062	438.2	7.112	-8.42	-8.05
TA12-8-C063	439.4	7.116	-8.65	-8.45
TA12-8-C064	440.6	7.121	-8.84	-9.33
TA12-8-C065	441.8	7.125	-8.86	-9.33
TA12-8-C066	443	7.129	-8.92	-9.50
TA12-8-D001	444.2	7.133	-8.77	-8.83
TA12-8-D002	445.4	7.137	-8.84	-8.26
TA12-8-D003	446.6	7.141	-8.70	-8.38
TA12-8-D004	447.8	7.145	-8.56	-7.92
TA12-8-D005	449	7.149	-8.56	-8.01
TA12-8-D006	450.2	7.154	-8.75	-8.32
TA12-8-D007	451.4	7.158	-8.75	-8.61
TA12-8-D008	452.6	7.162	-8.85	-8.74
TA12-8-D009	453.8	7.166	-8.61	-8.72
TA12-8-D010	455	7.170	-8.60	-8.31
TA12-8-D011	456.2	7.174	-8.64	-8.66
TA12-8-D012	457.4	7.179	-8.68	-8.37
TA12-8-D013	458.6	7.183	-8.70	-8.34
TA12-8-D014	459.8	7.187	-8.60	-8.40
TA12-8-D015	461	7.191	-8.83	-9.33
TA12-8-D016	462.2	7.195	-8.95	-9.66
TA12-8-D017	463.4	7.199	-9.04	-8.29
TA12-8-D018	464.6	7.204	-9.02	-8.97
TA12-8-D019	465.8	7.208	-8.82	-9.18
TA12-8-D020	467	7.212	-9.00	-9.46
TA12-8-D021	468.2	7.216	-8.92	-9.29

Sample ID	Depth (mm)	Age (ky BP)	δ^{18}O-raw (‰VPDB)	δ^{13}C-raw (‰VPDB)
TA12-8-D022	469.4	7.220	-9.00	-9.04
TA12-8-D023	470.6	7.224	-8.76	-8.91
TA12-8-D024	471.8	7.228	NaN	NaN
TA12-8-D025	473	7.232	-8.87	-9.20
TA12-8-D026	474.2	7.237	-8.80	-8.73
TA12-8-D027	475.4	7.241	-8.87	-8.42
TA12-8-D028	476.6	7.245	-8.97	-8.51
TA12-8-D029	477.8	7.249	-8.88	-8.30
TA12-8-D030	479	7.253	-8.98	-7.63
TA12-8-D031	480.2	7.257	-8.89	-8.32
TA12-8-D032	481.4	7.261	-8.90	-7.97
TA12-8-D033	482.6	7.265	-8.87	-7.51
TA12-8-D034	483.8	7.269	-8.92	-7.40
TA12-8-D035	485	7.273	-8.55	-7.73
TA12-8-D036	486.2	7.278	-8.68	-7.55
TA12-8-D037	487.4	7.282	-8.64	-7.99
TA12-8-D038	488.6	7.286	-8.55	-7.95
TA12-8-D039	489.8	7.290	-8.63	-8.17
TA12-8-D040	491	7.294	-8.94	-7.85
TA12-8-D041	492.2	7.298	-8.93	-8.01
TA12-8-D042	493.4	7.303	-8.84	-8.38
TA12-8-D043	494.6	7.307	-8.70	-8.11
TA12-8-D044	495.8	7.311	-8.73	-8.08
TA12-8-D045	497	7.315	-8.59	-7.94
TA12-8-D046	498.2	7.319	-8.59	-8.08
TA12-8-D047	499.4	7.323	-8.63	-7.92
TA12-8-D048	500.6	7.328	-8.77	-8.42
TA12-8-D049	501.8	7.332	-8.49	-8.40
TA12-8-D050	503	7.336	-8.83	-8.56
TA12-8-D051	504.2	7.340	-8.49	-7.99
TA12-8-D052	505.4	7.344	-8.71	-7.69
TA12-8-D053	506.6	7.349	-8.59	-7.39
TA12-8-D054	507.8	7.353	-8.71	-7.49
TA12-8-D055	509	7.357	-8.57	-7.11
TA12-8-D056	510.2	7.361	-8.65	-7.24
TA12-8-D057	511.4	7.365	-8.81	-7.83
TA12-8-D058	512.6	7.369	-9.00	-7.69
TA12-8-D059	513.8	7.374	-8.83	-7.86
TA12-8-D060	515	7.378	NaN	NaN
TA12-8-D061	516.2	7.382	-8.72	-8.06
TA12-8-D062	517.4	7.386	-8.73	-7.98
TA12-8-D063	518.6	7.390	-8.86	-8.21
TA12-8-D064	519.8	7.394	-8.93	-8.09
TA12-8-D065	521	7.398	-8.95	-7.85

Sample ID	Depth (mm)	Age (ky BP)	$\delta^{18}O$-raw (‰VPDB)	$\delta^{13}C$-raw (‰VPDB)
TA12-8-D066	522.2	7.403	-8.98	-7.62
TA12-8-D067	523.4	7.407	-8.84	-8.28
TA12-8-D068	524.6	7.411	-8.97	-8.52
TA12-8-D069	525.8	7.415	-8.88	-8.32
TA12-8-D70	527	7.419	-8.65	-7.97
TA12-8-D71	528.2	7.424	-8.60	-7.61
TA12-8-D72	529.4	7.428	-8.74	-7.58
TA12-8-D73	530.6	7.432	-8.74	-7.74
TA12-8-D74	531.8	7.436	-8.76	-7.75
TA12-8-D75	533	7.440	-8.78	-7.48
TA12-8-D76	534.2	7.445	-8.71	-7.16
TA12-8-D77	535.4	7.449	-8.39	-6.75
TA12-8-D78	536.6	7.453	-8.21	-6.13
TA12-8-D79	537.8	7.457	-7.91	-5.52
TA12-8-D080	539	7.461	-8.50	-6.55
TA12-8-D081	540.2	7.465	-8.48	-7.08
TA12-8-D82	541.4	7.470	-8.05	-5.90
TA12-8-D83	542.6	7.474	-8.44	-6.65
TA12-8-D84	543.8	7.478	-8.42	-6.35
TA12-8-D85	545	7.482	-8.47	-6.79
TA12-8-D86	546.2	7.486	-7.95	-5.39
TA12-8-D87	547.4	7.490	-8.15	-6.04
TA12-8-D88	548.6	7.495	-8.08	-5.93
TA12-8-D89	549.8	7.499	-7.87	-5.40
TA12-8-D90	551	7.503	-8.39	-6.75
TA12-8-D91	552.2	7.507	-7.86	-5.39
TA12-8-D092	553.4	7.512	-8.24	-6.37
TA12-8-D093	554.6	7.516	-8.00	-5.89
TA12-8-D94	555.8	7.520	-8.09	-6.14
TA12-8-D95	557	7.524	-7.92	-5.58
TA12-8-D96	558.2	7.529	-8.14	-6.16
TA12-8-D97	559.4	7.533	-8.14	-6.16
TA12-8-D98	560.6	7.537	-8.08	-5.97
TA12-8-D99	561.8	7.542	-7.94	-5.50
TA12-8-D100	563	7.546	-7.90	-5.09
TA12-8-D101	564.2	7.550	-8.07	-5.20
TA12-8-D102	565.4	7.555	-8.05	-5.16
TA12-8-D103	566.6	7.559	-8.17	-6.19
TA12-8-D104	567.8	7.563	-8.21	-6.16
TA12-8-D105	569	7.568	-8.32	-6.58
TA12-8-D106	570.2	7.572	-7.90	-5.54
TA12-8-D107	571.4	7.576	-7.83	-5.54
TA12-8-D108	572.6	7.581	-8.31	-6.45
TA12-8-D109	573.8	7.585	-8.21	-6.52

Sample ID	Depth (mm)	Age (ky BP)	δ^{18}O-raw (‰VPDB)	δ^{13}C-raw (‰VPDB)
TA12-8-D110	575	7.589	-8.24	-6.45
TA12-8-D111	576.2	7.594	-8.39	-6.63
TA12-8-D112	577.4	7.598	-8.81	-7.60
TA12-8-D113	578.6	7.602	-8.52	-7.21
TA12-8-D114	579.8	7.607	-8.45	-7.20
TA12-8-D115	581	7.611	-8.58	-7.62
TA12-8-D116	582.2	7.615	-8.71	-7.71
TA12-8-D117	583.4	7.619	-8.28	-6.96
TA12-8-D118	584.6	7.624	-7.84	-5.76
TA12-8-D119	585.8	7.628	-7.66	-5.74
TA12-8-D120	587	7.632	-7.87	-6.58
TA12-8-D121	588.2	7.636	-7.91	-6.53
TA12-8-D122	589.4	7.641	-7.76	-5.67
TA12-8-D123	590.6	7.645	-7.74	-5.91
TA12-8-D124	591.8	7.649	-7.93	-5.74
TA12-8-D125	593	7.653	-7.89	-5.81
TA12-8-D126	594.2	7.657	-7.84	-6.06
TA12-8-D127	595.4	7.662	-7.74	-5.53
TA12-8-D128	596.6	7.666	-7.72	-5.57
TA12-8-D129	597.8	7.670	NaN	NaN
TA12-8-D130	599	7.674	-7.81	-5.53
TA12-8-D131	600.2	7.679	-7.79	-5.71
TA12-8-D132	601.4	7.683	-8.15	-6.71
TA12-8-D133	602.6	7.687	-8.26	-7.37
TA12-8-D134	603.8	7.692	-7.71	-5.25
TA12-8-D135	605	7.696	-8.04	-6.33
TA12-8-D136	606.2	7.700	-8.57	-7.60
TA12-8-D137	607.4	7.705	-8.27	-7.62
TA12-8-D138	608.6	7.709	-8.60	-8.11
TA12-8-D139	609.8	7.713	-8.71	-8.35
TA12-8-D140	611	7.718	-8.78	-8.55
TA12-8-D141	612.2	7.722	NaN	NaN
TA12-8-D142	613.4	7.726	-8.82	-8.63
TA12-8-D143	614.6	7.731	-8.61	-8.38
TA12-8-D144	615.8	7.735	-8.50	-8.04
TA12-8-D145	617	7.739	-8.83	-8.91
TA12-8-D146	618.2	7.744	-8.96	-9.11
TA12-8-D147	619.4	7.748	-9.00	-9.22
TA12-8-D148	620.6	7.753	-8.88	-9.09
TA12-8-D149	621.8	7.757	-8.89	-9.00
TA12-8-D150	623	7.761	-8.72	-8.55
TA12-8-D151	624.2	7.766	-8.74	-8.39
TA12-8-D152	625.4	7.770	-8.81	-8.12
TA12-8-D153	626.6	7.774	-8.77	-8.10

Sample ID	Depth (mm)	Age (ky BP)	$\delta^{18}O$-raw (‰VPDB)	$\delta^{13}C$-raw (‰VPDB)
TA12-8-D154	627.8	7.779	-8.66	-7.80
TA12-8-D155	629	7.783	NaN	NaN
TA12-8-D156	630.2	7.788	-8.83	-8.01
TA12-8-D157	631.4	7.792	-8.80	-8.01
TA12-8-D158	632.6	7.797	-8.89	-8.21
TA12-8-D159	633.8	7.801	-8.88	-8.14
TA12-8-D160	635	7.806	-8.94	-8.40
TA12-8-D161	636.2	7.810	-8.71	-7.62
TA12-8-D162	637.4	7.815	-8.73	-8.14
TA12-8-D163	638.6	7.819	-8.86	-8.26
TA12-8-D164	639.8	7.824	-8.84	-8.09
TA12-8-D165	641	7.829	-8.77	-8.11
TA12-8-D166	642.2	7.834	-8.70	-7.97
TA12-8-D167	643.4	7.838	-8.54	-7.68
TA12-8-D168	644.6	7.843	-8.71	-8.23
TA12-8-D169	645.8	7.848	-8.87	-8.61
TA12-8-D170	647	7.853	-8.89	-8.62
TA12-8-D171	648.2	7.858	-8.66	-8.24
TA12-8-D172	649.4	7.863	-8.76	-8.24
TA12-8-D173	650.6	7.868	-8.66	-7.73
TA12-8-D174	651.8	7.873	-8.37	-7.23
TA12-8-D175	653	7.878	-8.39	-7.24
TA12-8-D176	654.2	7.884	-8.44	-7.32
TA12-8-D177	655.4	7.889	-8.66	-7.72
TA12-8-D178	656.6	7.894	-8.58	-7.55
TA12-8-D179	657.8	7.899	-8.45	-7.49
TA12-8-D180	659	7.905	-8.55	-7.70
TA12-8-D181	660.2	7.910	-8.53	-7.77
TA12-8-D182	661.4	7.915	-8.31	-7.19
TA12-8-D183	662.6	7.921	-8.38	-7.45
TA12-8-D184	663.8	7.927	-8.57	-7.57
TA12-8-D185	665	7.932	-8.69	-7.74
TA12-8-D186	666.2	7.938	-8.46	-7.23
TA12-8-D187	667.4	7.943	-8.42	-7.31
TA12-8-D188	668.6	7.949	-8.51	-7.39
TA12-8-D189	669.8	7.954	NaN	NaN
TA12-8-D190	671	7.960	-8.44	-7.54
TA12-8-D191	672.2	7.966	-8.36	-7.51
TA12-8-D192	673.4	7.971	-8.61	-7.83
TA12-8-D193	674.6	7.977	-8.34	-7.28
TA12-8-D 194	675.8	7.983	-8.62	-7.36
TA12-8-D195	677	7.989	-8.57	-7.72
TA12-8-D196	678.2	7.995	-8.63	-7.51
TA12-8-D197	679.4	8.000	-8.85	-8.06

Sample ID	Depth (mm)	Age (ky BP)	$\delta^{18}O$-raw (‰VPDB)	$\delta^{13}C$-raw (‰VPDB)
TA12-8-D198	680.6	8.006	-8.75	-7.96
TA12-8-D199	681.8	8.012	-8.59	-7.60
TA12-8-D200	683	8.018	-8.87	-8.32
TA12-8-D201	684.2	8.024	-8.86	-8.40
TA12-8-D202	685.4	8.030	-8.88	-8.37
TA12-8-D203	686.6	8.035	-8.66	-7.83